Universidad
Carlos III de Madrid
www.uc3m.es

PhD THESIS

Advanced PIV in Flows of Industrial Interest: Errors Characterization

Author:

Roberto Jiménez Sánchez

Directors:

José Ignacio Nogueira Goriba

Mathieu Legrand

Tutor:

José Ignacio Nogueira Goriba

Thermal and Fluids Engineering Department

Leganés, May 2017

Universidad Carlos III de Madrid
www.uc3m.es

TESIS DOCTORAL

PIV Avanzado en Flujos de Interés Industrial: Caracterización de errores

Autor:

Roberto Jiménez Sánchez

Directores:

José Ignacio Nogueira Goriba

Mathieu Legrand

Tutor:

José Ignacio Nogueira Goriba

DEPARTAMENTO DE INGENIERÍA TÉRMICA Y DE FLUIDOS

Leganés, Mayo 2017

Universidad Carlos III de Madrid
www.uc3m.es

(a entregar en la Oficina de Posgrado, una vez nombrado el Tribunal evaluador , para preparar el documento para la defensa de la tesis)

TESIS DOCTORAL

Advanced PIV in Flows of Industrial Interest: Errors Characterization

Autor: *Roberto Jiménez Sánchez*

Directores: José Ignacio Nogueira Goriba
Mathieu Legrand

Firma del Tribunal Calificador:

Firma

Presidente:

Vocal:

Secretario:

Calificación:

Leganés, de de

Acknowledgements (Reconocimientos)

Los trabajos realizados en el trascurso de este doctorado han sido parcialmente financiados por los siguientes proyectos:

- TERMOPIV-2: PIV avanzado en flujos de interés térmico (ENE2011 - 28024) y la beca asociada BES-2012-055996.
- HOT: European Humidity Optimization Tool. Entidad financiadora: Unión Europea (Clean Sky). SP1-JTI-CS-2013-02-80.

In addition, the activities and results obtained in the course of the stays completed by the PhD student have been partly funded by:

- The turbulent boundary layer measurements have partly been conducted in the framework of the DFG-project "Analyse turbulenter Grenzschichten mit Druckgradient bei großen Reynoldszahlen mit hochauflösenden Vielkameramessverfahren" (grants KA 1808/14-1 and SCHR 1165/3-1).
- The helicopter fuselage model measurements have been partially funded by the European Community's Seventh Framework Program (FP/2007-2013) for the Clean Sky Joint Technology Initiative under grant agreement number: CSJU-GAM-GRC-2008-01. In addition, the PhD student would like to thank PIVTec for permitting to use their software free of charge for analysis of the measurement campaign data.

Personal Acknowledgments (Agradecimientos)

Quisiera comenzar por expresar a José Ignacio Nogueira y Mathieu Legrand, mis directores de tesis, mi más profundo agradecimiento por todo el tiempo que han dedicado a que esta tesis saliese adelante; además de por todos los conocimientos compartidos conmigo, que me han permitido finalizar la tesis doctoral. Gracias también por su paciencia mostrándome en qué cosas estaba equivocado.

También expresar mi gratitud a los diferentes compañeros de despacho, en particular a Ricardo y Ciro, por compartir los momentos más duros de la tesis y olvidarlos aunque fuese momentáneamente a base de risas y alguna cerveza. Por similares razones agradecer a Rubén, Raquel y Antonio Famiglietti todo el apoyo moral.

A los catedráticos Antonio Lecuona y Pedro Rodríguez agradecerles toda su ayuda y sus valiosos consejos relacionados con la instalación experimental; también sus ánimos a lo largo de toda la tesis.

Quisiera continuar expresando un especial agradecimiento a los técnicos de laboratorio: Manuel Santos, David Díaz e Israel Pina, por su ayuda con las distintas instalaciones experimentales realizadas. Espero que hayan notado cierta mejoría en mis instalaciones; el recibir menos broncas de Manolo en las últimas instalaciones me resulta casi tan satisfactorio como terminar esta tesis.

Ahora, para agradecer a las personas que me apoyaron durante las estancias que realicé en el transcurso de esta tesis doctoral tengo que cambiar al inglés. I would also like to show my gratitude to the experimental aerodynamics PIV department in the DLR: Andreas Schröder, Daniel Schanz, Matteo Novara, Janos Agocs and Reinhard Geisler. I am really thankful for teaching me so much about the PIV technique and sharing an excellent insight into the German culture.

I wish also to express my appreciation to Fabrizio De Gregorio, from CIRA, which showed me many “secrets” on how to successfully perform PIV measurements and to keep them properly organized, an issue with which I struggled a lot. I would like to extend my thanks to Giovani Fatigati and Giuseppe Ceglia for their help in carrying out the CIRA experimental campaign.

También quisiera agradecer a mis amigos por todo su apoyo. Gracias por ayudarme a desconectar en los momentos difíciles, que no han sido pocos.

Por último, agradecer a mi familia todo su apoyo moral y aguantar quejas como los que más. Todos han sufrido bastante con esta tesis y espero que su finalización les satisfaga tanto como a mí.

Abstract

Turbulence is present in many flows of interest and is also one of the dominant factors over relevant phenomena. Some examples are aircraft drag and noise, pollutants dilution and spreading, combustion flames stabilization, etc. As such, it has always gathered much interest from the Fluid Dynamics community. Nevertheless, the problem of turbulence is not completely understood yet. Among the many means to study turbulent flows of interest, the PIV technique is the one on which this PhD focuses. PIV has always been considered of high value for turbulence measurements because of its ability to provide snapshots of the flow spatial distribution. The spatial distribution allows discriminating information with the flow length-scales; this distribution is highly useful as some physical magnitudes are associated with the large scales (e.g. the turbulent kinetic energy) and others to the small scales (e.g. the kinetic energy dissipation rate).

In order to study turbulent flows with the PIV technique, it is of importance to know the confidence interval of the PIV measurements. Nevertheless, given the complexity of turbulent flows and of PIV itself the confidence interval is not perfectly determined. Among other matters, the effect of the different error sources in the length-scale information that can be extracted from PIV demands for additional work.

Within this framework, this PhD focuses in characterizing the PIV errors produced by the interaction of the laser sheet thickness with turbulent spatial gradients. In addition, as the laser sheet thickness also influences on the errors from out-of-plane motion, and in that error source the time between laser pulses (Δt) comes into play, the interaction between both parameters has also been researched.

In order to study the influence of the errors in the length-scale information that can be extracted from PIV, an analysis of functions used in turbulence research to provide length-scale information has been performed. For the specific case of PIV measurements the second order longitudinal velocity structure function has been found as the most convenient tool.

As to the error characterization, the PhD recurs to the following set of tools. Firstly, a bibliographical research has been conducted to list, classify and model theoretically the error sources that can appear in PIV turbulence measurements, with special focus on their relative magnitude and behavior along the flow scales. The low pass filter effect and peak splitting have been identified as the preponderant error sources related to turbulent spatial gradients. In order to isolate their effect from that of other error sources a new tool (called PIV Simulator) has been implemented. In addition, a synthetic image generator is used to create images based on a homogeneous isotropic turbulence flow from a DNS simulation; those images include other error sources not given in the PIV Simulator. Finally a measurement campaign, tailored to checking the coherence of the numerical results in real PIV images, has been completed also. All these tools serve to reveal the errors expected to occur when measuring this type of flows, as well as to show the relative importance of the error under study with respect to other error sources.

The results obtained in this work include the total average error of PIV turbulence measurements as well as the length-scale distribution of those errors. In both cases, variations with the time between laser pulses and with the laser sheet thickness are presented. The interaction of the Δt with the laser sheet thickness through turbulent out-of-plane motions and turbulent spatial gradients is also clarified. Additionally, the interaction of the errors produced by large displacement differences in the interrogation volume (for large Δt) with image discretization errors (for low Δt) is also characterized.

The results of this work allow identifying the smallest turbulent length-scale that has the error under a certain level, due to the influence of the laser sheet thickness. From the results of this work, guidelines for performing optimized PIV turbulence measurements are obtained, in which the errors are meant to be kept to a minimum value. In line with these results, this work also includes error maps of both the instantaneous total error and of the error in the turbulent kinetic energy, as a function of the time delay and the laser sheet thickness.

Resumen

En este doctorado se analiza la capacidad de la técnica de Mono-PIV para medir flujos turbulentos. La turbulencia se da en muchos flujos de interés y además es un factor de gran importancia para muchos fenómenos relevantes. Algunos ejemplos son la resistencia de los aviones y el ruido que producen, la estabilización de llamas de combustión, etc. Por ello, siempre ha atraído el interés de la comunidad científica. Sin embargo, la problemática de los flujos turbulentos aún no está resuelta. Entre las distintas posibilidades para estudiar estos flujos, la técnica de PIV es en la que este doctorado está enfocado. La técnica de PIV siempre ha sido considerada de gran utilidad para estudiar flujos turbulentos, por su capacidad de proporcionar instantáneas de la distribución espacial del flujo. Esta distribución espacial permite discriminar información con las escalas espaciales del flujo, lo cual es de gran utilidad ya que ciertas cantidades físicas están asociadas con las escalas grandes (la energía cinética turbulenta) y otras con las escalas pequeñas (como por ejemplo la disipación de energía cinética).

Para estudiar flujos turbulentos con la técnica de PIV, es de importancia conocer el intervalo de confianza de las medidas de PIV. Sin embargo, dada la complejidad de los flujos turbulentos y de la propia técnica de PIV, el intervalo de confianza aún no ha sido determinado. Entre otras cuestiones, el efecto de las distintas fuentes de error en la información de las escalas de longitud que se puede obtener con PIV requiere de trabajo adicional.

En este marco de trabajo, esta tesis doctoral está focalizada en caracterizar los errores producidos por la interacción de los gradientes espaciales de turbulencia con el espesor de plano láser. Adicionalmente, como el espesor de plano láser también influye en los errores producidos por movimientos de partículas en perpendicular al plano, y en esta fuente de error el tiempo entre los pulsos láser (Δt) también entra en juego, la interacción entre ambos parámetros también ha sido investigada.

Para poder estudiar la influencia de los errores en la información de las escalas de longitud que se puede obtener con PIV, las distintas funciones usadas en investigación de turbulencia con este fin han sido analizadas. La función longitudinal de estructura de segundo orden ha sido identificada como la herramienta más conveniente.

En cuanto a la caracterización del error, esta tesis recurre a las siguientes herramientas. En primer lugar, se ha llevado a cabo una investigación bibliográfica para enumerar, clasificar y modelar teóricamente las fuentes de error que pueden aparecer en medidas de PIV de flujos turbulentos, con énfasis especial en su magnitud relativa y su comportamiento con las escalas de longitud. Así, el efecto de filtrado pasa-bajos y la separación de los picos de correlación se han identificado como las fuentes de error más relevantes relacionadas con los gradientes espaciales. Para estudiar su efecto de manera aislada, una nueva herramienta de análisis (llamada “Simulador de PIV”) ha sido implementada. Adicionalmente, un generador de imágenes sintéticas ha sido empleado para crear imágenes basadas en un flujo de turbulencia homogénea e isótropa, obtenido de una simulación DNS. Estas imágenes incluyen otras fuentes de error que no se dan en el

PIV Simulator. En último lugar, una campaña de medidas específicamente desarrollada para verificar la coherencia con los resultados numéricos ha sido completada también. El conjunto de estas herramientas permite revelar los errores que se pueden esperar en medidas de PIV de este tipo de flujos, así como mostrar la importancia relativa de los errores objetivo de la tesis comparados con otras fuentes.

Los resultados obtenidos en este trabajo incluyen el error total promedio así como la distribución con las escalas de longitud de los errores. En ambos casos, se incluyen variaciones del valor del error con el tiempo entre los pulsos láser y con el espesor de plano láser. Esto permite aclarar el error inducido por la interacción de ambos parámetros. La interacción entre los errores producidos por importantes diferencias de desplazamiento dentro del volumen de interrogación (para Δt alto) y los errores debidos a la información discreta de las imágenes (Δt bajo) también está caracterizada en este trabajo.

Los resultados de este trabajo permiten identificar la escala turbulenta más pequeña que tiene el error bajo un cierto nivel, debido a la influencia del espesor de plano láser. Los resultados de este trabajo permiten obtener directrices para realizar medidas de PIV optimizadas, en las que los errores se mantienen a un nivel mínimo. En la misma línea, este trabajo también incluye mapas de error tanto del error total de la velocidad instantánea como del error de la energía cinética turbulenta, en función de Δt y del ancho de plano láser.

Nomenclature

Roman symbols

a	Displacement difference inside the interrogation volume (cf. 5.3.5).
A	Constant that relates the turbulent fluctuations, the integral scale and the mean dissipation rate ($\epsilon = Au'^3/\mathcal{L}$) (Chapter 6).
$C_{u\varepsilon}(r)$	Covariance coefficient between velocity and error field (cf. 5.2.1.3).
d_D	Correlation peak-width.
D_G	Size of a bar rod on a grid for turbulence generation (Chapter 6).
D_H	Diameter of the hole of a perforated plate (Chapter 6).
D_I	In-plane dimension of the interrogation window projected in the measurement region.
D_{NOZZLE}	Outlet diameter of the contraction nozzle employed in the experimental setup described in Chapter 6.
d_P	Particle tracers diameter (cf. 5.3.14).
D_P	Particle image size defined between the e^{-2} waist points.
d_r	Camera pixel size.
d_τ	Airy disk size measured at the first dark ring.
$E(\kappa)$	Energy Spectrum Function (cf. 5.1).
$E_{LL}(\kappa)$	One-dimensional longitudinal spectrum (cf. 5.1).
IW_p	Interrogation window size in pixels (Chapter 6).
$\mathcal{L}$	Turbulent integral scale size.
M_0	Magnification factor.
M_G	Distance between the centers of two consecutive bar rods on a grid for turbulence generation (Chapter 6).
M_H	Distance between the holes of a perforated plate (Chapter 6).
p_{out}	Proportion of outlier vectors (Chapters 5 & 7).
px	Measure in pixels in the camera sensor.
r_A	Ratio of areas in the correlation map. Ratio between the area that actually contributes to the correlation and the area that contains the correlation information (cf. 5.3.5).
Re	Reynolds number.
Re_λ	Taylor micro scale Reynolds number.
$S_{LL}(r)$	Second order longitudinal velocity structure function at distance r (cf. 5.1).
$S_{LL}(r)\{u\}$	Second order longitudinal structure function at distance r calculated from the velocity field.
$S_{LL}(r)\{u_R\}$	Second order longitudinal structure function at distance r calculated from the real velocity field.
$S_{LL}(r)\{u_M\}$	Second order longitudinal structure function at distance r calculated from the measured velocity field.
$S_{LL}(r)\{\varepsilon\}$	Second order longitudinal structure function at distance r calculated from the error field.
$S_{LLL}(r)$	Third order longitudinal velocity structure function at distance r (cf. 5.1).
$\mathcal{S}_{PP}$	Perforated plate solidity.
T	Turbulent integral scale characteristic time (Chapter 3).
Th	Laser sheet thickness.
$\boldsymbol{U(x;t)}$	Velocity vector at a position $\boldsymbol{x}$ and at time instance t.
u'	Turbulent rms velocity fluctuation: average of u_i' in the three directions of space.
u_i'	Turbulent rms velocity fluctuation in direction i.

u_T	Velocity of the largest turbulent scale in the inertial range.
u_η	Kolmogorov turbulent scale characteristic velocity.
u_{out}	Outlier vectors magnitude (cf.).
u_R	Real velocity.
u_M	Measured velocity.
x	For a generic Mono-PIV measurement, one of the in-plane directions. On the case of the dedicated experimental setup designed in Chapter 6 and with the results in Chapter 7, it is the streamwise direction contained inside the measurement plane.
y	For a generic Mono-PIV measurement, one of the in-plane directions. On the case of the dedicated experimental setup of Chapter 6, it is the transversal direction contained inside the measurement plane.
z	For a generic Mono-PIV measurement, the out-of-plane direction.

Greek symbols

$\Delta S_{LL}(r)\{u\}$	Differences between the $S_{LL}(r)\{u_M\}$ calculated with different measurement conditions, or difference between $S_{LL}(r)\{u_R\}$ and $S_{LL}(r)\{u_M\}$ (cf. 5.2.1.1).
Δt	Time delay between the laser pulses.
ϵ	Mean dissipation rate.
ε_{LPF}	Low-pass error (cf. 5.3.3 and 5.3.5).
ε_{PL}	Peak-locking systematic error (cf. 5.3.7).
$\vec{\varepsilon}$	Error field.
η	Kolmogorov scale size.
λ	Taylor micro length-scale.
μ	Dynamic viscosity.
ν	Kinematic viscosity.
ξ_{PL}	Random error induced by peak-locking (cf. 5.3.8).
$\xi_{\Delta I}$	Random error induced by the particles light intensity change (cf. 5.3.9).
$\xi_{\Delta u}$	Random error induced by particles misplacement (cf. 5.3.4).
$\xi_{\Delta x}$	Random errors in determining the correlation peak location (cf. 5.3.10).
ρ	Density of a fluid.
τ_P	Particles relaxation time.
τ_T	Characteristic time of the largest turbulent scale in the inertial range.
τ_η	Kolmogorov turbulent scale characteristic time.

Acronyms

ppp	Particles per pixel.
PG	Propylene-Glycol.
AU	Arbitrary units.
SNR	Signal to Noise Ratio.
PVC	Polyvinyl chloride.
PP	Perforated Plate.
FOV	Field of View.
FFT	Fast Fourier Transform.
CFD	Computational Fluid Dynamics.
PIV	Particle Image Velocimetry.
SPIV	Stereo Particle Image Velocimetry.
TKE	Turbulent Kinetic Energy.

Contents

Introduction

Turbulent flows are of high relevance to many areas nowadays: aeronautical and vehicle industry, heat transfer, species dilution (e.g. pollutants) as well as biological flows. Their study could be tackled by different approaches: (i) analytical or theoretical rationale, (ii) computational fluid dynamics (CFD) or (iii) experimentally.

The analytical approach has limited reach since in general it can only be applied to particular cases involving simple geometries. In turn, computer simulations have experienced an increasing use owing to higher computational speed and capacity. Thanks to these improvements, it is possible to solve by Direct Numerical Simulations (DNS, simulations that incorporate the full turbulence phenomenology) more and more demanding problems. Nevertheless, DNS are not yet capable of dealing with large Reynolds numbers and complex geometries and even when DNS can be applied they require of very expensive computers and long simulation times. For these reasons, other CFD codes recur to models which simplifications need to be tuned and validated. For these CFD models experimental data is useful.

In addition, experimental tests are used in the industry in the development of new designs. Typically, experimental validation is the last step in the process. Being usually expensive, the number of test cases is generally alleviated by numerical simulations. The most promising prototypes from the numerical simulations are tested on experiments to validate the results.

The theoretical and the numerical simulations approaches permit to obtain many physical magnitudes at the same time. However, experimental techniques normally provide one or two physical quantities. In that regard, in the field of experimental Fluid Dynamics the velocity is a commonly measured propriety. The particle image velocimetry (PIV) technique is widely used nowadays to provide experimental velocity field measurements. As compared to other experimental techniques that measure the velocity, it has the advantages of (i) being non-intrusive and (ii) providing the velocity of the fluid in multiple spatial points instantaneously. Consequently, PIV measurements permit to observe the turbulent spatial structures, or to calculate spatial derivatives, which are features of interest in the study of turbulent flows. The technique can be especially useful for tuning or validating numerical simulations, since those simulations typically provide properties values in a mesh of points, as PIV does.

For these purposes, it is of importance to provide the confidence interval of the measurement. That permits to interpret the differences (if any) to the results of numerical simulations. However, owing to PIV intrinsic complexity and the many available variants, PIV errors are not yet fully characterized nor completely understood, especially because of the multiple error sources and their possible interactions.

It is within the error assessment topic that this PhD makes its contribution. This work focuses on the capacity of the PIV technique to measure turbulent flows. The research group hosting the PhD student is specialized on this measurement technique and has

already contributed into the field of error assessment. In that sense, this PhD thesis focuses on characterizing the errors related to the illumination plane effective thickness and time delay between two images in the presence of turbulence. The PhD thesis is part of research project "TERMOPIV-2: PIV avanzado en flujos de interés térmico" (ENE2011 - 28024), that deals with the characterization of thermal flows of relevance for the industry by means of PIV, with emphasis in errors characterization. Further research in this line of work should allow optimizing the acquisition parameters in order to enhance the spatial resolvable range. Thus, the contribution of this PhD thesis is of relevance to the experimental PIV community, for developing error assessment procedures.

Additionally, the use of the PIV technique has already extended beyond the academic field and successful measurements are performed for the industry. The technique is gaining in importance and in users, which increases the possible diffusion and impact of the results of this PhD thesis. For all these reasons, the PhD was focused in this field.

The **outline** of the PhD is as follows:

- In the first chapter, the PIV technique is introduced, with the aim of showing how it developed to be a convenient tool for turbulence measurements. Additionally, some aspects of turbulent flows of relevance to this study are described as well. A previous research work (Nogueira *et al.*, 2012) that lays out the main constraints to perform turbulence measurements with PIV is explained as a starting point for the present work.
- Chapter 2 deals with the motivation and objectives of this thesis and describes the methodology stablished.
- In Chapter 3, the numerical tools required for characterizing errors along the length scales are described. This involves the development of a synthetic image generator aiming at emulating the acquisition of real images from a known turbulent flow. Another tool is also developed in this chapter devoted to simulating the PIV response to turbulence.
- Chapter 4 is devoted to the application and implementation of error related methodologies in the framework of wind-tunnel facilities. The PhD student has participated in two experimental campaigns during his two stays in PIV leading research centers, which helped on learning the measurement technique and error handling protocols.
- In Chapter 5 the theoretical rationale required for the analysis of the results is stablished. It offers a compilation of different error sources identified in previous research.
- Chapter 6 is dedicated to the experimental campaign designed to validate the results of the developed numerical tools in the previous chapters.
- Chapter 7 presents the results from the measurement campaign and its comparison with those of numerical tools. The results are analyzed and discussed in detail.
- Finally, Chapter 8 draws the conclusions of this work.

Chapter 1 **Introduction**

1.1 THE PIV TECHNIQUE

1.1.1 General characteristics

The Mono-PIV technique employed in this PhD can be classified as follows (Raffel *et al.* 2007):

- It is a multi-point technique, i.e. it provides the velocity in several points simultaneously as opposed to other techniques, e.g. HWA (Hot Wire Anemometry) or LDA (Laser Doppler Anemometry), that provide the velocity in a single point.
- Non-intrusive technique. As compared to other velocimetry techniques that require of probes to make a measurement (and eventually perturb the flow), the PIV technique is an optical technique which does not require introducing any probes in the flow.
- Indirect velocity measurement. PIV measures the velocity of the tracer particles in order to provide that of the fluid carrying it.
- 2D-2C: the velocity data is furnished in a measurement plane, i.e. in two spatial directions. Additionally, not the full velocity vector is provided for each mesh point and only the projection of the vector in the measurement plane is provided (2 components).

1.1.2 PIV working principles, major developments and error assessment

1.1.2.1 *Main components*

The PIV technique estimates the velocity of the flow by measuring the displacement of particles (or tracers) carried by the flow. The displacement is obtained by imaging the particles a certain number of times thanks to a camera. In order for the particles to form images, they need to scatter enough light, which is achieved by recurring to powerful light sources, usually pulsed lasers. In the case of the 2D-2C implementation of PIV, only the particles contained inside the illuminated plane contribute. The sketch in Figure 1.1 indicates the different components required to perform this type of measurement.

In the particular case of the technique as used in this PhD, the displacement field is calculated from the particles illuminated with two laser pulses. The light scattered by the particles for each of the laser pulses is stored into a different frame in the camera. This is identified as double-frame single-exposure recording (Raffel *et al.*, 2007). Normally, each of the laser pulses is provided by a different laser head achieving very small time delay between pulses. The laser beams produced by each of the laser heads are combined in the laser optics. For single-exposure PIV to be possible it was necessary for the cameras to achieve low times between both expositions, typically in the order of microseconds. In the past, when cameras technology did not allow for this type of measurement, both laser pulses were stored in the same frame: that was single-frame double-exposure PIV. However, the displacement allowed needed to be large enough for both particle images to be separated and there was a directional ambiguity (Willert and Gharib, 1991). The different components needed to perform PIV measurements are briefly described below.

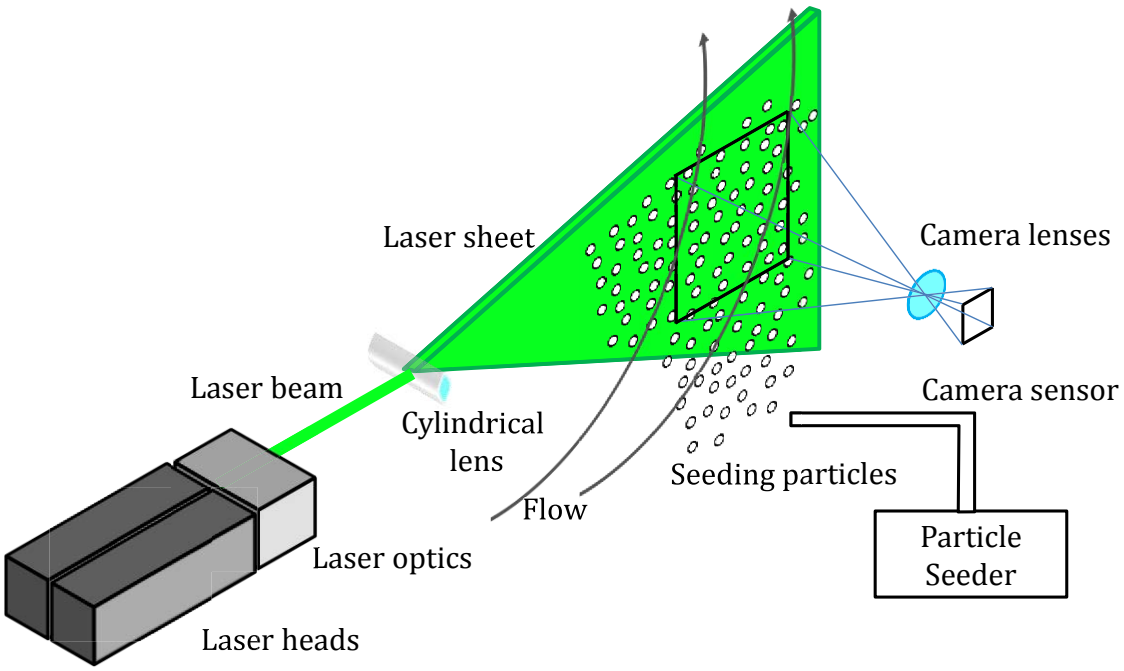

Figure 1.1 Components of a PIV measurement.

PIV tracers can be naturally present on the flow or they can be artificially seeded into it. It is desired for the particles motion to resemble that of the flow as much as possible. The particles are moved by the drag exerted by the flow over them and are deviated from it due to other forces such as buoyancy, weight or inertial forces (Adrian and Westerweel, 2011). The capacity of inertia to induce a lag in the movement of particles with respect to the flow is reduced by recurring to particles with similar density to that of the fluid (Adrian and Westerweel, 2011), when possible. As to the size, particles need to be small enough (small inertia) to capture the flow variations and large enough to scatter sufficient light (large surface).

For liquid flows, the density of tracers can resemble much more that of the fluid and therefore particles do not need to be very small (on the order of a few tens of micrometer, Adrian and Westerweel, 2011). For gaseous flows, density matching is more complicated, which is compensated by recurring to smaller particles than for liquid flows (on the order of the micrometer, Adrian and Westerweel, 2011). Recently, soap bubbles filled with helium permit to match the density of tracers to that of the gas medium measured, allowing for larger particle sizes (sizes of the order of 200-300 μm) and larger measurement volumes (Raffel *et al.*, 2007).

Depending on the particles size, the light power required for them to produce distinguishable images will vary. For PIV measurements, the use of **pulsed lasers** is widely spread. The laser pulse duration has to be in the order of nanoseconds, in order to produce frozen particle images instead of streaks (Raffel *et al.*, 2007). Additionally, this type of light source has the advantages of (Raffel *et al.*, 2007) (i) being concentrated into a beam, which allows forming easily a light sheet, (ii) being powerful enough, thus allowing the use of micrometric particles and (iii) the light emitted can be monochromatic, thus

avoiding chromatic aberrations. Solid-state Nd:YAG lasers are amongst the most common nowadays for PIV (Adrian and Westerweel, 2011). In order to produce the light sheet, the laser beam goes through a cylindrical lens as indicated in Figure 1.1. The laser sheet thickness in the measurement region can be adjusted; commonly, a combination of spherical and cylindrical lenses is employed with that purpose.

As to the **cameras** used for PIV recording, digital cameras are mainly used (Raffel *et al.,* 2007). As compared to photographic methods, the fact that (i) the images are obtained immediately, which allows assessing the measurement on-site and (ii) avoiding any photochemical process, reducing the time required overall to obtain the results, can be mentioned as advantages. In the digital sensors the light (photons) is transformed into electric charge (electrons) in an array of sensitive elements (pixels), forming the images (Raffel *et al.,* 2007, Adrian and Westerweel, 2011). Different technologies are available; for PIV the more widespread are CCD (charge coupled devices) and CMOS (Complementary Metal Oxide Semiconductor) sensors. Desired characteristics for PIV cameras are a high sensitivity to light, low noise and in the particular case of single-exposure PIV low time delay between camera exposures.

Additionally, the cameras and the laser need to be synchronized. In the case of double-frame single-exposure PIV, where two images are taken containing one laser pulse each, each laser pulse should be fired during the exposure time of the corresponding image. This is sketched in Figure 1.2. The exposure time is the interval during which the camera acquires light to give the image. This is typically achieved by dedicated electronic equipment that sends the orders to each component.

The images acquired by the cameras are divided into interrogation windows (Raffel *et al.*, 2007) and a displacement is provided for each of them, as illustrated in Figure 1.2. The displacement is calculated by means of statistical methods. The displacement determined in such a way is transformed into a velocity by taking into account the time elapsed between the two laser pulses (Δt in Figure 1.2) and the camera lenses properties. Specifically, the magnification is required, which can be seen as the ratio between lengths in the image plane and the projected length in the measurement plane. The magnification can be calculated from distances z_0 and Z_0 in the figure as (Raffel *et al.*, 2007):

$$M_0 = z_0/Z_0$$

The velocity is obtained then as:

$$\vec{u} = \vec{d}/\Delta t M_0$$

The lenses employed also give the size of particle images. Since particles are typically very small in size (somehow equivalent to a distant point source), the image of a particle over the sensor is not a point anymore. Instead, a PIV particle forms a Fraunhofer diffraction pattern (Raffel *et al.*, 2007). The circular pattern is known as Airy disk, and the minimum image diameter obtained for a set of lenses and coherent light is given by (Raffel *et al.*, 2007):

$$d_\tau = 2.44 f^{\#}(M_0 + 1)\lambda$$

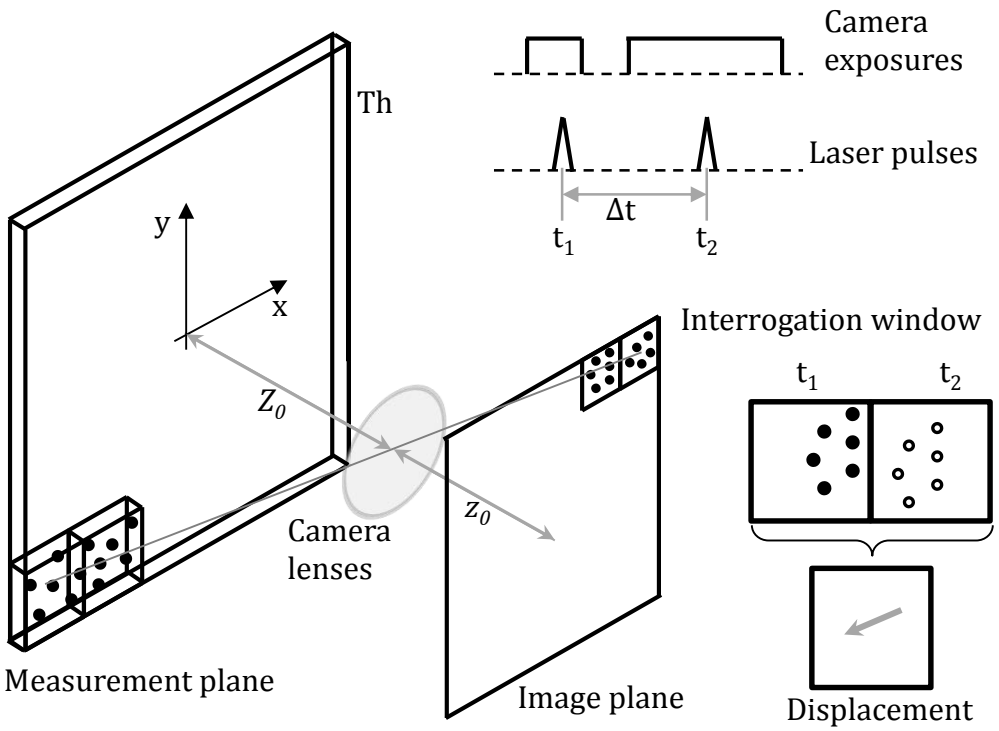

Figure 1.2 Sketch of how a displacement is obtained in a PIV measurement.

The expression above is valid for particles that are focused. The f-number can be calculated from: $f^{\#} = f/D_a$ with f the focal length and D_a the aperture diameter of the lenses (Raffel *et al.*, 2007). In PIV, this image diameter is only given when measuring small particles (of the order of a few microns) at low magnifications, as is the case of the measurements presented in this PhD. If that is not the case, the geometric projection of the particle in the sensor has to be taken into account.

1.1.2.2 *Interrogation process and limitations*

In this subsection, the PIV interrogation process, as it was performed on the first digital measurements (Willert and Gharib, 1991), is described. The limitations that were identified on those first works are also outlined. For the description in this subsection, it is assumed that both image frames are divided in the same interrogation windows. An interrogation spot with the particles images at the first (I_1) and the second (I_2) laser pulse is sketched below. The particles from both frames are plotted overlaying in the right image, with the displacement of each particle image indicated.

Usually, for the double-frame single-exposure images, the displacement is obtained by the cross-correlation between the two interrogation windows intensity fields, which is defined as (for continuous image fields):

$$R_{I_1 I_2}(\Delta x, \Delta y) = I_1 \star I_2 = \int_x \int_y I_1(x,y) I_2(x+\Delta x, y+\Delta y) \mathrm{d}x\mathrm{d}y$$

Where I_1 and I_2 indicate the interrogation windows intensity fields for both laser pulses, x and y are the in-plane coordinates and $\star$ is used to indicate the cross-correlation operation. The integration is performed in the whole interrogation window area.

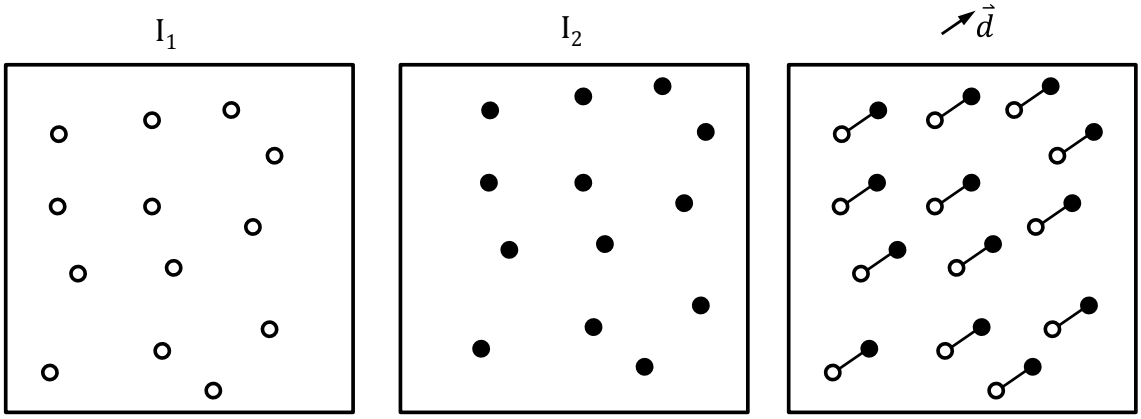

Figure 1.3 Particle images in the first frame (left), second (center) and overlaying (right).

In the past, when the technique was analogical, the displacement was obtained with Young fringes (Adrian, 2005). However, for digital PIV (which is the support used nowadays) the correlation has replaced this method.

For discrete image fields I_1 and I_2 would be defined over the pixels of the sensor and the integrals would have to be replaced by sums (Raffel *et al.*, 2007):

$$R_{I_1 I_2}(\Delta x, \Delta y) = \sum_{x=-K}^{K} \sum_{y=-L}^{L} I_1(x,y) I_2(x+\Delta x, y+\Delta y) \qquad (1.1)$$

A discrete correlation map as defined above is plotted below in Figure 1.4, for a uniform displacement. The correlation value is in arbitrary units and the shifts are in pixels. The highest peak is associated with the displacement of the particles in the interrogation window. The rest of peaks are produced by the correlation of a particle image with a different particle image in the second frame (cross-talk peaks) or from the correlation of particles images with the sensor noise.

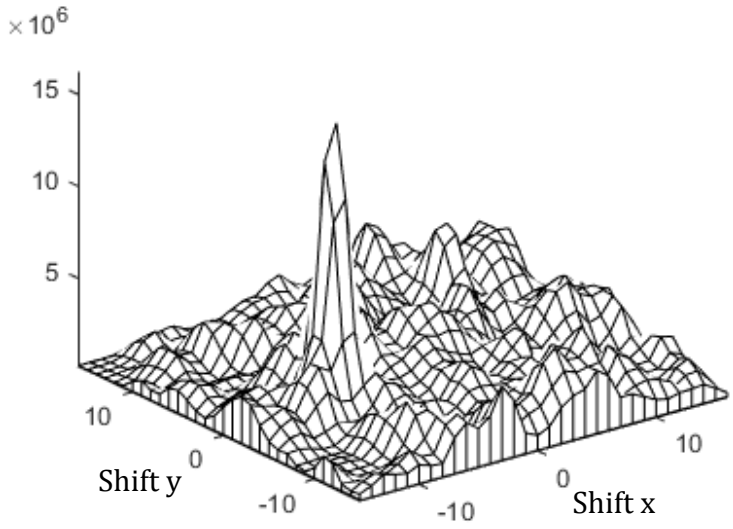

Figure 1.4 Example of a discretized correlation map.

Normally, in order to speed up the calculation of the cross-correlation, the operation is performed in Fourier space. By recurring to the correlation theorem (Raffel *et al.*, 2007) the cross-correlation calculated by expression (1.1) can be approximated in terms of the Fourier transforms of I_1 and I_2, exactly by the complex conjugate multiplication:

$$\hat{R}_{I_1 I_2} = \hat{I}_1 \cdot \hat{I}_2^* \Leftrightarrow R_{I_1 I_2} = I_1 \star I_2$$

Where the circumflex accent ^ is used to indicate the Fourier transform of a function and the * superscript indicates the complex conjugate.

The calculation speed is improved thanks to the Fast Fourier Transform algorithm. With this algorithm and by recurring to the computation in the Fourier domain, if N is the width in pixels of the square interrogation window, the number of operations is of the order of $[(N^2 \cdot \log_2 N)]$. However, the number of operations required by the direct correlation of expression (1.1) is of the order of $[(N^4)]$ (Raffel *et al.*, 2007).

In addition to both those methods, there are other ways to compute the correlation. Some of those were tested in Chapter 4 and are described there. Whatever the method, the discretized correlation map (which has a resolution of a pixel, as the images) is used to obtain the final displacement value, normally by some kind of subpixel interpolation (or otherwise the uncertainty in the displacement would be of ±1/2 pixel, Raffel *et al.*, 2007).

A common approach is to fit the correlation data with a known function, from which maximum the subpixel displacement is obtained. Normally, for narrow particle images, the correlation from three adjoining points in each direction is used to define the function (Raffel *et al.,* 2007). Different methods can be used with this purpose, for example, peak-centroid, parabolic peak-fit or Gaussian peak-fit. The Gaussian peak-fit is the one used in this PhD, and it is also commonly used by the PIV community. This is so, because the correlation displacement peak should resemble a Gaussian function. The Airy pattern that describes the intensity distribution of a particle over the sensor is fairly well adjusted by a Gaussian function. If the particles intensities distributions are Gaussian functions, so is the correlation between them (Raffel *et al.,* 2007). Choosing a Gaussian function to retrieve the displacement seems like a convenient fit then.

In any case, the three point estimators mentioned above work following the same process. First, the maximum correlation value is found. This correlation value is identified as $R_{(i,j)}$ below. Then, the correlation values at the two adjoining points are taken: for the first direction those points are (i-1,j) and (i+1,j) with the correlation values $R_{(i-1,j)}$ and $R_{(i+1,j)}$ respectively. From all three correlation values, the subpixel displacement in that direction is (for the Gaussian peak-fit case, Raffel *et al.,* 2007):

$$d_x = i + \frac{\ln R_{(i-1,j)} - \ln R_{(i+1,j)}}{2 \ln R_{(i-1,j)} - 4 \ln R_{(i,j)} + 2 \ln R_{(i+1,j)}} \tag{1.2}$$

Due to non-linear response of the camera sensor, image discretization, background noise, or random peaks in the correlation map, the displacement peak may not be exactly Gaussian. As a result, the displacement measured has an error $\xi_{\Delta x}$. Typical error values calculated by Monte-Carlo simulations and analytically are between $\xi_{\Delta x} \sim 0.05$ pixels to 0.1 pixels (Willert and Gharib, 1991, Westerweel, 1997, Westerweel, 2000, Raffel *et al.*, 2007, among others). The error value depends on the particle image size, out-of-plane motion, and spatial gradients, among other things. Further details onto this error are provided in section 5.2; for now, the important aspect is the limitation stablished on the low displacements, $\xi_{\Delta x}$.

In consequence, it is of interest to set a Δt such that the displacements are larger than that error, so it has a low importance over the displacement. The dynamic velocity range (DVR) is defined as the ratio of the maximum velocity to the minimum resolvable velocity (Adrian, 1997). By translating the error into velocity units:

$$\xi_u = \frac{\xi_{\Delta x}}{M_0 \Delta t}$$

$$DVR = \frac{u_{max}}{\xi_u} = \frac{u_{max} M_0 \Delta t}{\xi_{\Delta x}}$$

The dynamic velocity range gives an idea of the velocity variations that can be measured. For a flow that varies in space, a large DVR allows measuring the low and high velocities present, by properly setting the experiment. Turbulent flows usually present a broad range of velocities (as shown in 1.2); in consequence, a large DVR is desired for measuring this kind of flows.

Limitations on the measurement of large displacements

The problems on the small displacements have been roughly illustrated above. As to the large displacements, $d_{max} = u_{max} M_0 \Delta t$, the common limitation is stablished by the signal-to-noise ratio of the correlation. As can be appreciated in Figure 1.4, in addition to the displacement peak (the signal), the correlation map contains other peaks not associated to a displacement (the noise). The quality of the signal is degraded from two factors (Keane and Adrian, 1992): (i) if the number of particle image pairs is low and (ii) due to the presence of spatial gradients in the interrogation window.

A reduction in the number of matching particle image pairs can be produced by:

- In-plane loss of pairs.
- Out-of-plane loss of pairs.
- Reducing the size of the interrogation spot.

The in-plane motion loss of pairs is induced by particles entering or leaving the interrogation spot. The importance of this phenomenon is given by the size of the interrogation window and the time delay between the laser pulses. The effect is sketched below, with particles from both frames overlapping. The particle images in the first frame are filled white and in the second frame in black. The loss-of-pairs is quantified by a factor F_I <1 that gives the effective interrogation area that has particles with a matching pair. This effect has been reduced thanks to the developments in the algorithm that are mentioned afterwards.

In addition, if the interrogation size is reduced, the factor F_I should get smaller, as the displacements would represent a larger ratio with respect to the window size.

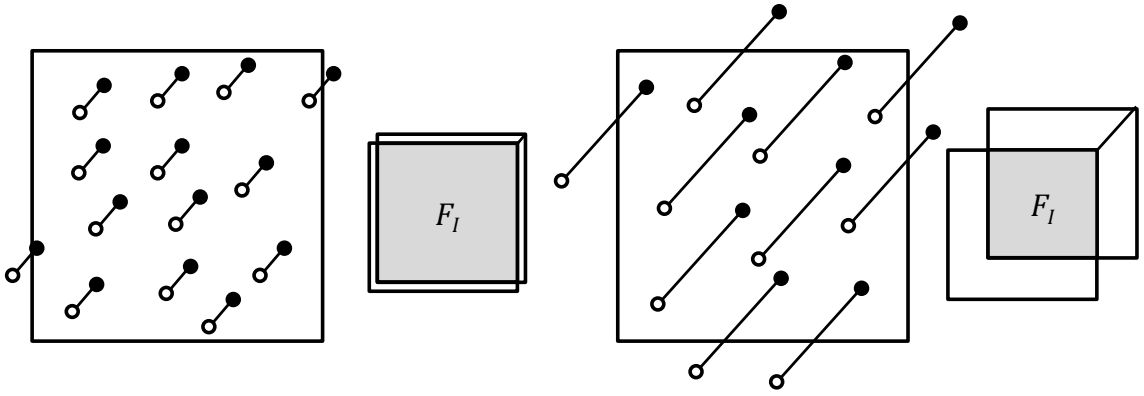

Figure 1.5 Effect of the in-plane motion in the effective number of particle image pairs and factor F_I to take into account this fact (after Westerweel, 1997).

The out-of-plane motion is produced when a 3D flow is measured by PIV, which is commonly the case of most flows (especially if the flow is turbulent). The velocity component perpendicular to the laser sheet induces a similar effect than in-plane motion and makes some particles to be present only on either of the two frames. Again, this effect is quantified by a factor F_0 <1. In the case of a uniform laser sheet profile, the value of the factor is depicted in Figure 1.6-right. This effect can be mitigated also by enlarging the second laser pulse thickness (Keane and Adrian, 1992); however, that requires more light power on the second pulse and the spatial resolution is penalized.

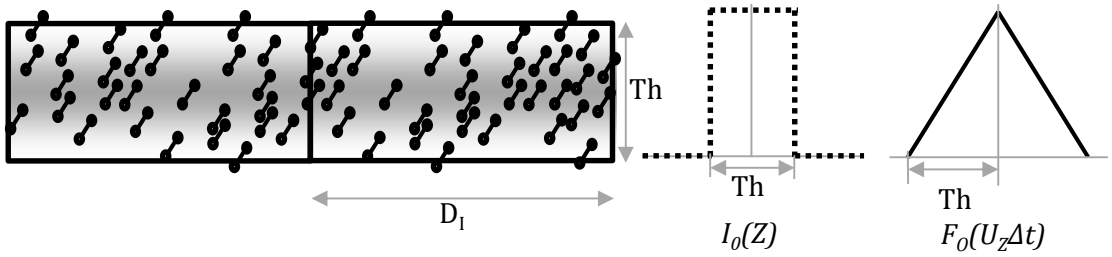

Figure 1.6 Left: interrogation spots with out-of-plane motion. Middle: Uniform laser profile. Right: Factor F_0 for a uniform laser profile(after Westerweel, 1997).

As a result, the number of matching particle image pairs can be expressed as: $N_I^* = N_I F_I F_0$, where N_I is the mean number of particle images in an interrogation window (Keane and Adrian, 1992, Westerweel, 1997, among others). As can be appreciated, increasing Δt to obtain large displacements results in a reduction of F_I and F_0, which is translated in a reduction of the matching number of particle image pairs. Eventually, if N_I^* is too low it is possible that the peak producing the maximum correlation value is not produced by the displacement. Keane and Adrian (1992) obtained the valid detection probability (the probability that the correlation displacement peak is larger than the random noise peaks) as a function of N_I^*, the results are in Figure 1.7. From those results, for single-exposure measurements, the advised effective number N_I^* was 7 (Keane and Adrian, 1992).

The other factor mentioned to degrade the correlation performance is spatial gradients (Keane and Adrian, 1992). The result of spatial gradients is that the correlation of each particle image with the matching pair in the second frame does not fall at the same displacement value, as in the case of uniform displacements. As a result the displacement peak is broadened and the valid detection probability reduced. In order to keep a high detection probability, Keane and Adrian (1992) suggest the following values:

- $M_0|\Delta \boldsymbol{u}|\Delta t/D_I < 0.03$, with $|\Delta \boldsymbol{u}| = (\partial \boldsymbol{u}/\partial \boldsymbol{x}) \cdot (L/2)$ where L is the larger dimension in the interrogation volume. $|\Delta \boldsymbol{u}|$ represents the velocity difference in the interrogation spot.

- $M_0|\Delta \boldsymbol{u}|\Delta t/d_\tau < 1$, where d_τ is the particle image diameter defined above.

A more detailed description of the gradient effects was given by Westerweel (2008). Those results and other error sources are described in more detail in section 5.2.

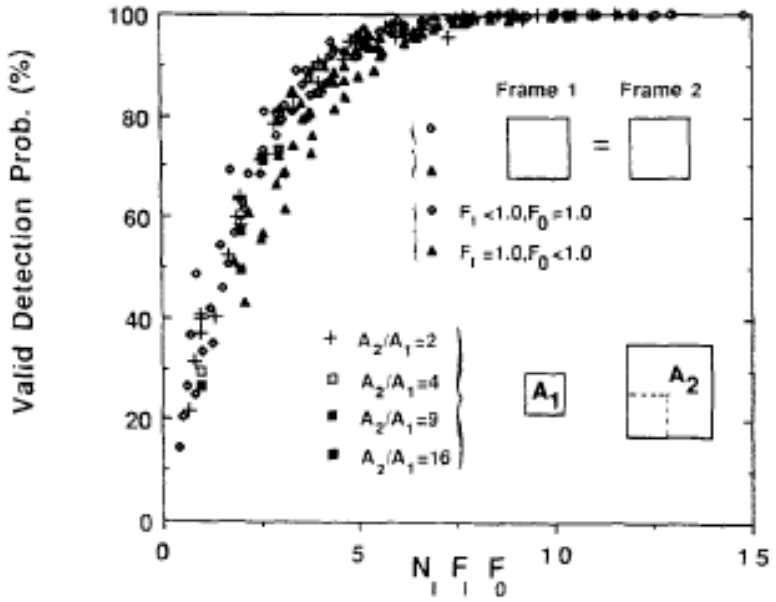

Figure 1.7 Valid detection probability against the effective number of image pairs $N_I F_I F_0$, for double-frame single-exposure PIV (from Keane and Adrian, 1992).

As can be appreciated, both the minimum N_I^* and the presence of spatial gradients impose a limitation on the time delay that could be used. Consequently, in order to have a large DVR, the interrogation window size should be enlarged. In turn, that results in a reduction of the spatial resolution and the smallest resolvable spatial variation is penalized (Adrian, 1997). Therefore, the experimentalist measuring with PIV had to prioritize what was more interesting to him. In the next subsection, some improvements of the technique that permitted to overcome some of these limitations are shown.

Limitation produced by the interrogation volume size

As mentioned above, PIV obtains the displacement by cross-correlation (either direct or in Fourier domain) of two interrogation windows. As a result, all the particles within the sensing domain (i.e. the interrogation volume) have the potential to contribute to the displacement value. The problem is quite complex and a more detailed description of what the correlation provides is studied in section 5.2 and as a matter of fact is object of study of the PhD. For this introductory chapter, the main point to retain is that due to the size of the interrogation window the spatial variations that can be resolved from PIV are limited. Typically, PIV is symplified as providing a moving average of the flow velocities inside the sensing domain. From that point of view, the effect of PIV is like that of a low-pass filter, it progressively suppresses the wavelengths smaller than the interrogation window size (Willert and Gharib, 1991). The spatial wavelength response of several windows is shown in Figure 1.12, after Willert and Gharib (1991).

1.1.2.3 *Development milestones*

The development of the technique is summarized briefly below by some milestones. More in-depth reviews of the technique and the different developments can be found in Grant (1997), Adrian (2005), Raffel *et al.* (2007) or in Adrian and Westerweel (2011). The idea is to illustrate the technique at the state it has been used in this PhD, focusing on developments of components or of the algorithms that improved the performance of PIV for measurements of turbulent flows.

The first PIV measurements, according to Adrian (2005), can be attributed to Meynart (1980 or 1982, among others). Those measurements were performed in a photographical support, analogically.

Willert and Gharib (1991) and Westerweel (1993) reported the first measurements on a digital CCD video camera. The digital support, which at the time did not have as many pixels as the analogical one, enabled for full analysis on computers, with the advantages mentioned previously. The three points Gaussian peak-fit was proposed by Willert and Gharib (1991), to obtain subpixel displacements. Also, Willert and Gharib (1991) used double-frame single exposure images and identified their advantages. However, as stated by the authors, the 30Hz acquisition rate of video cameras only allowed for analysis of low-speed flows. Higher speed flows had to be recorded in multiple exposure frames.

Kodak developed interline-transfer video cameras for the PIV market convinced by Lourenço *et al.* (1994), according to Adrian (2005). Such cameras permitted to store two consecutive images within a very short time delay, by transferring the first image into an on-chip storage well (Adrian, 2005). With these cameras, obtaining double-frame single-exposure images was also made possible for high speed flows.

Prior to the development of cameras, solid-state Nd:Yag lasers -according to Adrian (2005)- were used first by Kompenhans and Reichmuth (1986). That permitted obtaining double-exposure images of micron sized particles that followed turbulent flows.

Keane and Adrian (1992) proposed the use of a window offset to remove the effect of in-plane loss of pairs mentioned previously. This was implemented by Westerweel *et al.* (1997), with an offset equal to the integer part of the displacement. The same work also showed the improvement in terms of noise reduction and optimization of the performance for the calculation of the displacement. Additionally, Westerweel *et al.* (1997) proposed the combination of a window offset with a reduction in the size of the interrogation window, to further reduce the measurement error.

Huang *et al.* (1993) may have been the first in using image distortion. The idea of image distortion (or image deformation) is to deform one of the PIV image frames (or both) with the displacement obtained in a previous iteration, so that in next iterations the displacement progressively approaches zero. It had been obtained (Westerweel, 1993, or Westerweel, 1997, among others) that for low displacement values the error was proportional to the displacement. Image deformation was deemed then to reduce measurement errors. Additionally, the effect of some in-plane spatial gradients in the correlation is reduced by this method.

Nogueira *et al.* (1999) implemented the image deformation method and managed to successfully resolve smaller spatial scales than the PIV interrogation window size. In addition to the image distortion, the authors also included an image window weighting procedure. This procedure weighs the intensity of the image pixels for the calculation of the correlation: the farther a pixel is from the IW center the less it contributes to the correlation map. Previously, the averaging of the interrogation window was a limiting factor on the scale size that could be resolved, as mentioned above and studied in more detail later (cf. 1.2.2 and 5.3.3).

The combination of a window offset with a progressive reduction in the interrogation window size proposed on Westwerweel *et al.* (1997) appears to have been introduced by Scarano and Riethmuller (1999). They referred to this method as *Window Displacement Iterative Multigrid* technique. The idea of the technique was to start at large interrogation windows and then use the displacement measured with those windows as an initial offset on progressively smaller window sizes. The combination of large interrogation windows at the beginning of the process with small ones at the end allows: (i) avoiding in-plane loss of pairs and obtaining a large signal to noise ratio in the correlation maps and (ii) obtaining a good spatial resolution. As a result of the multigrid technique, the displacements allowed could be larger, without that resulting in a penalty on the spatial resolution. The method was later updated to incorporate image deformation in the iterative process, and this is the PIV evaluation process used on this PhD. A review on the possible different implementations of this method is provided in Scarano (2002).

As a result of these developments, in-plane loss of pairs is no longer a limitation to the Δt and the interrogation window size that can be used. That allows measuring with a large DVR without having to penalize the spatial resolution. Additionally, the image deformation methods manage to provide lower subpixel errors $\xi_{\Delta x}$ (Astarita and Cardone, 2005), further increasing the DVR. In conclusion, those developments made the technique more suitable for measurements of turbulent flows (cf. 1.2.2).

Developments of the technique to yield more data

In parallel to the improvements above, the technique has been extended to provide more data. Although the measurements reported in this PhD are of the Mono-PIV type (2D-2C) the developments are mentioned to illustrate the state-of-to-art of the technique and the possible value of the additional information. Only those considered more common are reported below. Further developments can be found in Raffel *et al.* (2007), Adrian and Westerweel (2011) or Westerweel *et al.* (2013), among others.

Stereo-PIV (SPIV): By recurring to a second camera, it is possible to reconstruct the out-of-plane component of velocity, but only on the measurement plane (i.e. SPIV is 2D-3C). Some research works that performed the first measurements with this technique are Arroyo and Greated (1991), Prasad and Adrian (1993), or Willert (1997), among others.

Tomo-PIV (Elsinga *et al.,* 2006). In this case the three velocity components are provided varying with all three spatial directions (i.e. it is 3D-3C). That gives access to the full velocity gradient tensor. Tomo-PIV measurements are usually performed with several cameras with different viewing angles. The technique requires the reconstruction of the particles positions in the measurement volume.

Holographic PIV (Hinsch, 1995, among others): makes use of the coherence of the laser light to record interference patterns. The interference patterns are obtained by superimposing a reference wave from the laser to the light scattered by particles (Raffel *et al.,* 2007), together in the recording platform (analogic or digital). A volume reconstruction of the velocity vector (3D-3C) is obtained with this technique, without having to recover particles positions in the volume (Hinsch, 2002, Raffel *et al.,* 2007).

Additionally, when in possession of high speed cameras and lasers, or for flows that evolve slowly, some of the measurement techniques mentioned above could provide **time-resolved** data. Temporal variations of the flow are resolved with sufficient resolution for these measurements. Usually, for conventional PIV equipment, the acquisition rates of PIV images is on the range of f~[1-10]Hz. High-speed cameras and lasers can achieve 10 kHz or higher acquisition rates (Raffel *et al.,* 2007).

The different techniques and what they provide are summarized in the image below (from Hinsch, 1995, the updated version of Scarano, 2013, is shown here):

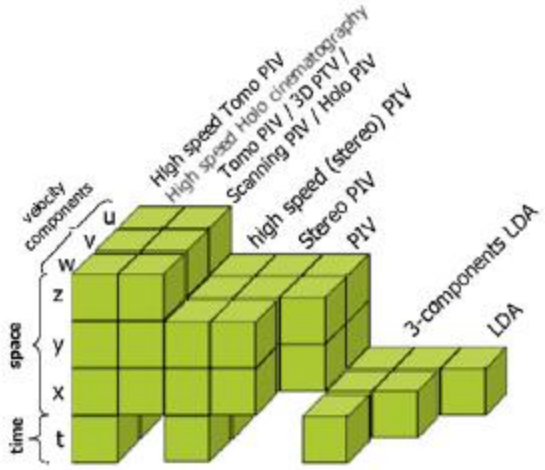

Figure 1.8 Measurement domain and measurement components of laser velocimetry techniques (after Scarano, 2013).

To the many techniques derived from PIV, the error objective of the PhD could be relevant. Mono-PIV is the simplest form of the technique and understanding the error characteristics on this case, should allow further developing the error characteristics for the rest of implementations. Additionally, Mono-PIV is still widely used because sometimes the characteristics of the experiment preclude from employing a more advanced PIV type. Plus, in some occasions, the data provided by Mono-PIV could be sufficient for the measurement objectives.

1.1.2.4 *Error assessment in PIV*

The developments in the technique have led to an increase in the use of PIV for turbulence measurements. As a matter of fact, the research published using the PIV technique surpasses that of Laser Doppler Velocimetry (LDV) and hot wire anemometry (the two other main velocity measurement techniques) in the last years (Westerweel *et al.*, 2013). Additionally, PIV data is used to obtain other physical quantities, as for example the vorticity, the dissipation of kinetic energy or even the pressure field. The importance of

knowing the error, as well as how to optimize it, is very useful information for the experimentalist working with PIV related techniques.

From the first research works studying the PIV technique, broad error estimations were provided. For example, Willert and Gharib (1991), Prasad *et al.* (1992) or Westerweel (1993) analyzed the technique and arrived to error values of ~0.1 pixels. Nevertheless, PIV is a technique that requires of many components to obtain a measurement and each component could induce a varying error value. That makes assessing the error value complex, and the error of the technique is not yet completely characterized, to the best knowledge of the PhD student.

Currently, error assessment is tackled from two complimentary approaches, as mentioned on a research work published from the PhD student (Jimenez *et al.,* 2016):

- Some authors seek tools that provide "a posteriori" a broad estimation of the measurement uncertainty by encompassing all the error estimation at each location as a function of a few input parameters.
- Other authors try to evaluate each error source separately: image discretization, capacity of the tracer particles to follow the flow, CCD induced errors, spatial velocity gradients, in-plane and out-of-plane motions, optical distortion, etc. In this last case, also the complex coupling between the different sources requires research effort.

Sciacchitano *et al.* (2015) summarize the four methods for the "a posteriori" error assessment:

- The *uncertainty surface* method (Timmins *et al*., 2012).
- The *particle disparity* approach (Sciacchitano *et al.,* 2013).
- The *peak ratio* criterion (Charonko and Vlachos, 2013).
- The *correlation statistics* method (Wieneke, 2015).

As to the "a priori" error assessment, it is an approach that should permit to identify the relevant error parameters for each error source and dissociate the interactions between them in the results (Lecordier *et al.,* 2001). The phenomena involved with each error source, and if the error is of random or systematic character can be understood. As a result, the deviations induced in the velocity measurements and/or on the quantities calculated from them can be studied. As examples Hjemfelt and Mockros (1966) studied the capacity of tracer particles to follow the flow; Lecordier *et al.* (2001) or Foucaut *et al.* (2004) study the effect of the interrogation window size in turbulence measurements; Lecuona *et al.* (2004) or Westerweel (2008) study the effect of spatial gradients; Nobach and Bodenschatz (2009) the effect of changes in light intensity of the particles between the laser pulses; and Legrand *et al.* (2014) studied CCD read-out errors.

Research effort in both conceptions should permit to eventually fully characterize the error of the technique. The error magnitude would be known when measuring under different measurement conditions. That should allow for optimizing the acquisition parameters and thus designing an experiment where the influence of the error is reduced, increasing the value of the technique.

1.2 FLOWS REQUIRING COMPLEX MEASUREMENTS: TURBULENCE

A fluid motion can be laminar or turbulent. Laminar motion is given on very viscous fluids or in flows that move very slowly; it is characterized for being smooth and regular. Turbulent motion, on the other hand, appears as chaotic and irregular (Davidson 2004). The transition between both types of motion was revealed by Reynolds in 1883 (Davidson 2004).

The importance of turbulence is from the fact that a lot of flows present a turbulent motion. The following examples can be mentioned: the wind blowing in the city, ocean currents, or the rapid flow around a body (Davidson, 2004). Turbulence influences on the drag produced by a car, an airplane or a building. It also increases mixing, and is responsible of dilution of pollutants emitted by cars to the atmosphere (Mathieu and Scott 2000). Given the importance of these phenomena, it is clear then that the capacity to predict turbulent flows or at least, their effects, is of much interest. In order to achieve such capacity, a lot of effort is being put into all three approaches mentioned in the introduction: theoretical, numerical simulations and experimental. Nevertheless, obtaining fair predictions can sometimes be quite elusive. This was nicely put by George *et al.* (2001): "A lot of turbulence 'prediction' is like predicting yesterday's weather —you change the model until you get the right answer. It works almost every time —but only for yesterday."

1.2.1 Aspects of relevance of turbulent flows

1.2.1.1 *Mean and fluctuating velocity fields*

Due to its chaotic-like behavior, turbulent motions are usually studied by recurring to statistical analysis. For statistically steady flows (Pope, 2000, Davidson, 2004, among others) the velocity field ***U(x;t)*** can be decomposed as:

$$\boldsymbol{U}(\boldsymbol{x};t) = \overline{\boldsymbol{U}}(\boldsymbol{x}) + \boldsymbol{u}(\boldsymbol{x};t)$$

Where $\overline{\boldsymbol{U}}(\boldsymbol{x})$ represents the time average of $\boldsymbol{U}(\boldsymbol{x};t)$ and $\boldsymbol{u}(\boldsymbol{x};t)$ is the random component of the motion. In this chapter, $\overline{\boldsymbol{U}}(\boldsymbol{x})$ is referred to as the mean flow and $\boldsymbol{u}(\boldsymbol{x};t)$ as the fluctuating field. The turbulent characteristics that are described below are related to the fluctuating velocity field.

1.2.1.2 *Turbulent eddies and the energy cascade*

A turbulent flow is composed of a set of eddies or vortices that span a range in sizes and velocities. The definition of an eddy in turbulence is not watertight, but it could be seen as a turbulent motion confined in a region of size ℓ which has certain coherence over that region (Pope, 2000). In Figure 1.9 two eddies have been plotted in regions where they could be located. A region where there is a large eddy could contain also smaller eddies; the result of the combination of those eddies produces the somehow chaotic and random appearance of turbulence. In the figure, the velocity over a whole line of data is plotted in the left (data from the flow described in section 3.1). Middle and Right graphs are the same data magnified progressively in the regions indicated by the broken line rectangles. Hereinafter, the characteristic velocity of an eddy of size ℓ is $u(\ell)$ and the timescale $\tau(\ell)$= $\ell/u(\ell)$ (notation from Pope, 2000).

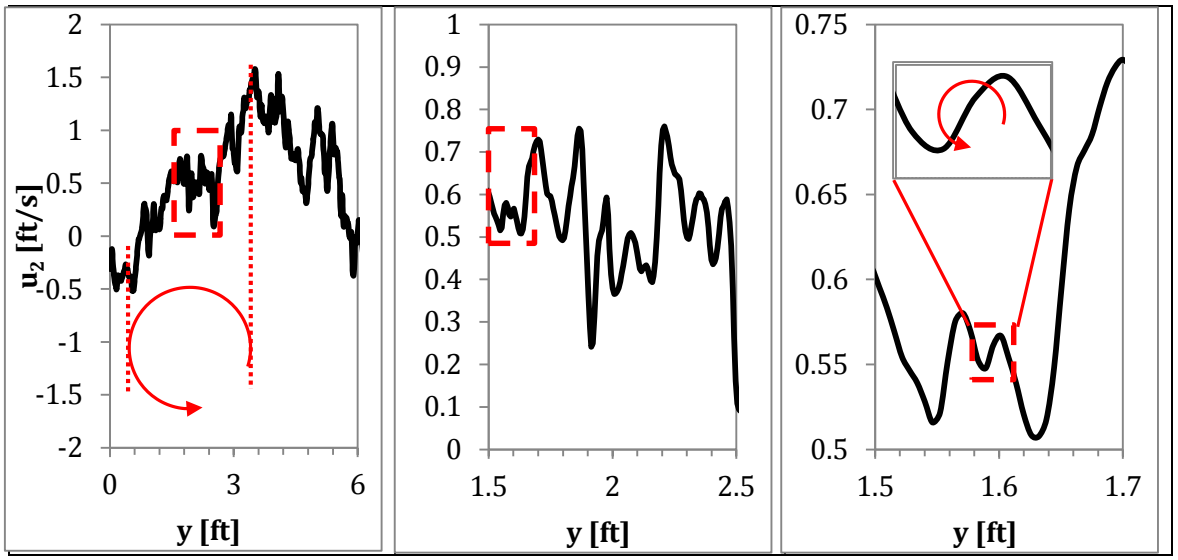

Figure 1.9 Spatial distribution of the second velocity component, following *y*-direction. Obtained from the flow of section 3.1 (Li *et al.*, 2008).

The reason because that set of different eddies is produced is for the need of a mechanism to dissipate the energy injected into a flow. The dissipation rate of turbulent kinetic energy depends on viscosity and in velocity gradients (Pope, 2000). A flow transitions to turbulence then when the gradients existing in laminar flow are insufficient to dissipate all the energy injected into the flow. A turbulent flow is then characterized by the existence of strong gradients, or at least, stronger than in the equivalent laminar flow, in order to dissipate the energy.

According to Pope (2000), Richardson (1922) introduced the concept of the *energy cascade*, which permits to explain the appearance of eddies of different characteristics in a turbulent flow. The large eddies are created by the mean flow gradients. For those large eddies $Re \gg 1$, as their characteristics are similar to those of the mean flow, and the mean flow has to fulfill $Re \gg 1$ for turbulence to exist. For those eddies viscosity is then negligible and no energy is dissipated by them. Richardson (1922) hypothesized that the large eddies are unstable and "break-up" into smaller eddies by inviscid processes (where no energy is dissipated). The eddies generated from those go through the same process. The energy cascade continues until an eddy size is reached such that $Re \sim 1$ and viscosity can dissipate these small eddies before they break up. In consequence, the energy is injected by the mean flow into the larger eddies and is dissipated by the smaller ones.

Since the kinetic energy of an eddy of size ℓ is $u(\ell)^2$, the rate of transfer of energy is then $\Theta(\ell) = u(\ell)^2/\tau(\ell) = u(\ell)^3/\ell$ (Pope, 2000). This is the energy that is being passed to the smaller eddies and the energy that is finally dissipated. If the large eddies are assumed to have a size ℓ_0 then the transfer of energy of the large scales $\Theta(\ell_0) \sim u(\ell_0)^3/\ell_0$ is kept through the smaller scales (Pope, 2000) and is dissipated by the smallest eddies at the end of the process. The dissipation rate is then $\epsilon \sim \Theta(\ell_0)$ (as illustrated in Figure 1.10).

The existence of this range of eddies of different sizes and velocities can be challenging to any measurement technique having to deal with them. Capturing all these characteristics can be quite demanding and it justifies the interest for a PIV measurement to have a large DVR and capacity to solve large and small velocity variations (a concept identified as Dynamic Spatial Range, DSR, Adrian, 1997).

1.2.1.3 *Kolmogorov hypotheses*

The other aspects of relevance to this PhD are those found out by Kolmogorov (1941). Kolmogorov hypothesized that, on the eddy break-up process, the directional and geometrical information that the large eddies have is lost. Therefore, the turbulent small scales can be considered statistically isotropic. That is to say, small scales statistics are independent of rotations and reflections of the coordinate axis. A domain within the flow can only be locally isotropic if it is locally homogeneous, i.e. the statistics are independent of the position of calculation (Pope, 2000). Therefore, the statistics of the small-scale motions are in a sense, universal, similar for every turbulent flow. That means that smaller eddies' statistics will not depend on the geometric characteristics of the large eddies and on how the energy is injected onto those large eddies.

Kolmogorov assumed then that the value taken by those statistics at the small scales should depend only on viscosity and on the energy arriving from the larger scales (which are the two dominant processes at those scales). The energy that arrives from the larger scales is then dissipated by the small scales, as mentioned above. That led **Kolmogorov** to state his **first similarity hypotheses** as (Pope, 2000): "For every high Reynolds number turbulent flow, the statistics of the small-scale motions have a universal form that is uniquely determined by ν and ϵ".

The range of scales that fulfil this property is referred to as the *universal equilibrium range.* Taking ℓ_{ER} as the upper bound of these scales, it must satisfy $\ell_{ER} \ll \ell_0$. That permits those scales to lose the directional information. Plus, the eddies in this range have a characteristic time-scale low enough that permits them to accommodate quickly to maintain a dynamic equilibrium with the energy transfer from the larger scales. This range, and others of importance defined later are plotted in Figure 1.10 below (after Pope, 2000). In the figure, the scales $\ell > \ell_{ER}$ identify the energy containing range, those are the scales that contribute more to the turbulent kinetic energy (Pope, 2000).

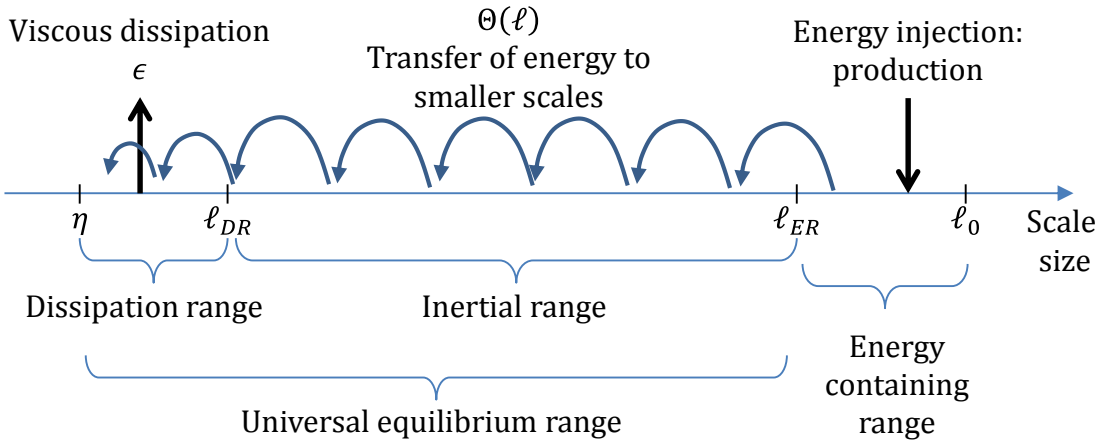

Figure 1.10 Different scale sizes and ranges of importance in turbulent flows (inspired from Pope, 2000).

There are unique length, time and velocity scales that can be formed from ν and ϵ (aside from multiplicative constants). These scales are referred to as Kolmogorov scales:

$$\eta \equiv (\nu^3/\epsilon)^{1/4} \tag{1.3}$$

$$u_\eta \equiv (\nu\epsilon)^{1/4} \tag{1.4}$$
$$\tau_\eta \equiv (\nu/\epsilon)^{1/2} \tag{1.5}$$

As can be appreciated, the Reynolds number for Kolmogorov scales: $\mathrm{Re}_\eta=\eta u_\eta/\nu=1$, indicating coherence to the fact that dissipation occurs for those scales sizes. From Kolmogorov scale definitions, it is easy to obtain the ratios to the large scale ℓ_0:

$$\eta = \left(\frac{\nu^3}{\epsilon}\right)^{1/4} \sim \left(\frac{\nu^3}{u_0^3}\ell_0\right)^{1/4} \sim \frac{\ell_0}{Re^{3/4}} \Rightarrow \frac{\eta}{\ell_0} \sim Re^{-3/4} \tag{1.6}$$
$$u_\eta/u_0 \sim Re^{-1/4} \tag{1.7}$$
$$\tau_\eta/\tau_0 \sim Re^{-1/2} \tag{1.8}$$

As can be appreciated from the ratio in (1.6), η/ℓ_0 reduces as Reynolds number increases. Kolmogorov assumed that at some point, there could be scales of size $\sim\ell$ that would be large enough to not be influenced by viscosity and small enough to still be contained in the universal equilibrium range, limited by ℓ_{ER}: $\eta\ll\ell\ll\ell_0$. The statistics of these scales have also a universal form, which in this case is uniquely determined by the energy transfer from larger to smaller scales (or equivalently by the dissipation ϵ), i.e. they are independent of ν. This hypothesis is identified as **Kolmogorov's second similarity hypothesis** (Pope, 2000). A characteristic velocity and time can be formed by recurring to the dissipation and the scale size ℓ:

$$u(\ell) = (\epsilon\ell)^{1/3} = u_\eta(\ell/\eta)^{1/3} \tag{1.9}$$
$$\tau(\ell) = (\ell^2/\epsilon)^{1/3} = \tau_\eta(\ell/\eta)^{2/3} \tag{1.10}$$

The scales that fulfill this hypothesis are identified as the inertial range, and are plotted in Figure 1.10. The lower limit on this range can be labelled as ℓ_{DR}, the scale for which dissipation is non-negligible anymore. ℓ_{DR} is around 70η (Davidson, 2004). From this scale definition, the identity $\Theta(\ell)=\epsilon$ assumed above is justified. It can be observed that for $\ell_2>\ell_1>\eta$, $u(\ell_2)>u(\ell_1)>u_\eta$ and $\tau(\ell_2)>\tau(\ell_1)>\tau_\eta$. Additionally, it is possible to sort spatial and temporal gradients:

$$u_2/\ell_2 < u_1/\ell_1 < u_\eta/\eta$$

$$u_2/\tau_2 < u_1/\tau_1 < u_\eta/\tau_\eta$$

The importance of these hypotheses is because the study developed in this PhD is based on a specific turbulent flow. The results are then valid for turbulent flows of similar characteristics. However, if the main conclusions of the study are dependent on the small scales of the flow, those conclusions can be extrapolated to other measurements of other types of turbulence, thanks to the similarity hypotheses of Kolmogorov.

1.2.2 PIV Response to Turbulent Features

Dealing with large spatial gradients and a large range of spatial scales is challenging for any velocity measurement technique. In particular the PIV response to these turbulent features is described here, so the motivation to carry out this PhD can be understood.

The group hosting the PhD student put together a set of constraints that appear when measuring turbulent flows (Nogueira *et al.,* 2012). The aim of that work was to study the capacity of PIV to measure this type of motion, from a theoretical point of view. The

maximum Reynolds number that can be studied if the objective is to correctly describe all the scales present in a turbulent flow was provided. The range of length-scales that can be properly characterized if the Reynolds number is above that one was calculated as well, by theoretically optimizing the time delay between laser pulses, Δt, and the laser sheet thickness Th. The physical constraints imposed on that previous work are reported below,.

For detailing the constraints, four length-scales are of importance: ℓ_T, ℓ_U, ℓ_L and ℓ_B. The subscripts correspond to top, upper, lower and bottom length-scale in order of decreasing size. The top and bottom scale are the largest and the smallest scale present in the turbulent flow, respectively. The bottom scale would be of the order of the one of Kolmogorov η, but the notation above is used for consistency with the paper. The "upper" and the "lower" scale indicate the largest and the smallest scale resolved by the PIV measurement, respectively. The characteristic velocity associated to any of those scales is expressed below by u with the corresponding subscript: u_T, u_U, u_L and u_B. The specific definitions of the characteristic velocity associated to the scale size are sketched in Figure 1.11. As indicated above, for the sizes defined decreasing in size, the velocities fulfill: $u_T \geq u_U \geq u_L \geq u_B$. The spatial gradients (produced over a size ℓ) would be sorted as: $2u_T/\ell_T \leq 2u_U/\ell_U \leq 2u_L/\ell_L \leq 2u_B/\ell_B$.

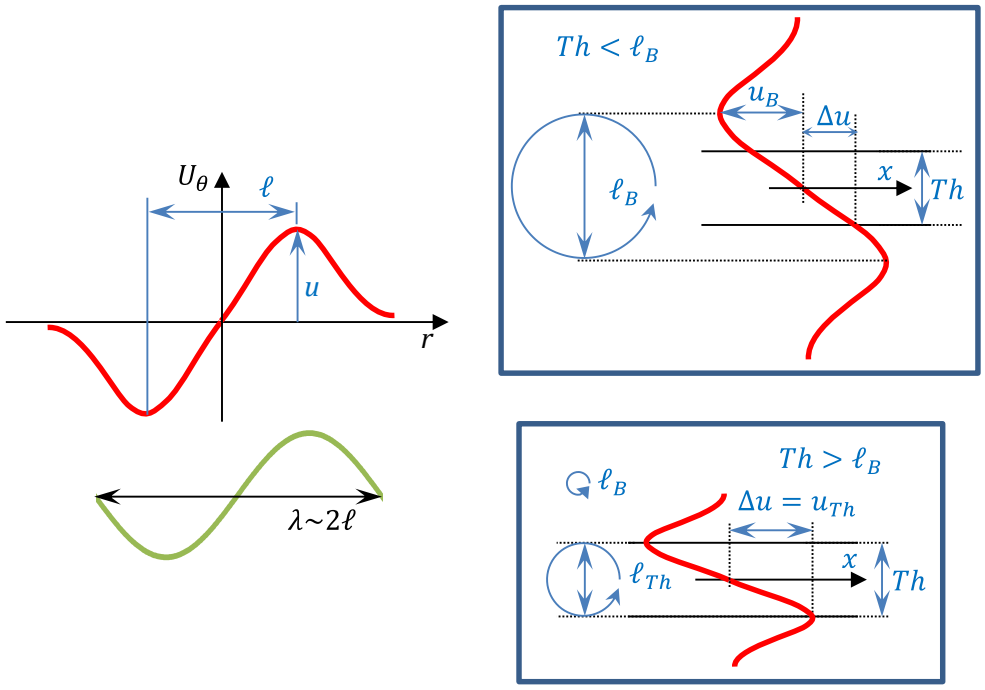

Figure 1.11 Left: definition of a scale and its velocity. Right: spatial gradients induced across the laser sheet thickness *Th*, for different bottom scale sizes ℓ_B respect to the thickness *Th*.

The length unit used in the constraints is the size of a pixel projected into the imaged field, e.g. if the field of view is a square of 100mm of side and the sensor is a square as well that contains 1000 pixels per side the size of a pixel is 0.1mm. That pixel size is the one used below, and not the size of a pixel in the CCD sensor. The constraints imposed in Nogueira *et al.* (2012) were updated in Nogueira *et al.* (2014) in a paper where the PhD student collaborated as coauthor. Below, the constraints for optimizing a turbulence PIV measurement from both works combined are enumerated. Also, previous works that have researched a specific issue and the limitation suggested is mentioned, so the maximum scales range that PIV can resolve can be obtained below.

1. The largest scale to be described, ℓ_U, is limited by the size of the flow field extension imaged by the CCD sensor. If the CCD sensor has N_{pix} then: $\boldsymbol{\ell_U \leq N_{pix}}$.

2. The laser sheet thickness, Th, has to be large enough so that the loss of particle pairs in PIV due to the largest turbulent out-of-plane motion is limited to a small percentage, $f_1 < 1$. For the homogeneous and isotropic flows analyzed in those works, the largest velocity, u_T, can be perpendicular to the laser sheet. The following constraint arises then: $\boldsymbol{u_T \cdot \Delta t \leq f_1 \cdot Th}$. In the works of Keane and Adrian (1992), Raffel *et al.,* (2007), or Nobach and Bodenschatz, (2009) the effect of out-of-plane motions on the error of the measurement and in the probability of occurrence of an outlier can be found. From those works, a f_1 value f_1=0.2 is imposed.

3. As mentioned in the introduction (cf. 1.1.2.2), PIV can resolve a displacement only to a certain subpixel resolution accuracy, $\xi_{\Delta x}$. The subpixel resolution varies depending on the velocity gradient, the size of particle images or the algorithm used to calculate the displacement, but it is generally accepted that 0.01 pixel < $\xi_{\Delta x}$ < 0.1 pixel (Prasad *et al.*, 1992, Keane and Adrian, 1992, Westerweel, 2000, among others). Δt has to be large enough to ensure that $\xi_{\Delta x}$ is significantly smaller than the distance traveled by the smallest velocity to measure, u_L. Considering a small factor, $f_2 < 1$, to define the allowable ratio, the constraint imposed on Δt gives: $\boldsymbol{f_2 \cdot u_L \cdot \Delta t \geq \xi_{\Delta x}}$. In order to obtain a solution below, a value of 0.05 pixel is imposed for $\xi_{\Delta x}$, $\xi_{\Delta x}$=0.05 pixels. As to the f_2 it is imposed arbitrarily to 0.2, so the error in the displacements of scale ℓ_L is limited to a 20%.

4. The laser sheet thickness, Th, has to be significantly smaller than the smallest spatial scale to be resolved, ℓ_L. In the first work of Nogueira *et al.* (2012) the limitation on Th was imposed through the velocity variations in the out-of-plane direction. Specifically, it was imposed that the out-of-plane displacement variation could not be larger than the largest permitted error: $f_2 \cdot u_L \cdot \Delta t$. Two possibilities were identified (plotted in Figure 1.11), depending on the size of the smallest length-scales with respect to the laser sheet thickness:
    a. If the laser sheet thickness is smaller than the smallest scale of the flow, $Th \leq \ell_B$, the largest velocity discrepancy between the laser sheet center and its border is produced by scale ℓ_B. As mentioned above, the velocity gradient is $2u_B/\ell_B$, which produces a displacement discrepancy $2u_B/\ell_B \cdot \Delta t \cdot Th/2$. Therefore, the constraint should be: $\boldsymbol{2u_B/\ell_B \cdot \Delta t \cdot Th/2 \leq f_2 \cdot u_L \cdot \Delta t}$.
    b. If the laser sheet thickness is larger than the smallest scale of the flow, $Th \geq \ell_B$, the largest velocity discrepancy is produced in this case by the largest length-scale contained within the laser sheet. The characteristic velocity of the scale $\ell_{Th}=Th$ is referred to as u_{Th}, which gives the following constraint: $2u_{Th}/\ell_{Th} \cdot \Delta t \cdot Th/2 \leq f_2 \cdot u_L \cdot \Delta t \Rightarrow \boldsymbol{u_{Th} \leq f_2 \cdot u_L}$.

    However, a displacement variation in the out-of-plane direction of a magnitude of $f_2 \cdot u_L \cdot \Delta t$ may not necessarily produce that error. Therefore, in Nogueira *et al.* (2014), the two possibilities above were updated simply as: $\boldsymbol{Th \leq f_3 \cdot \ell_L}$, with f_3 a factor <1. In this case, a value for f_3 has not been found in the literature. Some

works have studied the issue of spatial gradients (Keane and Adrian, 1992, Lecuona *et al.,* 2004, Westerweel, 2008, or Theunissen, 2012) but the case of complex turbulent gradients seems not clarified, to the best knowledge of the PhD student. As a consequence, this PhD focuses on characterizing this issue and obtaining a coherent value for f_3 factor, as is described in the motivation. For now and in order to show how the constraints interact a value of f_3=0.2 is imposed.

5. In a conventional correlation PIV algorithm, the size of the interrogation window imposes a limit on the smallest scale that can be resolved (Willert and Gharib, 1991). In Figure 1.12 the normalized response of a conventional PIV algorithm is plotted, with respect to the spatial wavelength of a sinusoidal displacement. To obtain this figure, the response of PIV is assumed to be the average in the measurement volume. The validity of this assumption and the response when the measurement departs from this one is studied in section 5.3. Considering a 16 pixels interrogation window and a 20% of error, the associated spatial wavelength is λ∼44 pixels. As indicated in Figure 1.11 that corresponds to $\boldsymbol{\ell_L \geq 22}$ **pixels**.

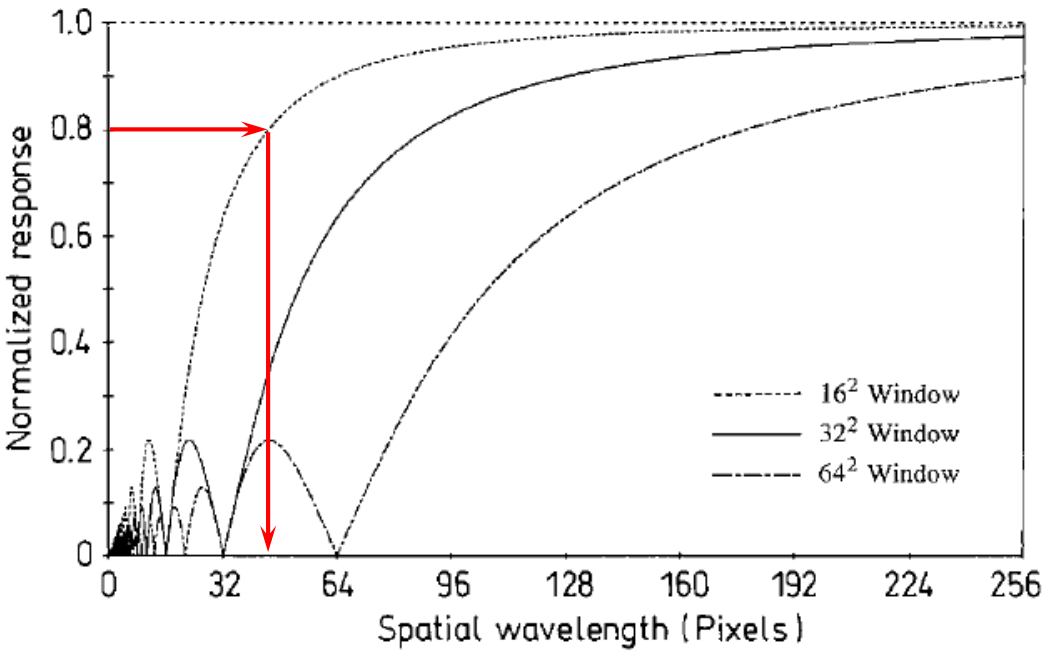

Figure 1.12 (after Willert and Gharib, 1991) Plot indicating the smallest wavelength that a conventional PIV algorithm can resolve.

1.2.2.1 *Maximum range of scales resolvable with PIV*

Combining constraint number (2) with constraint number (4) in the updated form ($Th \leq f_3 \cdot \ell_L$) yields:

$$u_T \Delta t \leq f_1 f_3 \ell_L$$

If this new constraint is divided with constraint number (3) gives:

$$\frac{u_T \cdot \cancel{\Delta t}}{f_2 \cdot u_L \cdot \cancel{\Delta t}} \leq \frac{f_1 f_3 \ell_L}{\xi_{\Delta x}} \Rightarrow \frac{u_T}{u_L} \leq \frac{f_1 f_2 f_3 \ell_L}{\xi_{\Delta x}}$$

By recurring to expression (1.9) a link between u_T/u_L and the scales ratio ℓ_T/ℓ_L can be stablished. That gives $\ell_T/\ell_L=(u_T/u_L)^3$ which when replaced in the constraint just above yields:

$$\ell_T/\ell_L \leq (f_1 f_2 f_3 \ell_L/\xi_{\Delta x})^3 \tag{1.11}$$

Constraint number (1), divided by ℓ_L and imposing that the largest scale resolved by the measurement, ℓ_U, is the largest one given in the turbulent flow, ℓ_T, the constraint reads:

$$\ell_T/\ell_L \leq N_{pix}/\ell_L \tag{1.12}$$

Both expressions (1.11) and (1.12) combined with $\ell_L \geq 22$ pixels obtained from constraint number (5) provide the limiting scales range that can be measured by PIV. The values of factors f are: f_1=0.2, f_2=0.2 and f_3=0.2 and $\xi_{\Delta x}$=0.05 pixels, as mentioned above.

With those factors value and expressions (1.11), (1.12) and $\ell_L \geq 22$ pixels, Figure 1.13 below can be obtained. In the figure, two different sensor pixel numbers, N_{pix}, are used, 2000 and 4000 pixels. The curves plotted correspond to the limiting value of ℓ_T/ℓ_L imposed by each expression, for example, from expression (1.11), $\ell_T/\ell_L = (f_1 f_2 f_3 \ell_L/\xi_{\Delta x})^3$ is plotted. The set of different measurements available would be that under the curves and to the right of the algorithm limit (ℓ_L=22 pixels) which has been plotted filled yellow, for the cases of N_{pix}=4000 and an interrogation window of 16 pixels. The largest scale range is indicated as well.

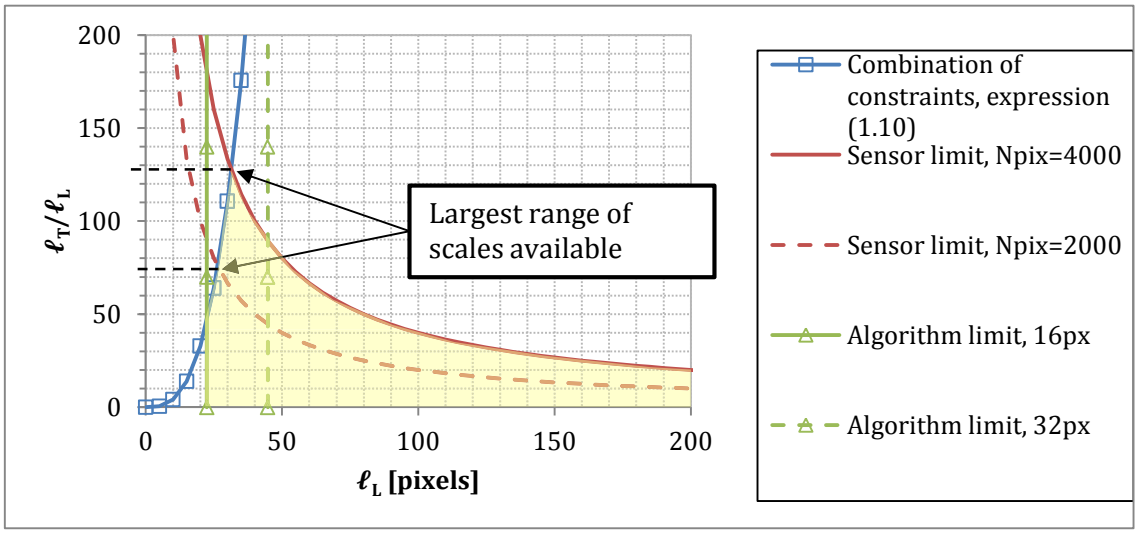

Figure 1.13 Limits in PIV turbulence measurements for the available scales range. (after Nogueira *et al.*, 2014).

It can be understood from the graph that the combination of constraints in expression (1.11) may have not been relevant in the past but that may not be the case anymore. Indeed, the PIV algorithms have improved in the past years so using 16 pixels algorithms is possible nowadays. The number of pixels of the sensors is also growing. As a result, whereas before the maximum ℓ_T/ℓ_L range was typically imposed by the intersection of the green and red graphs (for example by the broken red and green lines plotted in the figure, for 32 pixels and 2000 pixels), nowadays this range could be imposed by the intersection of the blue and red graph. For this reason, it was deemed important to properly characterize f_3 factor.

In the case of the sensor with 4000 pixels, the scales ratio obtained is $\ell_T/\ell_L \cong 130$. When the smallest scale resolved by PIV is the smallest one produced by the turbulent flow, $\ell_L = \ell_B$. That permits to obtain the maximum Reynolds number that can be solved by PIV, by recurring to expression (1.6):

$$\ell_T/\ell_B = 130 = Re^{3/4} \Rightarrow Re \cong 660$$

It is important to remark that, if the measurement conditions allow using 16 pixels interrogation windows, the limitation on the smallest scale that PIV can resolve is imposed by expression (1.11). That constraint linked out-of-plane gradients with out-of-plane motions. Resolving the constraint imposed by the spatial gradients in the out-of-plane direction is of importance then, as it could be the limiting factor on the maximum resolvable range. For this reason, the PhD was focused on providing a value to f_3 factor.

Chapter 2 **Motivation, Objectives and Methodology**

2.1 MOTIVATION

This PhD thesis is part of the research project "*PIV avanzado en flujos de interés térmico*" funded by the Spanish Ministry of Education and Science (ENE2011 - 28024). This project deals with the characterization of thermal flows of relevance for the industry, with emphasis on the error characterization and error assessment procedures. In this frame, turbulent flows are of special interest.

As was shown on the previous chapter, turbulent flows are composed of eddies with a large range of characteristic sizes and velocities. Interestingly, some relevant physical quantities are related to the large scales, as the turbulent kinetic energy, and others to the smaller scales, as the dissipation. Therefore, a characterization of the length-scales has always been considered of importance and turbulence is often studied from that point of view. In that regard, the PIV technique, which allows measuring instantaneous snapshots of the flow spatial distribution, can provide useful information. For these reasons, assessing the capacity of PIV to measure a turbulent flow is of high value and the PhD is framed in this specific field.

In that context, previous work from the hosting research group (Nogueira *et al.,* 2012) analyzed theoretically the limits of PIV for measuring turbulent flows and for optimizing the range of scales characterized. In the introduction the constraints imposed in that paper were enumerated. It was also mentioned that, whereas some of the constraints are supported by previous research, that is not the case for spatial gradients across the laser sheet thickness.

Indeed, in previous research works, it is found that the laser sheet thickness in turbulence measurements is usually imposed to be small, but no reference has been found detailing a proper way to set this parameter. As examples, Saarenrinne and Piirto (2000) suggest to keep the laser sheet thickness as low as possible, to have a good spatial resolution. Lavoie *et al.* (2007) suggest a laser sheet thickness of half the size of the interrogation window. More recently, McCleney *et al.* (2016) performed time resolved PIV of an axisymmetric turbulent jet. They emphasize the need to measure with a thin laser sheet so "the small scale structure does not get lost inside the measurement volume". As can be seen, the laser sheet thickness is sought to be small, but the specific influence of the parameter is not completely characterized. Additionally, the distribution of the error associated to the laser sheet thickness across the length-scales of the flow appears to require further research effort. Consequently, these reasons motivated carrying out the PhD in this specific topic.

Moreover, the laser sheet thickness cannot be varied with complete freedom, as the out-of-plane constraint links both the sheet width and the Δt. In order to reduce the laser sheet thickness (so the smaller scales are resolved) the Δt would have to be reduced as well, but that could result in an insufficient dynamic velocity range. Consequently, there is an interaction through both parameters of the errors induced by: (i) the small scales gradients and (ii) the large scales out-of-plane motion. Indeed, smaller scales have larger gradients than the large, but the velocities are sorted the opposite way. Understanding

that coupling, the governing parameters and the errors induced on the PIV technique by the presence of turbulent spatial gradients, motivates the PhD.

2.2 OBJECTIVES

The main objective of this PhD thesis is to produce a contribution on the capacity of PIV for measuring turbulent flows. The scope has been focused on the laser sheet thickness influence on the error and its possible coupling with other error sources. This research is framed within the "a priori" approach (cf. 1.1.2.4), which can allow optimizing acquisition parameters such as the laser sheet thickness and Δt before measuring. Within this frame, the objectives of the thesis are presented below:

I. To characterize the error induced by the interaction of turbulent spatial gradients with the laser sheet thickness. Specifically:
    1. How is the error produced, i.e. provide the theoretical rationale that describes the error. The relevant parameters that permit to characterize the error value should be identified.
    2. Provide a distribution of the error along the length-scales present in turbulent flows; for such purpose, a way to provide length-scale information has to be proposed.

II. To clarify the interaction between the small scales gradients and large scales out-of-plane motion, which occurs induced by two measurement parameters: the time between the laser pulses (Δt) and the laser sheet thickness (Th). The sensibility of measurement errors to these acquisition parameters should be provided as well. That allows identifying which are the sources that are actually producing the measurement error, so the relative importance and magnitude of each source under study can be assessed.

III. To provide the measurement possibilities envelope for both parameters of interest: Δt and Th. This implies providing an assessed value of parameter f_3 (ratio between the laser sheet thickness and the smallest scale that can be properly characterized) in the measurement constrains established previously in Nogueira *et al.* (2012).

2.3 METHODOLOGY

The following steps were devised in order to fulfill the objectives of this PhD thesis:

1. Get acquaintance and expertise with the PIV measurement technique and with the specifics of turbulence flows. For that purpose, realize a bibliographic study and participate in relevant measurement campaigns to learn the technique. In addition to measurements with the hosting group, two stays in renowned PIV centers were planned to apprehend the specifics of measurements of the PIV technique in wind tunnels. This also allowed observing the measurement protocols with regards to error handling.

2. Perform a dedicated bibliographic study on PIV errors and especially on those that are related to turbulence. From that study, create a theoretical model that permits to predict the error induced by spatial gradients depending on the measurement parameters: Δt and Th. The bibliographic study and the theoretical model are given in section 5.3.

3. Develop the numerical simulation tools that permit to analyze the error values and their variation with the measurement parameters of interest.

   (i) In PIV, it is common to recur to generators of synthetic images to study the errors of the measurement technique. A synthetic image generator has been included on the methodology of this PhD, based in a turbulent flow.

   (ii) Additionally, preliminary results advised the development of an additional tool. Indeed, this was considered necessary to uncouple the variations of some error sources that can be found in synthetic images. This tool has been identified as "PIV Simulator" and it allows studying the non-linear effects induced by the interaction of turbulent spatial gradients with the PIV correlation.

   Both tools are described in Chapter 3. The error vector can be obtained from these tools, so the error distribution with the length-scales of the flow can be studied.

4. Design a dedicated experiment to validate the results from the theoretical rationale and the numerical tools. This step is necessary to show the importance of the errors characterized throughout the previous points in real PIV images. The requirements, development process and final solution attained can be found in Chapter 6.

5. Choose a function that is convenient to provide the length-scale information required. Given the nature of turbulence, of being composed of a range of eddy sizes, many functions that provide information in spatial frequencies have been proposed in the literature. In Chapter 5, a comparison between some of the functions found in the bibliography is provided and the one considered most convenient is indicated.

The turbulent flow upon which this PhD is based is the one identified as homogeneous turbulence. This is the simplest kind of turbulence; however, measurements on this type of flow are used to tune numerical models (George *et al.*, 2001). It is characterized by lack of spatial gradients in the mean flow, which results in no energy injected by the mean flow into the large scales to feed the energy cascade process. As such, it is identified also as

freely decaying turbulence, i.e. the eddies that were generated somehow are left on their own until they are completely dissipated. Freely decaying turbulence would be obtained for example after stirring energetically the water inside a vessel. Additionally, homogeneous turbulence fulfills the property that any statistical quantity is independent of the position of calculation.

Chapter 3 **PIV Simulator and Synthetic Image Generator**

In this chapter, two dedicated tools to evaluate PIV measurement errors are detailed. A known test field is required for both tools. The selected flow field corresponds to a Direct Numerical Simulation (DNS) of a homogeneous turbulent flow. For the shake of completeness, the first section of this chapter details this DNS flow field.

The first tool, fully developed in this PhD, (henceforth identified as *PIV Simulator*) is aimed at providing "measured velocity fields" from the DNS database by emulating the PIV correlation process. However, no images are generated in order to isolate error sources associated to the correlation from those associated to the images. By emulating the correlation process, the PIV Simulator maintains the intrinsic PIV non-linearity to allow for a better identification of the different contributions on the related measurement error.

The fundaments of the second tool come from the early days of Digital PIV (Westerweel, 1993). It has been regularly used since then. It consists in generating synthetic images from the DNS velocity field and processing them with real PIV algorithms. The Synthetic Image Generator developed in this PhD creates image pairs of randomly distributed particles, as classically done in PIV for error studies (Raffel *et al.*, 2007, among others). Between the two frames of an image pair the particles are moved according to the selected flow field and then interrogated with PIV.

3.1 SELECTED FLOW FIELD

The selected flow to assess the capability of the PIV measurement, when dealing with turbulence, is an isotropic forced turbulent flow. The actual vector field corresponds to a Direct Numerical Simulation, publicly available at: http://turbulence.pha.jhu.edu/ (Li *et al.,* 2008). The research undertaken in this *PhD* originated from the findings of Nogueira *et al.* (2012) which were obtained for a homogeneous isotropic turbulent flow. The selected flow is thus aimed at continuing with that line of work. In addition, thanks to Kolmogorov similarity hypotheses (Kolmogorov, 1941) the conclusions withdrawn from studying the errors of PIV when measuring this flow could be extrapolated to other types of turbulent flows.

3.1.1 Specifics of the flow database

The flow database contains the space-time history of a flow of forced isotropic turbulence obtained by direct numerical simulation (DNS). It is detailed in Li *et al.* (2008). Following the authors, also homogeneity is assumed as there is no privileged location in the vector field.

The velocity and the pressure fields of the flow are stored on a cube of 1024^3 regular grid points for 1024 time instances[1], for a total of 1024^4 data points. The cube has periodicity conditions imposed on all sides. On Figure 3.1, below, the velocity following direction y is shown for the last time instance on an arbitrary plane of the database.

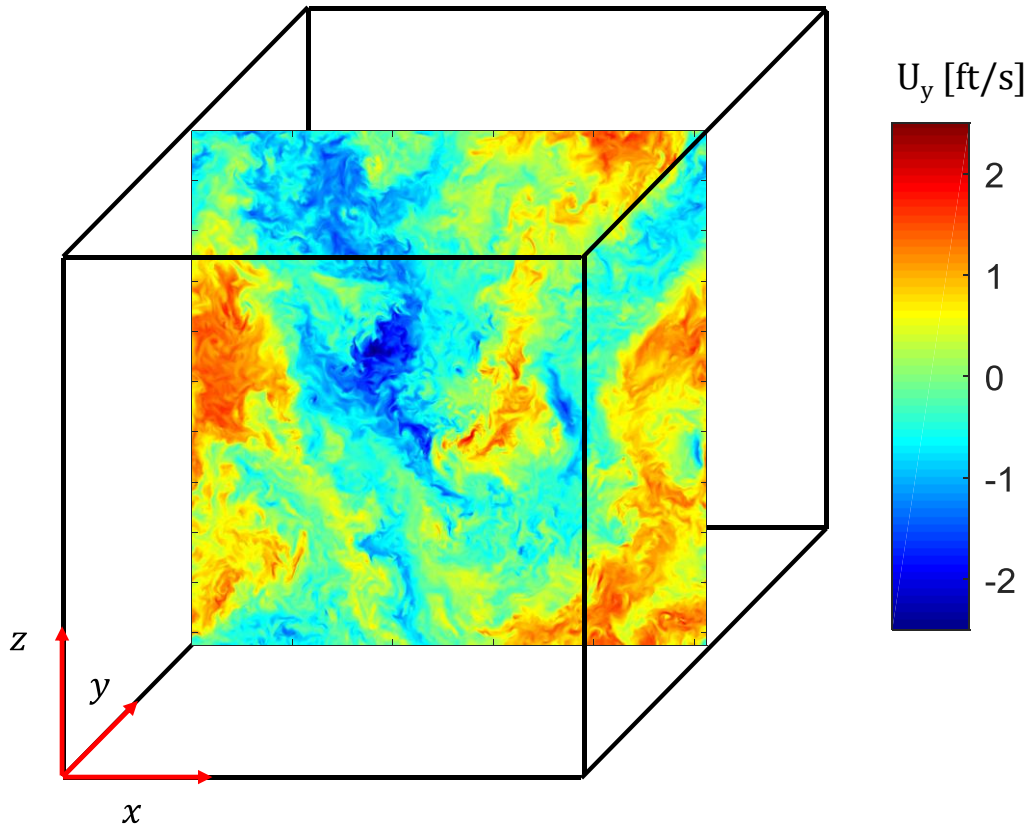

Figure 3.1 Sketch of the cube of data with the *y*-velocity contour (1024x1024 plane)

[1] On October 19th, 2016, the database was extended to 5024 time instances. However, this occurred after all the results have been analyzed and thus, the number available originally is kept in this dissertation.

The values of some physical magnitudes that characterize the turbulence are presented in Table 3.1, as obtained from Li *et al.* (2008). Due to the scalability of the flow, the authors do not indicate physical units. Nevertheless, the magnitudes are coherent with air, using feet for the length unit and seconds for the time one. So, hereafter, any DNS quantity is expressed in the units mentioned above, just for simplicity.

Table 3.1 Parameters of the flow and of the DNS. Reproduced from Li *et al.* (2008)

Resolution, N	1024
Viscosity, ν [ft^2/s]	0.000185
Time interval between stored data sets, Δt_{DNS} [s]	0.002
Total kinetic energy, $E_{tot} = \langle \sum_{\boldsymbol{\kappa}} (1/2)\, \hat{u} \cdot \hat{u}^* \rangle_t$ [ft^2/s^2]	0.695
Mean dissipation rate, $\epsilon = \langle \sum_{\boldsymbol{\kappa}} \nu \kappa^2 (1/2) \hat{u} \cdot \hat{u}^* \rangle_t$ [ft^2/s^3]	0.0928
r.m.s. velocity fluctuation, $u' = \sqrt{\frac{2}{3} E_{tot}}$ [ft/s]	0.681
Taylor micro length scale, $\lambda = \sqrt{15 \nu u'^2 / \epsilon}$ [ft]	0.118
Taylor micro-scale Reynolds number, $Re_\lambda = u' \lambda / \nu$	433
Kolmogorov length scale, $\eta = (\nu^3/\epsilon)^{1/4}$ [ft]	0.00287
Kolmogorov time scale, $\tau_\eta = (\nu/\epsilon)^{1/2}$ [s]	0.0446
Kolmogorov scale velocity, $u_\eta = (\nu \epsilon)^{1/4}$	0.0644
Integral length scale, $\mathcal{L} = \pi/(2u'^2) \int (E(\kappa)/\kappa) \mathrm{d}\kappa$ [ft]	1.376
Integral time scale, $T = \mathcal{L}/u'$ [s]	2.02

On Table 3.1, $\hat{u}$ stands for the Fourier transform of velocity and $\hat{u}^*$ for its conjugate. κ is the wavenumber. The operator $\langle \cdot \rangle_t$ means average over the available time instances.

From Table 3.1, the relation between the Kolmogorov scale and the integral scale can be extracted ($\mathcal{L}/\eta \approx 480$), which gives an idea of the range of scales present in the flow. Additionally, the integral length-scale as compared to the edge of a cube (L_0=2π feet) gives $L_0/\mathcal{L} \cong 4.6$. The time stored (1024·0.002=2.048 seconds), as compared to the integral time scale gives $T_0/T \cong 1$. These ratios are further discussed in 3.1.3 as they are of importance for the usage of all the available data. Also, to identify error characteristics, Chapter 5 details the construction of dimensionless parameter with some of the magnitudes of Table 3.1.

3.1.2 **Aspects of relevance of the numerical solution**

In this point, three details of the database are discussed: (i) the cube boundary condition of periodicity, (ii) the maximum effective wavenumber and (iii) the fact that the flow is forced (i.e.: not freely decaying), as explained by Li *et al.* (2008). These details make the DNS flow differ from the one that is obtained experimentally (described in Chapter 6). They are considered of relevance because they could affect the application of the tools for length-scale information. The discussion is useful to understand their possible effects on the objectives of the PhD.

(i) Periodicity of the cube: According to Davidson (2004) the **periodicity of the cube**, which is an imposition that will be not likely found in real turbulent flows, is used because it allows employing particularly efficient numerical algorithms (identified as pseudo-spectral methods). The effect of periodicity in the velocity field is that it imposes a certain degree of anisotropy, but mostly in large scales, as Davidson (2004) shows. For example, the data replicates advancing a distance of

2π feet in the x direction, in Figure 3.1. However, the distance for replication advancing on the bisector of axis x and y would be $\sqrt{8}\pi$ feet.
Nonetheless, although large scales can be affected by the periodicity condition, the turbulence originated from them does not have to be. As stated by Kolmogorov universality hypotheses (Kolmogorov, 1941): for sufficiently high Reynolds number, the small scale turbulent motions ($\ell \ll L$) are statistically isotropic and have a statistically universal form determined by ν and ϵ. That is, the directional information is lost in the scale-reduction process. Since the aim of the vector fields is to observe the effects of the small scales of turbulence in the measurement (independently of the turbulence being physical or not), periodicity should not cause any interference with the study. Hence, the conclusions should be valid for other flows.

(ii) The **maximum effective wavenumber:** the maximum wavenumber solved is $\kappa_{max} \approx 482$ (feet)$^{-1}$, because of the de-aliasing introduced in the simulation. Figure 3.2 depicts the longitudinal and transversal one-dimensional spectra (where wavenumber κ_1 corresponds to x direction). For a detailed definition of the spectra see Chapter 5. The effect of the maximum effective wavenumber can be appreciated, as energy goes to 0 abruptly for $\kappa_1 = 482$.
That imposition gives a minimum length-scale effectively solved of $\ell_{min}/\eta = 4.5$, although the grid-spacing (Δx) gives $\Delta x/\eta = 2.1$. It could seem by these values that not all turbulent scales are solved, something that does not fit the definition of a DNS (which should solve all scales) and which could induce differences on the study with respect to a real turbulent flow. As it turns out, the Kolmogorov length-scale is defined as an order of magnitude where the dissipation occurs, but that does not imply dissipation occurs exactly at that scale. Pope (2000), shows that the bulk of the dissipation occurs in the range ℓ/η between 8 and 60 and it is likely than the cut-off in eddy size is larger than the Kolmogorov scale (Davidson, 2004). For this reason, Direct Numerical Simulations do not usually discretize the space domain down to Kolmogorov length-scales.
Therefore, care should be taken and no scales smaller than the one effectively solved should be used for extracting conclusions. For this PhD the minimum scale solved is larger than the one the DNS effectively solves, so no problem is foreseen from the wavenumber cut-off.

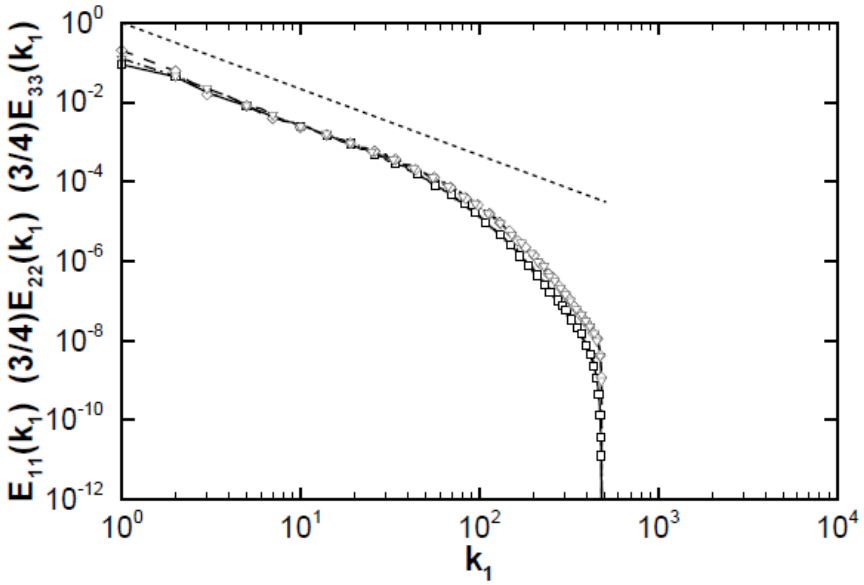

Figure 3.2 One-dimensional energy spectra: Solid line and squares: $E_{11}(\kappa_1)$, dashed and diamonds: $(3/4)E_{22}(\kappa_1)$, dash-dotted and triangles: $(3/4)E_{33}(\kappa_1)$. Thin dashed line indicates −5/3 slope. Reproduced from Li *et al.,* 2008.

(iii) Forced turbulence: The final remark is that for the flow stored in the database, **turbulence is forced**, i.e. it is not freely decaying. On a DNS of forced isotropic turbulence, a source of kinetic energy is employed to attain a statistically steady state, as Sagaut and Cambon (2008) state, among others. In this particular case, energy is injected by keeping constant the total energy in modes such that their wavenumber magnitude is less or equal to 2 (Li *et al.,* 2008). For the results derived from the flow, the fact that the flow is forced and the characteristics do not vary with time, allows using the velocity fields at different time steps to calculate more robust statistics. However, the forcing may influence on the large-scales not being physical (Sagaut and Cambon, 2008). As stated for the periodicity condition, the fact that the large-scales could not be physical is not relevant for the aim of this PhD.

As a conclusion, the database is based in a flow which may not be found in nature; nonetheless, it has the features needed to undertake the objectives of the PhD: to determine the capability of the PIV measurement when applied to turbulent spatial and temporal variations. Basically, it contains a range of different turbulent structures, it provides 3D velocity data stored and the time evolution of that data.

3.1.3 **Data used by the tools**

As stated above, 1024^4 data points are available, which sum up to 20 Terabytes of information. The ideal option is to use only the necessary data to generate a number of vector fields that permits to fulfil the objectives set for this part. This is so to keep an amount of information not oversized, to use acceptable computational times and to adapt to reasonable storage needs.

The compromise solution has been to generate the 2D2C vector maps at an integral scale distance (both in time and in the 3D spatial directions). A DNS edge is L_0=2π feet size, with

the integral scale $\mathcal{L}$=1.376 feet yields $L_0/\mathcal{L}$=4.6. The volume for generation of a vector map is formed by a cube side and the laser sheet width (a slab of data). 4 of those slabs could be fit parallel to each cube side with at least one integral length-scale distance, giving 12 for the whole cube. As example, the mid-plane of the 4 slabs taken parallel to the *'xy'* side are shown in Figure 3.3. The time spanned by the simulation is 2.048 seconds, slightly larger than the integral time scale (T=2.02 seconds). In this case t_{stored}/T~1. That allows creating 12 vector maps at the beginning of the simulation and another 12 at the end, giving a total of 24 vector fields (or 24 image pairs in the case of the synthetic image generator). For the generation of those 24 vector fields, the slabs of data downloaded required ~300 GB of storage.

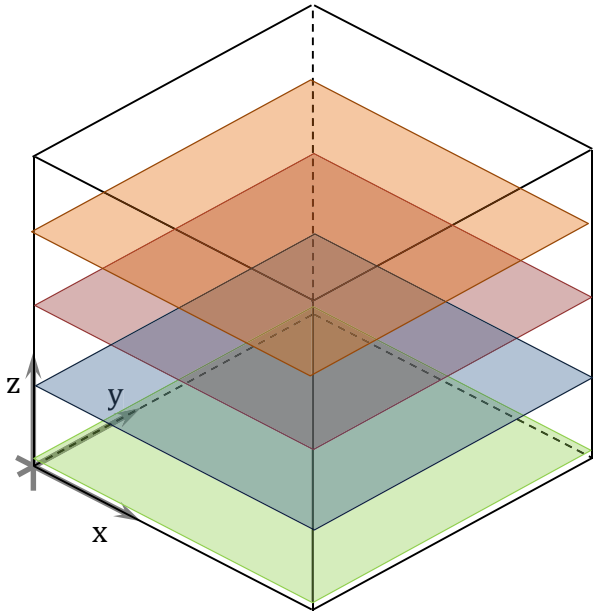

Figure 3.3 Representation of the 4 middle planes of the slabs of data parallel to the *'xy'* direction that are used by the computer tools.

On the case of the vector fields generated from the tools described in this chapter, the objective is to characterize the influence of the measurement parameters on the error (both on the error distribution with the length-scales of the flow and on the global error). The number of vectors should be then sufficient to allow a proper statistical identification of the errors variations with the measurement parameters.

For the largest scale, $\mathcal{L}$, each 2D2C slab contains at least 4x4 = 16 independent zones. This gives 24x16 = 384 independent zones for the largest scales. For smaller scales where this PhD focuses, typically, the error is considered uncorrelated for non-overlapping interrogation windows (Poelma *et al.,* 2006, Adrian and Westerweel, 2011). With that in mind, the number of vectors available for each set of measurement parameters is greatly increased, taking into account that typically at least 100x100 vectors are contained in each 2D2C vector map. In conclusion, the number of vectors seems a priori sufficient for obtaining converged error values.

3.2 THE PIV SIMULATOR

3.2.1 Introduction

The *PIV Simulator* is a tool that generates 2D2C vector maps in which some of the effects of the PIV measurement process are retained while others are avoided.

At present time, synthetic images are a common tool for PIV errors study and on this PhD it is a resource used as well. However, a series of first tests with synthetic images revealed an excessive number of interactions between the different factors, which precluded from distinguishing the contribution of each error source. Effects like the presence of outliers or peak-locking interfered with the effect of turbulence on the measurement. As a consequence, to properly identify the effects introduced by turbulent spatial flow variations in a PIV measurement, the *PIV Simulator* has been developed. This way the number of error sources on the generated vector fields can be reduced (as compared to synthetic images, and even more compared to real images).

The *PIV Simulator* emulates a PIV measurement on the following aspects: (i) it divides the measured region into interrogation volumes which contain particles, and (ii) for each of those volumes a measured displacement is provided by means of a correlation.

However, it is important to remark that no images are created; the displacement correlation map is obtained from the velocities of the particles, the time delay between laser pulses Δt and the particles image size D_P. Indeed, from those parameters the positions and shape of the cross-correlation peak of each individual particle with itself (particles self-correlation peaks) can be calculated. When those peaks are added, a correlation map is obtained. When the correlation map is discretized with a high enough resolution the peak-locking effects can be avoided, and the maximum correlation value provides the measured displacement. The production of outliers is avoided because on the displacement correlation map there is no contribution from noise or from cross-talk within the correlation. This way, the effects like the correlation no-linear averaging in presence of spatial flow gradients can be studied without interference of other effects like CCD discretization or correlation cross-talk.

3.2.2 Algorithm

For each of the 24 slabs of data detailed on section 3.1.3, the *PIV Simulator* follows the same process. The inputs of the algorithm are the following ones: interrogation volume dimensions (size of the square interrogation window and laser sheet thickness), overlap of those volumes, time delay between the laser pulses, particles' image diameter and number of particles per interrogation volume.

The sequence of steps is the following; while details on each step are given further below the steps list:

1. The data is divided into interrogation volumes.
2. Each volume is seeded with the number of particles specified by the user.
3. For each volume and with the input parameters, the emulated displacement-correlation maps (without cross-talk) are created.
4. The displacement that provides the maximum correlation value is obtained, for each of the correlation maps.

Related to the first step, the algorithm inputs are restricted to ensure there is a database vector at the center of each interrogation volume. Both the interrogation window size (square) and the laser sheet thickness must be an odd number of gaps between database vectors. The overlap is restricted as well for this reason. This restriction is imposed so all the volumes have at the center a database data point. Its velocity can be used for comparison and error assessment. Then, each of the slabs of the cube is divided in as many interrogation volumes as possible as the number of in-plane vectors permits.

Once the measured volume is divided into interrogation volumes, all of them are seeded with the number particles specified by the user. The particles positions are randomly chosen by recurring to the pseudo-random generator of Matlab, which is of the Mersenne Twister type (Mathworks, 2015).

Related to the third step, the algorithm obtains the velocities of the particles from the database. Then, taking into account the time delay and the diameter of the particles, the analytical expression of the displacement correlation map is calculated. To do so, each of the particles self-correlation peaks are calculated assuming particles follow a straight line in the direction of the velocity they have; then, the individual self-correlation peaks are added to give the displacement correlation map without cross-talk. The intensity of a particle self-correlation peak in the correlation map is the square of the particle intensity. The particle intensity is dependent in the initial out-of-plane position. Those positions are used to determine the intensity by taking into account the type of laser sheet (top-hat or Gaussian profile). The out-of-plane velocity of particles has no effect on the self-correlation peaks, to remove the influence on the random error of the change of light intensity of a particle (cf. 5.3.9 or Nobach and Bodenschatz, 2009). The in-plane motion has no influence either, as is the case when a multi-grid scheme with image deformation is used. The self-correlation peaks are assumed to be of Gaussian shape, as is the case when particles are Gaussian (Raffel *et al.,* 2007). If the particles have an imposed image diameter D_P (defined as twice the distance from the particle position for which the Gaussian surface light distribution reaches the e^{-2} intensity ratio) the diameter of the self-correlation peaks is $\sqrt{2}D_P$. The cross-correlation between different particles has been avoided, as Figure 3.4 depicts.

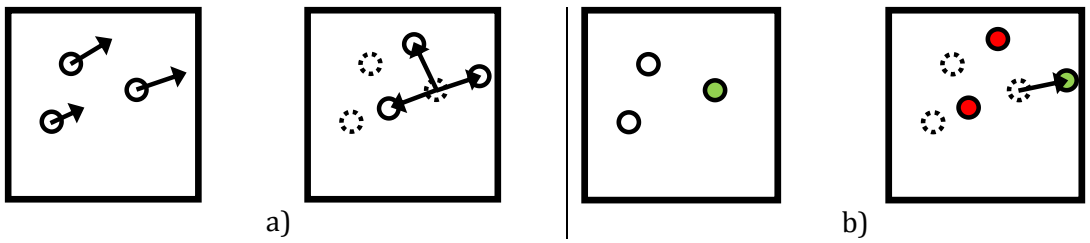

Figure 3.4. a) For a certain displacement, a PIV correlation would correlate each of the particle images in the initial interrogation window with all the particle images in the final interrogation window. b) In the case of the *PIV simulator*, only the correct particle images are correlated, avoiding cross-talk.

Finally, the displacement that maximizes the correlation is sought in two iterative steps. On the first step the correlation map is numerically calculated in 50x50 data points spanning from the minimum displacement minus $D_P/5$ to the maximum displacement plus $D_P/5$, in each in-plane direction. The displacement providing the maximum correlation value is calculated in this region (displacement identified as $\overrightarrow{d_1}$). Then, centered on $\overrightarrow{d_1}$, the correlation map is recalculated on a finer mesh of 100x100 data points spanning a smaller

region. The displacement that gives the maximum correlation value is taken as the measured displacement. The second region is the smaller of these two: (i) the region that spans from $\overrightarrow{d_1} \pm D_P/4$ for each in-plane direction or (ii) the first iteration region. The calculation in two steps of high resolution allows reducing the discretization error to a minimum, as is verified below. Thanks to the two steps discretization, there is no need of any peak fitting algorithm, as compared to a PIV process.

Related with this step, if the self-correlation peaks are very sparse (as in Figure 3.5) the algorithm could find a maximum correlation value at the first step which is not placed at the highest correlation peak. For example, in Figure 3.5 the highest correlation value is given at the displacement peak labelled as 1, but on the first step the algorithm could find the maximum correlation value at the peak labelled as 2. When that happens, the second iteration will be centered in a displacement peak which is not the one containing the largest number of particles self-correlation peaks in the map. Nevertheless, the displacement will still be given by self-correlation peaks of particles images and never by a random peak in the map, as could be the case on synthetic images or on a real PIV analysis. That is, outliers are avoided, as was one of the objectives of the tool.

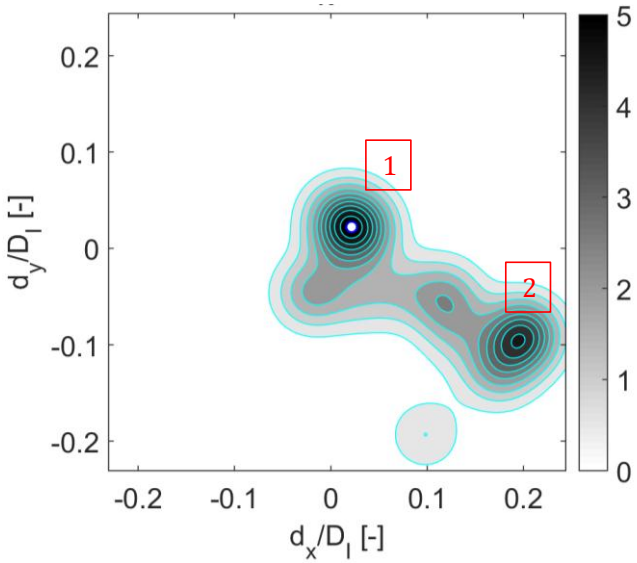

Figure 3.5 Correlation map obtained from the *PIV Simulator* for a case with 20 particles. The axes are displacement divided by the interrogation window size (D_I) and the colorbar indicates the correlation value (arbitrary units).

In addition to the simulated correlation process described above, an additional calculation possibility has been implemented in the PIV Simulator, for the purpose of error study. This additional possibility is an average of the velocities of the particles seeded inside the corresponding measurement volume (the theoretical value of the correlation for $D_P \rightarrow \infty$). For this calculation, each particle is weighted with the light intensity provided by its out-of-plane position. This calculation is considered to represent an ideal moving-average low-pass filtering measurement (that is described in 5.3.3).

Thanks to this simplified version of a PIV measurement, the effects produced by the interaction between (i) the correlation non-linear averaging, (ii) the laser sheet thickness and (iii) the presence of spatial gradients are assessed in the PhD. This is done, as commented before, avoiding the presence of outliers from particle cross-talk in the

correlation space or from out-of-plane movement, and without peak locking and other effects. The results obtained from the vector fields created with the *PIV Simulator* are reported in section 7.1.

3.2.3 **Limitations**

The first limitation of this tool is that the effect of temporal variations of the flow has not been included. This is so, because for the results presented in this work the smallest interrogation volume is of a size $\ell \sim 5\eta$. On the other hand, the largest time delay is $\Delta t \sim 0.2\tau_\eta$. In consequence, spatial variations are much more relevant than temporal ones and the effect of temporal variations should be negligible on these results.

Also, as can be observed from the steps described above, the limit with which a displacement is resolved by the PIV Simulator is of $D_P/200$. This limit is equivalent to solving a displacement from PIV images with a resolution of 0.01 pixels (for the particle images diameter used in this work of ≈2 pixels). In the figure below, the effect of changing the resolution in the function used for error analysis (defined in Chapter 5 section 5.2.1.1) is shown, for the lowest Δt studied with the PIV Simulator. The line with square symbols is obtained from solving the displacements with a resolution of $D_P/200$, the line with diamonds solves the displacements with $D_P/40$ and the line with plus signs solves the displacements with $D_P/40$.

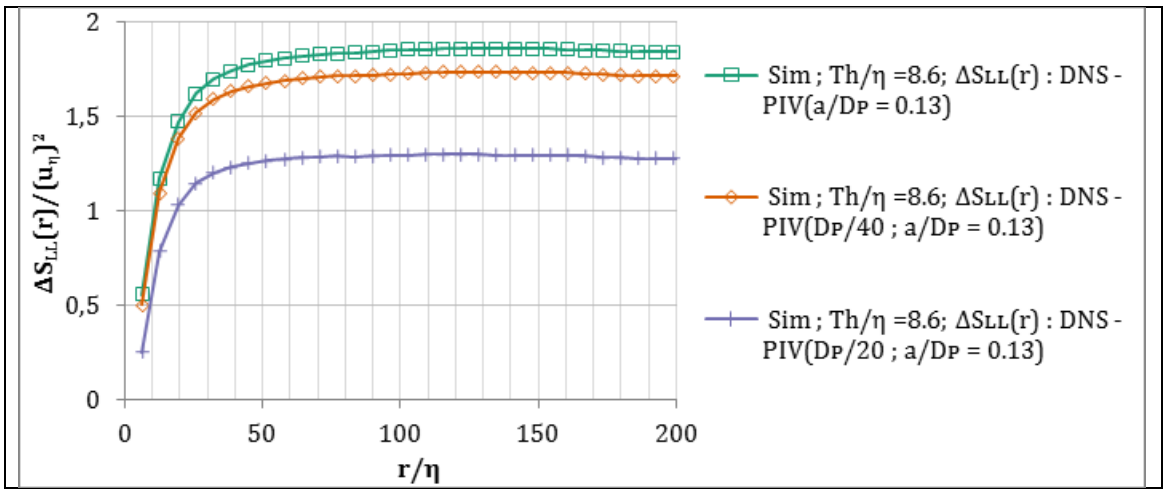

Figure 3.6 Effect on $\Delta S_{LL}(r)\{u\}/(u_\eta)^2$ of the resolution of the correlation map on the PIV Simulator results.

As can be appreciated, even in the case with the lowest Δt where this limitation should be more important, changing the resolution from $D_P/200$ to $D_P/40$ barely affects the result. The difference is $\sim 0.1(u_\eta)^2$ and in the results shown in Chapter 7 much larger variations are given. In consequence, the resolution of $D_P/200$ should properly allow characterizing the errors of interest and it can be considered that the algorithm determines perfectly the correlation maximum position (for the time delays used in this work).

3.3 SYNTHETIC IMAGES ALGORITHM

3.3.1 Introduction

The generation of synthetic image pairs with the computer, from a known vector field is a method to which PIV researchers usually recur to (Raffel *et al.*, 2007, among others), in order to assess the accuracy of PIV measurements. This method allows controlling the error sources that affect the measurement. Also, since the velocity field is known, it allows calculating the value of the error. Additionally, in the case of this PhD, it serves as an intermediate step between the analysis of the results derived from the *PIV Simulator* and the results of the real images from a dedicated experimental set-up. Indeed, the fact that images are generated and that a PIV analysis is performed adds error sources not present in the *PIV Simulator* (such as peak-locking, in-plane and out-of-plane losses of particles or presence of outliers). Analyzing these errors coupled with the ones analyzed with the PIV Simulator with a single tool would have been complex. But once the basic errors are separately assessed thanks to the PIV Simulator, this second tool allows for the assessment of the additional error sources, completing the whole picture, closer to the reality of an experiment.

3.3.2 Algorithm

Each of the 24 image pairs generated is obtained following the next sequence of steps:

1. Selection of the volume of the database that contributes to the synthetic photographs.
2. Distribute a certain number of particles (N_P) randomly inside the photographed volume, which is 3D.
3. The particles are moved according to their position using the selected flow detailed in 3.1.
4. Remove the particles that are too far away to shed an important amount of light into the sensor, for both distributions of particles from points 1 & 2.
5. Generate the images of both distributions of particles.

In the following, the specific details of the code for each of the steps are given. All the scripts have been written in Matlab® r2015a in this PhD work.

The following assumptions are made: (i) the laser is assumed to have a Gaussian profile, (ii) both lasers are assumed to be perfectly aligned and provide the same maximum intensity and (iii) particles are mono-disperse in size. Additional assumptions are detailed in the appropriate part of the algorithm. The software that is used to obtain the vector fields from the synthetic images is Davis 7.2®. Where a specific aspect of the software has to be taken into account for the generation of the images it is mentioned on the text.

3.3.2.1 *Selection of the photographed region*

The volume that is taken to create each of the images of a pair is defined by the following boundaries. The thickness of the laser sheet (*Th*), which is a parameter entered by the user, is defined as the distance between the two points where the laser intensity profile (with Gaussian shape) reaches the e^{-2} ratio with respect to the maximum intensity of the profile. However, the images are generated with all particles that by their out-of-plane

position scatter at least a 5% of the maximum laser intensity value. Therefore, $\approx 1.2Th$ size is used in the out-of-plane direction to generate the images.

As to the in-plane size of the region to be photographed, to ensure that each displacement vector provided by PIV has a corresponding DNS vector to compare (so that the error of a vector can be calculated) the relations between the photographed region and the camera sensor are restricted. Imposing these restrictions is preferred over the other option which would be to interpolate either of the data (the PIV vector map or the DNS vector field) to compare the vectors. The problem of the latter option is that it introduces an additional error to the ones under study.

In order to fulfill the previous restriction, the user has to provide the resolution the posterior PIV analysis will have (in pixels). The resolution of the PIV analysis is obtained from the interrogation window size and the overlap imposed on the software to evaluate the images. This implies that the processing parameters, which are usually chosen based on the images, should be known beforehand. In addition, the separation the PIV vectors projected onto the DNS domain have, has to be provided as well. Finally, the number of pixels of the sensor has to be given.

With all those inputs, the in-plane DNS data spanned is fixed. Depending on the inputs, some images could require more data than available on the database, which is solved by recurring to the periodicity of the data.

With the sizes of the photographed volume defined, it is possible to move onto the step of creating a cloud of particles inside the DNS data that provides the synthetic photo obtained at the first laser pulse.

3.3.2.2 *Particles positions at the first laser pulse*

Once the volume that contributes to an image is defined, the volume of particles that is moved can be calculated. The size of the DNS volume filled with particles is larger than the size of the DNS volume that contributes to the image, to take into account possible particles coming in or going out of the photographed volume. This extra volume serves as well to obtain the same number of particles per pixel (*ppp*, which is an input parameter of the algorithm) for cases with different time delay between the laser pulses.

The difference between the two volumes (for every dimension of the volume) is calculated as the maximum velocity found in the data: 3ft/s multiplied by the time delay between the laser pulses, i.e.: the maximum expected displacement. This is illustrated in Figure 3.7, where the filled blue volume is the photographed volume defined by the thickness of the laser and the size of the sensor projected onto the database, the green line indicates all the particles that contribute into a photo and the red line limits the volume that contains all the particles that are moved. The black lines are for the DNS cube.

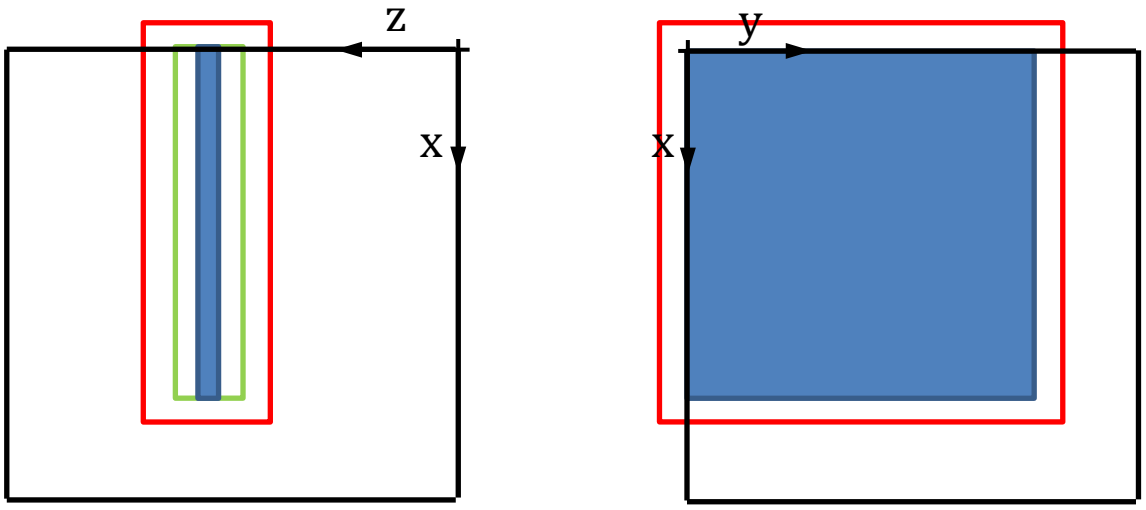

Figure 3.7 Left image: projection of the different volumes employed onto the x-z plane (with z being the out-of-plane direction). Right image: projection of the different volumes employed onto the x-y plane (both are the in-plane components). For both images the filled blue volume is the photographed volume defined by the thickness of the laser and the size of the sensor projected onto the database, the green line indicates the volume of all the particles that contribute into a photo and the red line limits the volume that contains all the particles that are moved. The black lines are for the DNS cube.

From the particles per pixel (henceforth, *ppp*) introduced by the user and the volume of the flow that needs to be filled with particles, it is possible to calculate the total number of particles that are introduced. Only the particles within the thickness of the laser sheet are considered to contribute into the *ppp* parameter introduced by the user (i.e. the particles inside the blue volume of Figure 3.7). The reason for this is to keep a constant number of *ppp* when the dime delay Δt or the laser thickness is changed on the image generator.

Once the number of particles and the domain that needs to be filled is known, the volume is filled by recurring to pseudo-random numbers with uniform distribution (generated by a Mersenne Twister algorithm, Mathworks, 2015) so the position of each particle within the previously defined boundaries is calculated.

This cloud of particles is used for the generation of the first image of a pair, the cloud of particles corresponding to the second image is obtained by moving this one with the selected flow of section 3.1. The first image of the pair is taken at a time instance relative to the database time evolution dependent on the PIV image deformation method, as is shown in the next subsection.

3.3.2.3 *Movement of particles: positions at the first and second laser pulses*

As stated in the previous point, the cloud of particles is inserted into the database in a specific time instance to move the particles from that moment. The time instance at which the particles are inserted is selected so that the vectors provided by the PIV analysis fall onto a time instance where DNS velocity data is available.

The time instance at which a PIV measurement provides the velocity map depends on the image deformation chosen in the analysis. According to Wereley (2001) if the deformation method is antisymmetric (only the second image of the pair is deformed), the velocity is being provided at the first laser pulse instance; however, if the deformation method is symmetric (i.e. both the first and the second frame are deformed) the velocity is being

provided in the middle time between the laser pulses occurring. Again in this case, prior to the creation of a set of images, a parameter that is chosen on the posterior evaluation of it must be entered. In Figure 3.8 below, the time instance at which particles are inserted can be understood.

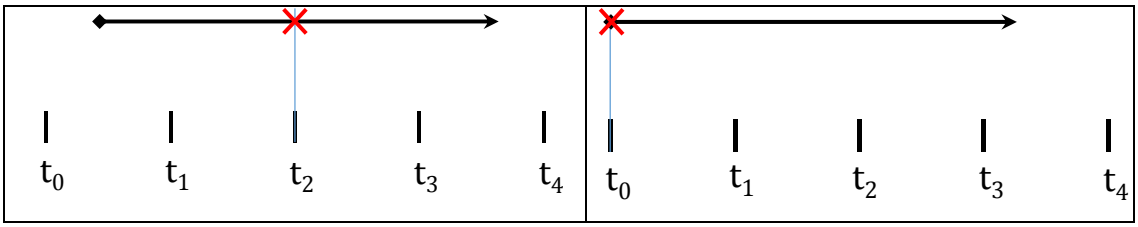

Figure 3.8 Both images: the vertical segments indicate the time instances where DNS data is available. The arrow indicates the time spanned between the two laser pulses (Δt). The diamond is where the particles are inserted and the arrow tip where they end. The red *x* indicates where PIV analysis provides the corresponding velocity field. The left image is for a symmetric deformation and the right image for antisymmetric deformation.

As appreciated from the Figure 3.8, depending if the deformation method chosen is symmetric, the particles could be inserted at a time instance where there is no DNS data available. In the case of antisymmetric deformation, the particles are always inserted at a time instance where DNS data is stored. Therefore, in the case of symmetric deformation, when the velocity at a certain time instance is needed and there is no data stored at that particular time instance, the method has been to use the velocity at the nearest data point.

For both possibilities, the time spanned between the two laser pulses could cover several stored database time instances (as in Figure 3.8), so a time integration scheme could be used. The choice has been to recur to an explicit integration scheme of first order, so the position of a particle and the velocity are recalculated after an amount of time δt has elapsed. For a single particle:

$$\boldsymbol{x_1}(t_0 + \delta t) = \boldsymbol{x_0} + \boldsymbol{V_0}\,(\boldsymbol{x_0}, t_0)\delta t$$

Where $\boldsymbol{x_1}$ is the position of a particle that started at position $\boldsymbol{x_0}$ and time t_0 with velocity $\boldsymbol{V_0}$. δt is the time elapsed between the two instances of calculation, which will be Δt_{DNS} or smaller, depending on the time instance the particles were inserted At the new position and at the time instance $t_0 + \delta t$ the velocity of the particle has to be recalculated, and from that it is possible to obtain the next position of the particle and so on, until the final position is reached. This is done for all particles.

The time steps where the positions and velocities are calculated depend again on the deformation scheme used. For the antisymmetric deformation method, the time steps are the same than those of the DNS data and there is never need of time interpolation of the velocity. However, for the symmetric deformation method, the data is taken from the nearest data point for the first step in the time integration. The discretization is made coherent with that choice, that is, the discretization points (red vertical lines in Figure 3.9) are fixed at the time instances where the velocity should take the value from the next data stored. Figure 3.9 illustrates with an example how are the time steps chosen for both the deformation methods:

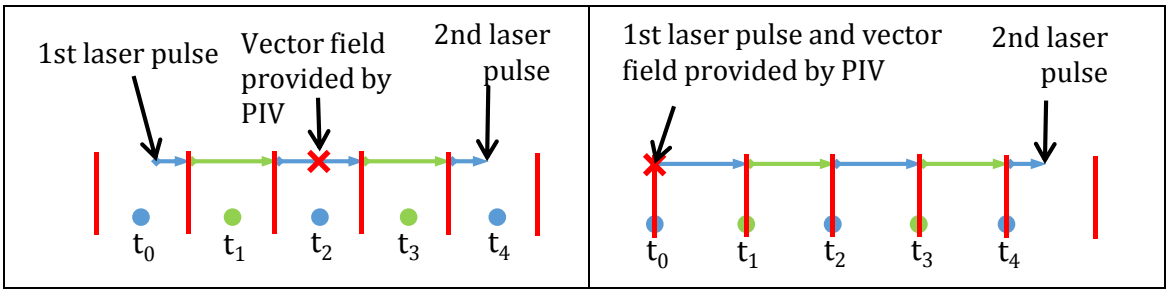

Figure 3.9 Both images: the filled dots indicate the time instances where DNS data is available. The red lines indicate the time discretization points: the time instances where positions and velocities are recalculated. The arrows indicate the movement completed by a particle for each time step and the color of the arrow indicates the DNS time instance used (which would be the closest filled dot with the same color). The red *x* indicates where PIV analysis provides the corresponding velocity field. The left image is for a symmetric deformation and the right image for antisymmetric deformation.

So far, the way the velocity of a particle is set depending on the time instance at which the particle is located has been clarified. However, the particles will be located all over the database volume and usually a particle position will not be coincident with a DNS mesh position. The velocity of a particle is determined then by trilinear interpolation. It must be noted as well that the particle has the velocity the flow has at the particle position, i.e. no slip is being introduced.

All the errors produced on the calculation of the final position of particles are estimated in 3.3.3. Those errors are from: (i) the time interpolation of the velocity for each particle, (ii) the spatial interpolation and (iii) the time integration.

3.3.2.4 *Remove particles*

As stated previously, the volume that was filled with particles was larger than the photographed volume (see Figure 3.7), to allow for particles to go in or out of the photographed volume. Once that the position of the particles at both laser pulses has been determined, there is no need to keep the particles that are outside the photographed volume, so those particles are removed from the calculations, for both time instances. This step helps to reduce the computation time.

3.3.2.5 *Generation of images*

In this stage of the algorithm, the particles positions at both laser pulses are projected onto the sensor of the camera and the images of all the particles within the photographed volume obtained.

The first step, which is the projection of the particles onto the sensor, is completed assuming the camera is very far from the photographed volume in respect with the depth of the illuminated volume. As a result, only the in-plane position of the particles in the photographed volume influences the position on the sensor of the projection of the particles. Unlike with other projection models the out-of-plane position has no effect on the projected position in the sensor.

The distribution of the particles physical diameter is assumed to be mono-disperse (of the same size), which means the light received in the sensor coming from a particle depends only in the out-of-plane position. As stated previously, the laser sheet is supposed to have a Gaussian profile, which gives the light intensity scattered by a particle depending on the

out-of-plane position of the particle and on the laser sheet thickness, following the equation below (Raffel *et al.*, 2007):

$$I_0(z) = I_{max}\, exp\left(-\frac{(z - z_0)^2}{1/8Th^2}\right) \tag{3.1}$$

Where I_{max} (chosen by the user) is the intensity of the laser at the center position z_0, z is the position of a particle and Th is the thickness of the laser sheet, as defined on 3.3.2.1.

All the particles are supposed to produce an Airy disk of the same size in the sensor, which is approximated by a Gaussian profile. At a distance of half the particle image diameter (D_P, entered by the user, in pixels) from the projection of the particle on the sensor the Gaussian distribution of light reaches e^{-2} of the maximum intensity value of that particle (which itself is given by the out-of-plane position). The light distribution of a particle in the sensor plane *I(x,y)* is given by (Raffel *et al.*, 2007):

$$I(x, y) = I_0(z)\, exp\left(\frac{-(x - x_0)^2 - (y - y_0)^2}{1/8D_P^2}\right) \tag{3.2}$$

Where $I_0(z)$, is the particle intensity as given by Raffel *et al.,* 2007 and x_0, y_0, is the position of the projected particle onto the sensor.

The signal provided by a pixel is given by integration of the Gaussian shape of the particle. The integration is performed by recurring to the error function (Raffel *et al.*, 2007) assuming that the pixels have a fill factor of one.

The Gaussian profile by which the light received on the sensor from a particle is modeled, never reaches light intensity zero; however, not every pixel of the sensor is filled with light coming from a particle, because that would require too much computational time. The criteria adopted is that only the pixels that are contained within a $(3D_P)^2$ square centered in the particle are filled with the light of the particle. The light intensity at a distance of 1.5 D_P from the particle is already $(6.6 \cdot 10^7)^{-1}$ of the maximum, so it is considered that the area of the sensor that is not filled with light from the particle would receive negligible amount of scattered light.

Finally, when two or more particles overlap in the sensor, the intensities produced by each particle are added.

3.3.3 **Synthetic image generator error**

Since the synthetic images generated are evaluated by means of PIV and then the vectors obtained are used to calculate the error of the measurement technique, the error introduced in the process of generating the images needs to be assessed. The steps of the process where error could be introduced into the particles positions at the end of the movement are the spatial and time interpolation (to obtain the velocity of a particle) and the time integration to move the particles.

3.3.3.1 *Time interpolation error*

This error is produced only when the synthetic images are generated for a PIV analysis with symmetric image deformation scheme. As was shown previously, for that

deformation scheme the time instances at which the particles are moved are not coincident with the time instances where DNS data is stored. Then, the velocity that a particle has is obtained from the DNS data at the nearest time instance.

The error produced by this fact can be obtained as follows. The time step between the stored DNS data is Δt_{DNS} = 0.002s, while the Kolmogorov scales characteristic time is τ_η = 0.0446s, giving $\Delta t_{DNS} \sim \tau_\eta/22$. A first estimate of the velocity changes in a DNS time step can be $\Delta V_{\Delta t_{DNS}} \sim u_\eta/22$, with u_η the characteristic velocity of Kolmogorov scale. Those velocity changes give the order of magnitude of the error that is produced, i.e. $\varepsilon \sim \Delta V_{\Delta t_{DNS}} \sim u_\eta/22$ which is indeed $1/20^{\text{th}}$ of one of the smallest characteristic velocities to be found in the flow and therefore considered negligible.

3.3.3.2 *Spatial interpolation error*

The error from 3D linear spatial interpolation is estimated from the error of linear interpolation of the one-dimensional case. The error of a linear interpolator *p(x)* of *U(x)* is (Burden and Faires, 2002):

$$\varepsilon_{1D} = U(x) - p(x) = \frac{d^2U(\xi_x)}{dx^2}\frac{1}{2}(x - x_0)(x - x_1)$$

Where x_0 and x_1 are the points used to interpolate and ξ_x is a point inside the interval $[x_0, x_1]$. The maximum value that this error takes is given by the maximum of the second derivate of *U(x)* inside the interval and by the maximum of the function $(1/2)(x - x_0)(x - x_1)$. When *x* is different than x_0 and x_1:

$$\max\left(\left|\frac{1}{2}(x - x_0)\,(x - x_1)\right|\right) = \frac{(x_1 - x_0)^2}{8}$$

Then, the maximum value for the error ε_{xyz} from using 3D trilinear interpolation would be (estimated from the first direction derivate, but any direction could be used):

$$\varepsilon_{xyz} \sim \frac{(x_1 - x_0)^2}{8}\left|\frac{\partial^2 U(x,y,z)}{\partial x^2}\right|_{max[x_0,x_1]} \tag{3.3}$$

Where the second derivate takes its maximum value inside the interval $[x_0, x_1]$.

In order to estimate the order of magnitude of the error, the second derivate value is estimated by (distance between x_1 and x_0 is 2.1η):

$$\frac{\Delta U}{\Delta x}\Big|_{\Delta x \sim 2\eta} \sim \frac{2u_\eta}{2\eta}$$

$$\frac{\partial^2 U}{\partial x^2} \sim \frac{2u_\eta}{(2\eta)^2}$$

Which gives an error value:

$$\varepsilon_{xyz} \sim \frac{(2\eta)^2}{8}\frac{2u_\eta}{(2\eta)^2} \sim \frac{u_\eta}{4}$$

This error could have a significant influence on a particle velocity, since it is quite close to Kolmogorov scale velocity. For this reason, the error is estimated also numerically by recurring to expression (3.3). On that expression, the maximum value of the derivate inside the interval cannot be calculated. Instead, a set of data points is used. The error is calculated for the 24 planes of data that are used to generate the images. For that data-points $\partial^2(\cdot)/\partial x^2$, $\partial^2(\cdot)/\partial y^2$ and $\partial^2(\cdot)/\partial z^2$ for all three velocity components are calculated. That gives 9 second derivates calculated over $\sim 20 \cdot 10^6$ data points, which should allow for a proper characterization of the error.

In order to estimate the second derivate a finite difference centered approximation of 5 points is used:

$$\left.\frac{\partial^2 U(x)}{\partial x^2}\right|_{x=x_i} = \frac{1}{12\Delta x^2}\left[-U(x_{i-2}) + 16U(x_{i-1}) - 30U(x_i) + 16U(x_{i+1}) - U(x_{i+2})\right]$$

Where x_i is the data point where the derivative is calculated, Δx the distance between successive data points and x_{i-2}, x_{i-1}, x_{i+2}, x_{i+1} the data points used for the calculation. This approximation has an error of order Δx^4.

The maximum of all data points and of the 9 second derivatives gives $\varepsilon_{xyz} \sim 3.6 u_\eta$. On the other hand, the rms of all data points and of the 9 second derivatives gives $\varepsilon_{xyz} \sim 0.06 u_\eta$. The maximum error value is large enough to influence on the results. However, as indicated by the rms value it should occur for very few particles, since the rms shows a low and acceptable value. Taking that into account, the overall effect produced by this error should be negligible, although some particles could have an important error.

3.3.3.3 *Time integration of the movement*

In order to move a particle from the first laser pulse time instance to the second laser pulse time instance an explicit integration scheme was chosen. The details can be found in 3.3.2.3. The result of the integration scheme is that the particle ends up at a position that may not be necessarily the one it would have reached, as shown in Figure 3.10 below.

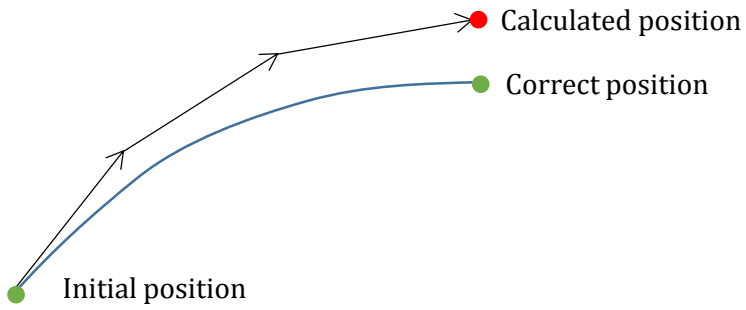

Figure 3.10 Error induced on the final position of a particle due to the time integration scheme implemented.

In order to estimate the error produced on the particles position at the end of the movement from this source, a set of particles is moved by using the time discretization of the DNS and a time twice that one (i.e. 0.002 seconds and 0.004 seconds). 30 million particles are placed inside a slab of DNS data and moved as described in 3.3.2.3 but using the two different discretization times, giving two different positions per particle. The error

is calculated for different time delays by obtaining the mean of the distances between the two positions where a particle ends. The error is calculated only for the symmetric deformation scheme, which is the one used for the whole set of images generated.

For an explicit integration scheme of order 1, the error is proportional to the time delay. The average error obtained for the different time delays, divided by the displacement induced by Kolmogorov scale velocity is of a 13%, i.e. $\varepsilon \sim 0.13 u_\eta$, and therefore should be negligible. This error is the largest of the three studied. Nevertheless, the value is independent of the acquisition parameters (when expressed in velocity units). Thus, it should not interfere with the characterization on the measurement errors variation with the acquisition parameters.

3.3.4 **Synthetic images analysis**

The synthetic images generated with the algorithm described in this section and the vectors obtained from them, have the following common characteristics (the results are in Chapter 7 section 7.2): the interrogation window size D_I and the vector fields' resolution is the same, 6.4η. Only a Gaussian laser profile is used on the study. The particles per pixel (ppp) are 0.09 which gives approximately 90 particles per interrogation volume. The number of pixels of the image is 7500x7500 and the percentage of a DNS edge spanned of ~70% (50% of a side surface). The full database length was not used due to too long computational times. The particles image size was of 2.2 pixels at the e^{-2} points. Magnification is such that η is 5px.

The images were not preprocessed. The PIV evaluation and processing parameters are the following:

- Multi-grid approach, 2 steps per IW size, from 256 pixels to 32 pixels. The results from each intermediate step are smoothed in regions of 3x3 vectors. Overlap on the intermediate steps is of 50% and on the final one of 0%. The total number of vectors obtained is of 234x234.
- Symmetric image deformation with a bilinear grey level interpolation in all the steps except for the last one, where Whittaker interpolation was applied.
- 3 points in each direction Gaussian subpixel peak-fitting.
- Round weighting on the last interrogation window size. The function is determined in section 3.3.4.1. The normalized response of PIV when this window is used is provided in 5.3.3 and is similar to the normalized response of a Gaussian function of D_I size at the e^{-2} waist points.

During the multi-grid intermediate steps the vectors are validated by a modified version of the median filter (available in Davis 7.2, Lavision, 2007), identified in the software as "strongly remove and iteratively replace". This filter is a 4-pass median filter which, according to the manual, is capable of rejecting groups of spurious vectors. It is based on Westerweel (1994) and Nogueira *et al.* (1997).

The median filter used works the following way: first, the vector in the center of a 3x3 vectors' region is compared to the median vector of that region. The vector will be removed if it surpasses the value of the median vector ± a factor multiplied by the standard deviation of the vectors in that region. On the second pass, all vectors which do not have at least n neighboring vectors left are also removed. On the third pass good

vectors are filled in. To determine if a vector is good or not it is compared against the median of the existing neighboring vectors ± a second factor multiplied by the standard deviation. The fourth pass removes groups of vectors with less than *n* vectors. On the case of the intermediate steps of the multi-pass scheme, the second and fourth steps are not carried out and the factors multiplying the standard deviation are 1.2 on the first step and 3 on the fourth one.

The vectors used for the calculations were validated by a post-processing of an allowable vector range. For a vector to be valid, its value had to contained within a range of ±3ft/s, which was the maximum velocity encountered in the selected flow field. The two closest lines of vectors at the borders of the image are removed for the calculations, to avoid their influence (since those vectors are more prone to have large error values).

In order to estimate the influence of outliers' occurrence in the results of Chapter 7 (following the estimations provided in Chapter 5 section 5.3.12), the same median filter validation than in the multi-grid intermediate steps is used to have an estimation of the proportion of outlier vectors. However, the second and fourth steps are performed with a number of 6 vectors. The results obtained from the vectors that pass both validation steps are plotted in Annex II. Those results have not been analyzed in full detail because of the following reasons:

1. It is not granted that all outlier vectors are removed. Although their effect in $S_{LL}(r)\{u\}$ (the tool chosen for length-scales characterization, as described in section 5.2) should be reduced, there will always be the doubt about if the remaining effects are from outliers not detected or from real displacement vectors.
2. The median filter can remove vectors which are really produced by a displacement peak but with large measurement errors. Therefore, it could conceal the errors that are being studied, acting somehow as a low-pass filter.

3.3.4.1 *Window weighting assessment*

The window weighting used had to be obtained from the software, as it was not specified in the software manual. In order to do so, the correlation map was obtained from two interrogation windows of 256 pixels size. One of the interrogation windows contained a horizontal line in the interrogation window center with light intensity 1024 counts, and the rest of pixels had zero intensity. The other interrogation window contained only one pixel (the one at the center) with light intensity 1024 and the rest of pixels had zero intensity. By proceeding this way, the following correlation values (normalized with respect to the maximum) are obtained in the central line of the correlation map:

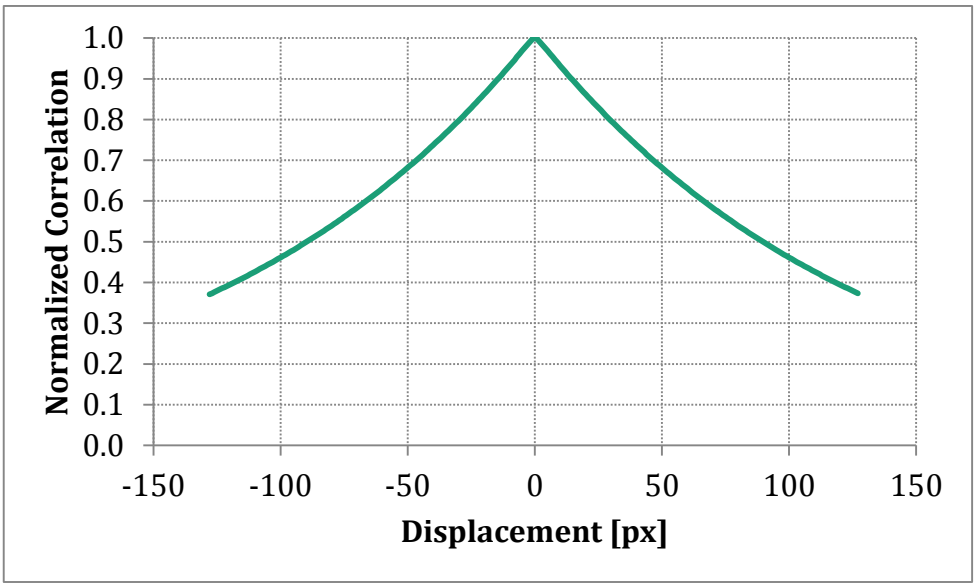

Figure 3.11 Window weighting function employed in the final PIV multi-grid step.

The normalized response of this weighting function, which is of importance for low-pass errors studied in this work, is determined in section 5.3.3.

Chapter 4 PIV Measurements in Wind Tunnels

In order to complete his formation and to apply his knowledge on PIV error assessment, the PhD student made two stay in renowned research centers. This chapter highlights his efforts and contributions in two large facilities:

- Measurement campaign in an adverse pressure gradient at the DLR Göttingen, Germany.
- Measurement campaign (CIRA) of the flow around a helicopter fuselage for assessing possible drag reduction incorporating vortex generators.

Apart from the measurements themselves, the PhD student was involved in data reduction as well as detailed error assessment.

4.1 ADVERSE PRESSURE GRADIENT BOUNDARY LAYER

In the course of the stay, the DLR together with the "Universität der Bundeswehr" of Munich completed a PIV measurement campaign in which the PhD student was allowed to take part. The flow field measured was a turbulent boundary layer submitted to an adverse pressure gradient, which is a problem of high interest to the aeronautical industry. Besides, the problem of an adverse pressure gradient turbulent boundary layer is not yet completely understood (Buschmann and Gad-el-Hak, 2003, or Maciel *et al.,* 2006, among others) and then requires further research effort. On this measurement campaign the pressure gradient imposed to the turbulent boundary layer was similar to the one that is encountered by a flow around a wing with the hyper-lift devices deployed.

4.1.1 Wind Tunnel and Measurements Description

The measurements were made in the Atmospheric Wind Tunnel of the "Universität der Bundeswehr" (University of the Army) of Munich. The wind tunnel is of open circuit type, the air enters upstream the test section and is expelled downstream, and thus it does not recirculate. Both the inlet and the outlet are located outside of the building where the wind tunnel is located. The air is forced inside the wind tunnel thanks to the aspiration of a compressor of 350kW. The wall of the test section (with a cross section of about $4m^2$) was used for the development of the turbulent boundary layer. To impose the adverse pressure gradient the flow went through an area increase, which diminished the velocity and therefore augmented the pressure. This area increase can be seen in Figure 4.3.

This wind tunnel was chosen because the length of the measurement section is large enough (L = 22m) to develop naturally a wide boundary layer (BL). Thanks to the large BL thickness value, the relative size of the laser reflection from the wall on the image is less important, which is a problem commonly encountered on PIV measurements close to walls. This is illustrated in Figure 4.1.

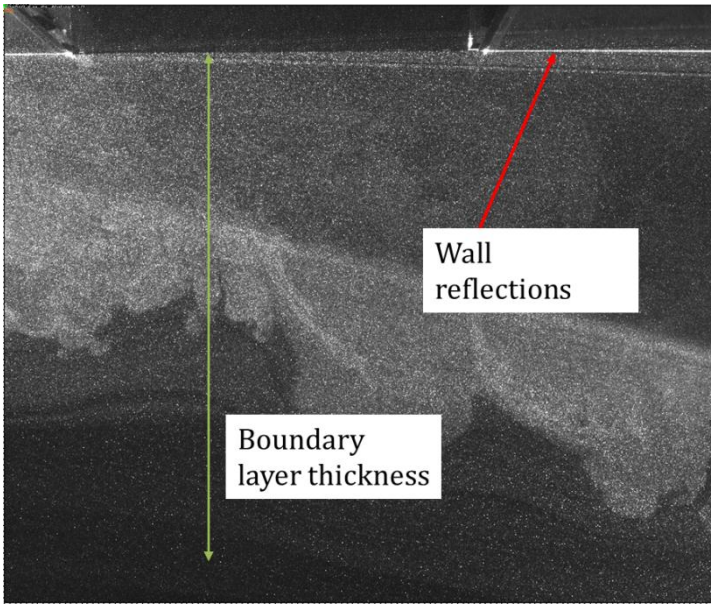

Figure 4.1 Importance of achieving a high boundary layer thickness to reduce the importance of reflections.

Several types of measurements were made of the boundary layer. The measurements performed during the stay of the PhD student in the wind-tunnel were Mono-PIV, Micro-PIV and Stereo-PIV. In addition, Tomo-PIV measurements were performed but the PhD student did not participate in them. The Tomo-PIV measurements, evaluated by the Shake-The-Box algorithm, are presented in Novara *et al.* (2016).

The Mono-PIV system was composed of 9 cameras shooting simultaneously with the Field of View (FOV) of adjacent cameras slightly overlapping. The aim of this configuration was to reconstruct a large FOV of the BL. This system is depicted in Figure 4.2 in blue color. There was also a Micro-PIV system that shot simultaneously with the Mono-PIV cameras (the red square in the figure). The FOV of the Micro-PIV system was contained within the larger FOV of Mono-PIV. The objective was to observe the relations between the phenomena at small and large length-scales. Additionally, this configuration allows obtaining a large spatial range. Hereinafter, the ensemble of both measurement techniques is referred to as long-range PIV. Further details on the long-range PIV system can be found in Reuther *et al.* (2015).

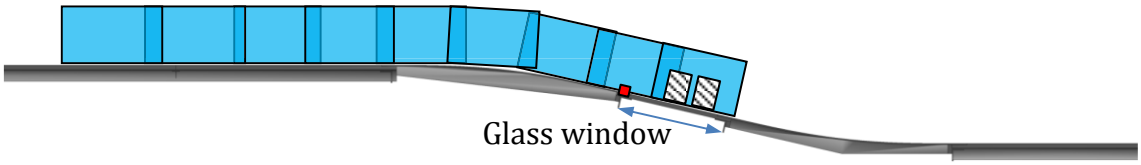

Figure 4.2 Different PIV measurements performed on the turbulent boundary layer. The flow comes from the left of the figure.

Additionally, two Stereo-PIV (SPIV) systems were measuring on the Adverse Pressure Gradient region. These systems are depicted as striped rectangles in Figure 4.2 and were not synchronized with the long-range PIV system. There was no overlap between the Stereo-PIV systems. The aim of the Stereo-PIV systems was to obtain velocity profiles to tune and validate numerical models, as shown in Knopp *et al.* (2015). For the SPIV cameras to look into the wind tunnel, a glass window was placed in the wall where the

boundary layer was developed, as indicated in Figure 4.2. The rest of the wall was polished metal.

Two laser sheets had to be employed in order to illuminate the whole long-range PIV system FOV without producing excessive reflections from the wall. The two lasers configuration is shown in Figure 4.3. Although in the figure the lasers color is different, both lasers emitted in green light at λ=532nm. For the SPIV measurements, the laser was placed on the opposite side of the wind tunnel of the cameras, in front of the window used by the cameras to look into the boundary layer. This configuration (labelled as "Laser SPIV" in the figure) permitted to eliminate the reflections from the borders of the window and also to place the cameras in forward scattering position from the particles, which permits to obtain brighter particles (Raffel *et al.,* 2007).

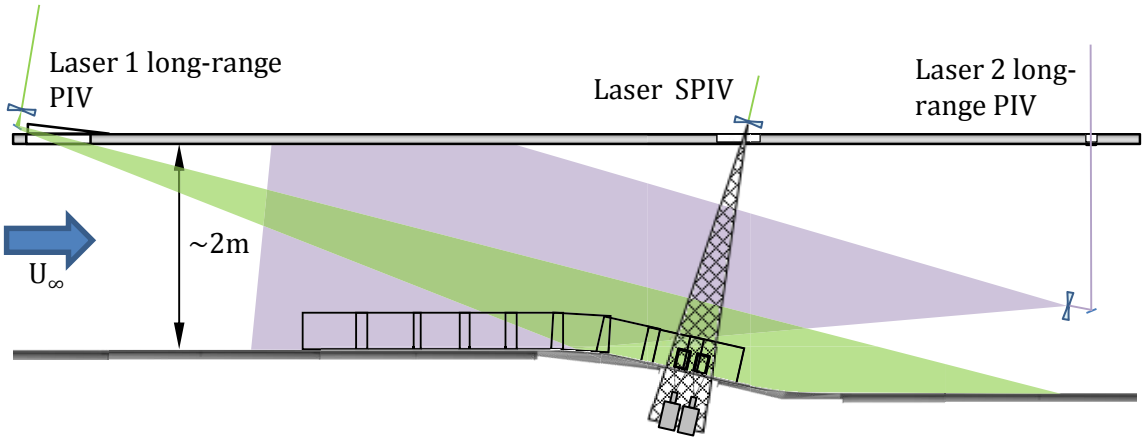

Figure 4.3 Representation of the two lasers employed for long-range PIV measurements and of the laser used for the SPIV measurements.

For all measurements three different velocities were recorded: 10m/s, 23m/s and 36m/s.

4.1.1.1 *Adjustment of the time delay and of the laser sheet thickness*

As the variation of PIV measurement errors with these parameters is studied in this PhD, how those parameters were set is described here.

As per the observations of the PhD student, the time delay between laser pulses, Δ*t*, was set to provide sufficiently large displacements. That allows characterizing the large and small displacements that are produced in a turbulent boundary layer. Different free stream velocities were used and the Δt was adjusted in each case. For the SPIV measurements (which are the ones the PhD student dealt with) the largest average displacements are ~20pixels.

As to the laser sheet thickness it was set based on previous experience, avoiding large out-of-plane motion rates. For the SPIV measurements it was around 2mm. This configuration was reached after some iterations; the laser 1 of the long-range PIV system was used first, but reflections from the wall precluded from an optimum measurement.

Also, the PhD student could observe how to obtain a characterization of the laser profile recurring to a laser beam profiler. This device is sketched below:

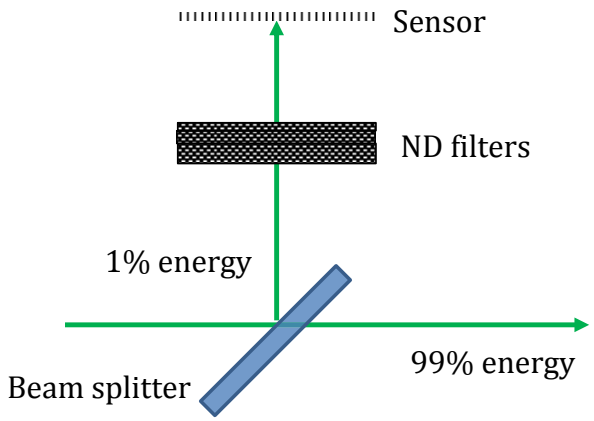

Figure 4.4 Laser beam profiler main components.

The device is composed of the elements sketched in Figure 4.4 plus a housing and software to evaluate the measurements. It permits to measure the laser beam or the laser sheet already formed. The first element encountered by the laser sheet is a beam splitter, which is basically a mirror which reflects ~1% energy and allows the other 99% to pass through. The 1% energy encounters neutral density filters of different darkening intensity to adjust the energy arriving to the sensor. Finally, the sensor array captures the light and sends it to the software for its evaluation. The device allows for a quick on-site evaluation of the laser profile.

4.1.2 **Measurement evaluation**

4.1.2.1 *Problems appeared on the images*

Two problems appeared in all measurements of both Stereo-PIV systems. The first one was that particles (either seeding particles or from the outside of the wind tunnel) settled down on the window through which the Stereo PIV cameras were looking. The second problem was that the laser reflections on the window appeared on the images.

Both effects are noticeable on Figure 4.5. There are two laser reflections on the measurement region, one closer to the wall than the other. The laser reflection closer to the wall (the one that appears in the middle in Figure 4.5) has an overall higher intensity (comparable to that of particles) and produces more problems on the PIV analysis. The laser reflection observed more on the left in the figure is outside the measurement region. Also, the coordinate directions used for the results are shown in the figure. The origin of x-coordinate (position along the wall) is placed at the most upstream vector provided in the analysis. The y-coordinate (wall normal distance) origin was placed at 100 pixels from the image border, which was more or less the wall position. The exact wall position was not known at the moment of analysis so the normal to the wall distance y is approximate.

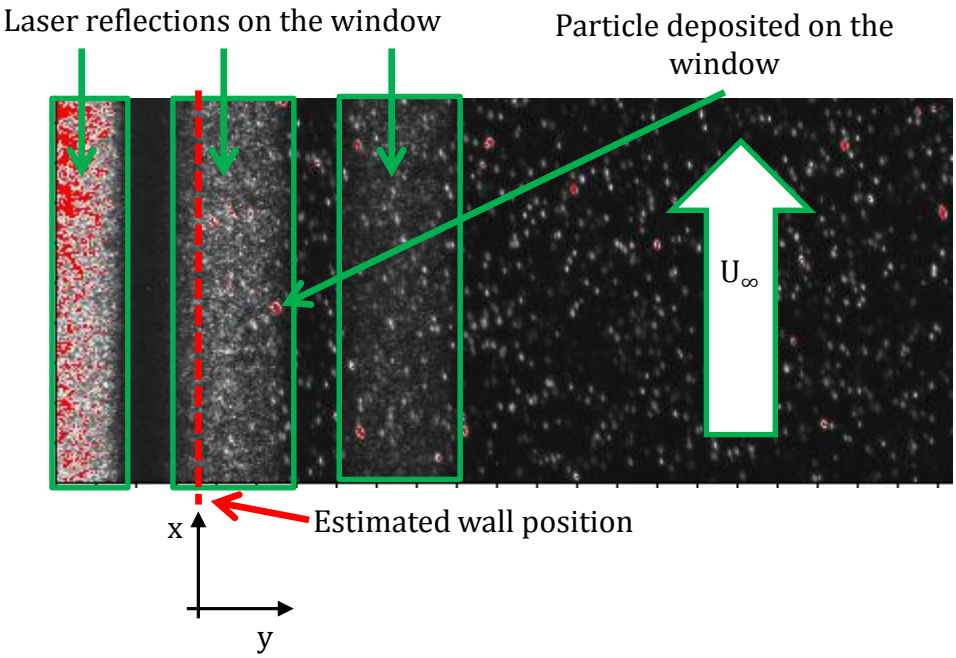

Figure 4.5 Region of a PIV image where the problems mentioned previously are highlighted. The coordinate directions used in this section are also indicated.

The effect of both problems on the PIV evaluation was the same, a local maximum in the correlation plane at 0 displacement. This is shown in Figure 4.6, where the two frames of an interrogation window under one of the laser reflections are plotted. Depending on the case, the peak with more intensity will be that induced by the particles displacement or by the problems mentioned above. As a result, displacements were observed to tend to 0 displacement in the regions where those problems appeared. This preliminary analysis was carried out to reduce that effect.

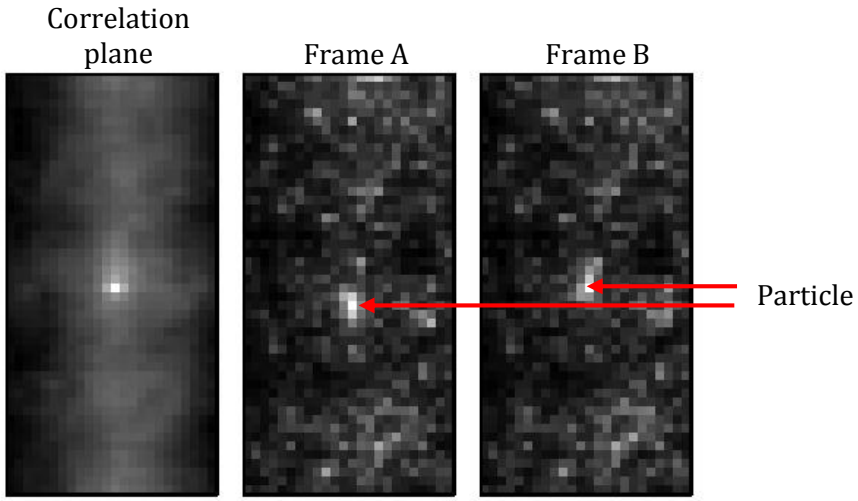

Figure 4.6 *Left*: correlation plane obtained from the two frames of a PIV Interrogation Window (which are in the *middle* and *right* position).

Since the number of deposited particles was usually small, their influence in the results is much less important than that of the laser reflections. In addition, the particles are effectively removed by a mask, so the analysis below focuses on reducing the laser reflections problem.

4.1.2.2 *Results*

The research was carried out by using two different approaches: the first consisted on changing the PIV evaluation parameters (specifically on the interrogation process to obtain the displacement) in order to reduce the effect of the aforementioned problems. The second approach was to diminish the importance of the problems directly on the images, by using image preprocessing methods.

The results of the different methods were compared based on the mean velocity profiles. Velocity must reach 0 at the wall and from there it increases until the free stream velocity is reached, as Figure 4.8 shows. Plus, since the flow is subjected to an adverse pressure gradient, the velocity parallel to the wall (as well as wall normal velocity gradient) decreases when advancing through the pressure gradient, as can be also appreciated in the figure. As was mentioned above, the exact wall position was not known when the analysis was performed, so the *y*-position at which velocity should be zero is not defined accurately. Plus, PIV algorithms employing interrogation windows usually are not capable to reach the 0 displacement at the wall (as stated in Kähler *et al.*, 2012). In any case, displacement should decrease close to the wall and also as the flow advances along the wall and this information is used for performance assessment of the different methods.

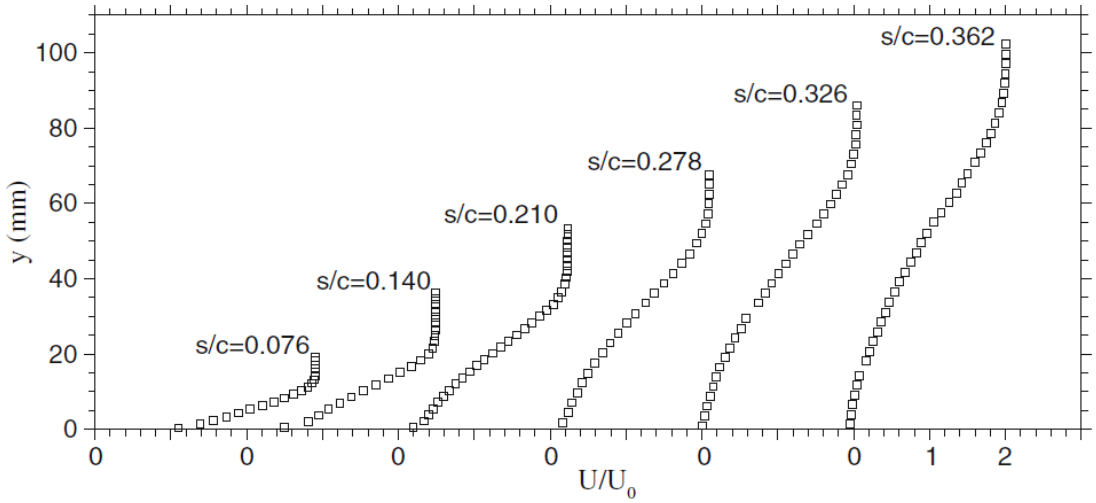

Figure 4.7 Streamwise evolution of mean velocity profiles normalized by the reference speed. s/c is the streamwise position divided by the effective chord length. From Maciel *et al.* (2006).

For all methods, the same set of images was analyzed, a subset of 1000 images from one of the test cases. The software used for the analysis was *PIVview v3.5.9*. For the measurement chosen, wind speed was the largest (36 m/s) and the analysis was made using only one of the two cameras of one of the Stereo-PIV systems. Only one of the two cameras of the Stereo system was chosen for the analysis because prior to obtaining a 3C vector field a coherent 2C vector map must be obtained by a single camera. This permitted to reduce the computational cost then. The following processing parameters were the same for all the results shown below:

- Multi-grid approach, starting with an IW of 256 pixels and ending at 32 pixels, for a total of 7 iterations (2 in the final window size). The overlap was of a 75% in the wall normal direction (8 pixels distance between consecutive vectors) and 25% in the parallel to the wall direction (24 pixels distance).

- Symmetric image deformation with B-splines of 5 points.
- Peak search by Whittaker reconstruction.

Vectors validation was realized by a normalized median filter with a threshold of 3 (Westerweel, 1994).

Displacement calculation methods results

The methods below were studied. For further details on any algorithm, the reader should refer to the software manual (PIVTec, 2010) or to the corresponding reference:

- Correlation by Fast Fourier Transform (FFT). This method is the most commonly used since its introduction by Willert and Gharib (1991).
- Multiple correlation method. In this case, the correlation map is calculated (using the FFT) by multiplication of two correlation maps of interrogation windows that are slightly separated (Hart, 2000). The distance between interrogation windows was set automatically by the software.
- Correlation by FFT with self-correlation disabled: this option ignores the peak (if there is any) at 0 displacement in the correlation map. This method cannot provide any displacement between 0 and 1 pixel and therefore its use may not be advised in some cases.
- Phase correlation: this method, introduced in Wernet (2005) makes use of the phase information of the FFT, discarding the amplitude. Following the author, it has the potential to obtain a narrower displacement peak and with an intensity that can reach even an order of magnitude greater than the traditional FFT.
- Direct correlation: instead of calculating the displacement in the spectral domain using a FFT the direct cross-correlation of both interrogation windows is used (only in the final iteration). The displacement peak search is limited to ± 5 pixels from the one obtained in the previous iteration. The interrogation window in the second frame is enlarged by 10pixels per side for the cross-correlation calculation.

First, Figure 4.8 shows the parallel to the wall displacement profiles obtained by the different PIV evaluation methods at two different *x*-positions along the wall. On the position plotted in the left of the figure, the laser reflection further from the wall had a larger intensity. As a result, some of the displacement evaluation methods present a local displacement minimum at the laser reflection position. This is not coherent with how the velocity should behave, indicating that those methods do not perform well for this particular problem. The methods that present the local minimum are the correlation by FFT and the Phase Only Correlation. However, for the other *x*-position where the laser reflection was less intense (Figure 4.8-right) this local minimum does not appear for any of the processing methods. This confirms then that the local displacement minimum is likely produced by the laser reflection and has not physical meaning.

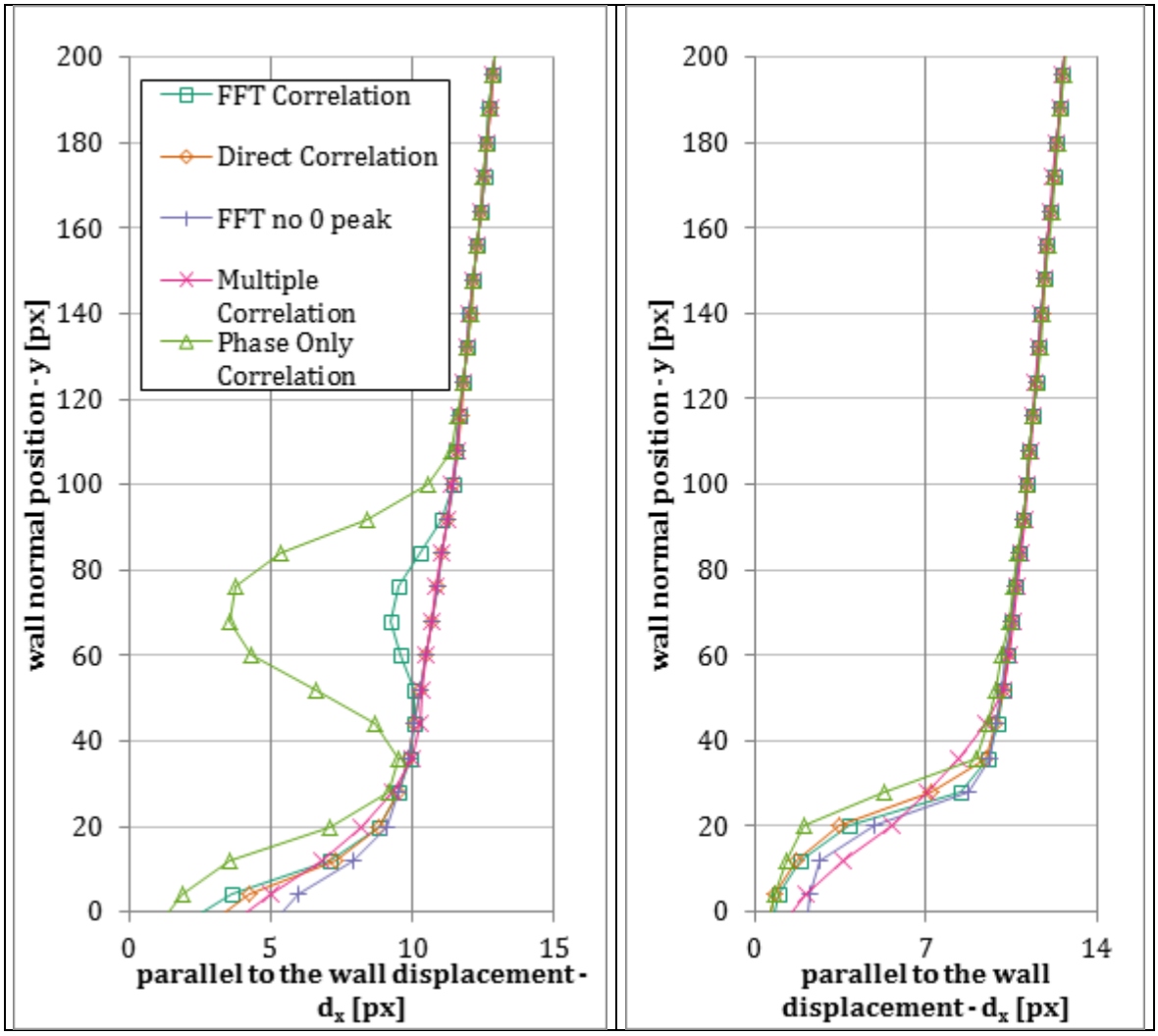

Figure 4.8 Evolution of the parallel to the wall displacement with the wall normal coordinate, at two different *x*-positions.

Under the strongest laser reflection, no PIV evaluation method is able to obtain a satisfying result. This can be observed in Figure 4.9. On this figure the displacement parallel to the wall is plotted, as it evolves at a constant wall distance. All processing methods have an unexpected displacement decrease at around x~600 pixels. This abrupt decrease does not seem physical and could be explained by the increase at that position in light intensity, also plotted in the figure. The light intensity has been calculated from the average image of the 1000 images, by averaging in the wall normal direction the lines under the laser reflection. It can also be remarked that the Phase only correlation method provides displacements that differ more to those of the rest of methods, even in the region with less light intensity, as happened for the previous figure. In any case, none of the methods seems to obtain satisfactory results, as the oscillations and the lack of coherence indicate. For that reason a study on preprocessing methods was also included.

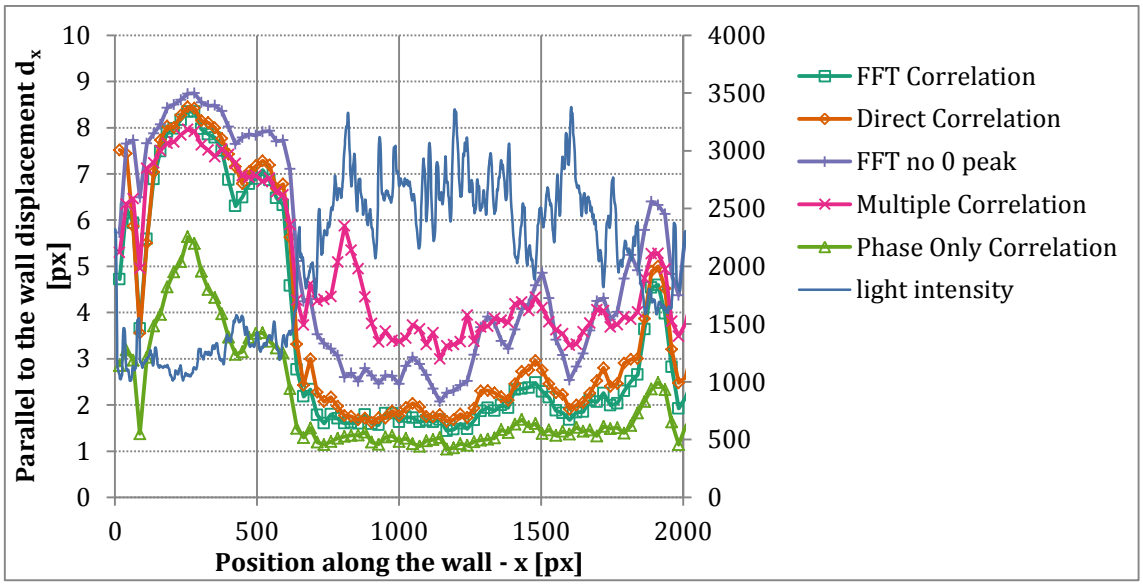

Figure 4.9 Evolution of the parallel to the wall displacement with the position along the wall for the different PIV evaluation methods tested. Wall distance *y*~12pixels

Preprocessing methods results

With regards to the preprocessing methods several possibilities were studied. Some of these possibilities are widely used in the PIV community and some of them were conceived to deal specifically with the problems present in the images. The methods for which results are plotted are:

- "Global" statistical image subtraction. An image obtained from the statistics of the 1000 images used is subtracted from each test image. Results were calculated subtracting the minimum image and the average image.

- "Local" statistical image subtraction. This case is different from the previous one in that the image subtracted is not obtained from the whole run but from a subset of images of the run. For each PIV image a statistical image is calculated. The local statistical image is calculated from a certain number of consecutive images, with the one to be preprocessed in the center of the sequence. Only performed with the local minimum.

- Non-linear image subtraction. This method is described just below.

- Non-linear image multiplication. This method is described just below.

New preprocessing methods

In an attempt to reduce as much as possible the laser reflection intensity, two preprocessing methods were conceived. The idea beneath these methods is that, as was mentioned, the laser reflection has some coherence over time and space; however, the particles do not. When an instantaneous image is compared with a statistical image the positions where there are particles should differ more from the statistical image than the positions where the laser reflection is dominant. By an appropriate method of comparison and setting an optimum threshold, it should be possible to keep the particles information and remove most of the noise. With this idea in mind, two methods were created and the performance was assessed. The methods are:

- **Non-linear image subtraction**: the original image is subtracted with a statistical image multiplied by a coefficient which takes a different value for each pixel, as follows:

$$I_1(x_i, y_j) = I_0(x_i, y_j) - c(x_i, y_j) * I_{st}(x_i, y_j)$$

Where $I_1(x_i, y_j)$ is the intensity on the pixel of the image after performing the preprocessing; $I_0(x_i, y_j)$ is the intensity on the pixel of the image before performing the preprocessing; $I_{st}(x_i, y_j)$ is the intensity on the pixel on the statistical image used; $c(x_i, y_j)$ is the coefficient that multiplies the statistical image.

In the image of coefficients is where the distinction between what is considered a particle or noise is established, as follows:

$$c(x_i, y_j) = \frac{I_0(x_i, y_j)}{I_{st}(x_i, y_j)}$$

For the pixels where the coefficient is above a threshold (which is set by the user), the coefficient is set to 0. Therefore, where the coefficient is above the threshold the original light intensity is recovered, in the rest of pixels the light intensity is removed completely. The coefficients image calculated over a small region of an image is below. The regions where 0 coefficient value are those detected as particles. The threshold value imposed on this image was 2.

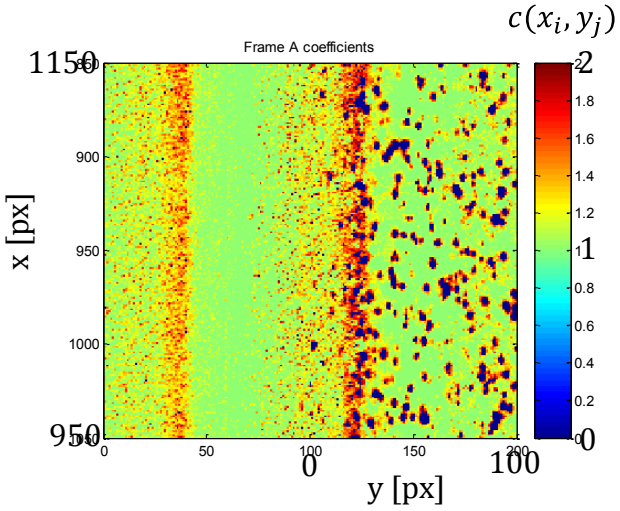

Figure 4.10 Value of the coefficients matrix described above.

Also, the effect of filtering the coefficients image was studied. The filters studied were averaging the value in a pixel with the values in a 3x3 pixels neighborhood or choosing the 2nd smallest value in a 3x3 neighborhood. More details on these filters can be found in Adrian and Westerweel (2011). The objective was to reduce the truncation of particle images produced by the calculation as described above. The truncation can be understood from the figure: it can be observed that just next to the detected particles the coefficients image reaches large values, indicating that there is still particles' light in those pixels. The results from filtering the coefficients image are not reported here,

as by the time the stay finished better results were provided by using the coefficients image without filtering.

- **Non-linear image multiplication:** the original image is multiplied by a ratio which depends on each pixel, as follows:

$$I_1(x_i, y_j) = r_1(x_i, y_j) * I_0(x_i, y_j)$$

The ratio image $r_1(x_i,y_j)$ has values which are comprised between 0 and 1, ideally where there are particles a 1 should be placed and where there is noise a 0. The ratio $r_1(x_i,y_j)$ is obtained the following way. First, the ratio $r(x_i,y_j)$ between the PIV image and the statistical image is calculated:

$$r(x_i, y_j) = \frac{I_0(x_i, y_j)}{I_{st}(x_i, y_j)}$$

Where $I_0(x_i, y_j)$ is the intensity on the pixel of the image before performing the preprocessing and $I_{st}(x_i, y_j)$ is the intensity on the pixel on the statistical image used.

The ratio $r(x_i,y_j)$ is normalized with the maximum value. Then, for all pixels that have the ratio above a threshold (the expected particles) the ratio is set to 1. The rest of the pixels ratios are scaled accordingly (i.e. the rest of pixels are divided by the threshold value). Finally, the ratio is raised to the power of n>1 chosen by the user, so:

$$r_1(x_i, y_i) = r(x_i, y_i)^n$$

This operation seeks that the pixels where the ratio is 1 the ratio stays the same and the rest of ratios are reduced depending on n; the greater n the bigger the reduction of the noise level.

Many possibilities can be varied for both methods. Below, only a few cases are plotted. The results plotted include two cases from the non-linear image subtraction (identified as NLS in the figure): (i) using the minimum from a subset of 3 images and with a threshold set at 2; (ii) using the average image of the whole set, with a threshold of 3.25 and subtracting the background intensity (≈300 counts) both in I_0 and in I_{st} before calculating the coefficients image. A case from the non-linear image multiplication (identified as NLM) is also plotted: the statistical image was the minimum of a subset of 5 images, the threshold was 0.03 and the reduction power (n) was 5.

Results

First, Figure 4.11 shows the displacement parallel to the wall as it evolves along the wall, obtained from the linear preprocessing methods. When the number of images is not stated in the legend, that indicates the statistical image was calculated from the 1000 images used (identified above as “Global statistical image”).

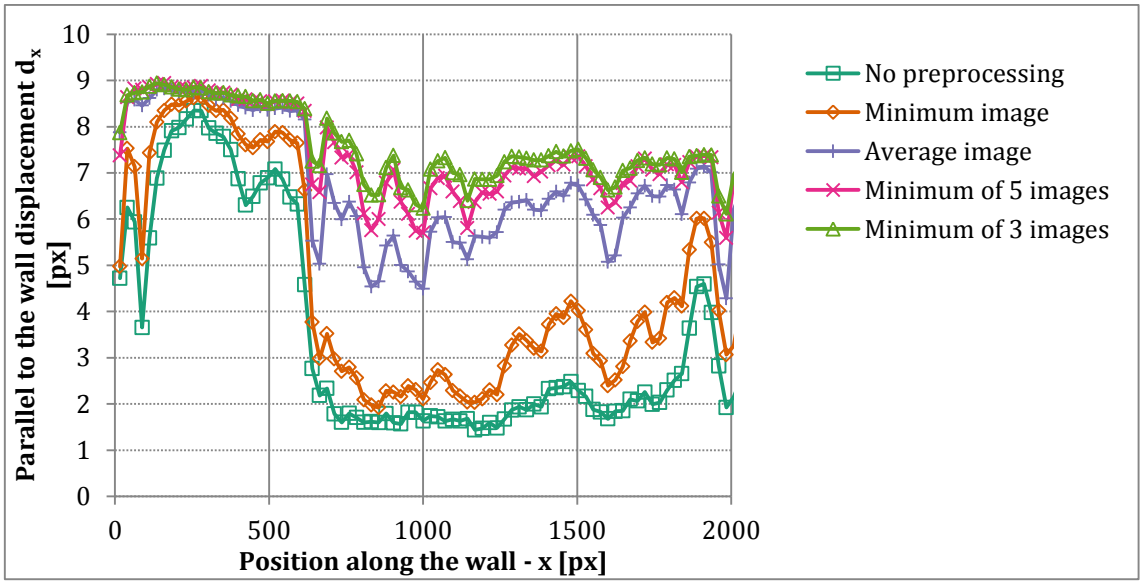

Figure 4.11 Evolution of the parallel to the wall displacement with the position along the wall for some of the preprocessing methods tested. Distance to the wall *y*~12pixels.

As can be appreciated in the graph, the results from all methods still oscillate for *x* larger than 600 pixels. Nevertheless, some of the preprocessing methods obtain a coherent tendency for x<600 pixels, where it can be observed that the displacement decreases with *x* position. As compared to the displacement evaluation methods, this coherence indicates already some improvement. The preprocessing methods that use the same statistical image (the so-called "global" methods) perform in general worse than the methods using a "local" statistical image: oscillations are larger and so is the abrupt displacement decrease at *x*~600pixels. This is produced very likely because the laser reflection intensity changed slightly between the images and thus when using a global statistical image a lot of background noise stays in the photos. Using "local" images increases greatly the computational time (because each image will have a corresponding statistical image), but on the other hand seem more efficient removing the laser reflection intensity.

The trend that seems to manifest is that with a preprocessing method that removes more light intensity from the laser reflection the displacement obtained is higher. However, the problem was not completely solved, not even in the case of using the minimum of a subset of 3 images.

Finally, Figure 4.12 shows the results from the so-called "non-linear methods".

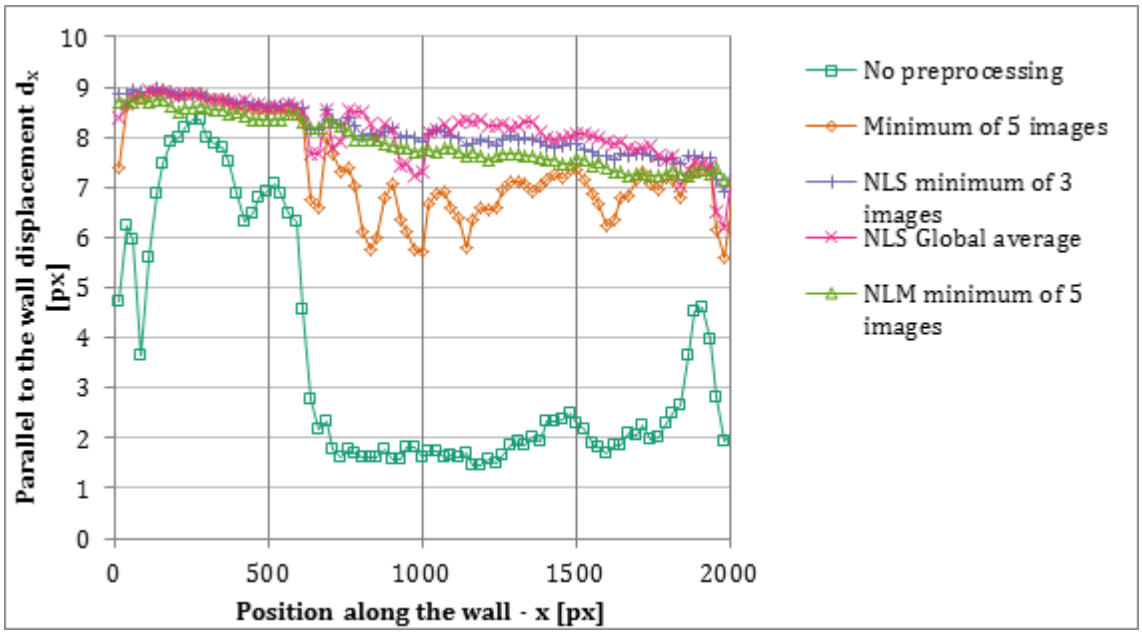

Figure 4.12 Evolution of the parallel to the wall displacement with the position along the wall for some of the preprocessing methods tested.

As can be observed, the new preprocessing methods yield similar results. As in the previous graph, when the statistical image is calculated from the whole set of images the results are noisier. All three cases, but especially those using "local" minimum images reveal a tendency of the displacement to decrease as the flow advances along the wall. This is coherent with the previous knowledge of boundary layers: when the boundary layer is submitted to an adverse pressure gradient the velocity decreases (see Figure 4.7).

4.1.3 Conclusions

In this section, the measurements in a wind tunnel of an adverse pressure gradient boundary layer have been presented. Performing this kind of measurements during the PhD was of importance to the student to become aware and learn how to solve the different difficulties that appear when PIV is used in large facilities, such as vibrations, optical access, reflections or limited measurement time.

Also a preliminary assessment was conducted to find a way to deal with particles depositing in the window of the wind tunnel and the laser sheet reflections on that window. The problems were investigated by varying the way the displacement is calculated and by preprocessing the images before calculating the displacement.

The analysis on the different correlation algorithms available proved that some methods provide better results when there are reflections present in an image. However, the preprocessing techniques seem to perform better, especially the two specifically conceived in this work. These two methods are the *Non-linear Image Subtraction* and *Non-linear Image Multiplication*. When these methods are used the displacement can be obtained, even under the brightest laser reflection. The drawback of these methods is a larger computational time.

4.2 HELICOPTER FUSELAGE FLOW CHARACTERIZATION

The PhD student also had the opportunity to collaborate in a measurement campaign with the experimental aerodynamics team in CIRA ("Centro Italiano di Ricerche Aerospaziali", the Italian Aerospace Research Center). In this case the flow around a helicopter fuselage mock-up was studied aiming at drag reduction evaluation.

The CIRA was working in this mock-up, based on the large carrier helicopter model AW101, in order to optimize the fuselage drag. This particular fuselage is characterized by a flat back door ramp at an upsweep angle with respect to the horizontal line, as can be seen in Figure 4.13. As it turns out, the ramp is responsible of a drag penalty. In consequence, flow control strategies are being studied currently, to reduce that drag increment. Active flow control strategies were studied with that same mock-up by the hosting group and are reported in De Gregorio (2014).

Following with that line of work, the measurement campaign on which the PhD student participated was focused in the modifications induced by passive flow control devices (Vortex Generators, VG's). The VG's were introduced just upstream the loading ramp with the objective of reducing the size of the detachment that appears downstream the upsweep line for some angles of attack. The VG's can be observed in Figure 4.13.

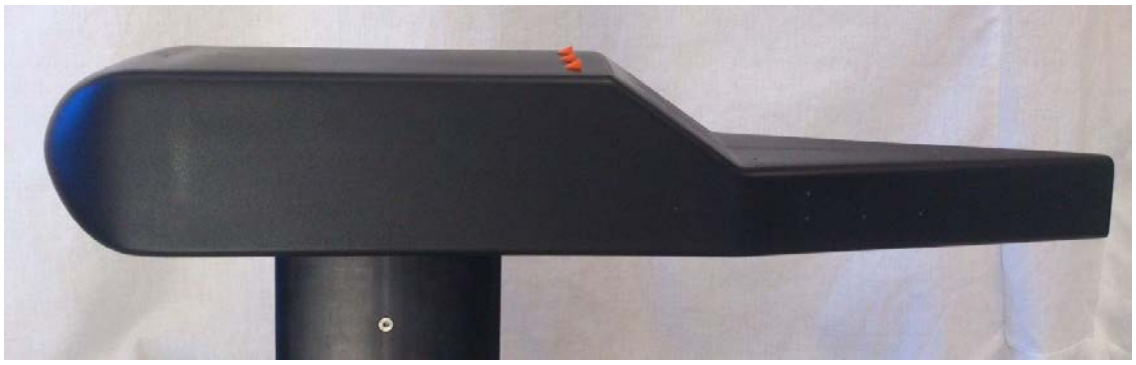

Figure 4.13 Helicopter mock-up (turned upside-down) with the Vortex Generators employed sitting on top (orange color).

The measurement campaign was carried out in CIRA CT-1 low speed tunnel, which is of open-circuit type. The characterization included variations of the angle of attack of the fuselage, with several values between -11º to 11º comprised. The measurement techniques employed were Mono-PIV and Stereo-PIV to study the flow behind the loading ramp and pressure taps to obtain the pressure on the surface of the model. The measurement campaign description and results have been published in the work Jimenez *et al.* (2016b) and the reader is referred to that work for further details. Currently, the results from that work are being researched further to publish two journal papers.

In addition to the publication of that work, the stay was a good opportunity for the PhD student to:

- Observe the equipment available at CIRA, which could be useful for designing experiments in the future. As examples, the PhD student got acquaintance with: an articulated arm that permits to adapt the laser sheet insertion position in the wind

tunnel, or automated devices for focusing the images from the computer and also adapting the Scheimflug angle.
- Run the measurement equipment and the wind tunnel in an autonomous way.
- Acquire and evaluate pressure taps measurements.
- Implement a multi-Δt methodology in order to characterize peak-locking and CCD read-out errors. This methodology was introduced in the works of Nogueira *et al.* (2009) and Legrand *et al.* (2012). A brief summary is also given in the research work of the PhD student (Jimenez *et al.,* 2016b). The errors were successfully assessed for the equipment of CIRA and for the setup of this campaign and are: ~0.06pixels (peak-locking) and negligible read-out errors.
- Learn to keep a proper measurement campaign test log, by noting down all parameters and incidences occurred during the measurements.

Also, it was possible for the PhD student to observe that there are constraints that come into play in the measurements that may preclude from selecting the most advisable measurement parameters in terms of error reduction. The following were given during this stay:

- In a previous measurement, the black paint covering the model had been burnt slightly by the laser. As a consequence the size of the laser reflections in the images was large. To avoid burning more paint and worsening the problem, the laser power had to be reduced and the laser sheet widened. In turn, the f-number of the lenses, $f^{\#}$, had to be set to low values (2 for Mono-PIV and 4 for SPIV) to obtain more light in the sensor. Finally, to avoid the small particle images that can be produced by those f-number values, the images were slightly defocused.
- Seeding density was not the maximum that the seeder device could deliver. This was selected in purpose to avoid having to clean the wind tunnel windows too often, which would result in more time to complete the measurement campaign.

Finally, related to the adjustment of the Δt and of the laser sheet thickness, the two relevant parameters in this PhD:

- The time between laser pulses was adjusted again to provide large enough displacements, seeking to optimize the velocity dynamic range. In this case, the target largest displacement was of ~10 pixels. The standard correlation process by FFT struggled to obtain valid vectors in the detachment region for those Δt values. As a consequence, the images were analyzed by multiple-correlation algorithm to mitigate this problem.
- As to the laser sheet thickness, it was already wide to avoid burning the model. During the preliminary tests it was slightly enlarged, due to the problem mentioned with the valid vectors in the detachment, which was attributed to out-of-plane motion. The experimental group in CIRA had no specific device to measure the laser sheet thickness; by visual estimation the value seemed around 2-3mm.

Chapter 5 **Theoretical rationale for results analysis**

This chapter offers the theoretical rationale for characterizing the errors under study in this PhD.

The first section of the chapter focuses on the selection of a proper tool for providing information on the length-scale distribution of the error. The most common tools, usually employed in turbulence research, are analyzed and their advantages and disadvantages studied.

The second section details how are the results analyzed, including the usage of the function identified in the first section.

The third section of the chapter offers a compilation of the different errors that may occur in PIV turbulence measurements. Based on the nature of these errors, an estimate of their magnitude is also provided. This is useful to check the coherence between the theoretical rationale unfold here and the results of the error analysis in Chapter 7. It also allows stablishing the most relevant error sources for each test case. This includes the length-scales distribution of these errors when analyzed with the tool selected in the first section of the chapter.

5.1 METHOD OF ANALYSIS FOR EXTRACTING LENGTH-SCALE RELATED INFORMATION

As was mentioned in section 1.2 a turbulent flow is composed by eddies, or vortices. They embrace a range of different sizes. This is the way for the turbulence to generate a path to transfer energy from its injection at large scales towards its dissipation at small ones. For this reason, the study of a turbulent flow involves the analysis of the structures that compose it. Some flow related magnitudes are affected mainly by the large and medium turbulent scales, (e.g. turbulent kinetic energy). Other magnitudes are affected by the small scales (e.g. viscous energy dissipation). This is detailed in many turbulent handbooks (Mathieu and Scott, 2000, among others). Therefore, the study of the different scales is fundamental to the understanding of a turbulent flow. Linked to this fact, fluid mechanic measurements benefit from the assessment of the magnitude of the measurement error for each scale. On this ground, understanding how the error is distributed among the different scales has been selected as the primary objective to unveil in this PhD Thesis, in relation to the errors analyzed.

Throughout the historical study of turbulence, different tools have been used in order to provide scale related information. Four relevant tools have been considered in this study. The suitability of them for the discrimination of the error distribution along different scales is analyzed in this chapter. These tools are already widely used in turbulence research. They are: (i) the longitudinal velocity structure function of order 2, (ii) the longitudinal velocity structure function of order 3, (iii) the Energy Spectrum Function and (iv) the longitudinal one-dimensional spectrum.

In this chapter, a brief theoretical definition of all four tools of analysis is provided. Afterwards, a more detailed characterization of each one is given, focusing on the objective of discriminating information from different turbulent scales for the specific case of PIV measurements and errors. The advantages or drawbacks for each of the tools are established. Also the calculation of the tools for the specific case of Mono-PIV measurements is commented. Finally the longitudinal velocity structure function of order 2 is chosen for the error analysis indicating the reasoning to make such choice.

It must be clear that the tools are not aimed at providing the error of the calculated turbulent length-scales. A methodology based on variation of the measurement parameters, on given test flow fields, is used for that purpose. Once the error is identified, the aim of the tool is to allow estimating the error distribution along the different flow length scales.

5.1.1 Formulation of the tools under study

The tools under study are defined as a function of the turbulent velocity fluctuations that are defined in the following paragraphs. For the purpose of this chapter, it is assumed that the turbulent flow instantaneous velocity field ***U(x,t)*** (dependent on position $\boldsymbol{x}$ an time t), can be considered a random variable. Through the entire chapter, bold letters indicate a vector magnitude and regular letters a scalar magnitude. Following Pope (2000) the one-point, one-time joint Cumulative Distribution Function of velocity at $\boldsymbol{x}$, t is defined as:

$$F(\boldsymbol{V}, \boldsymbol{x}, t) = P\{U_i(\boldsymbol{x}, t) < V_i, i = 1,2,3\}$$

And then the joint Probability Distribution Function (PDF) is:

$$f(\boldsymbol{V}; \boldsymbol{x}, t) = \frac{\partial^3 F(\boldsymbol{V}, \boldsymbol{x}, t)}{\partial V_1 \partial V_2 \partial V_3}$$

From the PDF is possible to define the mean velocity field at a position and time instance:

$$\langle \boldsymbol{U}(\boldsymbol{x}, t) \rangle = \iiint_{-\infty}^{+\infty} \boldsymbol{V} f(\boldsymbol{V}; \boldsymbol{x}, t) dV_1 dV_2 dV_3 \tag{5.1}$$

Through this part of the chapter, the average operator $\langle \cdot \rangle$ refers to the one above. Afterwards, on 5.1.2, the way those averages can be approximated is indicated. With the average field, it is possible to define the fluctuating velocity field, which can be considered as well as a random variable:

$$\boldsymbol{u}(\boldsymbol{x}, t) = \boldsymbol{U}(\boldsymbol{x}, t) - \langle \boldsymbol{U}(\boldsymbol{x}, t) \rangle \tag{5.2}$$

5.1.1.1 *Longitudinal velocity structure function of orders 2 and 3*

In any given flow, the velocity difference $\delta\boldsymbol{u}$ between two points can be calculated as:

$$\delta\boldsymbol{u}(\boldsymbol{x}, \boldsymbol{r}, t) = \boldsymbol{u}(\boldsymbol{x} + \boldsymbol{r}, t) - \boldsymbol{u}(\boldsymbol{x}, t) \tag{5.3}$$

Where $\boldsymbol{r}$ is the separation vector, pointing to a second position to calculate the corresponding velocity difference. The fluctuation velocity field $\boldsymbol{u}(\boldsymbol{x};t)$ is used for the calculation of the difference. If $\boldsymbol{u}$ is a random variable, so is $\delta\boldsymbol{u}$.

The velocity structure functions are defined by projecting these velocity differences on a given direction, raising to the power of n and averaging. In particular, longitudinal velocity structure functions of order n (which will be henceforth designated by S_{L^n}) are those obtained when the velocity difference is projected on the direction of $\boldsymbol{r}$:

$$\begin{aligned} S_{L^n}(\boldsymbol{x}, \boldsymbol{r}, t) &= \left\langle \left[\left(\boldsymbol{u}(\boldsymbol{x} + \boldsymbol{r}, t) - \boldsymbol{u}(\boldsymbol{x}, t) \right) \cdot \frac{\boldsymbol{r}}{|\boldsymbol{r}|} \right]^n \right\rangle \\ &= \left\langle \left[\delta\boldsymbol{u}(\boldsymbol{x}, \boldsymbol{r}, t) \cdot \frac{\boldsymbol{r}}{|\boldsymbol{r}|} \right]^n \right\rangle \end{aligned} \tag{5.4}$$

Where the operator $\langle \cdot \rangle$ indicates the average of the random variable, as defined in expression (5.1). For the flows under study on this PhD, which are statistically steady (flows for which all statistics are invariant under a shift on time, Pope, 2000), the average is independent of time so henceforth, dependence on t will be not shown. Additionally, for the case of statistically homogeneous flows (i.e. all statistics are invariant under a shift in

position, Pope, 2000), the average is independent of the position, so dependence on $\boldsymbol{x}$ is dropped as well:

$$S_{L^n}(\boldsymbol{r}) = \left\langle \left[\left(\boldsymbol{u}(\boldsymbol{x}+\boldsymbol{r}) - \boldsymbol{u}(\boldsymbol{x}) \right) \cdot \frac{\boldsymbol{r}}{|\boldsymbol{r}|} \right]^n \right\rangle \tag{5.5}$$

If the turbulence is isotropic, the result is independent of the orientation of $\boldsymbol{r}$. The velocity difference projected in the longitudinal direction is identified as $\delta u_L(r)$ (for a generic direction).

For n = 2 and for n = 3 in expressions (5.4) and (5.5) we obtain the longitudinal structure functions of orders 2 ($S_{LL}(r)$) and 3 ($S_{LLL}(r)$)[2].

Higher order functions have not been considered for the analysis. A series of first tests revealed that structure functions of orders 2 and 3 can be sufficient to characterize the error. Additionally, structure functions of higher order require more samples to obtain converged measurements due to a more important influence of the tails in the pdf of δu_L, which is always inconvenient (Mathieu and Scott, 2000; among others).

5.1.1.2 *Energy Spectrum Function*

In general, swapping between the time and the frequency domain can be calculated by means of the Fourier transform:

$$G(\omega) = \mathcal{F}\{g(t)\} \equiv \int_{-\infty}^{\infty} g(t) e^{-\mathrm{i}\omega t} dt \tag{5.6}$$

Where $\mathcal{F}$ indicates Fourier transform of a function. $G(\omega)$ and $g(t)$ are called a *Fourier transform pair* (following Stein, 2000). By recurring to the inverse Fourier transform ($\mathcal{F}^{-1}$) is possible to obtain $g(t)$ from $G(\omega)$. Time and temporal frequency can be exchanged by length and spatial frequency.

The *Energy Spectral Density* provides the distribution of energy in the frequency domain. Expressing a generic complex function in the frequency domain as $G(\omega) = A(\omega)e^{\mathrm{i}\phi(\omega)}$, the Energy Spectral Density would be: $E(\omega) = |A(\omega)|^2$.

Among the different spectra that can be calculated from a turbulent velocity field, the *Energy Spectrum Function* (Pope, 2000; among others) is identified as $E(\kappa)$. $E(\kappa)$ is obtained from the velocity field as shown below:

First, the two-point velocity correlation tensor (for a case of homogeneous turbulence and statistically steady, where it is independent of $\boldsymbol{x}$ and t) is calculated from (Pope 2000, i,j=1,2,3):

$$R_{ij}(\boldsymbol{r}) = \left\langle u_i(\boldsymbol{x}) u_j(\boldsymbol{x}+\boldsymbol{r}) \right\rangle \tag{5.7}$$

$R_{ij}(\boldsymbol{r})$ and the velocity-spectrum tensor, $\Phi_{ij}(\boldsymbol{\kappa})$, form a Fourier-transform pair (Pope, 2000):

[2] For the structure function or the velocity difference, if at some cases it is labelled with a numeric subscript instead of a letter (for example $\delta u_1(\boldsymbol{e_1} r_1)$ or $S_{11}(\boldsymbol{e_1} r_1)$) the number indicates the specific velocity component used for the calculation.

$$\Phi_{ij}(\boldsymbol{\kappa}) = \frac{1}{(2\pi)^3} \iiint_{-\infty}^{+\infty} R_{ij}(\boldsymbol{r}) e^{-\mathrm{i}\boldsymbol{\kappa}\cdot\boldsymbol{r}} dr_1 dr_2 \mathrm{d}r_3 \tag{5.8}$$

Where $\boldsymbol{\kappa}$ is the wavenumber vector, i.e. $\boldsymbol{\kappa} = (\kappa_1, \kappa_2, \kappa_3)$. The wavenumber is defined as $\kappa_1 = 2\pi/\ell_1$, where ℓ_1 would be the corresponding wavelength. Note that compared with (5.6), in order to obtain the velocity-spectrum tensor, all three spatial coordinates need to be Fourier transformed. Finally, $E(\kappa)$ is obtained from the velocity-spectrum tensor by removing all directional information (Pope, 2000). This is done by the integration of the diagonal values of the velocity spectrum function for each wavenumber magnitude:

$$E(\kappa) = \iiint_{-\infty}^{\infty} \frac{1}{2} \Phi_{ii}(\boldsymbol{\kappa}) \delta(|\boldsymbol{\kappa}| - \kappa) \mathrm{d}\kappa_1 \mathrm{d}\kappa_2 \mathrm{d}\kappa_3 \tag{5.9}$$

Where $\Phi_{ii}(\boldsymbol{\kappa})$ indicates the sum over index *i*, δ stands for the Dirac function and κ is a variable independent of $\boldsymbol{\kappa}$. (5.9) is equivalent to defining a sphere in wavenumber space, $\mathcal{S}(\kappa)$, with radius κ and centered at the origin; integrating over the surface of the sphere:

$$E(\kappa) = \oint \frac{1}{2} \Phi_{ii}(\boldsymbol{\kappa}) \, \mathrm{d}\mathcal{S}(\kappa) \tag{5.10}$$

5.1.1.3 *One-dimensional spectrum*

In addition to $E(\kappa)$ other turbulent spectrum function is analyzed as possible tool to discriminate scale related information. The one-dimensional spectrum is defined from the velocity spectrum tensor as (Pope, 2000):

$$E_{ij}(\kappa_1) = 2 \iint_{-\infty}^{\infty} \Phi_{ij}(\boldsymbol{\kappa}) \mathrm{d}\kappa_2 \mathrm{d}\kappa_3 \tag{5.11}$$

It can be alternatively related to the two-point velocity correlation by (Pope, 2000):

$$E_{ij}(\kappa_1) = 2 \frac{1}{2\pi} \int_{-\infty}^{+\infty} R_{ij}(\boldsymbol{e_1} r_1) \; e^{-\mathrm{i}\kappa_1 r_1} \mathrm{d}r_1 \tag{5.12}$$

Where the vector $\boldsymbol{e_1} r_1$ indicates that the variations of R_{ij} are only considered in the first direction. Hereafter, this notation will be abbreviated by $R_{ij}(r_1)$. The one-dimensional spectrum could be defined all the same in other wavelength direction κ_2 or κ_3.

Among the possible *ij* combinations, as in the case of the structure functions, only the longitudinal one-dimensional spectra will be considered for the analysis: $E_{ii}(\kappa_i)$, (for i=1,2, or 3) which on the case of isotropic turbulence should be independent of the direction. For the rest of the chapter, a generic longitudinal one-dimensional spectra will be referred to as $E_{LL}(\kappa)$.

5.1.2 **Calculation of the tools under study for discretized data**

As indicated on the previous definitions, all the analyzed tools require the calculation of an average at some point. In consequence, as a first step, the way the averages are obtained for Mono-PIV measurements is clarified here. For the definition of the functions, an average based on the PDF of random variables was used (5.1). However, that type of

average cannot be calculated from discretized data from a measurement. Since all the flows analyzed on this PhD are statistically steady (all statistics are invariant under a shift on time) the average is calculated by measuring at different time instances and using those different realizations to obtain the average.

Also, for the flows that are homogeneous (all statistics are invariant under a shift in position); the value of the magnitudes at different positions can be used as well as to estimate the averages. Hereinafter, to clarify, a subscript will be used on the average operators to indicate how is the average performed, $\boldsymbol{x}$ will indicate an average in different positions and t in different time instances.

5.1.2.1 *Longitudinal velocity structure function of orders 2 and 3*

Related with the specifics of the calculation of both longitudinal structure functions under study ($S_{LLL}(r)$ and $S_{LL}(r)$), the process would be to calculate the $\delta u_L(r)$ where data is available, raise to the corresponding power and average. As stated above, if the flow is homogeneous and statistically steady, the average can be done in all positions and time instances available. For example, for the first velocity component for 2D data $S_{11}(r_1)$ would be calculated by:

$$S_{11}(r_1) = \frac{1}{N_t}\frac{1}{N_x}\frac{1}{N_y}\sum_t\sum_x\sum_y\left(u_1(x+r_1,y;t) - u_1(x,y;t)\right)^2$$

Where N_t would be the number of time instances recorded and N_x and N_y the number of available vectors for each in-plane dimension.

5.1.2.2 *Energy Spectrum function*

Related to the calculation and as can be extracted from the process illustrated from (5.7) to (5.9), obtaining $E(\kappa)$ requires 3D-3C data stored from -∞ to +∞. The problem of having data to infinity can be overcome if the flow measured is periodic or if the two-point velocity correlation tensor goes to 0 by itself inside the measurement region. Still, Mono-PIV measurements -the technique being characterized in this PhD- provide a 2D-2C vector field, so there is no 3D-3C data straight from a measurement. Additionally, flows found in nature are very rarely periodic in space, and this type of flows is almost only found in the solution of numerical tools.

This is obviously a problem, because the measurement technique, generally, does not provide for all the necessary data to obtain $E(\kappa)$. From the 2D-2C data obtained by Mono-PIV is possible to obtain $E(\kappa)$ if the data in the third direction and for the third velocity component can be inferred from the 2D-2C available (e.g. when the flow is isotropic in the three directions). In that case, several possibilities to calculate $E(\kappa)$ have been compiled in Annex I.

5.1.2.3 *One-dimensional longitudinal spectrum*

As described in section 5.1.1.3, the one-dimensional spectrum can be calculated from the velocity spectrum tensor (expression (5.11)) or from the two-point velocity correlation defined in expression (5.12). In the particular case of this PhD, where only 2D-2C data is available, expression (5.12) is the only possibility. This is so, because calculating the velocity spectrum tensor requires the flow to be isotropic, as in the previous point. The

calculation process is given for $E_{11}(\kappa_1)$ although it is valid for all the one-dimensional spectra. Expression (5.12) gives then:

$$E_{11}(\kappa_1) = 2\frac{1}{2\pi}\int_{-\infty}^{+\infty} R_{11}(r_1)\ e^{-i\kappa_1 r_1} dr_1$$

The problem with this expression is that $R_{11}(r_1)$ will not be defined at infinity for any measurement. It is possible to calculate this integral when R_{11} reaches 0 for the data available. However, that is not typically the case. Other functions that admit a representation in terms of a Fourier decomposition are periodic functions. For example, on the case of the selected flow of section 3.1, which is periodic, $E_{11}(\kappa_1)$ is calculated by (*Li et al.,* 2008):

$$E_{11}(\kappa_1) = \langle \tilde{u}_1(\kappa_1)\tilde{u}_1^*(\kappa_1)\rangle \qquad (5.13)^3$$

Where $\tilde{u}_1(\kappa_1)$ is the Fourier transform of u_1 on direction *x* and $\tilde{u}_1^*$ the complex conjugate of $\tilde{u}_1$. The average is performed by the authors on different *y,z* positions.

Changing (5.12) by (5.13) is possible because the longitudinal correlation function (for example in direction one) can be seen as a convolution. Thanks to the properties of Fourier analysis, the convolution could be calculated on Fourier space by just multiplying the transforms, which is what (5.13) illustrates.

5.1.3 **Advantages and drawbacks for the tools under study**

Following, the analysis of the tools under study ($S_{LL}(r)$, $S_{LLL}(r)$, $E(\kappa)$ and $E_{LL}(\kappa)$) unveils the following advantages and drawbacks:

5.1.3.1 *Second order longitudinal structure function - $S_{LL}(r)$*

Factors associated to the function definition

Figure 5.1 plots u_2 and some δu_2 differences for an excerpt of a line of the DNS data used by the numerical tools (cf. section 3.1). The difference δu_2 is plotted for r_2 distances of 0.012, 0.141 and 1.411 feet. The usefulness of the structure functions can be understood thanks to this graph. It can be appreciated that all the velocity differences oscillate around 0 velocity, while the velocity u_2 never reaches 0 for this fragment, something that is produced by turbulent structures of a size larger than that of the excerpt. The velocity differences at a scale should permit to better characterize the turbulence dynamics at that scale, because they emphasize the variations of the velocity (Mathieu and Scott, 2000, among others). They could be seen like a sort of filter of large scales that bring attention to the scales of the order of *r*. Indeed, when the distance r_2 is increased, the amplitude of the oscillations of the velocity differences increases as well. $S_{LL}(r)$, which is constructed from the velocity differences, should keep the features of the velocity differences and emphasize the dynamics of the scale of the characterization.

[3] As compared to the definition of (5.9), there would be a 2 factor multiplying missing in this expression. This factor is added or not depending on the reference considered.

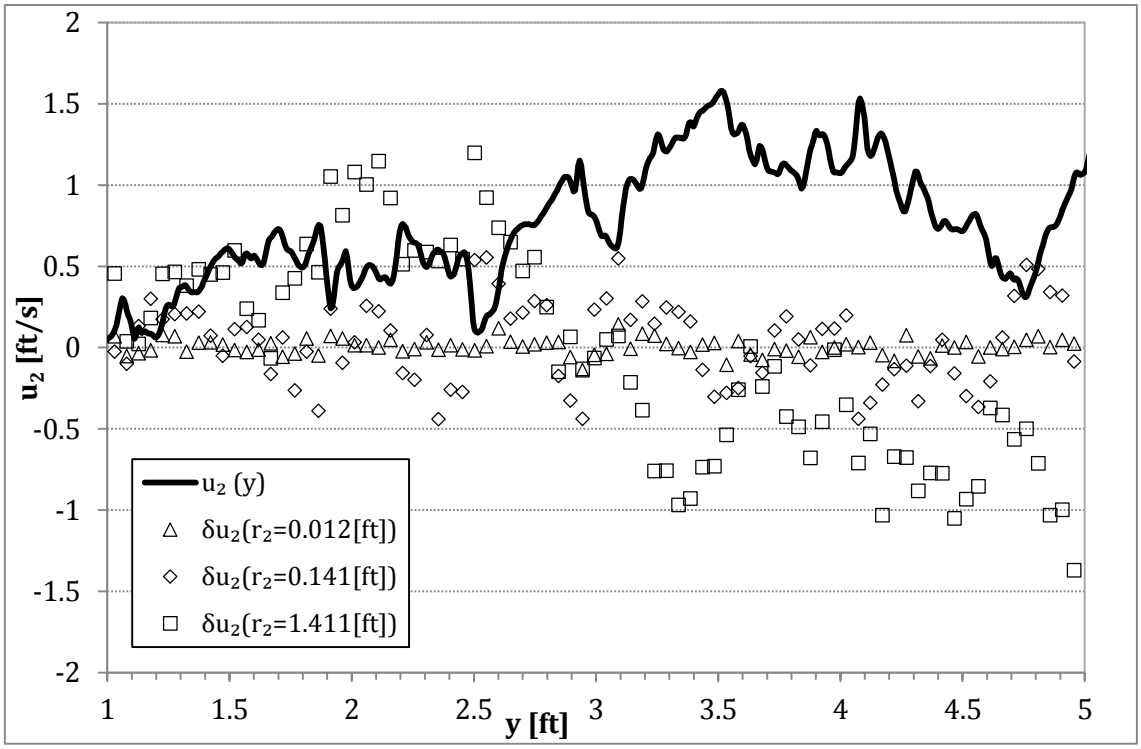

Figure 5.1 Velocities and velocity differences for a fragment of a line of DNS data (for the second velocity component). Just one every 8 points is plotted for the velocity differences.

Nonetheless, the fact that the velocity differences act like a sort of filter that focus on the variations produced by smaller scales than r is not exactly true, as revealed in Davidson (2004) and shown here.

In Figure 5.2, two hypothetical flows are sketched, one composed of a set of eddies of a size smaller than the distance r at which $S_{LL}(r)$ is being calculated (left image) and the other as composed of an eddy larger than r (right image). Both flows have the capacity to create velocity differences $\delta u_L(r)$. Those velocity differences will be squared and then averaged in different positions and time instances to produce $S_{LL}(r)$. The fact that the velocity differences $\delta u_L(r)$ are squared makes all contributions at all positions and time instances to contribute to $S_{LL}(r)$. A turbulent flow will be composed of eddies of very different sizes, so contributions to $S_{LL}(r)$ of both smaller and larger eddies can be expected for a distance r.

The contribution of smaller eddies to $S_{LL}(r)$ can be estimated as of $\mathcal{O}(u_\ell^2)$, where u_ℓ is the characteristic velocity of the eddy. In consequence, smaller eddies than r add to $S_{LL}(r)$ by a quantity of the order of their energy. This is indicated in expression below by the first term. However, eddies larger than r will create a velocity difference $\mathcal{O}\big((\partial u/\partial r)r\big) \sim ((u_\ell/\ell)\, r)$ (where ℓ is the characteristic size of the eddy) and so the contribution to $S_{LL}(r)$ will be $\sim((u_\ell/\ell)\, r)^2$. The function can be then expressed as (Davidson, 2004):

$$S_{LL}(r) \sim \sum_{\ell<r} u_\ell^2 + \sum_{L>r} u_L^2 (r/L)^2 \tag{5.14}$$

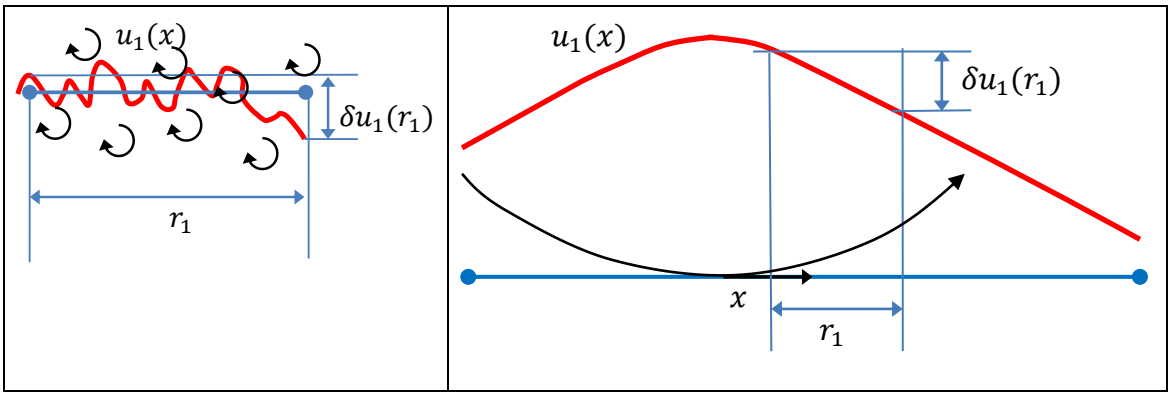

Figure 5.2 Sketches of the longitudinal velocity differences $\delta u_1(r_1)$ produced by smaller eddies than r (left figure) or larger eddies than r (right figure). For both figures the red line is the velocity profile $u_1(x)$ following the blue horizontal line between dots.

This feature, which stems from the definition of the function, is its main disadvantage: the contribution of all scales into the characterization of one of them. Luckily, while smaller scales than r contribute through their energy, larger scales than r contribute through a magnitude that diminishes with the square of the scale relation.

Despite this disadvantage, if the orders of magnitude of the contributions of eddies of different sizes is checked, it can be appreciated that generally the largest differences should be produced from the eddies of size close to r. This is shown below for eddies on the inertial range of the turbulent energy cascade. The dissipation ϵ can be used to stablish a relation between the velocity of an eddy u_ℓ an its size ℓ, as was shown in the introduction (cf. 1.2):

$$\frac{u_\ell^3}{\ell} = \epsilon \tag{5.15}$$

As stated above, eddies of size smaller than r will contribute to $S_{LL}(r)$ by their energy $\sim u_\ell^2$. For an eddy of size ℓ_1 larger than another eddy of size ℓ_2 it can be appreciated that by (5.15) $u_{\ell_1} > u_{\ell_2}$. The conclusion is that although all eddies of size $\ell < r$ can produce a $\delta u_L(r)$, the largest difference should come from those eddies of $\ell \sim r$.

On the other hand, eddies of size $\ell > r$ create differences $\delta u_L(r)$ due to the change of velocity they induce. The velocity difference induced by two eddies of different sizes (ℓ_1 and ℓ_2, with $\ell_2 > \ell_1$) is $\sim(u_{\ell_1} r/\ell_1)$ and similarly for the eddy of size ℓ_2. It can be observed that:

$$\frac{u_{\ell_1} r/\ell_1}{u_{\ell_2} r/\ell_2} = \frac{u_{\ell_1}}{u_{\ell_2}} \cdot \frac{\ell_2}{\ell_1} = \frac{u_{\ell_1}}{u_{\ell_2}} \cdot \left(\frac{u_{\ell_2}}{u_{\ell_1}}\right)^3 = \left(\frac{u_{\ell_2}}{u_{\ell_1}}\right)^2 > 1$$

So the velocity difference $\delta u_L(r)$ induced by the eddy of size ℓ_1 is larger and again eddies of size $\ell \sim r$ produce the larger velocity difference.

In conclusion, the second order longitudinal structure function is constructed from the velocity differences at the desired distance. Although the velocity differences emphasize the variations at the scale of calculation, all eddies can contribute to them, following expression (5.14). Nevertheless, the large eddies contribution to $S_{LL}(r)$ is attenuated by a

factor $(r/L)^2$ and since the characteristic velocity grows with size at a slower pace ($\propto L^{1/3}$ in the inertial range) this contribution can be neglected, giving:

$$S_{LL}(r) \sim \sum_{\ell<r} u_\ell^2 \tag{5.16}$$

A simplification to which some authors have already recurred to in the past (Townsend, 1976). This simplification is only valid though for $r>\eta$, i.e. it requires for the existence of eddies of smaller size than the distance of calculation, as is the case for the flows analyzed in this PhD.

An additional remark that can be made related with the evaluation of $S_{LL}(r)$ is the reason why the longitudinal two-point correlation function has not been analyzed separately. As it turns out, both $S_{LL}(r)$ and $R_{LL}(r)$ are closely related by expressions like the one below, for the second component of the velocity:

$$S_{22}(r_2) = 2\left(u_2'^{\,2} - R_{22}(r_2)\right) \tag{5.17}$$

where $u_2' = \sqrt{\langle u_2^2(\boldsymbol{x};t)\rangle_{\boldsymbol{x};t}}$.

As stated above, $S_{22}(r_2)$ should emphasize the dynamics of the scale of characterization (because it is calculated from velocity differences) while $R_{22}(r_2)$ does not (it is not defined to do so). For these reasons, the two-point correlation functions were not considered for the analysis.

Calculation related factors

The only consideration is that when dealing with PIV data, there may be interrogation windows that do not obtain a vector that passes the validation criteria. On those cases, the non-valid vectors can be left out of the calculation of the function. The calculation process with missing data is robust and should not introduce additional errors; this is considered as an advantage of velocity structure functions.

5.1.3.2 *Third order longitudinal structure function - $S_{LLL}(r)$*

Factors associated to the function definition

Contrarily to the case of $S_{LL}(r)$, a connection of $S_{LLL}(r)$ with scale discriminated magnitudes is complex. Following expression (5.4), both $S_{LLL}(r)$ and $S_{LL}(r)$ are obtained from the longitudinal velocity differences $\delta u_L(r)$. The difference between both functions is that in the case of $S_{LL}(r)$ the sign of $\delta u_L(r)$ does not affect the calculation (due to the square power) while on the case of $S_{LLL}(r)$ the sign does affect. As a result, while on $S_{LL}(r)$ all the contributions from all vortices sizes (as shown on the sketch of Figure 5.2) are kept, on $S_{LLL}(r)$ some of those contributions will cancel and the remaining ones will provide the value of $S_{LLL}(r)$. Thus, understanding if $S_{LLL}(r)$ is obtained from the contributions of larger or smaller length-scales than r is more diffuse than in the case of $S_{LL}(r)$. This lack of a physical connection with the spatial scale is considered a disadvantage of the function.

An additional consideration related with the calculation of $S_{LLL}(r)$ is that random errors will introduce deviations in both senses (positive and negative) to the actual values of $\delta u_L(r)$, deviations which will probably cancel (to a certain point) in the averaging process. This error cancellation could be useful for calculations derived from $S_{LLL}(r)$, for example the dissipation, as De Jong *et al*. (2009) state. Also, the random error cancellation could be useful to reveal other errors of non-random nature; for example Lavoie *et al.* (2007) claim the usefulness of $S_{LLL}(r)$ for revealing the effect of the resolution of the experiment. However, since in the present study the measurements can contain random errors that have to be characterized as well, the fact that the error could cancel is considered as a disadvantage of the function.

Calculation related factors

As in the case of $S_{LL}(r)$ the robust calculation process is considered as an advantage of structure functions.

5.1.3.3 *Energy Spectrum Function E(κ)*

Factors associated to the function definition

Conventionally, the Energy Spectrum Function is considered to provide the energy in wavelength space of the turbulent velocity field (Davidson, 2004).

Nonetheless, following Davidson (2004), since $E(\kappa)$ is obtained by recurring to Fourier analysis, on the energy distribution provided by $E(\kappa)$ it is implicitly assumed that the flow is composed of a combination of sinusoidal functions. As stated previously, a turbulent flow is composed of eddies and not of sinusoids. The consequence of this is that for example, the Energy Spectrum Function of a multitude of eddies of the same size shows a maximum at the wavelength corresponding to the size of the eddies but contains energy on many more wavelengths than the one of the eddies (Davidson, 2004). Hence, the representation $E(\kappa)$ is not perfect (in the sense that $E(\kappa)$ does not provide the energy of each of the turbulent structures). In this sense, the mixing between different spatial scales is present in this function as it was in $S_{LL}(r)$. Again, reasoning about scale contributions would be necessary for this function.

Calculation related factors

In Annex I several possibilities to calculate $E(\kappa)$ from 2D-2C data have been compiled. Any of them could be used for the velocity fields obtained from the tools described in Chapter 3. However, the flow obtained from the dedicated experimental set-up in Chapter 6 is not isotropic, and for those reasons the Energy Spectrum Function has been discarded as possible tool of analysis. Even when a flow is isotropic, since the measurement should have an error, nothing grants that the measurement will remain isotropic and therefore those methods may not be valid anymore. In addition, the presence of outliers or not valid vectors would affect the calculation in a much more complex way than for the case of S_{LL} (as for example Poelma *et al.,* 2006, show).

5.1.3.4 *One-dimensional longitudinal spectrum*

Factors associated to the function definition

In expression (5.13), $E_{11}(\kappa_1)$ has been linked to the Fourier transform of the velocity: $E_{11}(\kappa_1) = \langle \tilde{u}_1(\kappa_1)\tilde{u}_1^*(\kappa_1)\rangle = \langle |\tilde{u}_1(\kappa_1)|^2\rangle$. From this expression, $E_{11}(\kappa_1)$ could be interpreted as the energy representation of u_1 in wavenumber direction κ_1 (as indicated in the formulation of the spectra, cf. 5.1.1.3), if the velocity depended only on *x*.

However, there are a few facts that preclude that interpretation from being correct. First, u_1 variations depends on all spatial directions. Only the variations of u_1 on the *x*-direction are transformed, variations that can be produced by structures just dependent on κ_1 or structures that could depend on the wavenumber vector $\boldsymbol{\kappa}$. However, $E_{11}(\kappa_1)$ is not capable of discerning those variations from uni-directional ones. That is actually what the expression linking the one-dimensional spectra and the velocity spectrum tensor indicates, which in the case of $E_{11}(\kappa_1)$ gives (obtained from expression (5.11)):

$$E_{11}(\kappa_1) = 2\iint_{-\infty}^{\infty} \Phi_{11}(\boldsymbol{\kappa})\mathrm{d}\kappa_2\mathrm{d}\kappa_3$$

As can be understood from the expression above, all variations of $\Phi_{11}(\boldsymbol{\kappa})$ in wavenumber directions κ_2 and κ_3 are integrated into wavenumber κ_1 for $E_{11}(\kappa_1)$.

Traditionally, $\Phi_{11}(\boldsymbol{\kappa})$ is the spectrum considered to represent the energy of the turbulent structures that produce u_1. However, this interpretation of $\Phi_{11}(\boldsymbol{\kappa})$ is not strictly correct, because as commented in the previous point, using sinusoidal functions as a representation of turbulent flows can give a flawed interpretation of the energy of the turbulent structures.

In conclusion, the interpretation of $E_{11}(\kappa_1)$ as the energy representation of u_1 is not strictly correct, because (i) it integrates all the information of $\Phi_{11}(\boldsymbol{\kappa})$ in the wavenumber plane $\boldsymbol{\kappa}$=κ_1 into wavenumber and κ_1 (ii) recurring to sinusoids to study the energy produces also a flawed point of view. In this sense, the mixing between different spatial scales is present in this function as it was in $S_{LL}(r)$.

Calculation related factors

In addition to the interpretation difficulties, the calculation of this function is also complex. The first problem comes from the fact already stated above for the calculation of $S_{LL}(r)$ (see 5.1.3.1), which is that depending on the PIV processing parameters there may be interrogation windows with no valid measurement. When those interrogation windows are left with no valid data, it is not possible to calculate $E_{LL}(\kappa)$ by recurring to the Fourier Transform of the velocity field in expression (5.13). On those cases, a possible solution to still be able to use expression (5.13) is to interpolate the velocity at the interrogation windows where there is no valid data. However, the interpolated values produce an error on the spectrum (Poelma *et al.*, 2006) so that option is discarded here. The authors also show an alternative which is to recur to the calculation of the one-dimensional spectrum from the longitudinal two-point correlation function, as given by expression (5.12).

That leads to the second problem that can be mentioned related to the calculation of the Fourier representation, which is the need for the two-point longitudinal correlation function, $R_{LL}(r)$, to be periodic or go to zero inside the measurement domain. Then, the Fourier representation would be given by the Fourier series or the Fourier transform, respectively. On the case where neither of the possibilities occurs, the Fourier representation of $R_{LL}(r)$ can be calculated anyway, but it will have to be assumed that $R_{LL}(r)$ fulfils either of the conditions above outside the measurement domain. The other alternative is to modify $R_{LL}(r)$ so it satisfies either of the conditions before calculating its Fourier representation.

As example, on Figure 5.3 the problem of calculating the Fourier representation without $R_{LL}(r)$ being periodic (and assuming that it is) is illustrated. All Fourier representations are calculated by recurring to Fast Fourier Transform algorithm. The function $R_{LL}(r)$ is obtained from the velocity fields that are used to generate synthetic images and the PIV simulator vectors (a DNS of homogeneous turbulence, Li *et al.*, 2008). $R_{LL}(r)$ is obtained from the average of $R_{11}(r_1)$ and $R_{22}(r_2)$, with directions 1 and 2 being the two in-plane directions. The same 24 data planes that are used by the numerical tools are used for this calculation (cf. section 3.1.3). On the figure, the Fourier representation is calculated for the following functions, (i) $R_{LL}(r)$ calculated as mentioned here. In this case $R_{LL}(r)$ is periodic (however, in real flows, that will not be typically the case). (ii) The same $R_{LL}(r)$ than in case (i) but removing the last point of the function (1 point of 1024). (iii) The same $R_{LL}(r)$ but adding an extra point on the function making use of its periodicity properties. In the figure, the dotted line is $\kappa^{-5/3}$, which is the slope of the spectrum for the inertial range of the cascade.

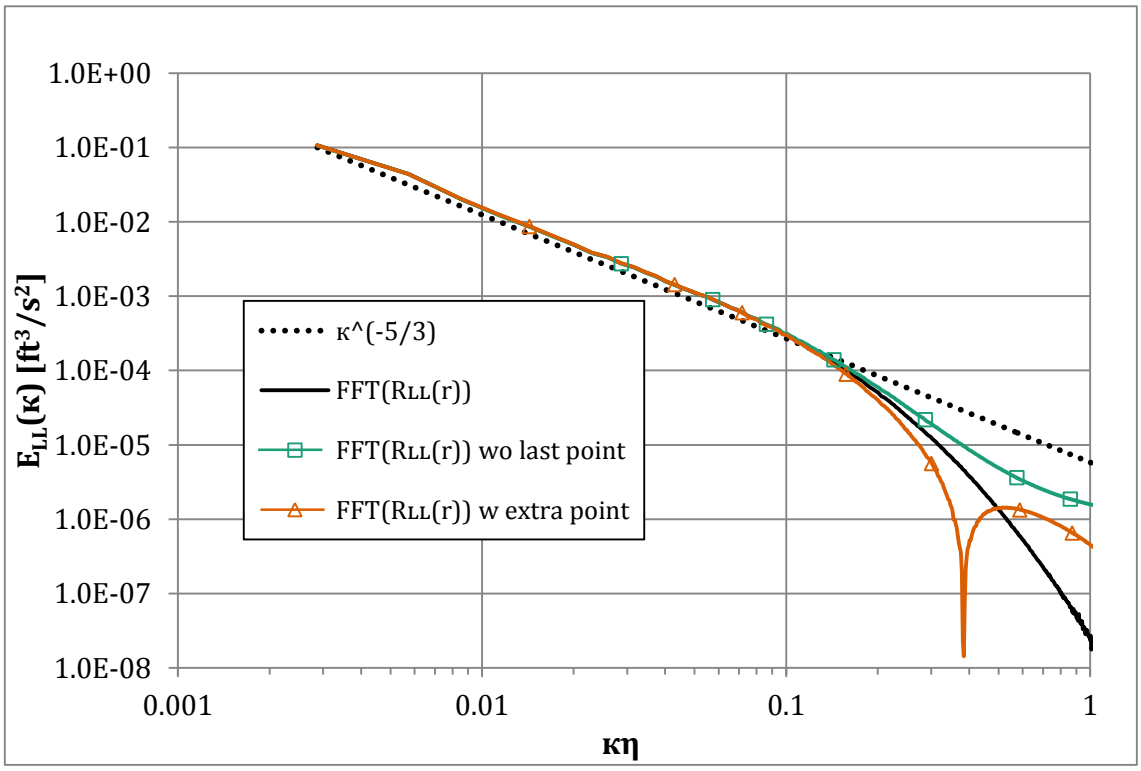

Figure 5.3 One-dimensional longitudinal spectrum calculated from $R_{LL}(r)$ obtained from a flow of a homogeneous isotropic turbulence DNS simulation (described in section 3.1).

It can be clearly appreciated on Figure 5.3 the effect of $R_{LL}(r)$ not being periodic on the calculation of $E_{LL}(\kappa)$: the spectrum shows influence on the high wavenumbers from adding or removing just one point of data (from a total of 1024). This modification of the energy distribution of $R_{LL}(r)$ is attributed to the discontinuity introduced at the border due to the implicit assumption of periodicity, and it gets more important with larger discontinuities (Stein, 2000).

For this reason, usually $R_{LL}(r)$ is modified before calculating $E_{LL}(\kappa)$ and typically the choice is to make $R_{LL}(r)$ periodic. Foucaut *et al.* (2004) showed the effect of different functions used to make $R_{LL}(r)$ periodic on the spectrum calculation. Those functions are usually identified as windowing functions (Stein, 2000). On those cases, it must be remarked that since $R_{LL}(r)$ is modified so will be $E_{LL}(\kappa)$. The modification introduced on the spectrum will depend on the choice of windowing functions and on the departing $R_{LL}(r)$. The fact that the energy content can be modified and the calculation complexity is considered as a disadvantage of $E_{LL}(\kappa)$.

5.1.4 **Summary and function choice**

In this section, 4 functions for length-scale analysis have been studied: the second and third order longitudinal velocity structure functions, $S_{LL}(r)$ and $S_{LLL}(r)$, the Energy Spectrum Function $E(\kappa)$ and the one-dimensional longitudinal spectrum, $E_{LL}(\kappa)$. In view of the analysis of this section, $S_{LL}(r)$ has been the function chosen, for the reasons summarized below.

$E(\kappa)$ has been discarded because it cannot be calculated for all the flows this PhD deals with, which would difficult putting together the conclusions if it is used in some cases and not in others.

As compared with $E_{LL}(\kappa)$, $S_{LL}(r)$ and $E_{LL}(\kappa)$ are related via the longitudinal two-point correlation function, $R_{LL}(r)$ (see expressions (5.12) and (5.17)). The main difference is that in one case the information is expressed in the physical space ($S_{LL}(r)$, in distances) and in the other in the Fourier space ($E_{LL}(\kappa)$, in wavenumbers). However, from the point of view of the calculation of the functions, $S_{LL}(r)$ should be obtained faster and with fewer problems: faster because to avoid problems with missing data, $E_{LL}(\kappa)$ has to be calculated from either $S_{LL}(r)$ or $R_{LL}(r)$, which have to be then expressed in Fourier space; with fewer problems because due to recurring to Fourier analysis, the original function - $S_{LL}(r)$ or $R_{LL}(r)$ - has to be adjusted to fulfill the criteria for the Fourier representation to exist or a modification of the energy content of the spectrum should be expected. Still, if it was clear that $E_{LL}(\kappa)$ can provide for a much better characterization of the error, these disadvantages would not suffice to discard it, but from the analysis conducted it is not clear if that it is indeed the case.

As compared to $S_{LLL}(r)$, $S_{LL}(r)$ can be linked more easily to the different turbulent structures, so understanding how is the error produced should be easier. In addition, for the calculation of $S_{LL}(r)$ random errors do not cancel with each other, while in $S_{LLL}(r)$ they may.

5.2 METHODS FOR ANALYSIS OF THE RESULTS

The results presented in chapter 7 are analyzed by the distribution of information with the length-scales and also by a global average error.

5.2.1 Length-scales representations

In order to represent the errors distribution along the flow scales, the dimensional second order structure function, $S_{LL}(r)$, has been chosen as key tool, as commented in section 5.1. The function is calculated in this work from the velocity field, indicated by $S_{LL}(r)\{u\}$, and from the error field, indicated by $S_{LL}(r)\{\varepsilon\}$.

For both cases, it has to be kept in mind that $S_{LL}(r)\{signal\}$, indicates the signal content for distances r, and this content includes the content from smaller scales, as was commented in 5.1.3.1. This means that a zone where $S_{LL}(r)\{\cdot\}$ does not increase is a zone where the signal has no additional contribution from those scales and the content comes from smaller scales (i.e. there are velocity differences at distances r but they come from structures of smaller scale). A zone with increasing $S_{LL}(r)\{\cdot\}$ is a zone with scales that contribute actively to the content of this function besides the content coming from smaller scales. Further details on $S_{LL}(r)\{u\}$ are provided in 5.1.3.1 and on $S_{LL}(r)\{\varepsilon\}$ further details are provided below. An additional length-scales representation is calculated from $S_{LL}(r)\{u\}$ and $S_{LL}(r)\{\varepsilon\}$, which is the correlation coefficient between the velocity and error fields, detailed below.

5.2.1.1 *Velocity field*

In order to describe how the chosen function is used in the results, $S_{LL}(r)\{u\}$ is plotted below in Figure 5.4. In the figure, $S_{LL}(r)\{u\}$ is obtained from the velocity fields that are used to generate synthetic images and the PIV simulator vectors (a DNS of homogeneous turbulence, Li *et al.*, 2008). $S_{LL}(r)\{u\}$ is obtained from the average of $S_{11}(r_1)\{u_1\}$ and $S_{22}(r_2)\{u_2\}$, with directions 1 and 2 being the two in-plane directions. The same 24 data planes that are used on the results of the numerical tools are used for this calculation (cf. section 3.1.3). Together with the function, two scaling laws are plotted as well. One corresponds to the dissipation range: $S_{LL}(r)\{u\} \propto (r/\eta)^{4/3}(r\epsilon)^{2/3}$represented by a purple dotted line and the other to the inertial range: $S_{LL}(r)\{u\} \propto (r\epsilon)^{2/3}$, represented by the broken brown line. Both laws can be found in Yeung and Zhou (1997).

In the results analysis, the scaling law in the inertial range is used to build a dimensionless representation, i.e. $S_{LL}(r)/(r\epsilon)^{2/3}$ is the representation chosen. This representation enhances both the smaller and medium scales where the effect of the errors is more important, as indicated through section 5.3. It allows obtaining an overall insight into the measurement errors given.

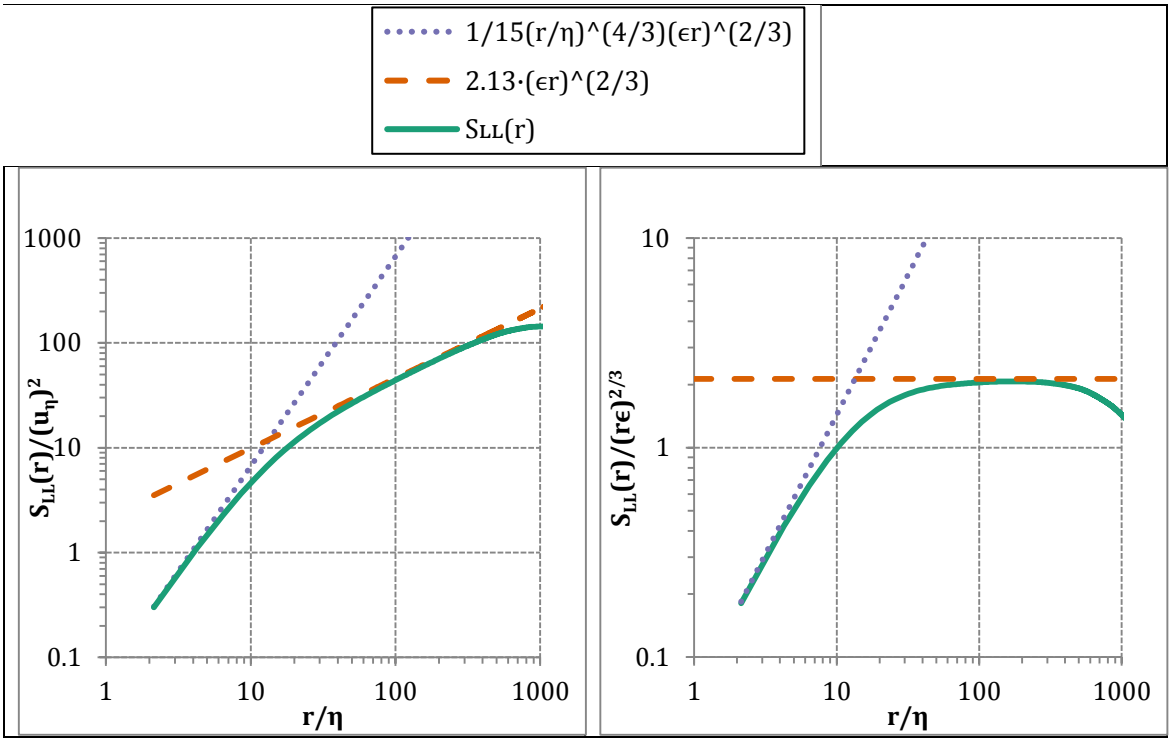

Figure 5.4 Representation of the second-order longitudinal structure function as a function of the distance *r* divided by Kolmogorov scale size. Left: $S_{LL}(r)$ divided by Kolmogorov scale velocity, u_η, squared. Right: $S_{LL}(r)$ divided by the scaling law at the inertial range, $(r\epsilon)^{2/3}$.

In addition, differences in $S_{LL}(r)\{u\}$ are plotted as well. The differences $\Delta S_{LL}(r)\{u\}$ allow for an error analysis over the whole range of length-scales which cannot be performed over $S_{LL}(r)\{u\}$ as it varies on the order of several orders of magnitude with r. For the numerical tools results those differences are calculated with respect to the real value of the function plotted above, $S_{LL}(r)\{u_R\}$ (see sections 7.1 and 7.2). Another advantage of this calculation is that it provides the error on measured velocity quadratic quantities for very large r, as expression below shows (from expression (5.19)):

$$\Delta S_{LL}(r \gg \mathcal{L})\{u\} = S_{LL}(r \gg \mathcal{L})\{u_R\} - S_{LL}(r \gg \mathcal{L})\{u_M\}$$
$$= 2[((u_R')^2 - R_{LL}(r \gg \mathcal{L})\{u_R\}) - ((u_M')^2 - R_{LL}(r \gg \mathcal{L})\{u_M\})]$$

$$\Delta S_{LL}(r \gg \mathcal{L})\{u\} \cong 2[(u_R')^2 - (u_M')^2] = \frac{4}{3}(TKE_R - TKE_M)$$

Where u_R' are the real rms velocity fluctuations, u_M' the measured rms velocity fluctuations and $\mathcal{L}$ is the integral scale. For $r \gg \mathcal{L}$, both $R_{LL}(r)\{u\}$ go to 0, which gives the expression above.

In the case of the results of the dedicated experimental setup $\Delta S_{LL}(r)\{u\}$ can only be calculated between cases with different measurement conditions, as described in section 7.3. The $\Delta S_{LL}(r)\{u\}$ are made dimensionless by recurring to Kolmogorov scale velocity u_η.

For both the dissipation and Kolmogorov scale velocity, when plotting the effect of a measurement parameter variation, ϵ and u_η are fixed. It would be possible also to calculate ϵ and u_η for each set of measurement parameters. However, calculating ϵ and u_η for each case could lead to representations of that are influenced twice by the errors: (i) because

the errors change the value of $S_{LL}(r)\{u\}$ and (ii) because they also change the value of ϵ and u_η calculated. As a result, the errors could be concealed on the plots.

As a matter of fact, that occurred on a previous measurement campaign (not reported here) and that could be the case also of the results of Lavoie *et al.* (2007). In that previous campaign, $S_{LL}(r)\{u\}$ was divided by the u'^2 calculated for each measurement test. That representation produced almost identical graphs, when in reality the values differed quite a lot. Although on this case the dimensionless form is another, the same could happen. For that reason, ϵ is fixed for the whole set of measurement parameters.

In the case of the results of the PIV Simulator (and also for synthetic images), the value of ϵ is taken from section 3.1 where the flow used to generate the results is described (obtained from Li *et al.,* 2008). Then, for the experimental results, since the turbulent flow is of different characteristics, a method of calculation is described in Chapter 6 section 6.5.3.

5.2.1.2 *Error fields calculation*

In order to clarify some aspects appeared on the analysis of $S_{LL}(r)$ applied to the velocity field, the second-order structure function is calculated from the error fields as well. The error vector at any position can be obtained from:

$$\vec{\varepsilon} = \vec{u}_R - \vec{u}_M$$

Where $\vec{u}_R$ is the real velocity vector at that position, $\vec{u}_M$ the measured velocity and $\vec{\varepsilon}$ the error vector.

If the error vector is decomposed into the two directions, the second-order longitudinal structure function can be calculated, as with the velocity field. The mathematical function which is $S_{LL}(r)\{\cdot\}$ does not distinguish between a velocity or an error field. The term between braces $\{\cdot\}$ indicates the field upon which $S_{LL}(r)$ is calculated. The same link to velocity field structures that was stablished in 5.1.3.1 can be stablished for the error field, i.e.:

$$S_{LL}(r)\{\varepsilon\} \sim \sum_{\lambda<r} \varepsilon_\lambda^2 + \sum_{\Lambda>r} \varepsilon_\Lambda^2 (r/\Lambda)^2 \tag{5.18}$$

On this case there is no such a thing as turbulent structures but there could be variations in the error field which present coherence over a certain distance, those are represented above by ε_λ and ε_Λ . Therefore, the variations in the error field with wavelength $\lambda<r$ contribute to $S_{LL}(r)\{\varepsilon\}$ with something of $\sim\varepsilon_\lambda^2$, i.e. the amplitude of the error for that wavelength squared. The variations in the error field with wavelength $\Lambda>r$ should give something of $\sim\varepsilon_\Lambda^2(r/\Lambda)^2$. The latter variations are weighed with $(r/\Lambda)^2$ and therefore their contributions to the function value should be much less important. In consequence, $S_{LL}(r)\{\varepsilon\}$ can be considered as a sort of cumulative error representation. For this reason $S_{LL}(r)\{\varepsilon\}$ is regarded as the distribution of the error with the scales of the flow squared: $\varepsilon(r)^2$. As mentioned above, the same goes to $S_{LL}(r)\{u\}$. As a consequence, $(S_{LL}(r)\{\varepsilon\}/S_{LL}(r)\{u\})^{1/2}$ is used on the measurement envelope quantification (cf. 7.4) to calculate the relative error of a scale and determine the advised bounds for the

measurement parameters. For $S_{LL}(r)\{u\}$ the value provided by the DNS (the one plotted in Figure 5.4) is used.

In addition, $S_{LL}(r)\{\varepsilon\}$ can also be linked to $R_{LL}(r)\{\varepsilon\}$, the two-point longitudinal error correlation (defined for the velocity in 5.1.1.2), by expression below:

$$S_{LL}(r)\{\varepsilon\} = 2(\varepsilon_T^2 - R_{LL}(r)\{\varepsilon\}) \tag{5.19}$$

Where $R_{LL}(r)\{\varepsilon\}$ is the two-point longitudinal error correlation and ε_T is the total average error, defined in 5.2.2 below.

By this relation, when $S_{LL}(r)\{\varepsilon\}$ increases, that is indicative of the error field having a certain spatial coherence (i.e. $R_{LL}(r)\{\varepsilon\}$ different to 0). This is the case observed in the results of chapter 7, i.e. the error is not completely random, as is seen in section 5.3.

5.2.1.3 *Correlation of velocity and error fields*

In the results, it is evident (see Chapter 7, sections 7.1 and 7.2) that $\Delta S_{LL}(r)\{u\}$ presents much larger variations than $S_{LL}(r)\{\varepsilon\}$. This draws the attention to the comparison between both functions, which can be obtained as follows:

$$\Delta S_{LL}(r)\{u\} = S_{LL}(r)\{u_R\} - S_{LL}(r)\{u_M\}$$

Replacing $u_M = u_R - \varepsilon$ in expression above, $S_{LL}(r)\{u_M\}$ yields:

$$S_{LL}(r)\{u_M\} = \left\langle \left[\left(u_R(x+r) - \varepsilon(x+r)\right) - \left(u_R(x) - \varepsilon(x)\right) \right]^2 \right\rangle$$

$$S_{LL}(r)\{u_M\} = \left\langle \left(u_R(x+r) - u_R(x)\right)^2 + \left(\varepsilon(x+r) - \varepsilon(x)\right)^2 - 2\left(u_R(x+r) - u_R(x)\right)\left(\varepsilon(x+r) - \varepsilon(x)\right) \right\rangle$$

When the average is performed, the first term gives $S_{LL}(r)\{u_R\}$ and the second $S_{LL}(r)\{\varepsilon\}$. It follows then that:

$$\Delta S_{LL}(r)\{u\} + S_{LL}(r)\{\varepsilon\} = 2\left\langle \delta u_L^R(r,\boldsymbol{x})\delta\varepsilon_L(r,\boldsymbol{x}) \right\rangle_{\boldsymbol{x}} \tag{5.20}$$

Where $\delta u_L^R(r,x)$ represents the real velocity longitudinal differences at distance r and position $\boldsymbol{x}$ and $\delta\varepsilon_L(r,x)$ represents the error longitudinal differences at distance r and position $\boldsymbol{x}$. The average then corresponds then to the covariance between velocity difference and error difference at distances r. When this term is normalized, the corresponding correlation coefficient can be obtained:

$$\mathrm{C}_{u\varepsilon} = \frac{\left\langle \left(\delta u_L^R(x,r)\delta\varepsilon_L(x,r)\right) \right\rangle_x}{\sqrt{\left\langle \left(\delta u_L^R(x,r)\right)^2 \right\rangle \left\langle \left(\delta\varepsilon_L(x,r)\right)^2 \right\rangle}} = \frac{1}{2}\frac{\Delta S_{LL}(r)\{u\} + S_{LL}(r)\{\varepsilon\}}{\sqrt{S_{LL}(r)\{u_R\}S_{LL}(r)\{\varepsilon\}}} \tag{5.21}$$

This coefficient is of importance for quantities that go with the square of velocity as for example the turbulent kinetic energy. This can be understood from expression below:

$$\langle (u_M)^2 \rangle = \langle (u_R)^2 \rangle + \langle \varepsilon^2 \rangle - 2\langle u_R \varepsilon \rangle$$

As can be appreciated, the third term in the right of expression above is the correlation of the real velocity field and the error field which is information similar to the one that can be observed from the difference above. The same applies to $\Delta S_{LL}(r)\{u\}$ which can be expressed as:

$$\Delta S_{LL}(r)\{u\} = 2C_{u\varepsilon}(r)\sqrt{S_{LL}(r)\{u_R\}S_{LL}(r)\{\varepsilon\}} - S_{LL}(r)\{\varepsilon\} \quad (5.22)$$

The coefficient also provides relevant information in terms of error topology. Indeed, as can be seen in section 5.3 some errors are correlated with the real velocity (as for example low-pass errors, see 5.3.3), some others should have no correlation (random errors) and others may produce negative correlation (for example group-locking errors, see 5.3.6).

5.2.2 **Total average error**

The total error average value is calculated in Chapter 7 as a way to introduce the length-scales characterization. The average error is defined for the first velocity component as:

$$\varepsilon_{1,T} = \sqrt{\frac{1}{N_i N_j N_m} \sum_{i,j,m} \left(\left(u_1(i,j,m) - u_{1_M}(i,j,m) \right)^2 \right)}$$

Where $u_{1_M}(i,j,m)$ and $u_1(i,j,m)$ are the measured and the real velocity at a position (i, j) of vector map m. N_i, N_j and N_m are the number of in-plane vectors in each direction and of vector maps, respectively. Then from each of the error components the total error is calculated:

$$\varepsilon_T = \sqrt{\frac{1}{2}\left(\varepsilon_{1,T}^2 + \varepsilon_{2,T}^2\right)}$$

This definition of the total error is similar to the one employed by Astarita and Cardone (2005).

5.3 THEORETICAL ANALYSIS OF THE ERRORS OF PIV TURBULENCE MEASUREMENTS

As PIV and related measurement techniques are reaching maturity, researchers are devoting increasing efforts in isolating and assessing measurement error sources. Especially the errors in turbulent measurement contexts are receiving much attention in the last years (Lavoie *et al.*, 2007, Tanaka and Eaton, 2007, Atkinson *et al.*, 2013, among others). Within this frame, the research group that hosts this PhD thesis has provided access to an error source compilation developed for a European project proposal (PIV-EUROTAMER: PIV European Treaty on Assessment and Management of Error). In it, the PIV process is outlined, together with the errors that can be produced in each step. This compilation is given in Table 5.1 below as reference frame, adding the reasons to include or discard each error for this Thesis study. The errors that are included in the study are shaded in grey in the table.

This section pursues mainly two objectives:

(i) To identify the sources related to spatial gradients error so that an estimation of the total average error can be provided. This is one of the focal objectives of this PhD. An estimation of the effect in the length-scales distribution that can be obtained with PIV is provided as well. This allows obtaining error estimates to other PIV experimentalists without the need of developing the numerical tools used in this work.

(ii) To compile the rest of errors that can be produced in PIV measurements of turbulence and obtain an estimate of the possible value those errors may have for the results of this work. Specifically, a rough estimate of the effect in the measured $S_{LL}(r)\{u\}$ is provided. That allows checking the coherence of the results obtained in the numerical tools with the real images included in the study. For real images, the error value is not known and the results are checked by comparing $S_{LL}(r)\{u\}$ with the value of the numerical tools.

Following, the EUROTAMER error compilation is analyzed, to later move onto the study of the error sources that have been identified in PIV turbulence measurements.

Table 5.1 Error sources, their location and if they need to be included on the preliminary analysis of this PhD.

Measurement Chain location and issue under study		Error source	Example of sources of additional information for error assessment	Possible Error Handling protocol (error assessment and partial correction)	Reasons to include or discard the error source on this analysis
Experiment setup	Flow characteristics	Interaction with laser sheet width, spatial velocity gradients, temporal variations	Flow parameter envelope based on effects of viscosity, perturbation frequency, buoyancy effects, etc.	Acquisition parameter constrains based on Reynolds, Strouhal, Grashof and other flow characterizing numbers.	This is the error which is the focus of the PhD, for homogeneous isotropic turbulent flows. The effect of other flow topologies is left to further study.
	Seeding	Deviation from flow (Stokes number)	Particle characterizing by vortex centre depletion or settling velocities	Based on Taylor or hypothesis or acceleration knowledge	The importance of this error relative to the one under study needs to be assessed. It is referenced as Particle slip along this PhD document.
		Spatial sampling	Seeding density	Based on mean distance between particles	It is taken into account to select a large enough seeding density, this way the limit on the resolution imposed by the distance between particles does not have any influence for this work.

Measurement Chain location and issue under study		Error source	Example of sources of additional information for error assessment	Possible Error Handling protocol (error assessment and partial correction)	Reasons to include or discard the error source on this analysis
	Illumination.	Background, stray light, ΔI (laser intensity variations).	Theoretical studies on these effects.	Based on parameters defining the magnitude of these effects in a measurement.	From these issues, the error produced by the change of particles light intensity (Nobach and Bodenschatz, 2009) is included, because turbulent flow together with Gaussian light profiles can induce this type of light difference as well as lasers misalignment or power differences. Background and stray light are not included in the study: the measurement conditions have been set carefully to avoid these sources.
	Calibration.	Misalignment between laser sheet and calibration.	Transparent calibration target procedures.	Based on good practice calibration procedure.	For single camera setups, good practice reduces this error to the order of 3 degrees. But even in that case, it would affect large scales (in the order of the image size), which are not the focus in this study.
			Self-calibration for multi-camera setups.	Based on variation of calibration parameters in the self-calibration procedure.	

Measurement Chain location and issue under study		**Error source**	**Example of sources of additional information for error assessment**	**Possible Error Handling protocol (error assessment and partial correction)**	**Reasons to include or discard the error source on this analysis**
	Camera-laser-flow rigidity.	Vibration.	Accelerometer, solid boundary recording.	Protocol to assess vibration.	This error is characteristic of flows generated by devices using heavy machinery close to the measurement area. This is not the case of the selected flows for this PhD.
Image Acquisition	Light path within the flow.	Refraction and aberrations.	Background Oriented Schlieren Shadowgraphy.	Absolute particle location uncertainty and relative variation in time. Calibration possibilities.	Related to refraction based on relevant temperature variations of the flow, which are not present for the flows under study.
	Acquisition parameters.	Δt uncertainty.	Monitoring with photodiode.	Data base on typical error magnitude.	The error given by the Q-switch ramp and the delay between the two Q-switches, which is given by the computer time card, should be in the order of the nanosecond (Legrand, 2008). Negligible with respect to the time delays of the order of micro-seconds which are used through this work.
		Laser sheet width.	Laser profile characterization.	Based on effective width for a given profile.	This is the main error objective of the PhD.

Measurement Chain location and issue under study		**Error source**	**Example of sources of additional information for error assessment**	**Possible Error Handling protocol (error assessment and partial correction)**	**Reasons to include or discard the error source on this analysis**
	Camera optics.	Astigmatism and higher order image aberrations, vignetting.	Lens calibration.	Based on lens calibration.	These effects are negligible for the lenses used (common photography lenses with small view angle).
	Image recording.	Saturation, read out error, sensor response.	Camera readout calibration.	Based on readout error modelling.	Saturation errors are avoided by properly selecting the measurement parameters. In CCD sensors, read-out errors cannot be avoided, they are studied below.
Image Reconstruction	Sub-pixel offset + Local field Correction.	Image grey level interpolation.	Peak locking pattern error (with 2 pixels period if symmetrical).	Based on peak locking magnitude and properties.	The vector fields obtained incorporate these errors; therefore, their magnitude and effects have to be assessed.
		Velocity sampling and interpolation.	Spatial response and instability.	Procedures to avoid error growth and instability.	Instabilities lead to an outlier production, which effect is included in the study. The effect of the spatial response is also considered and its magnitude evaluated.

Measurement Chain location and issue under study		**Error source**	**Example of sources of additional information for error assessment**	**Possible Error Handling (error protocol assessment and partial correction)**	**Reasons to include or discard the error source on this analysis**
	2D3C stereo reconstruction.	Simplified reconstruction.	Moiré patterns in the velocity magnitude.	Based on pattern recognition.	On the PhD only 2D2C PIV errors are studied; not included.
	3D tomographic reconstruction.	Ghost particles.	Sub-voxel information.	Based on sub-voxel information.	Same than previous issue.
	Correlation algorithm	Background contribution to correlation	Correlation interaction between particles and background	Based on correlation properties.	Error source that cannot be separated from the one under study; included on the analysis.
		Spatial frequency response.	Theoretical frequency response.	Based frequency response modification.	Same than previous.

Measurement Chain location and issue under study		**Error source**	**Example of sources of additional information for error assessment**	**Possible Error Handling protocol (error assessment and partial correction)**	**Reasons to include or discard the error source on this analysis**
Vector and other magnitudes extraction	Sub-pixel correlation peak fitting.	Non Gaussian particle shape and average background level	Autocorrelation characteristics.	Extrapolating autocorrelation characteristics to the cross correlation analysis	Same than previous.
		Sub-pixel reconstruction assumptions	Theoretical limitations of the reconstruction.	Based on experimental assessment of the theoretical limitations	Same than previous.
	Prediction and correction procedures	Spatial frequency response.	Stability analysis.	Based on stability analysis.	If the measurement converges, it does so to a velocity with the errors under study; if it diverges, an outlier vector is be obtained, which is a case included as well on the study.
	Higher order and combined statistics.	Vector spatial and time location uncertainty.	Multidimensional Taylor expansions.	Adequate finite difference schemes.	These errors are incorporated on the vector fields that are studied; therefore, their importance is assessed below.

5.3.1 **Errors in turbulence measurements**

The sources that have been identified that require further analysis are quoted below. The organization differs from that of Table 5.1; some sources of Table 5.1 are divided into different effects and others have been grouped into one single source. This has been done to match the bibliographic research papers where those effects are studied and seeking a clearer exposition.

The different error sources are grouped under each of the different tools devised in the methodology for error analysis, which are:

- PIV Simulator: as mentioned in section 3.2, the PIV Simulator obtains the displacement by performing what could be called a "perfect" correlation: there is no background noise, cross-talk between particles or loss of particles; and the position of the correlation maximum is perfectly determined by the algorithm. It allows studying the sources that are the focal point of this PhD, i.e. the sources associated to spatial gradients interaction with the laser sheet thickness.
- Synthetic images: compared to the PIV Simulator, PIV images are generated and the full PIV evaluation is performed. The errors related to the experimental setup have not been included in the synthetic images of this work.
- Real PIV images: all error sources associated to a PIV experimental setup are encountered.

The error sources, which are listed below, are shown only on the first tool that should encounter them, e.g. synthetic images contain all the error sources of the PIV Simulator plus those grouped under the synthetic images point, and so on. The error sources are then:

- Errors present in the PIV Simulator:
  - Vector and other magnitudes extraction.
  - Low-pass errors (Willert and Gharib, 1991).
  - Particles misplacement errors.
  - Peak-splitting phenomenon.
  - Group-locking errors (Lecuona *et al.,* 2004).
- Additional errors present in synthetic images:
  - Peak-locking systematic error (Westerweel, 1998, Nogueira *et al.*, 2001, or Astarita and Cardone, 2005, among others).
  - Peak-locking random error (Nogueira *et al.*, 2011).
  - Random error induced by particles light intensity change (Nobach and Bodenschatz, 2009).
  - Random error in determining the correlation peak-location (Westerweel, 1998).
  - Spatial gradients systematic biases (Westerweel, 2008).
  - Outliers' occurrence.
- Additional errors present in real images:
  - CCD read-out errors (Nogueira *et al.*, 2009, Atkinson *et al.*, 2014, Legrand *et al.*, 2014).
  - Particle slip (Hjelmfelt and Mockros, 1966, Adrian and Westerweel, 2011).
  - Perspective projection errors (Raffel *et al.,* 2007)

As mentioned at the beginning of this section, a model is proposed for both the total average error value, ε_T, and for the measured $S_{LL}(r)\{u\}$, for the whole set of errors given in the PIV Simulator. The estimation depends on both Δt and Th and allows obtaining predictions in different conditions to those studied in this PhD. Both estimations have been validated with the results of the PIV Simulator in Chapter 7. Aside from that, the order of magnitude of the rest of error sources is provided. When the order of magnitude of an error advises so, a rough estimate of their effect in $S_{LL}(r)\{u\}$ is also given, in order to verify coherence of the results in real PIV images. For such purpose, each error source is considered to act independently of the rest. The whole set of errors given in PIV images are not combined into a single estimate, as that is out-of-scope of this work.

The variations of function $S_{LL}(r)\{\varepsilon\}$ with r are not provided because the function is directly linked to ε_T for large r (cf. 5.2.1.2) and it does not present important variations for $r>Th$, a region of the function which contains inevitably too large relative error content.

5.3.2 **Vectors extraction**

On standard PIV algorithms, the velocity is placed at the centre of the interrogation volume and supposed to occur at the middle time between the laser pulses (for symmetric image deformation, Wereley and Meinhart, 2001). However, when and where the measured velocity occurs in reality (if it does) is actually uncertain.

In order to assess which dimension produces a larger error, the time or the volume, Taylor series are used to estimate the real velocity value. Assuming the real value of velocity is $\boldsymbol{u}(x,y,z;t)$ and that instead the value at $(x_0,y_0,z_0;t_0)$ has been the one provided by the measurement (with x_0,y_0,z_0 placed inside the interrogation volume and t_0 between the laser pulses), the difference between the two gives (assuming a square interrogation window):

$$\boldsymbol{u}(x,y,z;t) \cong \boldsymbol{u}(x_0,y_0,z_0;t_0) + \frac{\partial \boldsymbol{u}}{\partial x} D_I + \frac{\partial \boldsymbol{u}}{\partial y} D_I + \frac{\partial \boldsymbol{u}}{\partial z} Th + \frac{\partial \boldsymbol{u}}{\partial t} \Delta t + o[D_I, Th, \Delta t]$$

Where Th is the laser sheet thickness, Δt is the time delay between the laser pulses and D_I is the interrogation window side size. From this point of view, the error induced by the out-of-plane dimension z is the error objective of the PhD.

In order to provide an estimate for temporal velocity gradients, $\partial u_1/\partial t$, the Kolmogorov characteristic time τ_η and velocity u_η are used. For any turbulent flow, those scales produce the largest temporal gradients, as:

$$\frac{u_\eta/\tau_\eta}{u_T/\tau_T} \cong Re^{1/4}$$

Where u_T and τ_T are the characteristic velocity and time of the largest turbulent scale in the inertial range cascade and Re is the Reynolds number of the flow. The ratio between the gradients is obtained from the relations in the inertial range: $u_T/u_\eta = Re^{1/4}$ and $\tau_T/\tau_\eta = Re^{1/2}$ (Pope, 2000).

Thus, the error due to misplacing the velocity in the time domain is estimated by:

$$\frac{\partial \boldsymbol{u}}{\partial t}\Delta t \sim \frac{u_\eta}{\tau_\eta}\Delta t$$

In the same sense, the error produced due to misplacing the velocity vector within the volume would be (in this case it is done in the out-of-plane direction because the Th is larger for all the measurements reported in this PhD):

$$\frac{\partial \boldsymbol{u}}{\partial z}Th \sim \frac{u_\eta}{\eta}Th$$

Where η is the Kolmogorov length-scale and Th is the laser sheet thickness. Again, Kolmogorov scale is the one with larger spatial gradients, as:

$$\frac{u_\eta/\eta}{u_T/\ell_T} \cong Re^{1/2}$$

Where ℓ_T is the size of the largest turbulent scale in the inertial range cascade. The relation is obtained from: $\ell_T/\eta = Re^{3/4}$ and the equivalent one for velocities given above.

If both errors are compared, that gives:

$$\frac{\frac{u_\eta}{\tau_\eta}\Delta t}{\frac{u_\eta}{\eta}Th} \sim \frac{\eta}{\tau_\eta}\left(\frac{\Delta t}{Th}\right) \sim u_\eta\left(\frac{\Delta t}{Th}\right) \sim \frac{u_T \Delta t}{Th}\frac{1}{Re^{1/4}} \ll 1 \qquad (5.23)$$

$u_T\Delta t/Th$ is related to the out-of-plane motion rate which is usually kept in PIV below 30% (Raffel *et al.* 2007) and so it is the case for the measurements reported on this thesis. Additionally it is divided by $Re^{1/4}$ which for turbulence to exist is much larger than 1. Therefore, the temporal misplacement errors are much smaller than those produced in the out-of-plane direction, which are the objective of the PhD, and are considered negligible on the subsequent analysis.

The error induced by the out-of-plane misplacement of the velocity vector can be considered from the following sources, which are detailed below: (i) it can happen that the PIV process provides something similar to an average of the displacement of the volume. This possibility is studied in 5.3.3. However, it is known that PIV may not provide a perfect average, and deviations from that case are studied in the points following 5.3.3.

5.3.3 **Low-pass filtering effect**

This effect is produced by the fact that the interrogation volume has a certain finite size. All the particles inside the interrogation domain can contribute to the final displacement. A straightforward simplification typically used in PIV consists in assuming that PIV provides the average of the flow velocities inside the domain (Willert and Gharib, 1991, or Lavoie *et al.*, 2007, among others). Lavoie *et al.* (2007) consider the interrogation domain as composed of 4 dimensions, the 3 spatial ones and the temporal one. The measured velocity u_{i_M} would be then:

$$u_{i_M}(\boldsymbol{x_0}) = \frac{1}{ThD_I D_I \Delta t} \int_{-\frac{\Delta t}{2}}^{\Delta t/2} \int_{-\frac{Th}{2}}^{Th/2} \int_{-\frac{D_I}{2}}^{D_I/2} \int_{-\frac{D_I}{2}}^{D_I/2} u_i(\boldsymbol{x_0} + \boldsymbol{s}, t)\mathrm{d}\boldsymbol{s}\mathrm{d}t \tag{5.24}$$

Where $\boldsymbol{s}$ and t are dummy variables and u_i is the real velocity. The interrogation window is supposed to be square in the in-plane dimension.

As was shown on 5.3.2 the temporal variations of velocity are much smaller than the spatial variations. Therefore, the integral in the time domain is simplified by:

$$\int_{-\frac{\Delta t}{2}}^{\Delta t/2} u_i(\boldsymbol{x_0} + \boldsymbol{s}, t)dt \approx u_i(\boldsymbol{x_0} + \boldsymbol{s})\Delta t$$

That leaves only the spatial variations effect. It is important to note that, in expression (5.24), all spatial positions contribute the same to the measured velocity. However, this may not be necessarily the case in reality, as weighting functions could be applied in any direction. The effect of a weighting function can be studied by multiplying the corresponding function with $u_i(\boldsymbol{x_0}+\boldsymbol{s})$ in the integral of (5.24). For example, the laser sheet profiles used in this work do not provide a uniform intensity, as can be observed in Chapter 6 section 6.3.1; and the numerical tools use a Gaussian light intensity distribution in the out-of-plane direction, to simulate this effect. Also, the interrogation window pixels can be weighted before calculating the correlation. In the results of Chapter 7, for both real and synthetic images an in-plane weighting function was used, as commented in 3.3.4 and 6.5.1 . The function employed is defined in 3.3.4.1. The PIV Simulator results are calculated without in-plane weighting.

In order to illustrate the response obtained when an average of the velocity in the sensing domain is performed, the effect of an average in one dimension is shown in the figure below. The figure plots the average value of a 1-D sinusoidal displacement of wavelength ℓ, with the maximum displacement always at the center of the 1-D interrogation window of size D_I. The horizontal axis is the dimensionless spatial frequency of the sinusoid, D_I/ℓ. The vertical axis in the graph is the normalized response, which is the amplitude of the measured velocity (the average) divided by the amplitude of the real signal. Three different cases are plotted. The first case (labelled "No Weight") is obtained by performing a 1-D average without weighting the real velocity field. The PIV Simulator employs windows without weighting. The second case, labelled "Davis W" is the normalized response given by multiplying the sinusoid with the in-plane weighting function used in this work for synthetic and real images. For the third case ("GW; σ/D_I=1.00") the real velocity field is weighted with a Gaussian function: $\exp(-8x^2/\sigma^2)$, where x corresponds to the coordinate upon which the displacement depends and is centered in the interrogation window. σ is the distance between the e^{-2} waist points. This is the weighting applied in the out-of-plane direction of the numerical tools and typically the PIV laser profiles are studied by recurring to equivalent Gaussian functions.

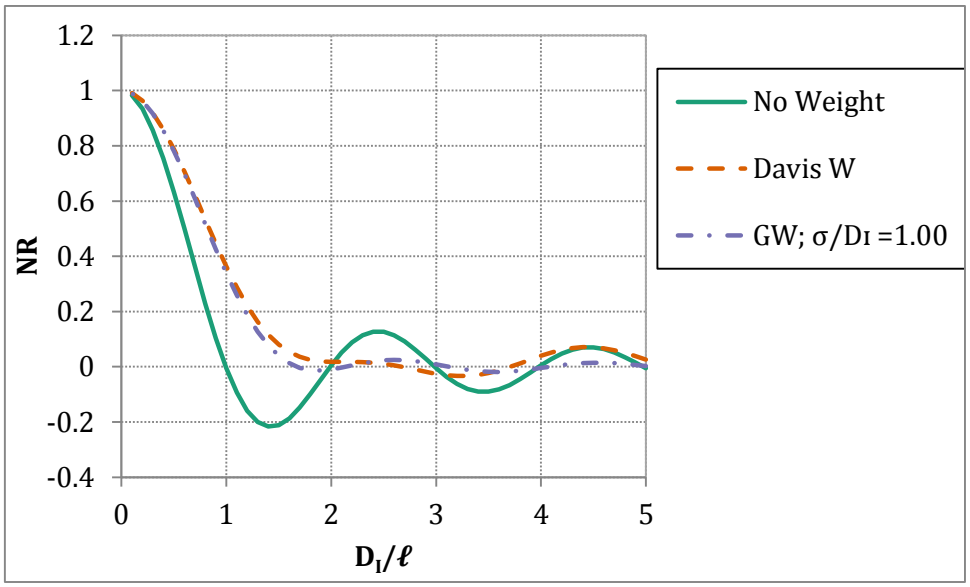

Figure 5.5 Spatial wavelength response of a 1D low-pass filter for different wavelength-sizes.

It can be appreciated in the figure that if the wavelength ℓ diminishes with respect to D_I the normalized response diminishes as well, thereby producing an error. The same would apply to the thickness. It can also be observed that the NR of the Davis Weighting function of size D_I is very similar to a Gaussian weighting of $\sigma=D_I$.

5.3.3.1 *Effect of the multi-grid PIV evaluation*

Synthetic images and the experimental setup images are evaluated with a multi-grid evaluation scheme (Scarano, 2002). That can modify the response in terms of low-pass filtering errors, and thus the effect is estimated here.

In order to estimate the effect, the spectral domain is used. In that domain, the velocity field to measure is referred to as V. On the first pass of the multi-grid algorithm, the first interrogation size will measure $V{\cdot}NR_1$, where NR_1 is the normalized response of the first interrogation window size, that has been defined in the previous subsection. At this point, the velocity estimation provided by the algorithm is also $V{\cdot}NR_1$. From that velocity estimate, each vector is replaced by the average of the 3x3 vectors centered in the vector. This operation, that smooths the measured velocity field, is implemented in the algorithm to avoid divergence of the iterative measurement (Lavision, 2007). This filter will have a normalized response $NR_{3x3,1}$. Afterwards, the image pair is deformed with this displacement, which leaves a displacement on the images that is $V\text{-}V{\cdot}NR_1{\cdot}NR_{3x3,1}$. This is the displacement that the second iteration of the multigrid algorithm has to measure, following the same steps than the first iteration. The multigrid evaluation is summarized in the table below, for synthetic images where 8 iterative steps are performed (cf. 3.3.4). For real images 6 iterative steps have been used (cf. 6.5.1), but the same rationale applies:

Table 5.2 Multi-grid algorithm iterative steps for the case of synthetic images

Step	Vector field to measure	Measured vector field	Velocity estimation	3x3 smoothing filter
1	$V_{10}=V$	$V_{11}=NR_1{\cdot}\,V_{10}$	$V_{12}=V_{11}$	$V_{13}=V_{12}{\cdot}NR_{3x3,1}$ $V_{13}=\underbrace{NR_1\cdot NR_{3x3,1}}_{ENR_1}\cdot V$

Step	Vector field to measure	Measured vector field	Velocity estimation	3x3 smoothing filter
2	$V_{20}=V(1-ENR_1)$	$V_{21}=NR_2 \cdot V_{20}$	$V_{22}=V_{13}+V_{21}$ $V_{22}=V(ENR_1+NR_2-ENR_1NR_2)$	$V_{23}=V_{22} \cdot NR_{3x3,2}=V \cdot ENR_2$
Reduction of interrogation window size				
3	$V_{30}=V-V_{23}$ $V_{30}=V(1-ENR_2)$	$V_{31}=NR_3 \cdot V_{30}$	$V_{32}=V_{23}+V_{31}$ $V_{32}=V(ENR_2+NR_3-ENR_2NR_3)$	$V_{33}=V_{32} \cdot NR_{3x3,3}=V \cdot ENR_3$
…	…	…	…	…
7	$V_{70}=V(1-ENR_6)$	$V_{71}=NR_7 \cdot V_{70}$	$V_{72}=V_{63}+V_{71}$ $V_{32}=V(ENR_6+NR_7-ENR_6NR_7)$	$V_{73}=V_{72} \cdot NR_{3x3,7}=V \cdot ENR_7$
8	$V_{80}=V(1-ENR_7)$	$V_{81}=NR_8 \cdot V_{80}$	$V_{82}=V_{73}+V_{81}$ $V_{82}=V(ENR_7+NR_8-ENR_7NR_8)$	Not performed

As indicated in the table, the final iteration step does not perform any smoothing of the measured velocity field. In consequence, the final measured velocity field is V_{82} and the equivalent normalized response is $ENR_8=(ENR_7+NR_8-ENR_7NR_8)$. In the table above, the different NR_i correspond to the normalized responses of the successive interrogation window sizes, which except on the final interrogation window size, have no weighting. The final interrogation window size uses the weighting function described in 3.3.4.1. Both normalized responses with weighting and without weighting are plotted in Figure 5.5.

In order to estimate ENR_8, so low-pass errors can be assessed for synthetic and real images, the normalized response of a 3x3 smoothing filter, needs to be roughly calculated. As mentioned above, the average velocity is calculated from 9 discretized data points. This operation is going to be replaced by an average in a continuous domain inside a square with a size imposed by the vectors separation, VS: $VS=D_I \cdot (1-OV)$, where OV is the overlap. It has been observed that for a sinusoid of wavelength $3VS$, the average of 3 discretized points taken from the sinusoid gives 0. This is considered then the equivalent distance that represents the smoothing filter, i.e. $NR_{3x3}(VS)=NR(3 \cdot VS)$, where NR is the conventional normalized response of a 1D continuous average that has been plotted in Figure 5.5. The 3x3 smoothing filter equivalent area has been sketched in the figure below, for a case with a 50% overlap. The sinusoid which average taking 3 discretized points gives 0 is also represented in the figure.

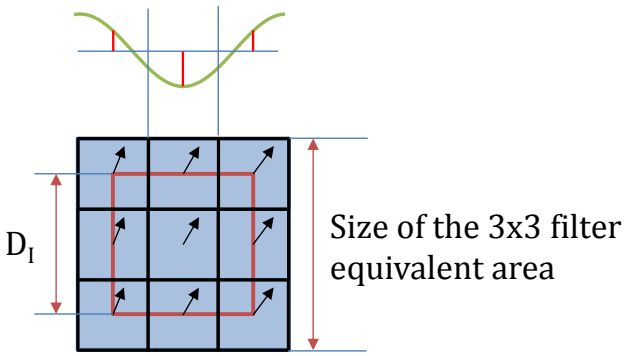

Figure 5.6 3x3 smoothing filter and its equivalent size.

With the equivalent size of a smoothing filter, ENR_8 can be calculated. It has been represented in the graph below, for the case of synthetic images. It has been verified that in the case of real images, the same final *ENR* is obtained than for synthetic images and thus it is not plotted. In the figure, the different interrogation windows normalized responses used in the multi-grid algorithm are also plotted. Additionally, the equivalent normalized response of step 7 is plotted as well as it is an important factor for the study of peak-splitting (cf. 5.3.5.3).

The horizontal axis is the final interrogation window size, D_I, divided by the wavelength, ℓ. D_I equals 32 pixels, for both synthetic and real images. In the figure the normalized response has been set to 0 for the region where the interrogation windows normalized responses would become negative. This has been done because the Nyquist criterion establishes that wavenumbers higher than the sampling wavenumber divided by 2 ($W_S/2$) cannot be characterized (Stein, 2000). The sampling wavenumber in the case of PIV is given by $W_S=1/(D_I(1-OV))$, which gives a Nyquist cutoff of $W_N=1/D_I$ for the 50% overlap used in the multigrid processing and thus the negative lobes cannot appear.

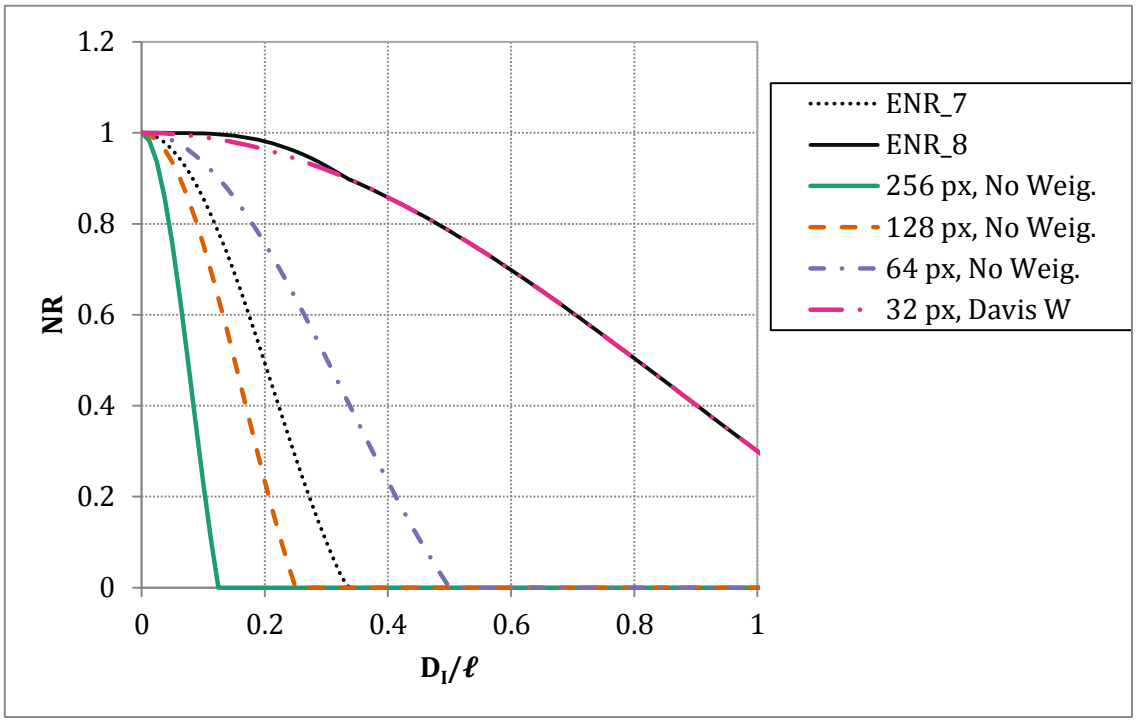

Figure 5.7 Normalized responses of the different interrogation window sizes used by the multigrid processing, for the case of synthetic images. The equivalent normalized responses, ENR, of the last two iterations are also plotted.

It can be observed on the graph that the improvement of the normalized response, due to the multigrid processing, is very small. In consequence it is assumed that the normalized response given by the last interrogation window size is the same than the one of the whole multigrid processing. That allows obtaining the error estimate below.

5.3.3.2 *Estimation of the error value*

A simple estimation is proposed below for the measurement error. The low-pass error is produced from the fact that the PIV measurement cannot recover the full kinetic energy of

the smaller turbulent scales, as indicated by the normalized responses provided in Figure 5.5. The energy that is lost for the different scales is accumulated giving a certain error value. A larger interrogation volume recovers yet less energy on the smaller scales, giving larger error values. As a result, the error in the measured velocity due to low pass effects, ε_{LPF}, can be roughly estimated as:

$$\varepsilon_{LPF} \sim (TKE\ lost(D_I, Th))^{1/2}$$

Where *TKE lost(D_I,Th)* indicates the turbulent kinetic energy lost due to the normalized response being smaller than 1.

As $S_{LL}(r)\{u\}$ roughly represents the cumulative energy of eddies smaller than r, ε_{LPF} should be related to the value of the function at a certain distance imposed by the measurement volume. It should be then possible to estimate ε_{LPF} by:

$$\varepsilon_{LPF} \approx B_1 \sqrt{S_{LL}\left(r = \overbrace{C_1 d_{eq,1D}}^{d_{er,1D}}\right)\{u_R\}} \tag{5.25}$$

Where $d_{eq,1D}$ would be an equivalent 1D size that encompasses the whole 3D interrogation volume filtering effect in the error value, B_1 is a constant and C_1 is the ratio that gives where $S_{LL}(r)\{u\}$ would have to be evaluated and is constant as well.

The results obtained by the numerical tools can be adjusted by expression above for single B_1 and C_1 values and a $d_{eq,1D}$ defined from the measurement volume. Those values are:

$$B_1 = 0.354$$

$$C_1 = 0.25$$

$$d_{er,1D} = 0.25\sqrt{Th^2 + D_I^2} = 0.25 d_{eq,1D}$$

As can be appreciated in the expression above, $d_{eq,1D}$ depends both in Th and D_I. The laser sheet thickness has always a Gaussian profile, but the interrogation window may or may not have a weighting function applied. In order to account for this fact, when D_I has no weighting applied, the equivalent distance used is $d_{eq,1D} = \sqrt{Th^2 + (4/3D_I)^2}$. The $4/3$ factor is used because an interrogation window with Gaussian weighting of size $4/3D_I$ has roughly the same NR than a window with no weighting of size D_I (for wavelengths $\ell < 4/3D_I$).

An important issue associated to low-pass effect, is that the error field produced should be correlated to the velocity field. This is of importance for the estimation of $S_{LL}(r)\{u\}$, as is shown in the next subsection. To illustrate this fact, a simple 1-D sinusoidal displacement field is plotted in the figure below. The measured displacement is imposed by the wavelength of the sinusoidal relative to the interrogation window size, in this example $D_I = \ell/2$. In that case, the normalized response is approximately 0.7, so $d_M(x) = 0.7 d_R(x)$. The measured displacement, and the error $\varepsilon(x) = d_R(x) - d_M(x)$, are plotted in the figure as well. As can be understood from the figure, since the error field is a sinusoidal as well and of the

same wavelength than the real displacement, the correlation coefficient between both should be 1.

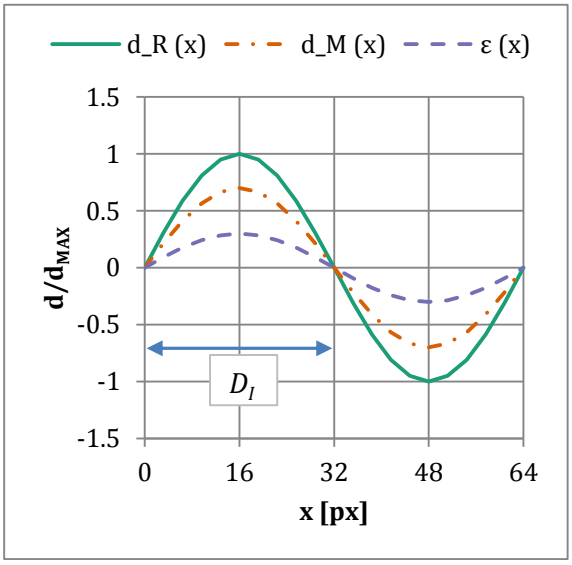

Figure 5.8 Real and measured displacements and measurement error, for the case of a 1-D sinusoidal displacement with low-pass errors.

In the case of a turbulent flow, the displacement is given by adding eddies of different sizes and velocities. In the error field only some of the wavelengths of the turbulent flow will appear; those for which the normalized response is substantially smaller than 1. In this case, the correlation between the real velocity and the error field does not reach 1 because the error field does not contain all the wavelengths that are given in the velocity field. In addition, in the error field the energy of the different coherent structures is not proportional to the energy of the same coherent structures in the velocity field. In the error field, the amplitude of a coherent structure of wavelength λ should be $\varepsilon_\lambda \sim (1-NR(\lambda;D_I,Th))u_\lambda$, where u_λ is the amplitude of that structure in the velocity field. Still, as the results of Chapter 7 show, the correlation between both fields is still important when the dominant error is low-pass, and plays a key role in the value of $S_{LL}(r)\{u_M\}$.

5.3.3.3 *Estimation of $S_{LL}(r)\{u\}$*

The effect of low-pass errors in PIV turbulence measurements was obtained by Lavoie *et al.* (2007). It is given by:

$$\Phi_{11}^{M}(\boldsymbol{\kappa}) = A^2(\boldsymbol{\kappa})\Phi_{11}(\boldsymbol{\kappa})$$

Where $\Phi_{11}(\boldsymbol{\kappa})$ and $\Phi_{11}^{M}(\boldsymbol{\kappa})$ are the real and the measured velocity spectrums, defined in expression (5.8), and $A(\boldsymbol{\kappa})$ is the product of the normalized responses for each wavenumber direction, as those that have been plotted in Figure 5.5. From $\Phi_{ii}(\boldsymbol{\kappa})$ it is possible to calculate the energy spectrum function $E(\kappa)$ and a measured energy spectrum function $E_{LPF}(\kappa)$, by recurring to expression (5.9). $E(\kappa)$ and $S_{LL}(r)\{u_R\}$ are linked by the expression below (Davidson, 2004):

$$S_{LL}(r)\{u_R\} = \frac{4}{3}\int_0^\infty E(\kappa)H(\kappa r)\mathrm{d}\kappa$$

Where $H(\kappa r)$ is a function defined by:

$$H(x) = 1 + 3x^{-2}\cos x - 3x^{-3}\sin x$$

The same link could be stablished between $S_{LL}(r)\{u_M\}$ and $E_M(\kappa)$. The problem of this process is that $\Phi_{ii}(\boldsymbol{\kappa})$ is a function that is not available when performing a measurement and even if available (for example it could be obtained from a model spectrum) the calculation of $S_{LL}(r)\{u_M\}$ is quite complex. In consequence, more simple ways of obtaining this estimate have been researched.

First, the variation of $S_{LL}(r)\{u_M\}$ with r in the case of low-pass errors (hereinafter $S_{LL}(r)_{LPF}$) is roughly described. For such purpose, the simplification of $S_{LL}(r)$ as a cumulative energy of eddies (cf. 5.1.3.1) is used:

$$S_{LL}(r) \sim \sum_{\ell<r} u_\ell^2$$

The velocity of an eddy recovered by PIV is modulated by the normalized response, as a consequence of the low-pass effect behavior. It would be then possible to estimate the measured eddy velocity by: $u_\ell^M \sim NR(\ell; D_I, Th)u_\ell$, where u_ℓ^M is the measured characteristic velocity and $NR(\ell;d_{eq,1D})$ is the equivalent normalized response in 1D. As a consequence, the value of $S_{LL}(r)_{LPF}$ under low-pass effect gives:

$$S_{LL}(r)_{LPF} \sim \sum_{\ell<r} (NR(\ell; D_I, Th)u_\ell)^2 \tag{5.26}$$

As can be appreciated in the graphs of Figure 5.5 the normalized response approaches 1 as ℓ increases. As a result, from some distance $r > r_1$ (for which $NR(r;D_I,Th)\sim 1$) $S_{LL}(r)_{LPF}$ should roughly grow at the same rate than $S_{LL}(r)$ and $\Delta S_{LL}(r)$ (the difference between $S_{LL}(r)\{u_R\}$ and $S_{LL}(r)\{u_M\}$) becomes approximately constant, as mentioned above. The definition of r_1 depends on what is considered as approximately constant. In the results analysis of Chapter 7, the distance r_1 is calculated as the distance for which $\Delta S_{LL}(r)$ reaches a 99% of value it has at very large r. As can be observed in that chapter, this distance is related to the measurement volume characteristic dimensions, and it is in first order of magnitude proportional to $d_{eq,1D}$.

In order to show the low-pass effect, the real value of $S_{LL}(r)$, the measured value under the low-pass effect and the difference between both are sketched below, for an illustrative case:

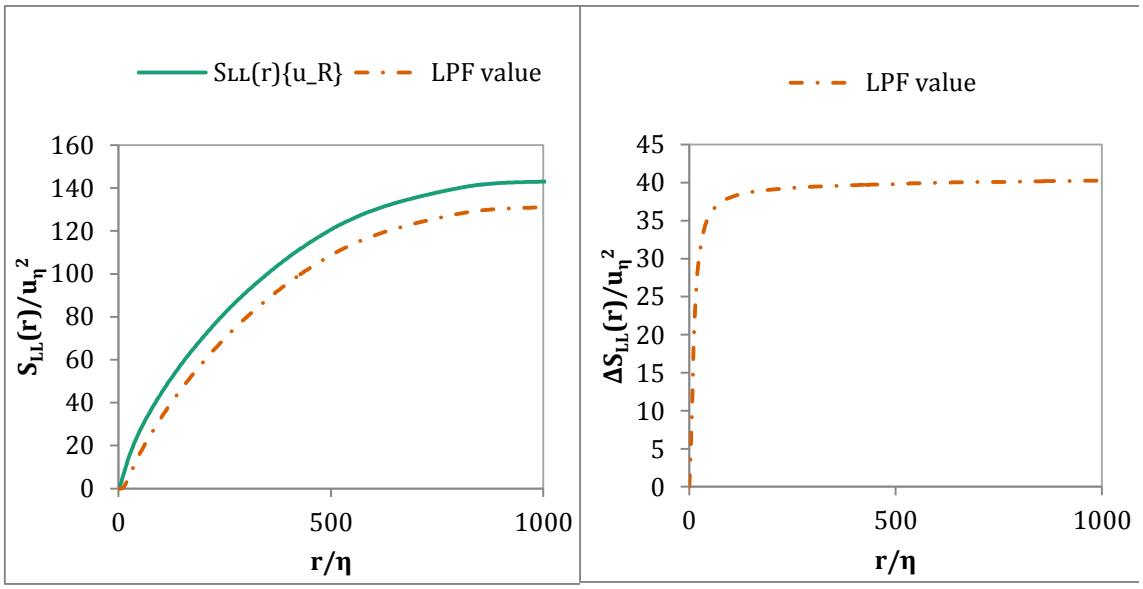

Figure 5.9 Left: Real and measured values of $S_{LL}(r)$, with the measurement response assumed to behave as a low-pass filter. Right: difference between the real and the measured $S_{LL}(r)$. The real value of $S_{LL}(r)$ was obtained from the flow described in 3.1.

The variation of $\Delta S_{LL}(r)$ with r under low-pass errors has not been precisely quantified in this work, as the main purpose of $\Delta S_{LL}(r)$ is to check the coherence of the results in real PIV images and for that the large r values suffice, which are studied below. Nevertheless, the variation with r is modelled as shown below. It has been assumed that $\Delta S_{LL}(r)$ increases with r following a parabola. The parabola starts at $\Delta S_{LL}(r=0)=0$ and it reaches its maximum value at $r=2d_{eq,1D}$, from where it is assumed that the model of $\Delta S_{LL}(r)_{LPF}$ becomes constant. The distance of $r=2d_{eq,1D}$ has been arbitrarily introduced as $\Delta S_{LL}(r)_{LPF}$ presents the bulk of variation in this r range (from 0 to $2d_{eq,1D}$) and it is a convenient fit to the numerical results. It shall be noted that this distance is not r_1, which is calculated as mentioned above. That gives the following model for $\Delta S_{LL}(r)_{LPF}$:

$$\Delta S_{LL}(r)_{LPF} = p\left(\frac{r}{d_{eq,1D}}\right)\Delta S_{LL}(r > r_1)_{LPF}$$

$$p\left(\frac{r}{d_{eq,1D}}\right) = 2\left(\frac{r}{2d_{eq,1D}}\right) - \left(\frac{r}{2d_{eq,1D}}\right)^2;\ \text{for } r < 2d_{eq,1D} \qquad (5.27)$$

$$p\left(\frac{r}{d_{eq,1D}}\right) = 1;\ \text{for } r \geq 2d_{eq,1D}$$

It remains then clarifying the value taken by the function at large r, $\Delta S_{LL}(r> r_1)_{LPF}$. For such purpose, two estimates have been constructed in the course of this work, and both are described below. The first one is based on reasoning over $\Delta S_{LL}(r)$ and the second one is based on the low-pass filtering error value obtained previously. The first approach was the option considered first, but discrepancies to the results of Chapter 7 advised for changing the approach and thus the second approach was developed. The best results have been obtained from the second estimate and that is the one used to compare to the results of Chapter 7. As mentioned above, the value of $\Delta S_{LL}(r)$ for large r is the one used to verify the coherence to the experimental setup results and thus an appropriate estimate is required. Additionally, as was seen in subsection 5.2.1.1, for sufficiently large r, $\Delta S_{LL}(r)$ gives the

error in velocity quadratic quantities, e.g. the TKE. The availability of an estimate can be quite useful then.

The first estimate is obtained following a similar rationale than for the error value. As $\Delta S_{LL}(r)$ gives the error in velocity quadratic quantities (for large r) it is hypothesized that a similar link than the one obtained for the low-pass error value can be established for $\Delta S_{LL}(r>r_1)$, i.e.:

$$\Delta S_{LL}(r > r_1)_{LPF} \approx B_2 S_{LL}\left(r = \overbrace{C_2 d_{eq,1D}}^{d_{\Delta S,1D}}\right)\{u_R\} \tag{5.28}$$

Where B_2 is a constant, $d_{\Delta S,1D}$ is the equivalent 1D size that encompasses the whole 3D interrogation volume filtering effect in $\Delta S_{LL}(r>r_1)$ (as in the previous case) and r_1 is the distance at which $\Delta S_{LL}(r>r_1)$ becomes constant, which is commented below. As can be extracted from expression (5.28) increasing the measurement volume size leads to an increase of $\Delta S_{LL}(r)$.

In this case, a value of the constant and the distance that allow a fair adjustment of the results are:

$$B_2 = 0.31$$

$$C_2 = 1 \Rightarrow d_{\Delta S,1D} = \sqrt{Th^2 + D_I^2} = d_{eq,1D} = 4d_{er,1D}$$

Again, for the calculation of $d_{eq,1D}$ if the interrogation window has no weighting, D_I would have to be multiplied by 4/3, as for the calculation of low-pass error (see the subsection above).

The second estimate starts from the low-pass error estimate obtained in expression (5.25). As was shown in 5.2.1.3, the second order structure function of the error field and of the velocity field are linked by expression (5.22), which is recalled below:

$$\Delta S_{LL}(r)\{u\} = 2C_{u\varepsilon}(r)\sqrt{S_{LL}(r)\{u_R\}S_{LL}(r)\{\varepsilon\}} - S_{LL}(r)\{\varepsilon\}$$

Where $C_{u\varepsilon}(r)$ is the correlation coefficient between the real velocity differences at distance r, $\delta u_R(r)$, and the error field differences at distance r, $\delta\varepsilon(r)$ (see 5.2.1.3 for further details).

As both $S_{LL}(r)\{\varepsilon\}$ and $\Delta S_{LL}(r)\{u\}$ reach constant values for $r>r_1$, the term $2C_{u\varepsilon}(r > r_1)\sqrt{S_{LL}(r > r_1)\{u_R\}}$ has to reach a constant value also. It should be noted that this term is above 0 because of the error field and the velocity field are correlated for the case of low-pass errors, as has been mentioned above. For random errors, this term should be 0 and other errors can have a negative correlation, e.g. group-locking errors (cf. 5.3.6).

The term $2C_{u\varepsilon}(r)\sqrt{S_{LL}(r)\{u_R\}}$ has been adjusted from the results of the PIV Simulator. Roughly, since $\Delta S_{LL}(r)\{u\}$ exhibits the largest variations up to $r\sim 2d_{eq,1D}$ the constant is based on that distance. The final estimation value, based on the results from the PIV Simulator is:

$$\Delta S_{LL}(r > r_1)_{LPF} \approx 2\sqrt{2}C_5\varepsilon_{LPF}\sqrt{S_{LL}(r = 2d_{eq,1D})\{u_R\}} - 2\varepsilon_{LPF}^2 \qquad (5.29)$$

Where C_5=0.67 and $d_{eq,1D}$ is the one defined in the subsection above ($d_{eq,1D}$=$\sqrt{(Th^2+D_I^2)}$) (cf. 5.3.3.2). $S_{LL}(r)\{\varepsilon\}$ has been replaced by its value for large r, i.e.: $S_{LL}(r > r_1)\{\varepsilon\} = 2\varepsilon_{LPF}^2$.

In conclusion, the estimate used for comparison to the results of Chapter 7 is:

$$\Delta S_{LL}(r)_{LPF} \approx p\left(\frac{r}{d_{eq,1D}}\right)\left[2\sqrt{2}C_5\varepsilon_{LPF}\sqrt{S_{LL}(r = 2d_{eq,1D})\{u_R\}} - 2\varepsilon_{LPF}^2\right] \qquad (5.30)$$

Where $p(r/d_{eq,1D}) = 2(r/2d_{eq,1D}) - (r/2d_{eq,1D})^2$ for $r<2d_{eq,1D}$ and $p(r/d_{eq,1D})=1$ for $r>2d_{eq,1D}$.

5.3.4 **Random deviation produced by particles misplacement**

On the previous point (5.3.3), the effect in the measured velocity due to the finite size of the measurement volume has been simplified as the average of the flow velocity inside the measurement volume. This produces a low pass effect. In this point and in the next one, the deviation that can be produced with respect to the measurement volume average is studied, considering only the facts that the correlation is a statistical process and that the velocity has a non-uniform value inside the measurement volume. These deviations are produced without considering the many additional effects of a real PIV measurement, as the light intensity change of particles image pairs, information discretization, background noise and so on, which are studied later. Two deviations from the flow velocity average in the measurement volume have been identified:

- Convergence errors, which are studied here.
- Peak-splitting phenomenon, studied in the next point.

The convergence or mean square error of an estimator is related with the efficiency of that estimator (Bendat and Piersol, 2010). For example, in the case of the sample mean $\tilde{u}$ (defined as $\tilde{u} = (1/N)\sum_i u_i$, where u_i are the samples and N is the samples number) the mean square error of $\tilde{u}$ is given by (Bendat and Piersol, 2010):

$$E[(\tilde{u} - \mu_u)^2] = \frac{\sigma_u^2}{N} \qquad (5.31)$$

Where $E[\cdot]$ is the expected value, μ_u is the real mean value of u and σ_u^2 the variance of u.

In the case of a PIV measurement the estimator is the displacement that maximizes the correlation map value. To simplify the assessment of the deviation, the displacement provided by the correlation is assumed to be the one given by the particles average displacement (i.e. the sample mean). This slightly differs from the previous subsection, where the displacement was supposed to be the flow real average in the sensing domain (cf. 5.3.3, expression (5.24)) which in the expression above would be associated to μ_u. Then, the mean square error of the correlation process with respect to the average in the interrogation volume is considered to be of the order of that provided by (5.31).

For the PIV correlation process modelled in this point by (5.31) σ_u is given by the turbulent fluctuations inside the interrogation volume, estimated below. N is given by the number of particle-image self-correlation peaks contained in the highest correlation peak, which without loss of pairs or peak-splitting is the number of particles in the measurement volume.

The convergence error is illustrated in Figure 5.10. On the figure, three correlation maps obtained from the PIV Simulator (cf. section 3.2) are plotted. The correlation maps are calculated for the same measurement volume and from the same measurement parameters, but changing the position of the particles in the first laser pulse. The number of particles is N=20 and σ_u/D_I~0.01. As can be appreciated on the figure, the maximum correlation value position (indicated by the white filled circle) shifts. This shift is induced simply by the samples taken to calculate the displacement. In the figure, the correlation value provided (in arbitrary units) is obtained from the PIV Simulator by summing the self-correlation peaks that each particle provides. The axes represent the vertical and horizontal displacements normalized by the interrogation window dimension. For all three images, the inverted green filled triangle is the displacement value obtained by the average defined in (5.24) but without time integration. The particles images self-correlation peaks are indicated by the red x-signs.

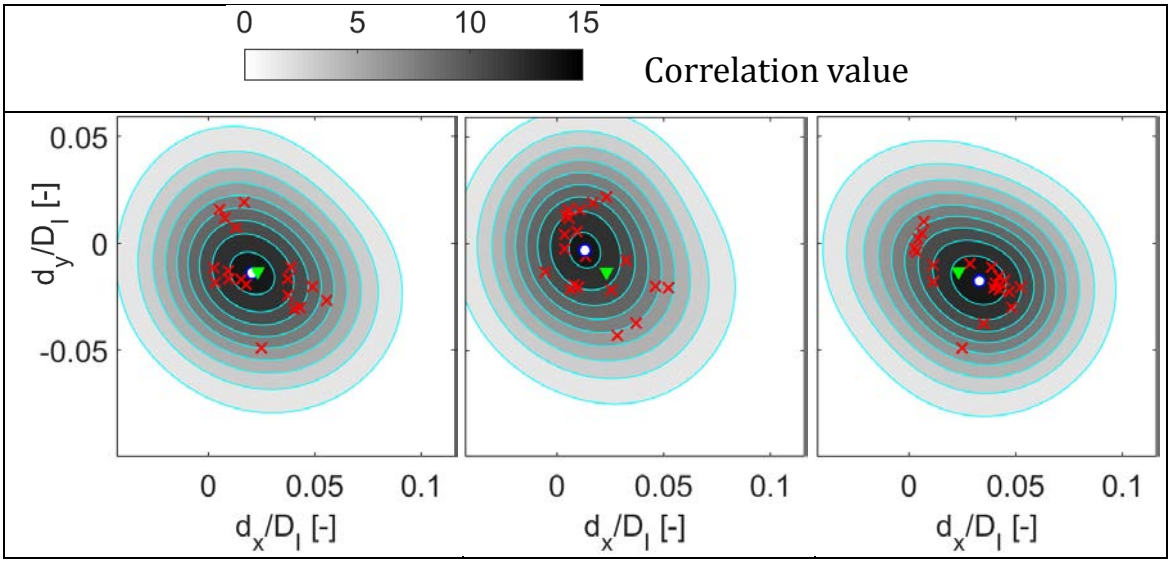

Figure 5.10 Correlation maps obtained for the same interrogation volume at the same time instance but for different initial particles positions.

It is worth to remark that this random deviation is determined by the particles positions in the measurement volume. Due to this fact, the error has been identified as "particles misplacement error". Depending in the particles position, if there is a certain particles agglomeration, those particles should have similar displacements. Then, the displacement value obtained by the correlation normally should be biased to the one of this group of particles, as can be appreciated in Figure 5.10 middle and right images. When particles are more evenly distributed, the different displacements present in the measurement volume appear in the correlation map and the displacement tends to the moving average one, as in the left image of Figure 5.10.

It is worth mentioning that this deviation influences on the maximum correlation peak position on the map. This error will not disappear with a perfect algorithm that managed to recover the real correlation maximum position (which is not the case either, as detailed in the next points, examples can be found in sections 5.3.7 or 5.3.10).

5.3.4.1 *Error estimation*

For estimating the value of this error expression (5.31) can be used. However, the value of σ_u is unknown for a measurement. Instead, the value of the characteristic velocity differences inside the measurement volume, $|\Delta u|$, will be used in this work. The velocity differences, in the case of this PhD, are produced by the turbulence. In this work, an estimate of $|\Delta u|$ can be obtained from the second order longitudinal structure function $S_{LL}(r)\{u\}$. Indeed, the characteristic velocity difference at a distance ℓ is given by $|\Delta u| \approx \sqrt{S_{LL}(r=\ell)\{u_R\}}$ where again $\ell = \max(D_I, Th)$. Therefore the error from this source, $\xi_{\Delta u}$, can be estimated as:

$$\xi_{\Delta u} \sim \frac{|\Delta u|}{\sqrt{N}} \sim \sqrt{\frac{S_{LL}(r = \max(D_I, Th))\{u_R\}}{N}} \tag{5.32}$$

Where N is the number of particles in the interrogation volume.

For estimating a value in any measurement (when $S_{LL}(r)\{u\}$ is not available), the scaling law of eddies in the inertial range is proposed, i.e. $|\Delta u| \sim \sqrt[3]{\epsilon \ell}$, where ϵ is the mean dissipation rate of the turbulent flow and ℓ is the largest dimension in the interrogation volume, as above.

In the figure below the effect of misplacement errors is represented. The black continuous line is the real displacement, obtained from a line of data of the turbulent flow used by the numerical tools (described in 3.1). The continuous green line is the value obtained by performing a moving average of the real displacement, with the size indicated by the green arrow. The effect of misplacement errors is that the measured displacement oscillates around the value given by the low-pass, which has been indicated by the error bars.

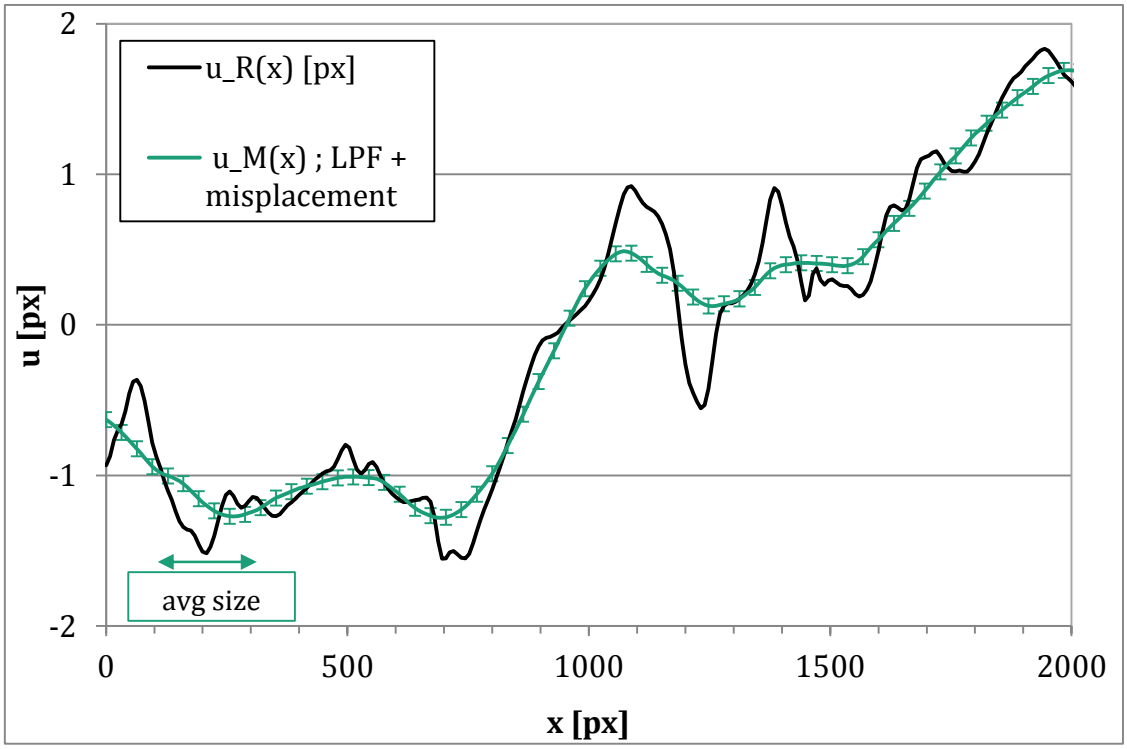

Figure 5.11 Real and measured velocity fields. The measured velocity field is obtained from a combination of low-pass and particles misplacement errors.

In order to estimate the total measurement error from the combination of these two sources the error is decomposed into two parts. On one hand, there is a systematic error induced by the low-pass effect of the average of the flow in the volume, of average error value of ε_{LPF}. On the other hand, there is a random component of the error, given by $\xi_{\Delta u}$. It can be assumed then that the error follows a probability distribution function with average error value ε_{LPF} and with standard deviation $\xi_{\Delta u}$, i.e. $\varepsilon \sim f(\varepsilon_{LPF}, \xi_{\Delta u})$, where f is the probability distribution function of the error. The total average error, ε_T, would be given then by (assuming the two error sources are independent):

$$\varepsilon_T^2 = E[\varepsilon^2] \sim \varepsilon_{LPF}^2 + \xi_{\Delta u}^2 \tag{5.33}$$

5.3.4.2 *Estimation of $S_{LL}(r)\{u\}$*

As in the case of low-pass errors, the two approaches that have been researched to obtain the effect in $S_{LL}(r)\{u_M\}$ are described below. Again, the first approach undertaken is based on reasoning over the velocity field and the second one is obtained starting from the error field. The second approach provides more approximate values and is the one compared against the results of Chapter 7.

The approach based in the velocity field starts from the following measured velocity decomposition:

$$\vec{u}_M = \vec{u}_{LPF} + \vec{u}_\xi \tag{5.34}$$

Where $\vec{u}_M$ is the measured velocity, $\vec{u}_{LPF}$ is the velocity provided by the low-pass effect of (5.24) and $\vec{u}_\xi$ the vector induced by the random deviation under study. The reason to suggest this decomposition is that for all errors described in this point, there should be

particles peak agglomeration on the correlation, associated to the low-pass effect, plus the random error.

Hence, $S_{LL}(r)$ for such measured velocity would be (operating over the first velocity component for simplicity):

$$S_{LL}(r)\{u_M\} = \left\langle \left(u_{1_M}(x + r_1) - u_{1_M}(x) \right)^2 \right\rangle$$

$$S_{LL}(r)\{u_M\} = \left\langle \left(\left(u_{1_{LPF}}(x + r_1) + u_{1_\xi}(x + r_1) \right) - \left(u_{1_{LPF}}(x) + u_{1_\xi}(x) \right) \right)^2 \right\rangle$$

Regrouping the terms above and squaring:

$$S_{LL}(r)\{u_M\} = \left\langle \left(u_{1_{LPF}}(x + r_1) - u_{1_{LPF}}(x) \right)^2 + \left(u_{1_\xi}(x + r_1) - u_{1_\xi}(x) \right)^2 + 2 \left(u_{1_{LPF}}(x + r_1) - u_{1_{LPF}}(x) \right) \left(u_{1_\xi}(x + r_1) - u_{1_\xi}(x) \right) \right\rangle$$

When performing the average for a large number of measurements, the first term would give $S_{LL}(r)_{LPF}$. The second term is considered to be equal to $(\xi_{\Delta u})^2$, the random deviation under study. The third term should cancel when making the average (for random deviations), because the errors should be not correlated. The result is:

$$S_{LL}(r)\{u_M\} \sim S_{LL}(r)_{LPF} + \xi_{\Delta u}^2 \tag{5.35}$$

As to the second approach, it starts from the same link between the error and the velocity structure function. In this case the link is made by recurring to expression (5.20), which is equivalent to the formulation employed for the low-pass case:

$$\Delta S_{LL}(r) = 2\langle \delta u_R(r, \boldsymbol{x}) \delta\varepsilon(r, \boldsymbol{x}) \rangle_{\boldsymbol{x}} - S_{LL}(r)\{\varepsilon\}$$

$\delta\varepsilon(r,\boldsymbol{x})$ is broken into a low-pass component and the random component, as was done above for the velocity field, i.e. $\delta\varepsilon(r,\boldsymbol{x}) = \delta\varepsilon_{LPF}(r,\boldsymbol{x}) + \delta\varepsilon_\xi(r,\boldsymbol{x})$. $\delta\varepsilon_\xi(r,\boldsymbol{x})$ should be of random nature as well, and thus should not correlate with $\delta u_R(r,\boldsymbol{x})$. As a result:

$$\Delta S_{LL}(r) \approx 2\langle \delta u_R(r, \boldsymbol{x}) \delta\varepsilon_{LPF}(r, \boldsymbol{x}) \rangle_{\boldsymbol{x}} - S_{LL}(r)\{\varepsilon\}$$

The expression above can be linked to the previous low-pass error estimation, with the first term in the right given by (for large r values):

$$2\langle \delta u_R(r, \boldsymbol{x}) \delta\varepsilon_{LPF}(r, \boldsymbol{x}) \rangle_{\boldsymbol{x}} = 2\sqrt{2} C_5 \varepsilon_{LPF} \sqrt{S_{LL}\left(r = 2d_{eq,1D}\right)\{u_R\}}$$

Taking into account that for large r, $S_{LL}(r)\{\varepsilon\} \approx 2(\varepsilon_{LPF}^2 + \xi_{\Delta u}^2)$ that gives the following final $\Delta S_{LL}(r)$ (assuming that only the errors associated to low-pass effect vary with r and the random errors are all introduced already at the smallest r)

$$\Delta S_{LL}(r) = \Delta S_{LL}(r)_{LPF} - 2\xi_{\Delta u}^2 \tag{5.36}$$

Where $\Delta S_{LL}(r)_{LPF}$ is the value given by expression (5.30).

The influence on the measured $S_{LL}(r)\{u_M\}$ of these errors is sketched just below:

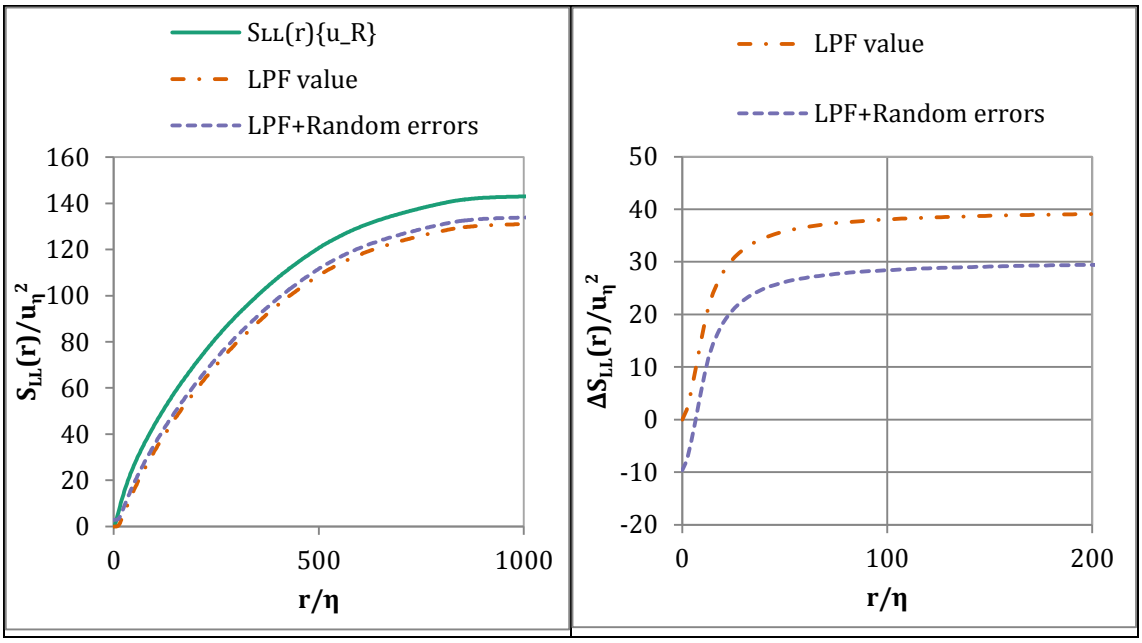

Figure 5.12 Real and measured values of $S_{LL}(r)$. Two measured values are provided: (i) assumed to behave as a low-pass filter and (ii) assumed to behave as a low-pass filter plus random errors, as described in this section. The real value of $S_{LL}(r)$ was obtained from the flow described in 3.1.

5.3.5 **Peak-splitting phenomenon**

For small particle images D_P, large time delays between laser pulses Δt or large local velocity gradients, the correlation maps could contain several correlation peaks (Westerweel 2008, among others). This phenomenon is referred to as peak-splitting. To quantify the probability of occurrence of peak-splitting, the dimensionless displacement difference a/D_P is used, as defined on Westerweel (2008). $a = |\Delta u|\Delta t M_0$, where $|\Delta u|$ is the maximum velocity difference inside the interrogation volume ($|\Delta u| \sim |\partial \boldsymbol{U}/\partial \boldsymbol{x}| \cdot L$, with L the largest dimension in the interrogation volume) and M_0 is the magnification. The characteristic $|\Delta u|$ is calculated as described in the previous point (cf. 5.3.4): $|\Delta u| \approx \sqrt{S_{LL}(r = \max(Th, D_I))\{u_R\}}$. Again, if $S_{LL}(r)\{u\}$ is not available, the characteristic velocity of eddies in the inertial range could be used: $|\Delta u| \approx \sqrt[3]{\epsilon \max(Th, D_I)}$.

In Figure 5.13 the influence of Δt and D_P on a correlation map is illustrated. As can be appreciated from the figure an increase in Δt or a decrease in D_P can lead to peak-splitting. When the correlation map has peak-splitting, the assumption of the displacement being provided by the average of all particles displacements, used in the previous point, is no longer valid. However, the displacement provided by the correlation should resemble the one given by the average of the particles' displacements which self-correlation peaks are under the highest correlation peak. Hereinafter, the displacement peak that achieves the higher correlation value will be referred to as the main correlation peak and the rest of displacement peaks will be referred to as secondary peaks.

In the figure, the axes represent the vertical and horizontal displacements divided by the interrogation window dimension. The white filled circle is the maximum correlation value

and the inverted red filled triangle is the displacement value obtained by a moving average of the displacements in the volume. In the figure, D_I/η = 10.5, Th/η = 25, total number of particles N=20. As can be appreciated in the figure, for low a/D_P values the self-correlation peaks of particles agglomerate into one single peak, a situation for which the displacement provided resembles the low-pass effect of the volume (except for the particles misplacement error).

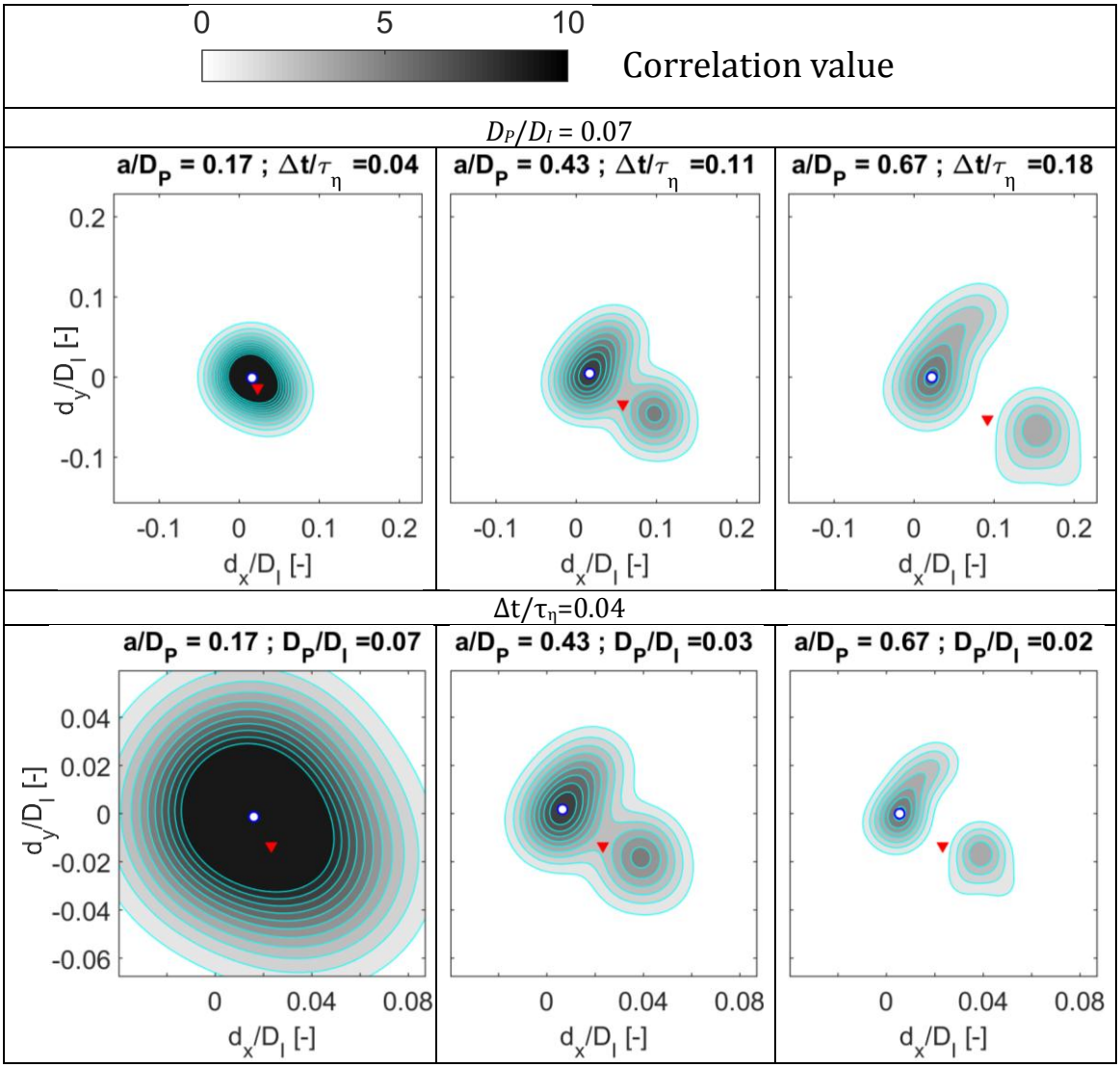

Figure 5.13 Correlation maps obtained for the same interrogation volume at the same time instance. The upper maps are obtained increasing Δt and the bottom maps decreasing the particle image diameter. For all images the correlation value is given above.

In order to clarify when peak-splitting phenomenon starts to appear the phenomenon is studied in 1-D and with just two particles. Each particle produces in the correlation map a self-correlation peak of size d_D=$\sqrt{2}D_P$, where d_D is the distance between the e^{-2} waist points. The 1-D correlation map with two particles is defined as follows:

$$c(d_x) = \exp\left[-\frac{8(d_x - s)^2}{d_D^2}\right] + \exp\left[-\frac{8(d_x + s)^2}{d_D^2}\right]$$

One particle self-correlation peak is placed at $+s$ displacement and the other at $-s$ displacement. The distance between both peaks is then $2s$. Below, the correlation map is

plotted for two different cases, one without peak-splitting (s=0.1pixels) and the other with peak-splitting (s=0.8pixels). The particles diameter is D_P=2pixels, so $d_D \cong$2.8pixels.

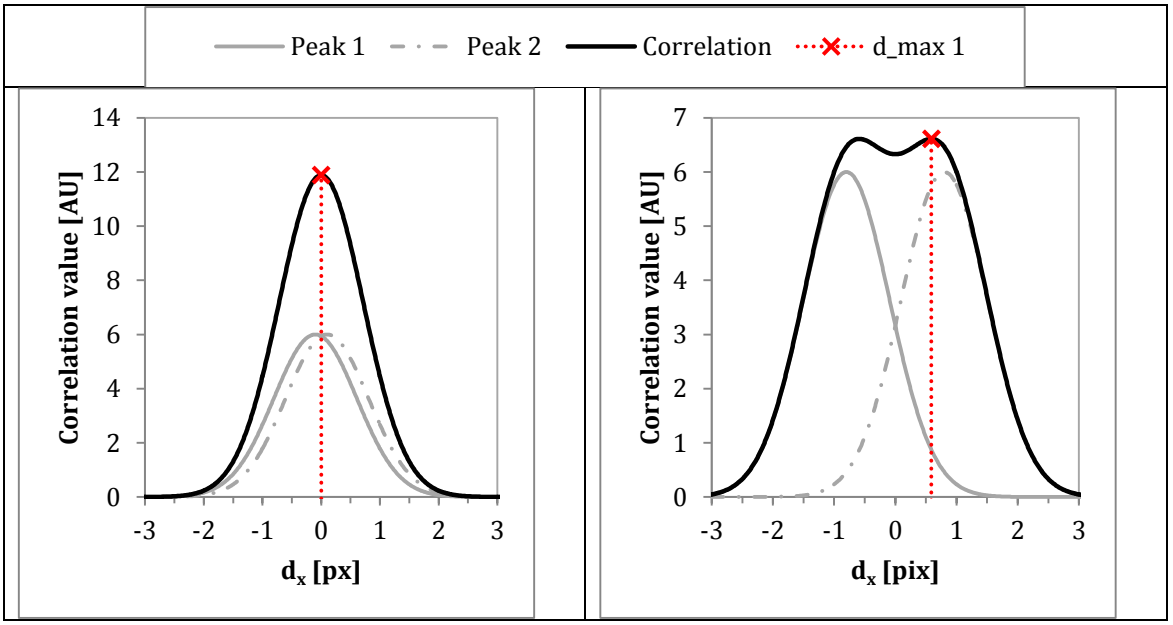

Figure 5.14 1-D correlation maps without and with peak-splitting.

It can be appreciated how at d_x=0 the correlation went from having a local maximum to having two local maxima and a local minimum in between. This latter fact is used to calculate the required distance between the particles to produce separated peaks: for the local maximum, the second derivative of $c(d_x)$ is negative and vice versa. Therefore, at the distance s for which the second derivative changes of sign, that gives the distance for which peak-splitting phenomenon is produced. The second derivative of $c(d_x)$ gives:

$$c''(d_x) = -\frac{16}{d_D^2}\left\{\exp[-8(d_x - s)^2/d_D^2] \cdot \left[1 - \frac{16}{d_D^2}(d_x - s)^2\right] + \exp[-8(d_x + s)^2/d_D^2] \cdot \left[1 - \frac{16}{d_D^2}(d_x + s)^2\right]\right\}$$

Which when evaluated in d_x=0px gives:

$$c''(d_x = 0) = -\frac{16}{d_D^2}\left\{\exp[-8s^2/d_D^2] \cdot \left[2 - \frac{32}{d_D^2}s^2\right]\right\}$$

$c''(d_x = 0)$ is equal to 0 for s=d_D/4. Therefore, the required distance between the self-correlation peaks for peak-splitting phenomenon to appear is 2s=d_D/2. This distance is used below to analyse the number of self-correlation peaks of particles that are actually giving the displacement and estimate the error value.

5.3.5.1 *Estimation of the error value*

The peak-splitting phenomenon is studied here as inducing two different effects: (i) an increased particles misplacement error and (ii) a reduced low-pass effect. Both are detailed below.

Increased particles misplacement error

The particles misplacement error should increase when peak-splitting phenomenon appears. The displacement provided by a measurement volume is that given by the main correlation peak. This peak has contributions of only a certain number of particles and those particles can be placed anywhere in the measurement volume. When there is no peak-splitting (case described in 5.3.4), there can be a skew towards the displacement of the larger particles agglomeration, but that skew was attenuated by the influence of other particles peaks, making the displacement provided to resemble that of the ideal low-pass. When the correlation peaks separate, the contribution of the particles that form secondary correlation peaks diminishes importantly, thereby increasing the particles misplacement error. The particles misplacement error estimation (expression (5.31)) should still be valid for this error, as the displacement given by the main correlation peak should be related to the average displacement of the particles forming that peak. However, the reduction of the number of particles N that contribute to the peak should be accounted for.

In order to estimate the number of self-correlation peaks contained in the main correlation peak, the schematic correlation map of Figure 5.15 is used. In the figure, the position within the correlation map of different self-correlation peaks of particles is plotted by the x-symbols. The largest distance between self-correlation peaks is given by a, for both in-plane directions. In this schematic example, the filled green circle is the one that gives the largest correlation value (the main correlation peak). The green x-symbols are the self-correlation peaks which maxima fall within the main correlation peak and the red x-symbols are those which maxima do not.

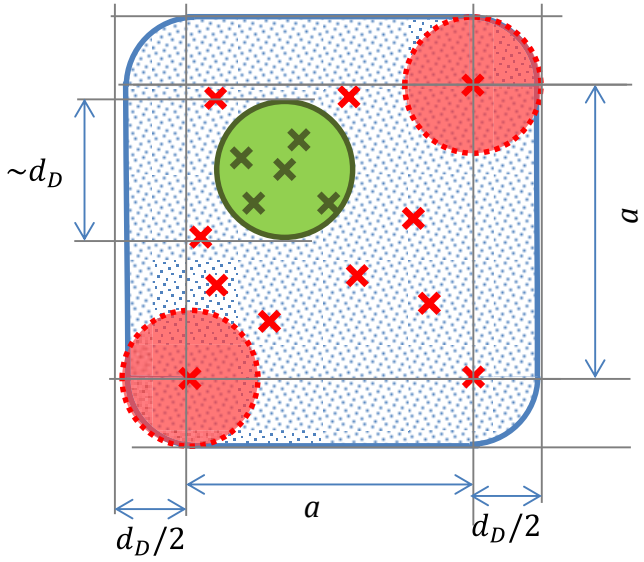

Figure 5.15 Area containing all the correlation displacements information of a measurement volume.

The number of particles required for the error estimation is obtained from the ratio of the areas depicted in Figure 5.15. It is considered that only the particles inside the green circle of diameter $\sim d_D$ contribute to the displacement value obtained (as the self-correlation peaks that are farther than $d_D/2$ from the green circle centre would give a different correlation peak). The rest of self-correlation peaks of particles (taking into account only the area of the self-correlation peaks contained within the e^{-2} waist points) occupy a square with round corners of side $\sim a+d_D$, as the one depicted in the figure above. The four

round corners give a circle of diameter $\sim d_D$. Roughly, this is the size of all the relevant information for the displacement obtained by the PIV correlation. When a=0 a circle of diameter d_D is obtained, as it should be. By dividing the area of the green circle with the total area with relevant information, the following ratio, r_A, is obtained:

$$r_A = \frac{A_{cont}}{A_{tot}} = \frac{\pi d_D^2/4}{a^2 + \frac{4ad_D}{2} + \frac{\pi d_D^2}{4}} = \frac{\pi/2}{\left(\frac{a}{D_P}\right)^2 + 2\sqrt{2}\left(\frac{a}{D_P}\right) + \frac{\pi}{2}} \tag{5.37}$$

Although not related with spatial gradients, the effective number of particles N contributing to the displacement can be further reduced from the following sources already reported in the literature (Keane and Adrian, 1992, among others):

- In-plane loss of pairs, characterized by a factor $F_I \leq 1$.
- Out-of-plane loss of pairs, characterized by a factor $F_O \leq 1$.

As the estimation has been based in the PIV Simulator, the effect of these factors on the estimated peak-splitting errors has not been included, because both F_I and F_O equal 1. In the PIV images, the in-place loss of pairs factor F_I should always have values close to 1, because the images are evaluated by a multi-grid approach with window deformation. The out-of-plane loss of pairs is also typically small (below a 20%, so that F_O>0.8), for the PIV images used in this work to study the peak-splitting errors estimate. Integrating these additional losses of pair into the peak-splitting errors is left for future work.

As a result the number of particles that actually contribute is estimated by: $N_{P,peak} = r_A N$. Therefore, the error due to particles misplacement under peak-splitting becomes:

$$\xi_{\Delta u} \sim \sqrt{\frac{S_{LL}(r = \max(D_I, Th))\{u_R\}}{N_{P,peak}}} \tag{5.38}$$

As in the previous error estimation (cf. 5.3.4.1), $|\Delta u| \sim \sqrt[3]{\epsilon \max(D_I, Th)}$ can be used in the expression above to replace $\sqrt{S_{LL}(r=\max(D_I,Th))\{u_R\}}$ when not available.

Reduced low-pass effect

The second effect is related to the possible benefit of having a correlation map with peak-splitting. This is illustrated in the figure below. In the figure, the cross view of 4 measurement volumes is depicted, for three different time delays, increasing from left to right. On the lowest Δt case, the particles agglomeration induces the low-pass effect from the whole measurement volume. When the time delay increases and peak-splitting phenomenon starts to appear the particles with velocities that differ more from the rest do not contribute anymore, leading to a smaller effective measurement volume contributing to the final displacement value. On the right image the Δt is increased drastically and only a few particles contribute to the final displacement value.

From this point of view, peak-splitting could result in better measurements somehow transforming the PIV averaging measurement in a sort of local "PTV like" measurement. This fact is used on the algorithm proposed by Masullo and Theunissen (2016). For that algorithm, when there is peak-splitting each group of particles is attributed its measured

displacement. However, that is not the case on conventional algorithms. On conventional PIV algorithms, the problem of peak-splitting is the fact that the displacement is always placed at measurement volume center, whereas the particles producing the displacement may not be there. If peak-splitting is beneficial or not can be clarified with the error estimate provided below.

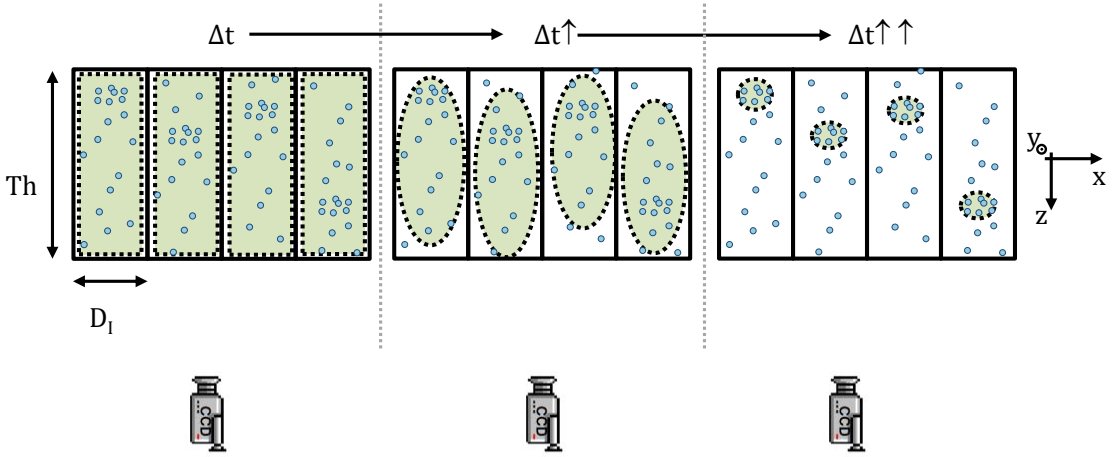

Figure 5.16 Sketch of the cross view (from in-plane direction *x*) of 3 measurement volumes at different time delays. The particles positions (for the first laser pulse) are depicted by a blue circle. The green filled circles are used to mark the particles which self-correlation peaks are under the highest correlation peak.

Indeed, the reduction in the number of particles contributing to the displacement estimated above should result in an equivalent reduction of the measurement volume. As a result, the low-pass error reduces. By recurring to the estimation in (5.25) and assuming that the number of particles reduction is translated directly into an equivalent reduction of the equivalent 1D distance of low-pass, that gives the following low-pass error under peak-splitting:

$$\varepsilon_{LPF} \approx B_1\sqrt{S_{LL}\left(r = r_A C_1 d_{eq,1D}\right)\{u\}} \tag{5.39}$$

In the graph below two measured displacements are plotted illustratively and compared to the real displacement (plotted in black). The green line represents a case with low a/D_P (close to 0); for this case, the effective measurement volume size is large but the error due to particles misplacement is small, which is indicated by the error bars. On the other hand, a case with larger a/D_P (so that peak-splitting is produced) the filtering size reduces due to peak-splitting effect, as indicated by the brown arrow size. However, the particles misplacement error increases, illustrated by the larger error bars.

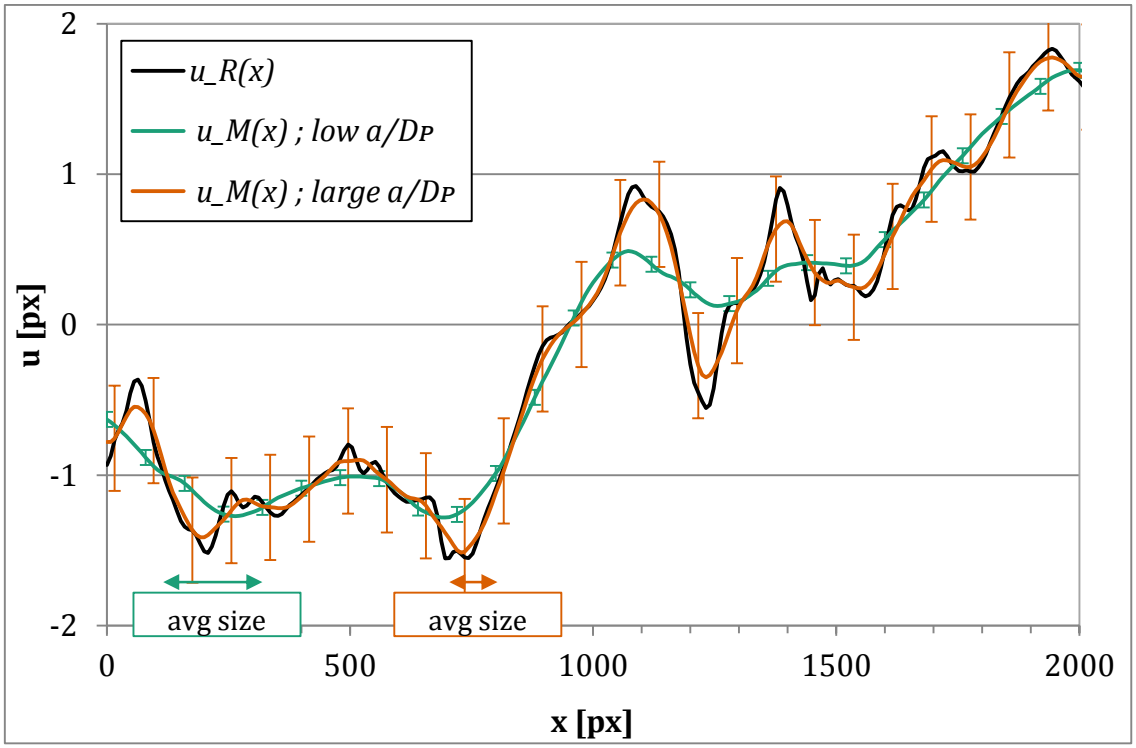

Figure 5.17 Real and measured velocity fields. The measured velocities are plotted as a combination of low-pass and particles misplacement errors, with the difference produced due to the occurrence of peak-splitting phenomenon for large a/D_P.

The total average error value can be obtained from expression (5.33) but with the updated values due to peak-splitting phenomenon of ε_{LPF} and $\xi_{\Delta u}$ provided in this point (expressions (5.39) and (5.38)). The updated total value becomes then:

$$\varepsilon_T^2 \sim 0.35^2 S_{LL}\left(r = 0.25 r_A \sqrt{D_I^2 + Th^2}\right)\{u_R\} + \frac{S_{LL}(r = Th)\{u_R\}}{r_A N} \qquad (5.40)$$

Where N is the number of particles in the interrogation volume and $r_A = \pi/2/\left((a/D_P)^2 + 2\sqrt{2}(a/D_P) + \pi/2\right)$.

5.3.5.2 *Estimation of $S_{LL}(r)\{u\}$*

The two approaches carried out up to this point are also kept here. As mentioned already, only the second one is compared against the results.

For the first approach, the same rationale than for the ensemble of low-pass and particles misplacement errors is used, with the updated LPF value given by the effective measurement volume size and with the additional random error produced by peak-splitting phenomenon. That gives the following expression:

$$\Delta S_{LL}(r)_{PS} \approx p\left(r/\left(r_A d_{eq,1D}\right)\right) 0.31 S_{LL}\left(r = r_A d_{eq,1D}\right)\{u\} - \xi_{\Delta u}^2 \qquad (5.41)$$

Where $p\left(r/r_A d_{eq,1D}\right) = 2\left(r/2r_A d_{eq,1D}\right) - \left(r/2r_A d_{eq,1D}\right)^2$ for $r<2r_A d_{eq,1D}$ and $p(r/d_{eq,1D})=1$ for $r>2r_A d_{eq,1D}$.

Related to the second approach, it was expected that the rationale shown in particles misplacement errors would work also here, which would give the following value for large r:

$$\Delta S_{LL}(r)_{PS} \approx 2\sqrt{2}C_5\varepsilon_{LPF}\sqrt{S_{LL}\left(r=2d_{eq,1D}\right)\{u_R\}} - 2(\varepsilon_{LPF}^2 + \xi_{\Delta u}^2)$$

However, this estimate provided values of $\Delta S_{LL}(r)$ a bit lower than the values obtained with the PIV Simulator. In consequence, it has been adjusted. Taking into account that in the first term of the expression above particles misplacement errors, $\xi_{\Delta u}$, were assumed to not contribute (cf. 5.3.4.2), this term has been slightly modified. The reason to this modification is that the decomposition of the error as a low-pass component, ε_{LPF}, plus a random component, $\xi_{\Delta u}$, is just a simplification. The extent to which that works is limited then. The reality is that, with peak-splitting, the number of particles giving the displacement reduces. That displacement can be more or less correlated with the real velocity in the measurement volume centre. Assuming that only the low-pass error component is correlated with the velocity gives a $\Delta S_{LL}(r)$ value that, compared to the reality of the PIV Simulator, is always below. In that scenario, many possibilities to modify the estimate can be used. Out of the different possibilities, it has been assumed that the term $2\sqrt{2}C_5(S_{LL}(r)\{u\})^{1/2}$ belongs to a more complex function, which incorporates a term related to low-pass effects and another to spatial gradients effects. The following function yields a good fit to the results of the PIV Simulator:

$$f\left(d_{eq,1D}, a/D_P\right) = 2\sqrt{2}\left(C_5\left(S_{LL}\left(r=2d_{eq,1D}\right)\{u_R\}\right)^{1/2} + \sqrt{2}u_\eta\, a/D_P\right) \qquad (5.42)$$

Where C_5=0.67, as defined for low-pass errors.

That gives the following final expression, for the $\Delta S_{LL}(r)_{PS}$ (it is assumed that only the terms related to low-pass errors vary with r and that random errors $\xi_{\Delta u}$ are introduced in $\Delta S_{LL}(r)$ from the beginning, which is what the other estimation provides, see (5.41)):

$$\Delta S_{LL}(r)_{PS} \approx p\left(\frac{r}{r_A d_{eq,1D}}\right)\left[f\left(d_{eq,1D}, a/D_P\right)\varepsilon_{LPF} - 2\varepsilon_{LPF}^2\right] - 2\xi_{\Delta u}^2 \qquad (5.43)$$

Where $p\left(r/r_A d_{eq,1D}\right) = 2\left(r/2r_A d_{eq,1D}\right) - \left(r/2r_A d_{eq,1D}\right)^2$ for $r<2r_A d_{eq,1D}$ and $p(r/d_{eq,1D})$=1 for $r>2r_A d_{eq,1D}$, as for the first approach.

It is worth mentioning that due to the appearance of peak-splitting phenomenon the real value $S_{LL}(r)\{u_R\}$ can be surpassed by the measured value $S_{LL}(r)\{u_M\}$, at small distances r. This is given by both estimations above, from which $\Delta S_{LL}(r)_{PS}$ can become negative. This is produced by a "mixing of information" from different depths in the laser sheet plane. This can be understood in the figure below. On the figure the upper view of a row of interrogation volumes is represented, for a case with large peak-splitting as represented in Figure 5.16-right. The group of particles that gives the displacement (indicated by the green area), can be placed at any out-of-plane position z. As a result the actual characteristic distance between particles could be larger than the distance r at which $S_{LL}(r)\{u_M\}$ is calculated, which gives $S_{LL}(r)\{u_M\} > S_{LL}(r)\{u_R\}$ for very low r distances. For example, for the case illustrated in Figure 5.18, a distance where $S_{LL}(r)\{u_M\}$ can be

calculated is the interrogation window size: $r=D_I$. However, the actual distance at which the particles are is larger. This is observed for some of the test cases of Chapter 7. This was commented already in the conference paper of Nogueira *et al.* (2014), a paper in which the PhD student participated, but the precise reasons that could induce the mixing of information were not clarified.

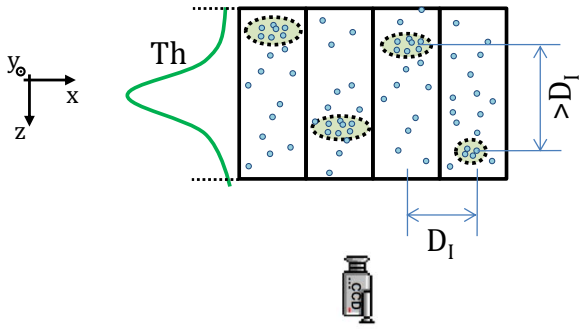

Figure 5.18 Sketch of the cross view (from an in-plane direction) of 4 measurement volumes. The particles positions (for the first laser pulse) are depicted by a blue circle. The green filled circles are used to mark the particles which self-correlation peaks are under the highest correlation peak.

5.3.5.3 *Differentiated effect in the PIV Simulator and in PIV images*

As mentioned in Chapter 3, the PIV Simulator obtains the correlation maps without creating any images. As it turns out, this fact and the PIV process can influence on the final error that can be induced by peak-splitting in PIV images. In particular, the fact that the correlation is discretized and the image deformation could reduce the peak-splitting effect.

Image discretization

The discretization of the correlation map influences in the final displacement value because of the subpixel interpolator employed. When there are split peaks (or a situation close to that one), the displacements between the peaks should have higher correlation values than the rest of displacements. Due to the existence of the higher correlation "plateau" values, the displacement obtained by the subpixel interpolator will be statistically more biased toward the displacements between the peaks than to those outside.

This is illustrated on the Figure 5.19 below, for a one-dimensional case. In the figure two 1-D correlation maps are plotted. On both maps a correlation identified as "PIV Sim" (the one that would correspond to the PIV Simulator) has been plotted, which is the correlation in a continuous domain. From that correlation, the discretized correlation value is obtained by performing an average of the PIV Simulator correlation values inside a pixel. Although a real discretized correlation may not provide that value, the correlation values should be similar and the rationale shown by the graphs should still be valid. The discretized correlation values are represented by the bars. A pixel is supposed to span the whole fractional value of a displacement (i.e. from 0 to 1, from 1 to 2, and so on). Both cases plotted below assume two displacement peaks separated 1.7 pixels and with amplitude of 6 and 3 arbitrary units (AU) (in the PIV Simulator perfect correlation). In the figure, the displacements obtained from the PIV Simulator correlation and from a Gaussian

subpixel interpolator fitted to the three highest discretized correlation values are plotted by the red dotted lines.

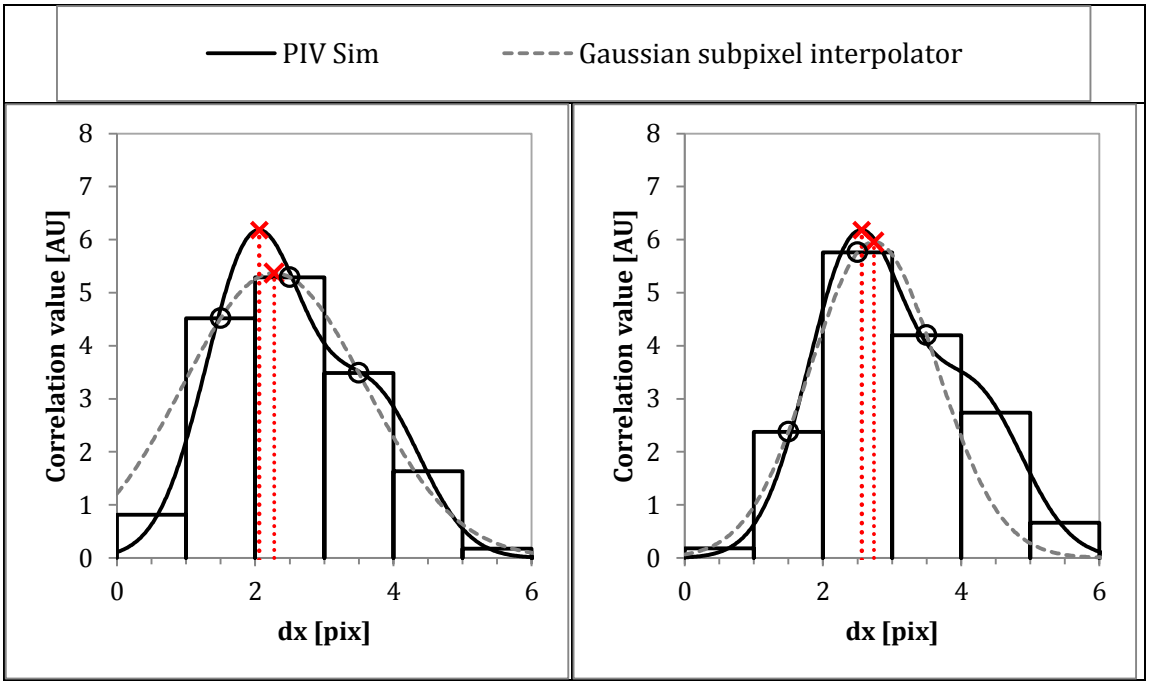

Figure 5.19 Illustration of the effect of the discretization on the displacement value obtained by correlation for two different maximum correlation position values, for a 1-D correlation map obtained from two correlation peaks separated 1.7 pixels.

As can be observed, due to the discretization of the correlation, the tendency of the displacement obtained is to move the measurement toward the low-pass displacement, which should be between both displacement peaks.

It is expected that this effect is of more importance for very small particle diameters ($D_P \rightarrow 0$), as in those cases the peak-splitting can be completely concealed due to the discretization of the correlation map. In consequence, an effective diameter is proposed for the analysis of PIV images, $D_{P,EFF}=\sqrt{(D_P^2+1)}$. This effective diameter is used instead the diameter of the particle images to calculate the parameter a/D_P in the case of the analysis of synthetic images and real images. For the particle image size of approximately 2 pixels in synthetic and real images, a/D_P reduces by a 10% due to this fact, thus reducing peak-splitting effects.

Image deformation

The image deformation is employed by the multi-grid PIV algorithm used in this work to evaluate the PIV images. As described in subsection 5.3.3.1, the displacement provided by the PIV algorithm is obtained iteratively, and the images are deformed with the displacement obtained in the previous iteration. By deforming the images, the effect of some in-plane spatial gradients can be reduced, thereby reducing peak-splitting effects.

In subsection 5.3.3.1, the velocity fields used to deform the images were characterized by equivalent normalized responses, *ENR*. The *ENR* of the last step where image deformation is performed gives then the displacement differences that can be corrected. The value of *ENR* is plotted in the graph below, labelled as ENR_7. For the real images, the last step where image deformation is performed is the step 5, but its equivalent normalized

response is coincident with the ENR_7 of synthetic images. When the images are deformed with the velocity field $V \cdot ENR_7$ the displacements of the wavelengths where ENR_7 approaches 1 are completely removed from the images and thus their effect disappears from the correlation maps. On the other hand, the displacement induced by the wavelengths with ENR_7 =0 is not removed and thus those wavelengths keep their effect in the correlation maps. As can be observed in the graph, for $\ell < 0.37 D_I$ no correction is achieved.

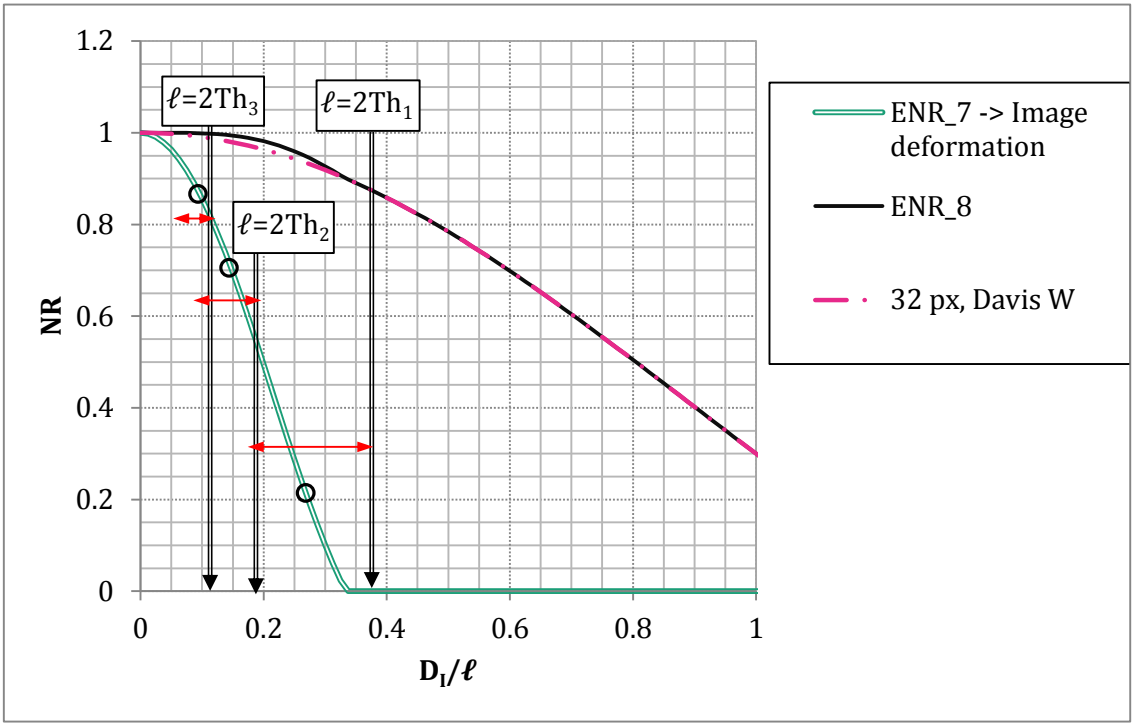

Figure 5.20 Equivalent normalized response that gives the correction achieved by deforming the images.

Up to this point, the displacement differences that can be corrected thanks to the image deformation have been commented. As mentioned already, the displacement differences, a, are given by $\sqrt{(S_{LL}(r=Th)\{u_R\})}$. It was also commented in section 5.1.3.1 that, for any distance r, both larger and smaller eddies can contribute to $S_{LL}(r)\{u_R\}$. In principle, the displacement differences induced by eddies of size $\ell < Th$ cannot be removed by the image deformation. Only the displacement differences induced by eddies with $\ell > Th$ should be removed by the image deformation, by a quantity given by ENR_7. In order to obtain how much of the displacement differences are produced by the large scales and how much by the smaller ones, the following decomposition of $S_{LL}(r)\{u_R\}$ proposed by Davidson (2004) is used:

$$S_{LL}(r)\{u_R\} \approx \frac{4}{3}\left[\int_{\pi/r}^{\infty} E(\kappa)d\kappa + \left(\frac{r}{\pi}\right)^2 \int_0^{\pi/r} \kappa^2 E(\kappa)d\kappa\right] \qquad (5.44)$$

Where $E(\kappa)$ is the energy spectrum function defined in subsection 5.1.1.2.

In the expression above, the first term would be the contribution of the smaller eddies into $S_{LL}(r)\{u_R\}$ and the second term the contribution of the larger eddies. As can be observed in the expression, the large eddies integral goes up to $\kappa = 2\pi/2r$, i.e. the wavelength ℓ that

stablishes the difference between both terms is ℓ=2r. This expression allows obtaining how much the large eddies contribute to $S_{LL}(r)\{u_R\}$, for each of the laser sheet thicknesses. The energy spectrum function used to determine the contribution of the large eddies for each of the laser sheet thickness has been obtained from the model *E(κ)* proposed by Pope (2000):

$$E(\kappa) = C\epsilon^{2/3}\kappa^{-5/3} f_L(\kappa L) f_\eta(\kappa\eta)$$
$$f_L(\kappa L) = \left(\frac{\kappa L}{[(\kappa L)^2 + c_L]^{1/2}}\right)^{5/3+p_0} \quad (5.45)$$
$$f_\eta(\kappa\eta) = \exp\left[-\beta\left((\kappa\eta)^4 + c_\eta^4\right)^{1/4} - c_\eta\right]$$

In addition to the flow parameters η, ϵ and L which for the numerical tools flow are given in 3.1.1 and for the experimental flow in 6.5.3, the following constants are required (from Pope, 2000):

Constant	Value
C	1.5
p_0	2
c_L	6.78
β	5.2
c_η	0.4

That gives that the large eddies contribution to $S_{LL}(r=Th)\{u_R\}$ is:

Table 5.3 Contribution to $S_{LL}(r=Th)\{u_R\}$ of the eddies larger than *Th*.

Th/η	Synthetic images	Experimental images
8.6	71%	70%
17.2	52%	47%
29.5	44%	35%

The only remaining issue is, of all the eddies of larger size than *Th*, which of them produce the most important contribution to $S_{LL}(r=Th)\{u_R\}$. This is provided by the term inside the large eddies integral in expression (5.44); calculating that term it is observed that it is the eddies of size close to ℓ=2r those that produce the most important contribution. In consequence, the reduction of the displacement differences achieved by image deformation should be given by the value of ENR_7 at the wavelengths ℓ slightly larger than twice the corresponding laser sheet thickness, *Th.* In Figure 5.20 the wavelengths equal to twice the three laser sheet thicknesses sizes used in this work have been indicated. A red arrow has been plotted as well, indicating the region of eddies of size twice those ones. A slightly larger or smaller region could be taken but that barely influences the final value. The average value taken by the *ENR* in this region of larger eddies is given in the table below, for the three Th/η values used in this work. The reduction of a/D_P expected due to performing image deformation is also provided in the table, taking into account the *ENR* correction value and the contribution of the large eddies to $S_{LL}(r=Th)\{u_R\}$ given in Table 5.3. The reduction is provided in terms of the ratio of a/D_P with image deformation divided by the value of a/D_P without image deformation.

Table 5.4 Reduction of the displacement differences achieved by the image deformation of the PIV algorithm.

		$(a/D_P)_{W.DEF.}/(a/D_P)_{WO.\ DEF.}$	
Th/η	*ENR* correction	Synthetic images	Experimental images
8.6	0.25	$\sqrt{(1 - 0.71x0.25)} \cong 0.9$	$\sqrt{(1 - 0.70x0.25)} \cong 0.9$
17.2	0.7	$\sqrt{(1 - 0.52x0.7)} \cong 0.8$	$\sqrt{(1 - 0.47x0.7)} \cong 0.8$
29.5	0.9	$\sqrt{(1 - 0.44x0.9)} \cong 0.8$	$\sqrt{(1 - 0.35x0.9)} \cong 0.8$

Both the total average error estimation and the $\Delta S_{LL}(r)$ estimation are calculated from the updated a/D_P values obtained with the ratios above.

5.3.6 **Group-locking**

Group locking is a systematic deviation on the correlation displacement peak location. Since it is a systematic bias, it is studied separated from the random deviations on the peak-location studied previously, produced by particles misplacement within the measurement volume. As mentioned in 5.3.4 and in 5.3.5, the random deviation, $\xi_{\Delta u}$, is produced because the random position of particles in the volume skews somehow the displacement towards those displacements of the largest agglomeration of particles. In the case of "group-locking" error the displacement is biased towards the most frequent displacement in the interrogation volume (Lecuona *et al.* 2004). For group-locking to appear, the presence of a displacement extremum (a maximum or a minimum) in the interrogation volume is required. Moreover, for the error to have a systematic behavior only one extremum (or several of them but contained in a small displacement range) can be given in the interrogation volume.

A question not addressed in the work of Lecuona *et al.* (2004) is if this error can be induced by turbulent structures that change on the out-of-plane dimension. As mentioned, the important aspect for group-locking to be possible, is the presence of just one local displacement extrema inside the interrogation volume. Hence, it should be produced as well by structures that vary in the out-of-plane direction. This error is produced then by sinusoidal-like structures which wavelength λ fulfils $\lambda \sim 2D_I$ or $\lambda \sim 2Th$ (so that the sinusoidal has only one extrema inside the measurement volume). On the other hand, the random deviation $\xi_{\Delta u}$ can be induced by all length-scales.

An example showing group-locking behavior was obtained by Lecuona *et al.* (2004) and is depicted in Figure 5.21. In the figure, the real displacement is plotted as a solid black line and is a 1-D sinusoidal harmonic of wavelength λ=64 pixels. The displacement obtained from synthetic images, for an interrogation window of 32 pixels size, is given by the circle symbols. It can be observed how all PIV displacements are deviated towards that of the extremum contained inside the interrogation spot. For some locations the extremum is a positive maximum and for others the negative minimum. In the figure, the low-pass effect value (without window weighting) is depicted as well as a solid green line, obtained from the normalized response graph given in Figure 5.5 taking $D_I=\ell/2$.

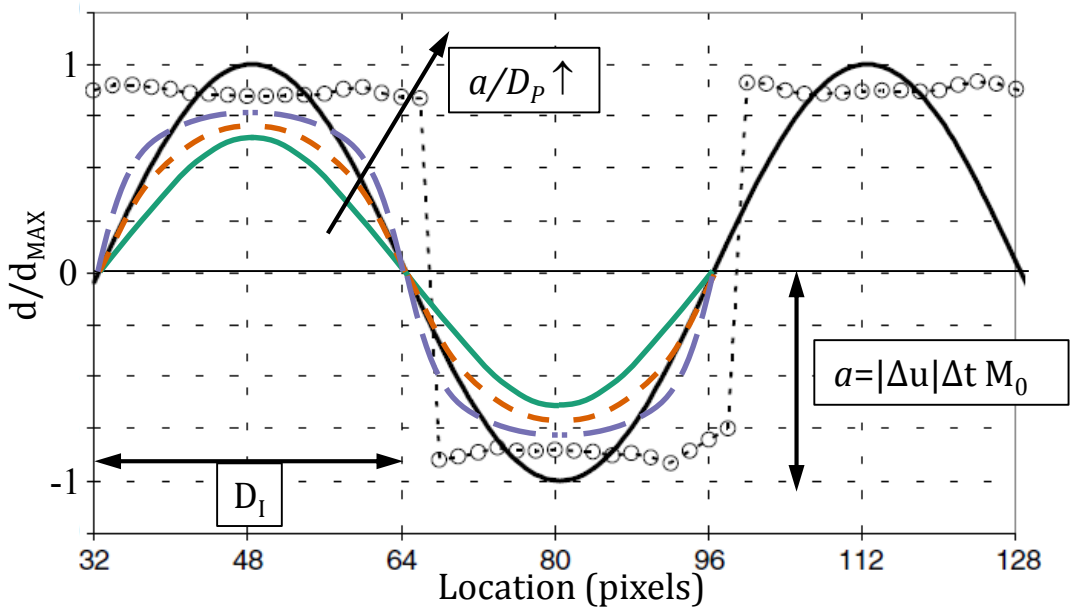

Figure 5.21 Results of conventional PIV processing of a synthetic image containing a 1D single harmonic displacement field. The solid line denotes real displacements, circles stand for results with D_I =32pixels. After Lecuona *et al.* (2004).

For the cases studied on that paper, all results are obtained for a very large a/D_P and the error values and shape observed in Figure 5.21 are not expected: in that work, a/D_P was ~4 whereas in this study the maximum value is ~1.2. Still, group-locking errors could be given in this work although less pronounced effects are foreseeable. The expected effect for varying a/D_P has been roughly sketched over the original figure. If either this error or the random one due to particles misplacement ($\xi_{\Delta u}$) would be produced depends on: (i) the size of the turbulent structures inside a particular interrogation volume and (ii) the number of particles inside an interrogation spot. Related to this second aspect, group-locking systematic behavior requires of a very large number of particles to occur. Indeed, when a lot of particles are present in the interrogation spot the displacement provided becomes independent on the particles' positions and is imposed by the most frequent displacement (as long as there is one). Therefore, the difference between both errors is stablished by the number of particles in the interrogation window. Clarifying when each error is produced exactly is left for future work.

Aside from that, the errors show many similarities: (i) both errors produce a deviation in the correlation displacement peak-position, (ii) both are influenced by the displacement differences inside the interrogation window $a=|\Delta u|\Delta t M_0$ and (iii) peak-splitting phenomenon enhances the value of $\xi_{\Delta u}$ (see 5.3.5) and should increase group-locking errors as well. In consequence, it has been assumed that the group-locking error estimation should be englobed by that provided in 5.3.5.

For the same reasons, it is also considered that the effect in $S_{LL}(r)$ is englobed in the peak-splitting estimation. This assumption is made because group-locking errors should only be produced on some interrogation volumes (those with extrema inside) which likely will not be together. As a consequence, any coherence in the velocity field induced by the systematic behavior should be lost or be almost negligible and the measured $S_{LL}(r)$ should resemble that of a random error. This may not be the case for very small r distances –

smaller than *Th*–, which are not of interest to this work as obviously for those scales the error is quite large anyway. Therefore, the estimation of $S_{LL}(r)_{PS}$ of expression (5.43) is considered to englobe also these errors.

The correlation coefficient between the velocity and the error fields (defined in 5.2.1.3) should allow clarifying how much does each error component (the random particles misplacement and the systematic group-locking) contribute to the final error value. As it turns out, group-locking errors should be correlated with the velocity field, as can be inferred from Figure 5.21. As can be appreciated, the error field changes of sign with respect to the LPF value, for large a/D_P values. With such error topology the correlation coefficient, $C_{u\varepsilon}(r)$ that is calculated from expression (5.21) should become negative. On the other hand, large peak-splitting random errors should give an error field not correlated with the velocity field, i.e. $C_{u\varepsilon}(r)$ should go to zero. In consequence, $C_{u\varepsilon}(r)$ should allow discriminating roughly the contribution of each error.

5.3.7 **Peak-locking systematic error**

Peak-locking identifies the error sources which produce a systematic deviation of the displacement towards integer values. Anti-peak-locking on the other hand is a systematic deviation towards fractional values. The error is originated from the fact that current PIV algorithms provide subpixel information, whereas the images contain the information with a resolution of one pixel. To obtain the subpixel displacement, interpolation or estimations have to be used based on the available information. Any interpolator can induce errors, since the interpolator is based on assumptions of the reality which may not be exactly fulfilled (for example the correlation peak being Gaussian). Those estimates or interpolation schemes can lead to systematic errors, which are identified as peak-locking (PL). Peak-locking errors can be originated from different sources. The following have been identified:

- Loss of information produced by image discretization (Westerweel, 1998).
- The interpolation performed by the subpixel peak fitting algorithm to obtain the displacement (Westerweel, 1998, Nogueira *et al.*, 2001, among others).
- Grey level interpolation to deform the images (Astarita and Cardone, 2005).
- Truncation of particles at the border of the interrogation window (Nogueira *et al.*, 2001). This particular source is greatly reduced by images deformation though.

In consequence, peak-locking error magnitude is influenced by the following factors:

- Particles image size (Westerweel, 1998 and Nogueira *et al.*, 2011, among others).
- The particles displacement (Westerweel, 1998, Astarita and Cardone, 2005, among others).
- The interpolation scheme chosen to deform the images (Astarita and Cardone, 2005).
- Whether only the second image of a pair is deformed (antisymmetric image deformation) or if both are (symmetric image deformation) (Astarita and Cardone, 2005).

- The particles position within the image pixel (Nogueira *et al.*, 2011). This factor influences mostly on the random error induced by peak-locking and is studied in 5.3.8.

Another characteristic of peak-locking and anti-peak-locking is that both are periodic with the displacement (not in space), with a period that could be of one or two pixels. Below, two measurements which have suffered peak-locking errors have been plotted. For the brown line measurement the peak-locking period is of 1 pixel and for the purple line of 2 pixels.

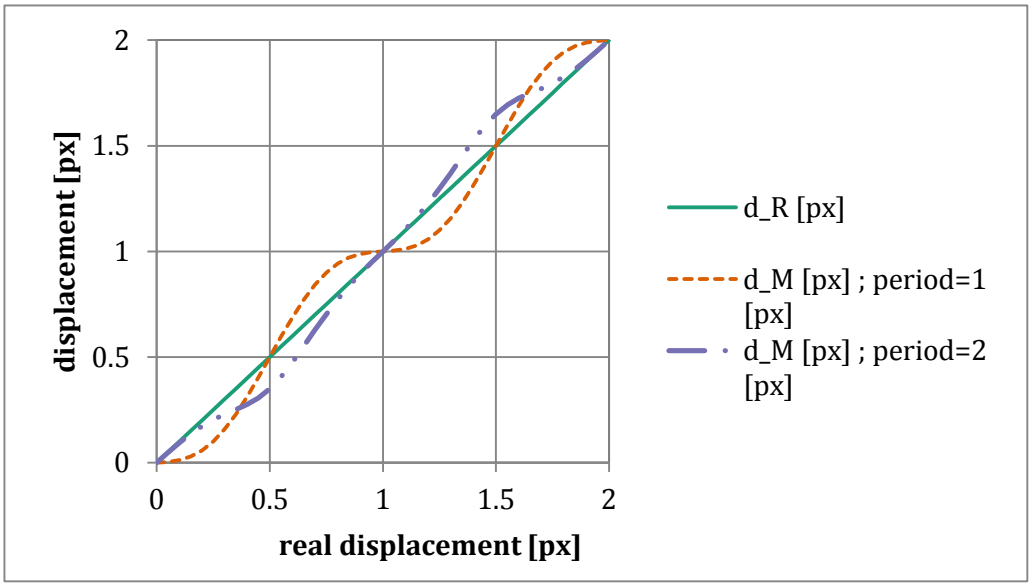

Figure 5.22 Real displacement and measured displacements with peak-locking errors. Two different peak-locking periods are plotted.

The error value and the type depend on a combination of several factors. Therefore, a detailed analysis is out of the scope of the PhD, since the objective error is another. Instead, the order of magnitude of peak-locking errors will be assessed as well as its possible effect on $S_{LL}(r)$.

5.3.7.1 *Peak-locking error estimation for the measurements of the PhD*

For this evaluation, the choices made on Chapter 6 regarding the experimental setup and the PIV processing parameters (which are employed for the results analysis of Chapter 7) need to be used. The choices relevant to peak-locking errors are:

- Symmetric image deformation, following the findings of Wereley (2001).
- Whittaker image deformation (Scarano and Riethmuller, 2000), which is accepted as one of the best deformation methods (Nobach and Bodenschatz, 2009). This is only for the last step on the multi-grid processing, for the rest of them Davis 7.2 uses bilinear interpolation (Lavision, 2007).
- The subpixel position of the maximum correlation value is found using a Gaussian peak-fit. For such purpose, a Gaussian curve is fit over the three adjoining displacements centered on the one with maximum correlation, for each direction. The maximum displacement in each direction is the one that maximizes the value of the Gaussian curve (see 1.1.2.2 for further details).

- Interrogation window weighted with a round function (see 3.3.4.1 where the function is described).
- The particle image diameter has been sought to be at ~2-3 pixels for the experimental setup described in Chapter 6, and it has similar values for the computer tools.

On the study on the effect of image deformation, from Astarita and Cardone (2005), all peak-locking error sources should be included into the characterization. The results from that work are used then to estimate the possible peak-locking error value based on the choices just above. From that work, the peak-locking is estimated to produce a bias error of ~0.05 pixels for bilinear interpolation, 0.04 pixels Whittaker image deformation with 4 points and 0.01 pixels for Whittaker image deformation with 6 points (in Davis 7.2 reference manual, Lavision, 2007, there is no reference to the number of points actually used in the interpolation, so the value for two different numbers is provided). For all interpolation schemes the period is 2 pixels. For the bilinear interpolation and Whittaker with 6 points, the magnitude of the measured displacement is larger than the real displacement: $|d_M|>|d_R|$ on the displacement range -1 to 1 (except for 0 displacement obviously) and then changes of sign. For Whittaker deformation with 4 points $|d_M|<|d_R|$ on the displacement range -1 to 1.

Although in principle the error value seems negligible, the results suggest influence of this error in $S_{LL}(r)\{u_M\}$. Thus, the effect is assessed below.

5.3.7.2 *Effect on the length-scales information*

For the analysis of the effect on $S_{LL}(r)\{u_M\}$, two cases are considered: (i) a generic case for which the displacements span a range larger than the peak-locking period (PL_{period}) and (ii) a particular case where all the displacements are below $PL_{period}/2$. The reason to study the particular case is that peak-locking error changes of sign at $PL_{period}/2$. Restricting the displacements to that range produces errors with the same sign. Additionally, it is a case that is encountered in the real PIV images.

As peak-locking error is related with the capacity of the PIV algorithm to obtain the displacement from the correlation map, it is assumed that peak-locking error is produced on the peak-splitting displacement. For this simplified analysis, it is assumed that displacements are centered around 0 displacement, which is indeed the case of the displacements analyzed in this PhD. Finally, the peak-splitting displacement is assumed to take a sinusoidal shape. Although the displacement given by peak-splitting has a more complex behavior (see Figure 5.17), this assumption is only used to show the influence of peak-locking errors. The rationale should be valid for other displacement shapes.

The problem is studied in 1D, with the peak-splitting displacement given then by:

$$d_{PS}(x) = A \sin\left(\frac{2\pi x}{\ell}\right) \tag{5.46}$$

Where x stands for an in-plane position of the two available in PIV, A is the amplitude of the signal in pixels and ℓ the period of the sinusoid, which is taken to be 256 pixels for both cases.

For this simplified analysis, the peak-locking deviation from the peak-splitting displacement is assumed to be of sinusoidal type as well (as has been done previously for example in Nogueira *et al.*, 2009 or Legrand *et al.*, 2012), which gives:

$$d_{meas}(x) = d_{PS}(x) - \varepsilon_{PL} \sin\left(\frac{2\pi d_{PS}(x)}{PL_{period}}\right) \tag{5.47}$$

where ε_{PL} is the amplitude of the peak-locking bias. For the case of anti-peak-locking, the right term in (5.47) would have a positive sign.

With that estimation, Figure 5.23-left shows the results for the first case (d_{PS}>PL_{period}/2) and Figure 5.23-right for the second (d_{PS}>PL_{period}/2). The period of peak-locking is 1 pixel and the amplitude is 0.15px. The amplitude of the peak-split sinusoidal displacement is 3.25 pixels for the left graph and 0.3px for the right one. An illustrative real displacement has also been plotted, which typically should be above the peak-split displacement due to the influence of low-pass errors.

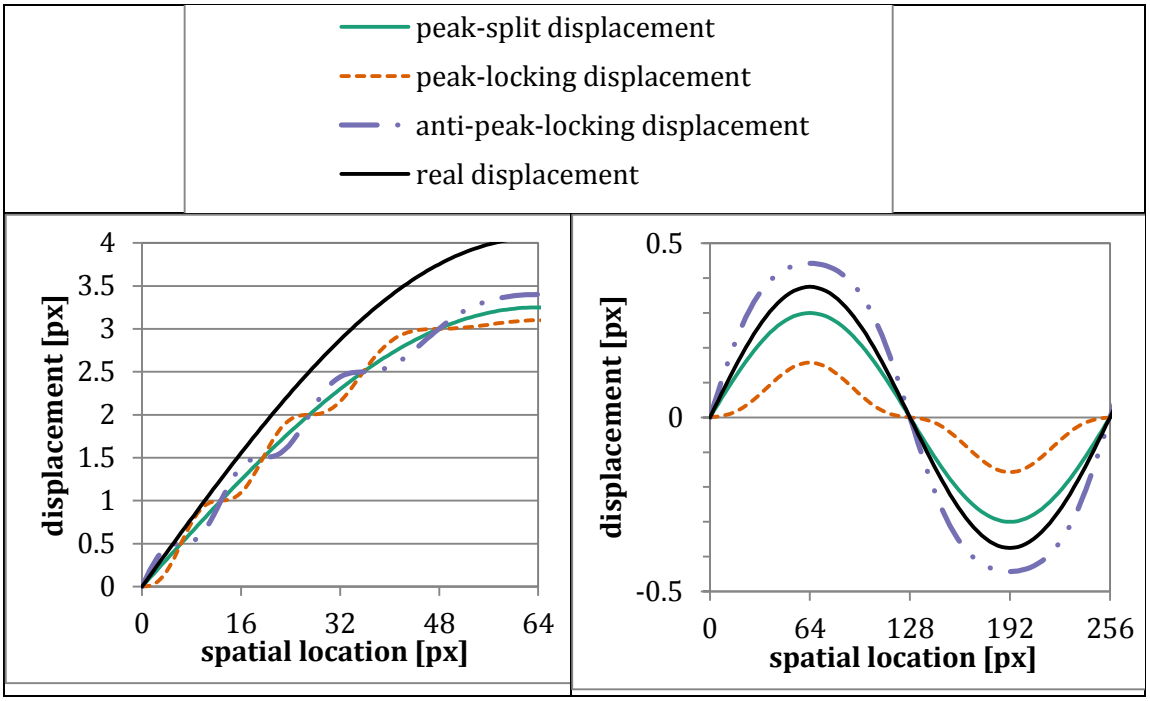

Figure 5.23 Measured displacements with and without peak-locking errors.

For the first case, it can be clearly appreciated that a spurious sinusoidal-like displacement is added to the peak-split displacement. The peak-split displacement, obtained from the combination of low-pass errors and particles misplacement errors, has a coherence with the real displacement, i.e. it reproduces the characteristic frequencies, as commented already in section 5.3.5.2. The same applies to the associated error field, which has an important correlation with the velocity field, as mentioned in 5.3.3.2. This is reflected in the estimation of $\Delta S_{LL}(r)$ obtained for peak-splitting errors, which contains a term associated with the correlation between the error and the real velocity field (see expression (5.41)). The presence of peak-locking errors induces a sinusoidal-like signal of a different frequency that is added to the error field, as can be observed in the figure below. In the figure the errors corresponding to the displacement fields of Figure 5.23-left

are plotted: the peak-splitting error (green continuous line) and the error for the ensemble of peak-splitting and peak-locking errors (broken brown line):

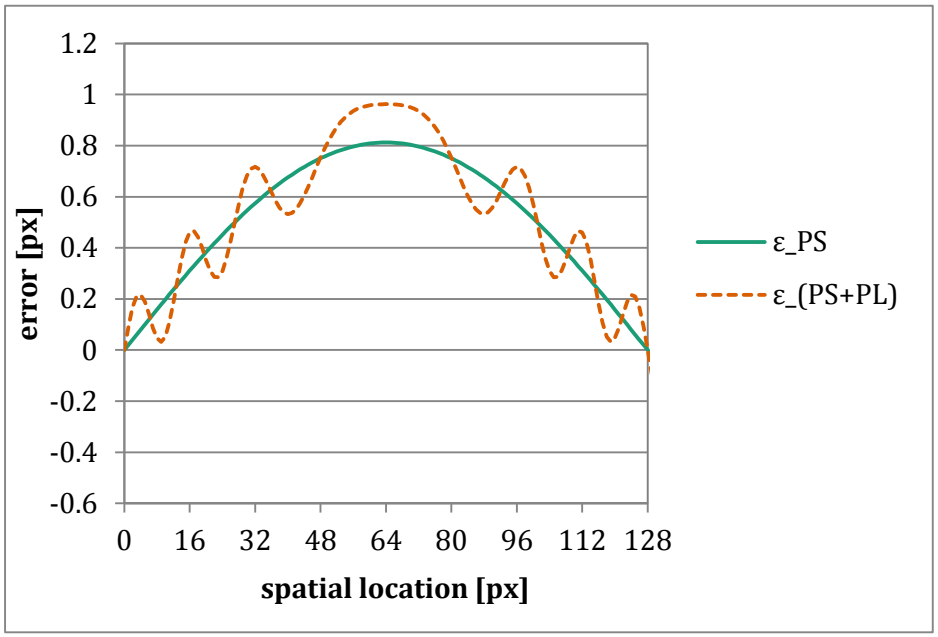

Figure 5.24 Low-pass and peak-locking errors for the case of a displacement much larger than the peak-locking period.

The appearance of the additional sinusoid produced by peak-locking errors makes the correlation between the error field and the velocity field to diminish. The total error value can vary as well; however, as mentioned in 5.3.1, for the errors not given in the PIV Simulator, only an order of magnitude of the effect in $\Delta S_{LL}(r)$ is pursued. In principle, for estimating the effect in $\Delta S_{LL}(r)$ from peak-locking errors the reduction in the correlation between the error and the velocity field is more important than the measurement error modification. Taking that into account, the following rough estimate of the effect is proposed:

Case(i):

$$\Delta S_{LL}(r)_{PL+PS} \sim \Delta S_{LL}(r)_{PS} - \sqrt{8}\left(C_6\left[S_{LL}(r = 2d_{eq,1D})\{u_R\}\right]^{1/2} + \sqrt{2}u_\eta\, a/D_P\right)\varepsilon_{PL} \quad (5.48)$$

Where $\Delta S_{LL}(r)_{PS}$ is the value of $\Delta S_{LL}(r)$ under peak-splitting errors given in expression (5.41), $\Delta S_{LL}(r)_{PL+PS}$ indicates the value of $\Delta S_{LL}(r)$ under both peak-locking and peak-splitting errors and C_6 is a constant. The reduction of the correlation induced by peak-locking has been modelled by introducing the additional term $-\sqrt{8}\left(C_6\left[S_{LL}(r = 2d_{eq,1D})\{u_R\}\right]^{1/2} + \sqrt{2}u_\eta\, a/D_P\right)\varepsilon_{PL}$, which has a similar effect. Constant C_6 has been taken arbitrarily to be half that of low-pass errors, C_6 =0.5C_5 =0.34, and ε_{PL} is considered to be 0.02 pixels, which is in between the different error values estimated in the subsection above. A more refined assessment of the effect of peak-locking errors is out of the scope of this PhD and is left for future work.

On the second case, with all displacements below $PL_{period}/2$ the error has always the same behavior. This is clearly appreciated in Figure 5.23-right. In this case, contrarily to the first

one studied, the correlation between the peak-split error and the velocity should be not affected, in first order of magnitude. However, the error value is clearly changed. For the error estimation it is assumed that the low-pass error (which is the one with systematic behavior) is modified by $\pm\varepsilon_{PL}$, with the positive sign for peak-locking and the negative for anti-peak-locking. By introducing this modification into the low-pass error value of expression (5.41), the following estimation of $\Delta S_{LL}(r)$ is retrieved (only valid on the second case of displacements, i.e. all displacements below $PL_{period}/2$):

Case (ii):

$$\begin{aligned}\Delta S_{LL}(r)_{PL+PS} \sim \Delta S_{LL}(r)_{PS} \\ + \sqrt{8}\left(C_5\left[S_{LL}(r=2d_{eq,1D})\{u_R\}\right]^{1/2} + \sqrt{2}u_\eta\, a/D_P\right)\varepsilon_{PL} \\ - 2(\varepsilon_{PL}^2) - 2\varepsilon_{PL}\varepsilon_{LPF}\end{aligned} \tag{5.49}$$

It is important to note that in the expression above the sign of peak-locking error influences, anti-peak-locking errors should be introduced with a negative sign and peak-locking errors with positive. The test case analyzed in section 7.3 that is in principle influenced by these errors, seems affected by anti-peak-locking errors.

In order to assess over the results analysis which case is given in the results analysis the following parameter is proposed:

- $u'\Delta t M_0/d_r$: turbulent rms fluctuations displacement divided by the pixel size. It gives a global impression of the displacements of the flow. Comparing the parameter to PL_{period} the case that should be expected of the two above can be assessed.

5.3.8 **Random deviation from peak-locking sources**

Nogueira *et al.* (2011) revealed that peak-locking sources can also produce an error of fluctuating nature, as well as the systematic bias error already studied on previous papers (Westerweel, 1998, Nogueira *et al.*, 2001, Astarita and Cardone, 2005, among others) and which is detailed on the previous point (cf. 5.3.7). The mechanism of generation of the error is related as well with the displacement being locked toward an integer pixel displacement value, except that in this case the integer displacement the correlation tends to, may not necessarily be the closest one and depends on the initial position of the particles inside the corresponding pixels, as shown by the authors. The magnitude of the error depends on the particles image diameter, on the number of particles per interrogation window, on the displacement, on the subpixel peak-fitting algorithm and on the fill factor of the CCD sensor. The values obtained for a particular case are in Figure 5.25.

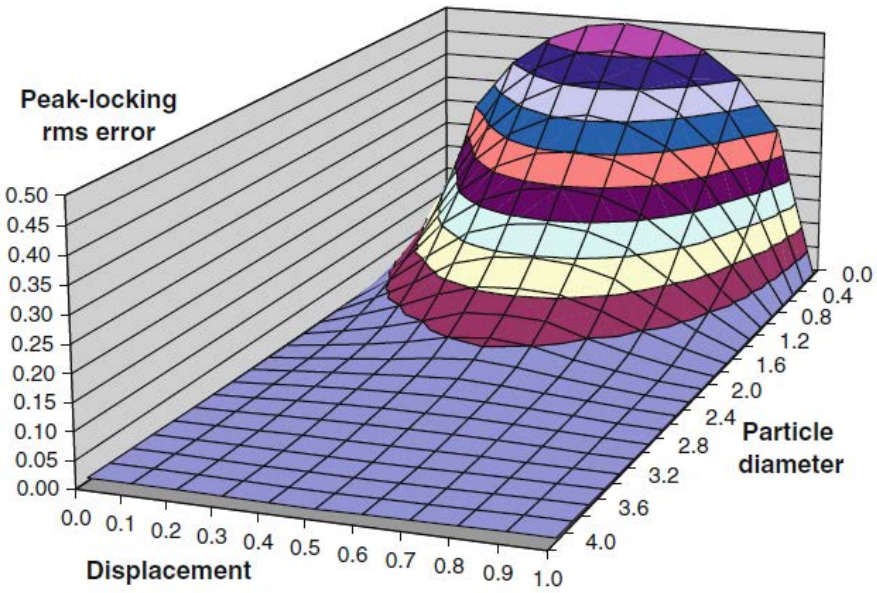

Figure 5.25 rms error for ensembles of 1 particle measurements. Gaussian profile particle, Gaussian peak-fitting, CCD fill ratio = 1. From Nogueira *et al.* (2011).

From Figure 5.25 a typical particle diameter of ~2 pixels gives a random error from this source of ~0.1pixels, for one particle inside the interrogation volume. Increasing the number of particles reduces approximatively this error by $\sqrt{N}$ (where N is the number of particles in the IW). The value of the error in velocity units becomes:

$$\xi_{PL} \sim \frac{0.1}{\sqrt{N}} \frac{d_r}{M_0 \Delta t} \tag{5.50}$$

As it turns out, the value of this error is roughly that of the random error in determining the correlation peak position divided by $\sqrt{N}$ (cf. 5.3.10), and therefore should be much smaller than that one. As a consequence, it is neglected for the rest of the PhD.

5.3.9 Random deviation produced by the light intensity change of particles

When particles that have overlapping images undergo a light intensity change between the two image frames, a random deviation can be produced on the displacement estimation (Nobach and Bodenschatz, 2009). This error depends on the out-of-plane motion, intensity profile of the light sheet, misalignments of the two light pulses and changes of the particle's scattering properties. This is sketched in Figure 5.26 (from Nobach and Bodenshatz, 2009) for an IW with two particles images overlapping. The particles images vary in intensity between the two frames, representative of an out-of-plane motion. However, they do not have an in-plane displacement.

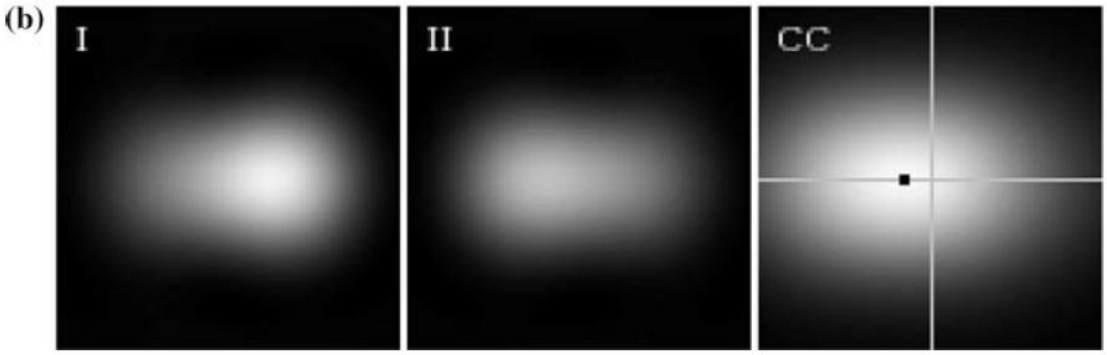

Figure 5.26 Effect of the out-of-plane motion in the correlation map for overlapping particles images. I and II represent the same IW for the first and second laser pulse. CC is the corresponding correlation map. I and II have been obtained by varying the image intensity of the two particles represented, equivalent to an out-of-plane motion. The displacement obtained is represented by the black dot and the grey lines indicate 0 displacement. From Nobach and Bodenshatz (2009).

As can be observed on the correlation map (right image), the displacement obtained is different from 0. This random deviation on the correlation map has been induced by the intensity change on the two particles. It only occurs for overlapping particles, for non-overlapping particles the correlation obtains the correct displacement. The reader is referred to Nobach and Bodenschatz (2009), for further information.

For this simplified study, the following correlation provided in the paper is used:

$$\xi_{\Delta I} = c_1 {D_I}^{c_2} e^{c_3 \Delta z/Th} \tag{5.51}$$

Where $\xi_{\Delta I}$ is the random error produced by the light intensity change (in pixels), D_I is the linear dimension of the interrogation area, Δz is the out of plane displacement and Th is the light sheet thickness. c_1, c_2 and c_3 are constants dependent on the PIV processing method. For Whittaker image deformation, Gaussian intensity laser profile and D_I=32px (which are the parameters found on the results), c_1=0.45, c_2=-1 and c_3=4.8, and the errors obtained are:

Table 5.5 Error produced by the light intensity change of overlapping particles, following Nobach and Bodenschatz (2009), for a Gaussian laser profile.

out of plane $\Delta z/Th$ [%]	$\xi_{\Delta I}$ [pixels]
0	0.01
10	0.02
20	0.04
40	0.10

In velocity units, this random error becomes:

$$\xi_{\Delta I} = c_1 {D_I}^{c_2} e^{\frac{c_3 \Delta z}{Th}} \frac{d_r}{M_0 \Delta t} \tag{5.52}$$

The error depends on the out-of-plane motion, which for the case of turbulent flows varies through the different interrogation windows, given the fluctuations of turbulent flows. The error produced on each interrogation window cannot be assessed since the specific out-of-plane rate of an IW will be unknown. Instead, in order to characterize this error the parameter $u'\Delta t/Th$ is proposed, based on the rms velocity fluctuations of the flow under

study. The parameter should give an overall estimation of the out-of-plane motion rate. In the case of the isotropic flows that this PhD deals with, u' can be estimated from the in-plane measurements of velocity, from which Δz can be calculated as $u'\Delta t$.

Finally, in order to estimate the effect in $\Delta S_{LL}(r)$ of these random errors, it is assumed that these errors are added to peak-splitting errors (as those are the ones obtained for a perfect correlation) but are independent of them. In consequence, the effect of these errors in the $\Delta S_{LL}(r)$ of peak-splitting (expression (5.43)) is as an additional error term but without influencing in the term associated with the error correlation with the velocity field. The same was obtained for particles misplacement errors of section 5.3.4.2. The following estimation is obtained then:

$$\left(\Delta S_{LL}(r)\right)_{\Delta I+PS} \sim \Delta S_{LL}(r)_{PS} - 2\xi_{\Delta I}^2$$
$$\left(\Delta S_{LL}(r)\right)_{\Delta I+PS} \sim \Delta S_{LL}(r)_{PS} - 2\left(c_1 {D_I}^{c_2} e^{\frac{c_3 u'\Delta t}{Th}} \frac{d_r}{M_0 \Delta t}\right)^2 \qquad (5.53)$$

As can be understood from the estimation above, the effect of these errors can become important for large $u'\Delta t/Th$. As in principle this random error influences from the lowest r values, it is for those scales where it should have the largest relative effect. For r distances of the order of Kolmogorov scale, $r\sim\eta$, $S_{LL}(r)\{u_M\}\sim(u_\eta)^2$. Hence, the displacement induced by Kolmogorov velocity, $u_\eta \Delta t M_0/d_r$, allows assessing the possible relative importance of these errors. A much larger value of u_η in pixels than $\xi_{\Delta I}$ should be associated to a reduced importance of these errors, and vice versa.

With the estimation provided in expression (5.53) it has been calculated that these errors should have in principle a negligible effect both in the synthetic images and in the real images studied in this work. For the cases of synthetic images for which $\Delta S_{LL}(r)$ is calculated, the largest $u'\Delta t/Th$ value encountered is of ~10%, which induces a $\xi_{\Delta I}\sim0.02$ pixels; the largest variation with respect to $\Delta S_{LL}(r)_{PS}$ is of $0.01(u_\eta)^2$. For the real images the largest $u'\Delta t/Th$ value encountered is of ~5% but there is an offset between the laser sheets of 0.2mm (cf. 6.3.1). This offset represents a maximum of an 18% compared to the laser sheets used. Considering an $u'\Delta t/Th\sim23\%$, the maximum error in pixels from this source is ~0.04pixels and the maximum variation with respect to $\Delta S_{LL}(r)_{PS}$ of $\sim0.1(u_\eta)^2$. As can be observed in sections 7.2 and 7.3 these variations are negligible with respect to the values actually encountered and thus this error is not analyzed further.

5.3.10 **Random errors in determining the correlation peak-location**

This random deviation is related with the ability of the PIV algorithm to retrieve the maximum correlation position (studied in Adrian - 1991, Westerweel - 1998, among others) from the discretized correlation maps. The following sources are studied together in this point: particles that do not have a perfectly Gaussian shape, the background sensor noise and cross-talk between different particles on the correlation map. As a result of those issues, the interpolator that determines the maximum correlation position can provide a position that is deviated randomly from the real maximum position. As was mentioned already, the interpolator used in this work is a 3-point Gaussian peak fit. This has been sketched in the image below. On the right image, the discretized correlation

values have been modified with respect to the value they should have (those in the left image), which makes the subpixel interpolator find an incorrect correlation maximum.

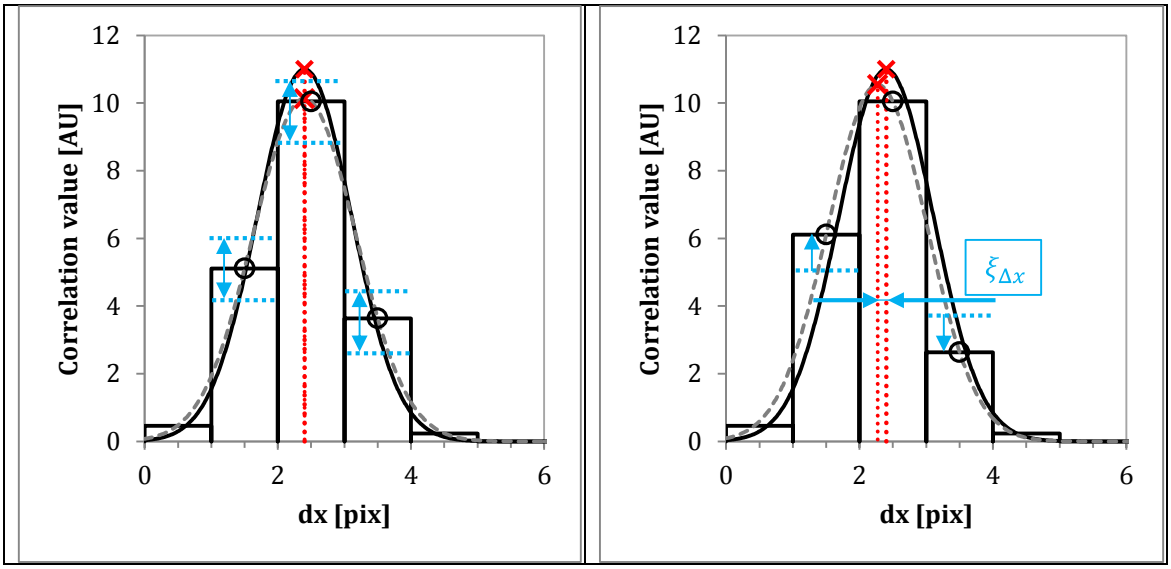

Figure 5.27 Sketch of the random errors in determining the correlation peak-location. Left image: case where the correlation values given at each pixel have deviated from its correct value; right image: case where the correlation values given at each pixel have deviated from its correct value.

This error is usually estimated as (Westerweel - 1998, Westerweel - 2008, among others):

$$\xi_{\Delta x} \sim c \cdot d_D \tag{5.54}$$

Where $\xi_{\Delta x}$ is the random deviation on the displacement calculation produced by the correlation peak-width, c is a constant and d_D is the diameter of the correlation map main displacement peak. The constant c is around 0.05, and depends on the signal-to-noise ratio (SNR) of the photographs (it is inversely proportional to it), on the number of particles, on spatial gradients and on the processing algorithm (Westerweel, 2000, Westerweel, 2008, among others). d_D is related to the particle image size, for uniform particle image sizes and without gradients, $d_D = \sqrt{2} D_P$. The values of $\xi_{\Delta x}$ found in the literature vary between 0.01 pixels and 0.1 pixels due to the many factors that influence on the error value.

The error expressed in terms of velocity units would be:

$$\xi_{\Delta x} \sim c \cdot d_D \frac{d_r}{\Delta t M_0} \tag{5.55}$$

Additionally, the correlation peak-width d_D could broaden when under spatial gradients, which would imply an increase of this error source. Westerweel (2008) derived an expression on the peak-width increase for two simple gradient cases. The first case is that of a simple shear gradient, with the displacement defined as:

$$\Delta X(y) = \Delta X_0 + \frac{a}{D_I}(y - Y_0)$$

Where $\Delta X(y)$ is the displacement, ΔX_0 is the uniform displacement of the particles, y is the in-plane direction perpendicular to the displacement and Y_0 and arbitrary in-plane

position. Under this displacement, the correlation peak-width (d_D) becomes (Westerweel, 2008):

$$d_D \cong \sqrt{2D_P^2 + \frac{4}{3}a^2} \tag{5.56}$$

The other case reported is that of uniaxial strain, for which the displacement is defined as:

$$\Delta X(x) = \Delta X_0 + \frac{a}{D_I}(x - X_0)$$

Where x is the position parallel to the main displacement, ΔX_0 the mean displacement, $\Delta X(x)$ the actual displacement and X_0 an arbitrary position. In this case d_D becomes (Westerweel, 2008)[4]:

$$d_D \cong \sqrt{2D_P^2 + \frac{1}{12}\left[\frac{a/D_I}{1 + a/D_I}\left(1 - \frac{\Delta X_0}{D_I} + \frac{1}{2}\frac{a}{D_I}\right)\right]^2} \tag{5.57}$$

As it turns out, the peak-width increase is larger in the case of the simple shear gradient. In order to estimate the order of magnitude of the effect of these errors in the measured $S_{LL}(r)\{u\}$, an characteristic error due to this source of 0.05pixels is assumed (for a/D_P=0), which is in the middle of the values found in the literature. From that value, the peak-width increase due to spatial gradients is supposed to be that given by expression (5.56). Finally, taking into account that the error is of random nature and then should produce a similar effect than the one shown in 5.3.9, that gives the following effect in $\Delta S_{LL}(r)$:

$$\Delta S_{LL}(r)_{\Delta x+PS} \sim \Delta S_{LL}(r)_{PS} - 2\left(\frac{0.05px}{\widehat{cd_D(a=0)}}\sqrt{1 + \frac{2}{3}\left(\frac{a}{D_P}\right)^2}\frac{d_r}{M_0 \Delta t}\right)^2 \tag{5.58}$$

As can be understood from the expression above, this error can induce an important effect in $S_{LL}(r)\{u_M\}$ for low Δt values. As for other random errors, this random error influences from the lowest r values, it is for those scales where it should have the largest relative effect. Again, $u_\eta \Delta t M_0/d_r$ can be used to obtain the relative possible importance of these errors: a large value of u_η in pixels should allow reducing the importance of these errors, and vice versa.

5.3.11 **Spatial gradients biases**

In addition to the effect already mentioned of increasing the correlation peak-width (with an associated increase in the random error) and of inducing deviations in the correlation peak location (from particles misplacement errors, group locking and peak-split cf. 5.3.4, 5.3.5 and 5.3.6), spatial-gradients can increase the bias that can appear in PIV due to in-plane loss of particle pairs (Westerweel, 1997, or Westerweel, 2008, among others).

[4] It shall be noted that the term between brackets in the expression has no dimension, whereas D_P has units of size, so there could be an error on the expression.

The in-plane loss of particles induces a bias towards smaller displacements. The bias is induced because larger displacements can induce more particles to get in and out of the IW, which as a result skews the displacement towards lower values. This has been sketched in Figure 5.28, where on the left image with low displacement, the in-plane loss of pairs is minimum and thus almost all particles have a matching pair and cross-talk peaks should have little influence. On the other case a lot of particles do not have a matching pair, due to the large displacement. Additionally, for those particles without matching pair there are many particles on the opposite direction of the real displacement that will induce cross-talk peaks in this opposite direction. As a result of both the peak degradation and cross-talk, the displacement is skewed towards lower displacements. Additionally, this bias is increased due to the peak-width increase produced by spatial gradients explained above (cf. 5.3.10).

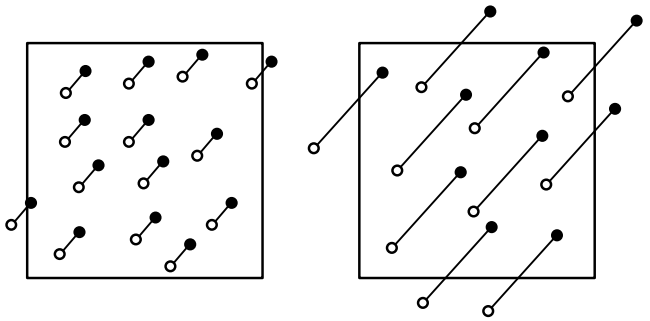

Figure 5.28 Illustration of why larger in-plane displacements can be more skewed towards null displacements. The particles not filled are the particles on the first frame, and the filled particles on the second frame of the image. The line joining them is the displacement.

The same two gradient types than in the random error in determining the peak location above (uniaxial strain and simple shear) are studied as bias sources in Westerweel (2008). Since both gradient types can be produced by a turbulent flow, an estimate is provided next based on the results of Westerweel (2008). As compared to the previous errors related with gradients (group-locking, cf. 5.3.6 and particles misplacement errors, cf. 5.3.4 and 5.3.5), the gradients studied on that work can only be produced by scales $\ell \gg D_I$ and $\ell \gg Th$. Otherwise, the other error sources are more likely to occur.

The uniaxial strain bias should be greatly reduced from the values provided on Westerweel (2008) when using a multi-grid approach with window image deformation, so that bias is neglected here. The simple shear bias cannot be removed when shear is in the out-of-plane direction; the variation of this error with the displacement difference a and the particle image diameter is plotted on graph below:

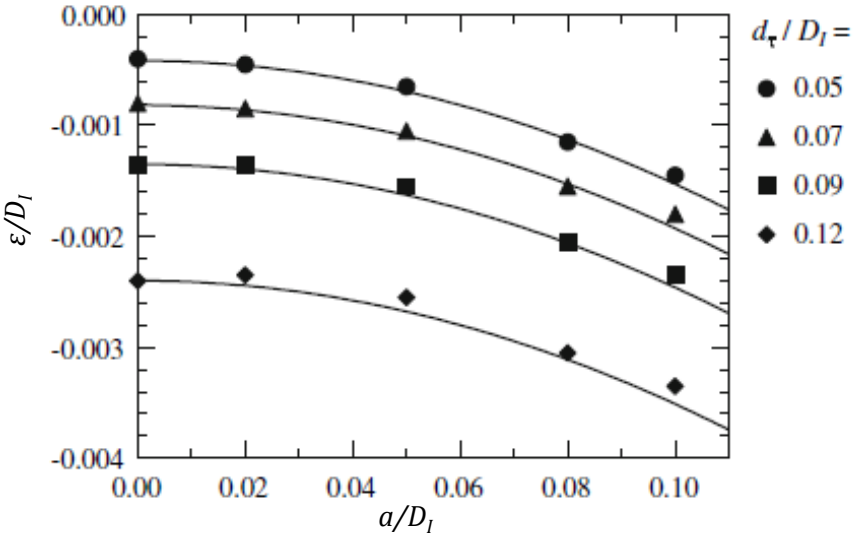

Figure 5.29 The displacement bias ε relative to D_I as a function of the local variation of the displacement a for a uniform simple shear plus a uniform translation of $\Delta X_0=0.25D_I$, for different values of d_τ/D_I (d_τ is the particle image diameter). From Westerweel (2008).

From the graph, and considering the maximum values that are found in this work of the displacement difference a (taking into account the parameters of the measurements of D_P~2pixels and D_I=32pixels):

- a/D_P is below 1.5.
- a/D_I is below 0.1.
- D_P/D_I is around 0.06.

That gives that the bias maximum value, for the parameters that will be used on this PhD would be: ε/D_I~-0.002, which produces a bias of -0.06pixels. As can be noticed on the graphs of Figure 5.29 the bias increase is the same for all d_τ/D_I values, it only depends on a/D_I. The bias value at a/D_I=0 is produced by the in-plane loss of correlation and is removed by a window offset. Window offset is inherent to multigrid technique employed on the results analysis of this PhD and thus the bias at a/D_I=0 should be removed. When the bias at a/D_I=0 is removed, the maximum bias produced by the shear goes to -0.03pixels. This bias is quite small and therefore can be neglected compared to other errors (for example the random error in determining the correlation peak location can reach 0.1pixels, cf. 5.3.10).

5.3.12 **Error generated by outlier occurrence**

Different factors can reduce the number of particles contributing to the highest correlation peak (e.g. in-plane and out-of-plane loss of pairs, peak-splitting) and that translates as well in a reduced maximum correlation value. This can be appreciated in Figure 5.13 in the case of peak-splitting. When that happens, a random peak produced by the interaction of noise with PIV particles or by cross-talk between different particles could give the maximum correlation value and be selected erroneously as the measured displacement. Such displacement is referred to as an outlier vector and the difference to the previous errors studied is that the displacement given by this vector is not a particles displacement.

The estimation of the effect in $S_{LL}(r)$ is calculated below:

$$S_{LL}(r)_{OUT} = \left\langle \left(u_{1_M}(x + r_1) - u_{1_M}(x) \right)^2 \right\rangle$$

In order to estimate $S_{LL}(r)_{OUT}$, a typical magnitude of outlier vectors of u_{out} and a proportion of p_{out} of outliers remaining on the vector fields are used. The average in the expression just above is calculated from the measurements at the different time instances and positions available. At each position and time instance, one of the following possibilities will occur: (i) $u_{1_M}(x)$ is an outlier (probability of p_{out}), (ii) $u_{1_M}(x + r_1)$ is an outlier (probability of p_{out}), (iii) both $u_{1_M}(x)$ and $u_{1_M}(x + r_1)$ are outliers (probability of p_{out}^2) or (iv) that neither of them is an outlier (probability of $1 - 2p_{out} - p_{out}^2$).

The average can be obtained as follows: all cases (iv) averaged should add to $S_{LL}(r)_{OUT}$ the quantity $(1 - 2p_{out} - p_{out}^2)S_{LL}(r)_M$, where $S_{LL}(r)_M$ is the measured value of the function, if there are not outliers (i.e. incorporating all the rest of errors). On first order of magnitude both $2p_{out}$ and p_{out}^2 are much smaller than 1 and are considered negligible, giving that all (iv) cases average to $\sim S_{LL}(r)_M$. It is assumed also that when an outlier occurs $u_{1_M} \ll u_{out}$ and therefore, for cases (i) and (ii) $\left(u_{1_M} - u_{out}\right)^2 \sim u_{out}^2$. Cases (i) and (ii) contribute then to $S_{LL}(r)_{OUT}$ with $2p_{out}(u_{out})^2$. Case (iii) is considered negligible compared to the sum of (i) and (ii) because it occurs in much smaller probability ($p_{out}^2 \ll 2p_{out}$). Adding the four terms finally gives:

$$S_{LL}(r)_{OUT} \sim S_{LL}(r)_M + 2p_{out}(u_{out})^2 \tag{5.59}$$

As a result, the modification induced in the measured $S_{LL}(r)\{u\}$ due to occurrence of outliers would be:

$$\Delta S_{LL}(r)_{OUT} \sim -2p_{out}(u_{out})^2 \tag{5.60}$$

In order to assess the importance of this error a rough estimate of the proportion of outliers is provided below. Both synthetic images and real images have been validated with two criteria, an allowable vector range (method 1) and a median filter (method 2), which details can be found in 3.3.4. In Chapter 7, the values of $S_{LL}(r)$ that are plotted are obtained from the vectors that pass the first validation criterion. The proportion of undetected outliers for those results has been calculated in two different ways:

1) p_{out} equal to the number of the detected outliers by the first method, i.e. p_{out}=1-$p_{valid,1.}$
2) By comparing the proportion of outliers detected by different validation methods. Then, p_{out}=$p_{valid,1}$ - $p_{valid,2.}$

The average outlier magnitude u_{out} is estimated on this PhD from the allowable vector range imposed, by taking half the maximum value allowed. Both possibilities to estimate p_{out} were compared to the results of synthetic images and real images. As it turns out, for synthetic images none of the estimates yielded coherent results over the whole set of measurement parameters (however, each estimate worked reasonably for a few test cases). In any case, the analysis of synthetic images does not require of outliers to explain the tendencies observed. For the real images analysis the first estimate of p_{out} gave results

coherent to the variations of $S_{LL}(r)\{u\}$ observed and allows to successfully clarify some aspects. In consequence, those are the only values presented in Chapter 7, and refining the estimate is left for future work.

5.3.13 **CCD readout**

This error is formed during the readout process of the CCD cameras employed for the PIV measurement. It is related with the transfer of the charges produced by the light received by the sensitive pixels.

The cameras that will be used for the measurements have already been characterized in Nogueira *et al.* (2009) and Legrand *et al.* (2014). On those works, the errors obtained go from 0.01 to 0.1pixels, depending mostly on the particles light intensity change between the two frames. These errors are approximately constant for each CCD quadrant if the light intensity change is constant as well; therefore, they should not influence on the final value of $S_{LL}(r)$.

In any case, in this work, the difference of CCD readout error between different quadrants is evaluated and its contribution subtracted from $S_{LL}(r)$. Its magnitude is characterized and commented in Chapter 6 section 6.5.4.

5.3.14 **Particles slip**

This error is related to the capacity of the particles to follow the flow. Particles are moved by the flow due to the drag, and forces like inertia, buoyancy or the weight may divert the particles from the fluid pathlines. The problem is in general quite complex; however, the particles relaxation time (Adrian and Westerweel, 2011) can give useful information on the capacity of the particles to follow the flow accelerations or decelerations:

$$\tau_P = \frac{(\rho_p - \rho_f) d_p^2}{18 \mu_f \phi} \tag{5.61}$$

Where ρ_p is the particle density, ρ_f the fluid density, d_p the particles diameter, μ_f the dynamic viscosity of the fluid and ϕ depends on the particle Reynolds number (Adrian and Westerweel, 2011).

However, the assessment of the capacity of particles to follow the flow variations depends also on the characteristic frequency of change in velocity (Hjelmfelt and Mockros, 1966). This frequency of change is characterized in Chapter 6, as it depends on the turbulence of the flow. For now, the response of particles to a homogeneous turbulent motion, provided in Hjelmfelt and Mockros (1966), is studied. The response is analysed in function of the Stokes number. Different definitions of the Stokes number can be used; for this characterization the one of Legrand (2008) is employed: $St=\omega\tau_P$, where ω is the angular frequency of the flow. The response of a single particle to the flow is given in terms of the amplitudes' ratio and the phase difference between the two velocities. The results are plotted in Figure 5.30 below:

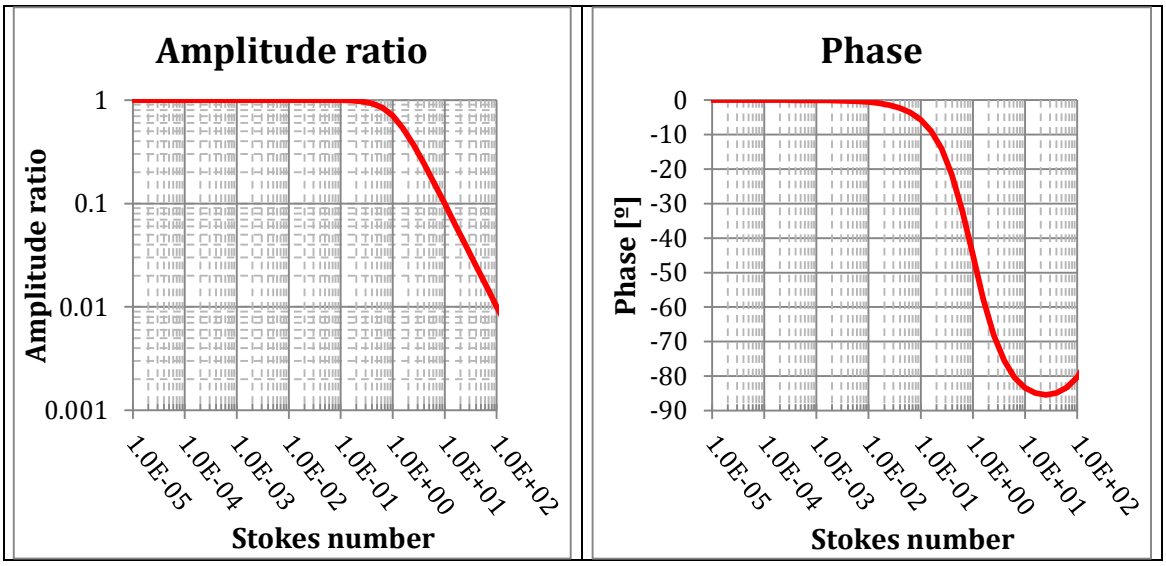

Figure 5.30 Left: amplitude ratio between the particle velocity Fourier transform and the fluid velocity Fourier transform, right: phase between the two mentioned transforms. From Legrand (2008).

An amplitude ratio smaller than 1 implies that not all the flow oscillation amplitude is recovered, equivalent to the low-pass effect of subsection 5.3.3. A phase non-zero indicates that the oscillation would be given with a time lag with respect to the fluid. From the results of Figure 5.30, a Stokes number smaller than 0.5 should allow recovering most of the oscillation amplitude. Related with the phase lag of the particles movement, it stays negligible for Stokes up to 0.05, being much more stringent than the amplitude response. However, a phase difference does not imply a loss of information, as opposite to an amplitude damping. The effect of phase difference is that the particles will replicate the flow velocity with a certain time delay. This problem is inherent to PIV, as stated on 5.3.2. Then, with a phase difference, the error of interest should still appear, unless there is a significant amplitude damping.

For the measurements of the PhD, the seeding generator characterized in Legrand *et al.* (2016) was employed, so the particle measurements on that study can be used here. As is shown in Chapter 6, for the seeding selected $\rho_p \cong 1000 kg/m^3$ and $d_p \sim 1.7 \mu m$, which gives a Stokes number of ~0.06. Consequently, a slight phase could be expected for some particles, but there should be no problems from this fact since the amplitude should be completely recovered.

5.3.15 **Perspective projection errors**

The cause of this error is the projection of the 3D motion into the 2D image plane. The error appears even when the particles displacement can be perfectly determined by the PIV algorithm, which as mentioned already may not be the case (cf. 5.3.7and 5.3.10). It is not related either with the error produced by light intensity change of particles, described in 5.3.9. For the order of magnitude estimation of the error, image distortions are not included. The error is studied here by simple trigonometric considerations, as in Raffel *et al.* (2007).

The perspective projection error occurs as illustrated in Figure 5.31. In the figure, a particle movement is depicted by the black broken arrow. x_0 and x_1 are the coordinates of

the initial and final particle position in the image plane, and X_0 and X_1 the corresponding coordinates in the measurement plane. The displacement of the particle in X direction in the measurement plane is D_X and the measured displacement in the image plane is d_x. In addition, the particle also moves in the out-of-plane direction a quantity D_Z. As can be appreciated in the figure, the measured displacement is composed by the sum of the projection of D_X plus an additional quantity related with D_Z, which is the projection error.

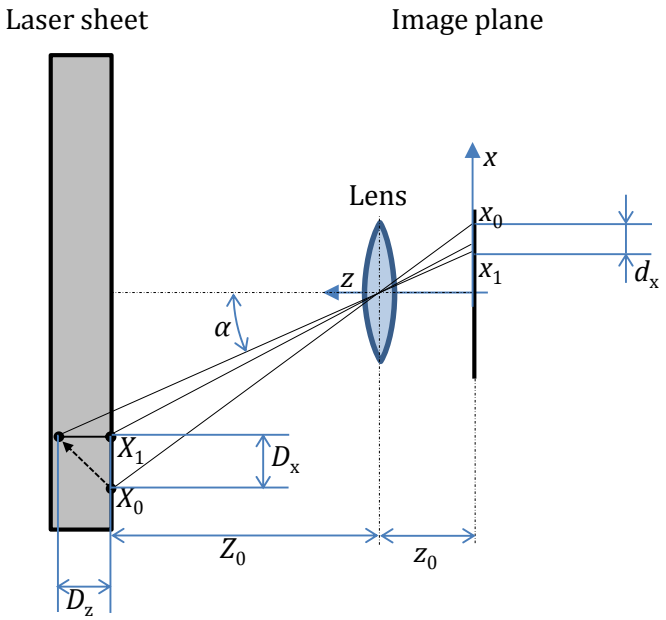

Figure 5.31 Perspective projection error example.

The measured displacement in X direction is:

$$d_x = -M_0(D_X + D_Z \tan\alpha) \tag{5.62}$$

The angle α can be determined from the relation:

$$\tan\alpha = x_1/z_0$$

Additionally, for the isotropic turbulent flows analyzed in this work the displacements in all directions should be of the same order of magnitude, i.e. $D_Z \sim D_X$, which gives:

$$d_x/d_{x,real} = -\left(1 + \varepsilon_{proj}/d_{x,real}\right) \tag{5.63}$$

Where $d_{x,real}$ is the displacement in x without projection errors, $M_0 D_X$, and ε_{proj} is the projection error $\varepsilon_{proj} \sim d_{x,real} \cdot (x_1/z_0)$.

This error is only present in the experimental setup images, as for synthetic images the out-of-plane position was not taken into account for determining the position of a particle in the image plane. As can be observed from expression above, this error is larger for the interrogation windows farther from the image sensor center. For those cases, it is estimated in Chapter 6 section 6.5.4 that the error can reach values $\varepsilon_{proj} \sim 0.05 d_{x,real} \cong 0.05 u' \Delta t M_0$. As is detailed on that chapter, this value is negligible with respect to the sources of error of interest.

5.3.16 **Dimensionless parameters of relevance**

The parameters governing the error values are highlighted below. Those parameters are provided in dimensionless form so the results from this study can be exported to other studies.

The turbulent scale that has been chosen for construction of dimensionless lengths is the one of Kolmogorov, η. This scale has been considered the most convenient because relative to the range of eddies that are produced in a turbulent flow, it is always at the end of the energy cascade process. That means that the smallest eddy observable has always the same size ratio to the Kolmogorov scale. In that regard, Kolmogorov scale should provide valuable information as to the different error values expected for a certain interrogation volume size. For example, it has been observed that low-pass errors depend on $S_{LL}(r)\{u_R\}$, a function that has universal form when expressed in terms of r/η (for low r/η distances). It also indicates if there are turbulent structures smaller than the interrogation volume, for spatial gradients effect assessment. Therefore, the parameters governing the errors would be:

- D_I/η: size of the interrogation window compared to Kolmogorov scale size. Allows assessing the low-pass effect, as well as the possible spatial gradients effects that can be produced.
- Th/η; laser sheet thickness compared to Kolmogorov scale size. Same errors than the previous parameter.
- $d_{eq,1D}/\eta$: for the assessment of low-pass errors in cases where $Th>D_I$, this parameter has been proposed, defined as: $d_{eq,1D} = \sqrt{Th^2 + D_I^2}$.
- D_P/d_r: particles image size compared to the pixel size. It is related to peak-locking errors and random errors from the correlation peak-width.
- $u'\Delta tM_0/d_r$: turbulent rms fluctuations displacement compared to the pixel size. It gives a global impression of the displacements of the flow. Allows for peak-locking assessment.
- $u_\eta \Delta tM_0/d_r$: displacement of the Kolmogorov scale compared to the pixel size. Allows assessing the relative importance of random errors in the smallest displacements of the flow: for example random errors in determining the peak location, light intensity change random errors or peak-locking.
- a/D_P: is the maximum displacement discrepancy produced inside the interrogation volume, compared to the particles image size. It allows assessing the different spatial gradients effects. In this work, two ways of calculating for turbulent flows have been proposed:
    - The characteristic a/D_P, calculated as $a/D_P = \sqrt[3]{\epsilon \max(D_I, Th)}\,\Delta tM_0/D_P$. This expression has been the one used to design the experimental setup and the matching numerical tools test cases, and in consequence is the one which value is provided in the results of Chapter 7. However, the error values are calculated from:
    - The maximum expected a/D_P, given by $a/D_P = \sqrt{S_{LL}(r = \max(Th, D_I))\{u_R\}}\Delta tM_0/D_P$.
- $u'\Delta t/Th$: turbulent rms fluctuations displacement compared to the laser sheet thickness. This parameter has been proposed to assess the out-of-plane motion

effects, which give loss of pairs in the correlation map and a random error from the particles light intensity change.

- Stokes number of Kolmogorov scales: St $=2\pi\tau_P/\tau_\eta$, is the largest Stokes number that should be encountered by tracers in a turbulent flow. The parameter serves for the characterization of particles' slip.

5.3.17 **Summary of error estimations**

The following errors have been analyzed throughout this section, and the following estimates of the values expected in this work have been obtained. The influence in the results of Chapter 7 is also commented:

- Low-pass errors (cf. 5.3.3), which estimate is provided in the peak-splitting phenomenon point.
- Particles misplacement errors, which estimate is provided in the peak-splitting phenomenon point.
- Peak-splitting phenomenon (cf. 5.3.5) modifies at the same time low-pass errors and particles misplacement errors, the following total error estimate has been proposed:

$$\varepsilon_T^2 \approx \overbrace{0.35^2 S_{LL}\left(r = 0.25 r_A\sqrt{D_I^2 + Th^2}\right)\{u_R\}}^{\varepsilon_{LPF}^2} + \overbrace{\frac{S_{LL}(r = Th)\{u_R\}}{r_A N}}^{\xi_{\Delta u}^2}$$

Where $r_A = (\pi/2)/\left[(a/D_P)^2 + 2\sqrt{2}(a/D_P) + \pi/2\right]$. In the expression above, the first term is associated to low-pass errors and the second corresponds to particles misplacement errors. This is the error on which this PhD focuses, as has been found as the most relevant related to the interaction of the laser sheet thickness and turbulent spatial gradients. As can be observed, this error depends on the measurement volume sizes: D_I/η and Th/η, on the turbulence of the flow and on the displacement differences a/D_P.

- Group-locking error (cf. 5.3.6) is assumed to be englobed in the random deviation produced by particles misplacement ($\xi_{\Delta u}$) given above. For the results analysis, both effects are referred to as "peak-splitting errors".
- Peak-locking systematic errors (cf. 5.3.7) should reach a maximum value around 0.01-0.05 pixels for the results of this work, with a systematic behavior as shown in Figure 5.22. This error seems to be of importance for the cases with low $u_\eta \Delta t M_0/d_r$ (around 0.1) and it seems to become much more important when $u'\Delta t M_0/d_r < PL_{period}/2$ (where PL_{period} is the peak-locking period, which should be of 2 pixels).
- Peak-locking random errors (cf. 5.3.8) should have a value of $0.1/\sqrt{N}$ pixels. Since N, the number of particles, is roughly 100 for the test cases analyzed, this error should be in principle negligible.
- Light intensity changes random errors (cf. 5.3.9) should present values between 0.01 and 0.1 pixels for $u'\Delta t/Th$ varying between 0 and 0.4. However, for the cases

where the error reaches a large value in pixels, $u_\eta \Delta t M_0/d_r$ is quite large and thus its effect in the velocity is in principle negligible.

- Random errors in determining the correlation peak-location (cf. 5.3.10), $\xi_{\Delta x}$, should be between 0.01-0.1pixels. As peak-locking systematic errors, this error seems to be of importance for the cases with low $u_\eta \Delta t M_0/d_r$.
- Spatial gradients systematic biases (cf. 5.3.11), should reach, in principle, a maximum value of 0.03 pixels, thanks to using a multi-grid approach. These errors are in principle negligible.
- Outliers' occurrence (cf. 5.3.12) is influenced by many factors. An estimate of the error has not been proposed (only the effect in $S_{LL}(r)\{u_M\}$ is given). This error source is of importance for some of the test cases presented in Chapter 7.
- CCD read-out errors (cf. 5.3.13) should be from 0.05 pixels to 0.1 pixels for the cameras used in this work. However, these errors should be easily removed as it is in principle roughly constant for each quadrant of the cameras. In this work its influence should be removed because the velocity fluctuations are used for the calculations and the constant shift produced by the error should be removed.
- Particles slip error (cf. 5.3.14 and 6.3.2) can induce a modulation of the flow oscillations amplitude if Stokes number surpasses 0.5 (see Figure 5.30); however, that is not the case for the seeding employed in this work and thus their effect should be negligible.
- Projection errors (cf. 5.3.15 and 6.5.4.2) are estimated to produce an error of $\varepsilon_{proj} \sim 0.05 d_{x,real} \cong 0.05 u' \Delta t M_0$, which is negligible compared to other errors.

The effect on $S_{LL}(r)\{u_M\}$ of the errors that are not negligible has been calculated approximately in this section, so they can be recognized when they are produced on the analysis of the results of Chapter 7.

As conclusion of this section, only those errors which should be not negligible for the analysis of real images are quoted below:

- Low-pass filtering errors (which can be reduced by peak-splitting phenomenon).
- Peak-splitting errors:
    - A random deviation produced by particles misplacement.
    - A systematic deviation produced by group-locking errors.
- Peak-locking systematic errors.
- Random deviation in determining the correlation peak location.
- Outliers' occurrence.

For synthetic images the same sources than for real images are given. For the PIV Simulator, the following sources are not given: peak-locking errors, the random deviation in determining the correlation peak-location and outliers' occurrence.

Chapter 6 **Dedicated experimental setup**

In this chapter, the dedicated experimental setup designed to validate the results from the PIV Simulator and synthetic images is described. The aim of this experiment is to generate a velocity field close to homogeneous isotropic turbulence, at least locally, in order to be able to compare with the previous tools. In addition this allows studying the error from the interaction of the laser sheet thickness with the turbulence of the flow on real PIV images.

The flow measured on the experimental campaign was the one usually referred to as grid turbulence. It presents the advantage to be easily generated and it is nearly homogeneous and isotropic in two directions. In the first part of the chapter, the requirements that the measurement campaign should fulfill are presented. In the second part, the reason to choose grid turbulence for the measurement campaign and how the requirements related with the flow can be attained is described. In the third part, the requirements associated to the PIV acquisition system and how can they be fulfilled is explained. The design process of the experiment is detailed in the fourth section. The last section indicates how the real images have been analyzed. This section includes the calculation of the dimensionless parameters summarized on 5.3.16 necessary to characterize the error. For the dedicated experimental setup, the real flow parameters are not known, so methods need to be identified to assess those parameters. Additionally, some errors not expected to be of importance for the results are evaluated in this section, as well as some deviations with respect to the ideal theoretical grid turbulence conditions.

6.1 REQUIREMENTS

The measurement campaign should cover a set of time delays (Δt) and laser sheet thicknesses (Th) in order to provide a complete error characterization. This is done to observe the effect of varying a parameter for different fixed values of the other. That allows better describing the tendencies given when varying the measurement parameters.

The requirements are focused in the errors induced by the interaction of spatial gradients with the laser sheet thickness. It would have been desired to add a laser sheet thickness where the predominant error source had been turbulent out-of-plane motion. However, that was not possible because the misalignment offset between the two laser beams precluded from doing so. The following requirements were identified then:

- Turbulent length-scales larger than the smallest laser sheet thickness and the interrogation window size should be present. Indeed, in order to understand the error introduced in the smaller length-scales, turbulent length-scales which have little influence from the laser-sheet thickness or the interrogation window need to exist. The largest turbulent scales ℓ_T should be of at least 4 times the smallest laser sheet or the interrogation window size, whichever is larger, for that reason. A ratio of 4 is considered as the value from which there is barely influence on the results from the interrogation volume size. This can be seen for example in Willert and Gharib (1991) or 5.3.3 on the error from the low-pass effect.
- Turbulent length-scales smaller than the larger laser sheet thickness. A series of first tests on synthetic images allowed identifying that a laser sheet of $\sim 30\eta$ (where η is the Kolmogorov scale size) should produce errors large enough to be differentiated. Additionally those small scales should produce strong enough gradients so that peak splitting phenomenon and related gradient effects appear. Westerweel (2008) as well as the tests conducted with synthetic images revealed that this error source is relevant for displacement variations in the interrogation volume $a \sim (2/3)D_P$ (for the definition of a see 5.3.5).
- Related to the small scales as well, it was considered that the Kolmogorov velocity in pixels should be above $\sim$0.05pixels for all Δt's. This was the value advised by a series of tests with synthetic images, for a particles diameter of $\sim$2 px and state of the art image deformation and subpixel peak fitting algorithm. This should allow an appropriate characterization of the smaller scales, without the errors that scale with the pixel size (as peak-locking and random errors in determining the correlation peak-location) interfering much.
- For the experimental results to resemble as much to those of synthetic images and the PIV Simulator, the flow should be as close as possible to the flow described in 3.1. Ideally, it should be uniform, homogeneous[5], isotropic and statistically stationary. Also, the flow with these characteristics should occupy most of the field of view of the camera.
- The turbulent out-of-plane motion parameter, $u'\Delta t/Th$ (cf. 5.3.9), should be at maximum $\sim$25% so it does not introduce important errors on the measurement

[5] In this chapter, homogeneous refers to the fluctuating velocity field $\boldsymbol{u(x;t)}$ being statistically invariant with respect to a shift in position. The uniform propriety refers to the average velocity field being statistically invariant with respect to a shift in position.

(Keane and Adrian, 1990, Raffel *et al.*, 2007, Nobach and Bodenschatz, 2009). A characterization of the variation of the errors with this parameter has not been found. Therefore, the limit suggested on the previous works for the mean out-of-plane motion rate is taken.

- Related to the previous point, all laser sheet thicknesses employed should have an overlap as high as possible, because as Grayson *et al.* (2016) report a misalignment may lead to a degradation of the correlation and outliers' production. A minimum overlap of ~70% can be advised from the results Grayson *et al.* (2016).
- At least the largest laser thickness should be larger than the interrogation window size, so their effects can be differentiated. The ratio between the largest laser sheet and the IW size should be of at least 4 (again, a 4 ratio is considered as the minimum necessary).
- The depth of field of the setup (the range of distances where the diameter of the particle image is given by diffraction and almost independent of the distance, Adrian and Westerweel, 2011) should be at least as large as the largest laser sheet thickness to be measured. Otherwise, the previous requirement would be limited by the depth of field which could preclude from obtaining the desirable effective laser sheet thickness. This was the case of the previous measurement campaign conducted during the PhD, not reported here, because the depth of field precluded from obtaining errors large enough.
- The field of view should be larger than the large turbulent scales so those scales can be properly studied.
- The particles images diameter can be neither too low nor too large: small particle image diameters can favor the increase of peak-locking errors (Westerweel, 1998, among others), which could hinder the characterization of the error of interest. On the other hand, large particle images may induce random errors due to large correlation peak-widths (Westerweel, 1998). A usual advisable compromise lies between 2 – 3 pixels.
- Particles should scatter enough light to not incur in low SNR and related errors.
- In order to ensure a large proportion of valid vectors, there should be a minimum number of particles per interrogation window: usually around 20 particles are considered sufficient (Keane and Adrian, 1990).
- Particles should be small enough to follow the turbulence of the flow. The particle slip velocity error was quantified on 5.3.14. In that subsection it was obtained that the Stokes number should be below 0.5 to recover almost all oscillation amplitude. Additionally, for the particles movement to not have any phase with respect to the flow, Stokes number should be below 0.05.

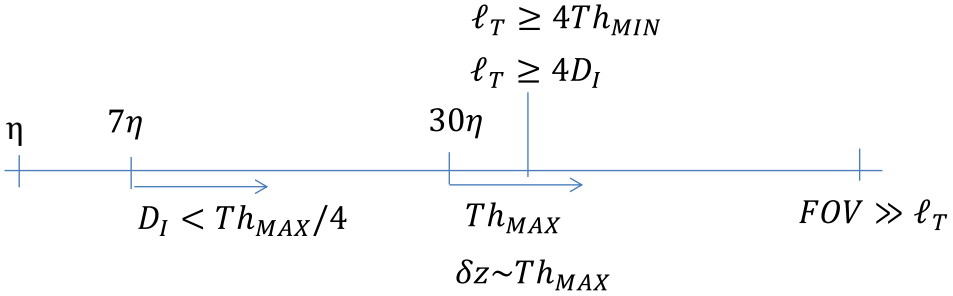

Figure 6.1 Summary of all the requirements related with a size.

6.2 FLOW SELECTION AND CHARACTERIZATION

A flow that fulfils the requirements mentioned in 6.1 of resemblance to the flow characteristics of the PIV Simulator and synthetic images is the one referred to as grid turbulence.

6.2.1 Flow selection

The flow selected to assess the error produced by the interaction between turbulence and the laser sheet on a PIV measurement is the one produced by **grid turbulence**. This flow is produced by placing a mesh perpendicularly to a uniform stream, which results in part of the kinetic energy of the flow being transformed in turbulent kinetic energy in the grid wake. The turbulence produced this way is considered to be as *freely evolving* turbulence. That means there is no interaction from the mean flow and the turbulence aside from the fact that the mean flow transports the turbulence with it (Davidson, 2004), i.e. there is no turbulence production.

This type of flow is used in turbulence research (Davidson, 2004) to test turbulence theories. Grid turbulence has also been characterized by means of PIV measurements, for example Lavoie *et al.* (2007) study the effect of finite spatial resolution on the error of the turbulent length-scales and Poelma *et al.* (2006) study the effect of missing data (the vectors detected as not valid) on the turbulent energy spectrum.

The interest of this type of flow for turbulence research lays in its resemblance to homogeneous isotropic flows. Being the simplest form of turbulence, the research work that motivated this PhD (cf. section 2.1) as well as the PIV simulator and synthetic images velocity fields, are based on this kind of flow. Plus, as per Kolmogorov universality hypothesis (cf. section 1.2.1.3) all turbulent flows are "universal" in the smaller scales and results should be exportable. Another advantage is that there is wide research on grid turbulence which can be used for data validation or as guidelines on designing the experiment.

For all these reasons, and since a priori the requirements related to the flow are fulfilled by grid turbulence, it was selected to obtain the real images.

6.2.2 Experimental setup description

Grid turbulence is usually divided into two regions, downstream of the grid (Hinze, 1975):

- Building up period or period of establishment, where the grid wake vortices interact. Initially, the vortices emitted by the grid bars can be laminar, but eventually turbulent cores appear, leading to the next stage. This region can be clearly appreciated in Figure 6.2, from Ertunc *et al.* (2010), on the left part of the image, where the grid wakes are noticeable. The distance up to which this region extends is not clearly defined and depends on the research work. As examples, this region extends up to $\sim 10 M_G$, according to Lavoie *et al.* (2007), or up to $\sim 40 M_G$ according to Ertunc *et al.* (2010), where M_G is the distance between bar rods (see Figure 6.3).

- Fully developed, almost homogeneous turbulence. The grid wake vortices interaction eventually leads to this state, for which turbulence is usually

considered isotropic and homogeneous, in a lateral sense (y and z directions in Figure 6.2). In this region, the freely evolving turbulence mentioned above is given. Batchelor and Townsend (1948) differentiated three periods within this region: an initial period, a transition period and a final period.

- In the initial period the energy containing eddies (the larger eddies) transfer energy by inertial mechanisms to the smaller eddies, where viscous dissipation dominates (Hinze, 1975). The smallest eddies decay fastest (Davidson, 2004) leading to the final period.
- In the final period the viscous effects dominate over the inertial effects on the whole wavenumber range (Hinze, 1975). The Reynolds based on the large eddy size is close to unity and the flow is then a very complex laminar flow (Davidson, 2004).
- The transition period lies between the other two periods.

In Figure 6.2 below, where the turbulent kinetic energy just downstream of a grid is plotted, the grid wake vortices can be appreciated. In the figure, x is the streamwise direction, y a transversal direction and M_G the distance between bar rods. Kinetic energy field was calculated by Reynolds stress components, which were normalized by the square of the bulk velocity U_m. The results are from Direct Numerical Simulations of Ertunc *et al.* (2010) on a pressure driven grid turbulence flow. It can also be observed on the image how the flow gets more homogeneous in the transversal direction y as the flow advances in x: the fluctuations in the lateral direction y get reduced.

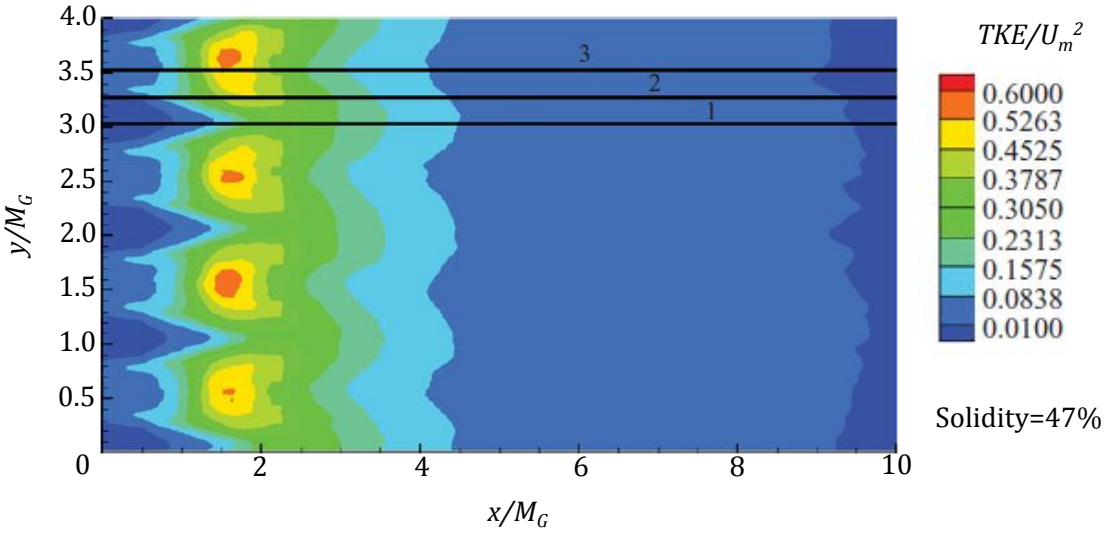

Figure 6.2 Kinetic energy field for x/M_G<10. The image is from Ertunc *et al.* (2010).

In the initial period of the fully developed turbulence stage is where a larger range of turbulent scales is found (Davidson, 2004, Sagaut and Cambon, 2008, among others). Therefore, it is found as the most convenient region for this measurement campaign.

There are different types of meshes which can be used to generate grid turbulence. Below, on Figure 6.3, sketches of some of the different turbulence generators that can be used to produce this type of flow are depicted (Roach, 1987). The bar rods in the square mesh and

in the parallel one could be round or square also. The geometrical parameters that describe each generator are identified in the figure.

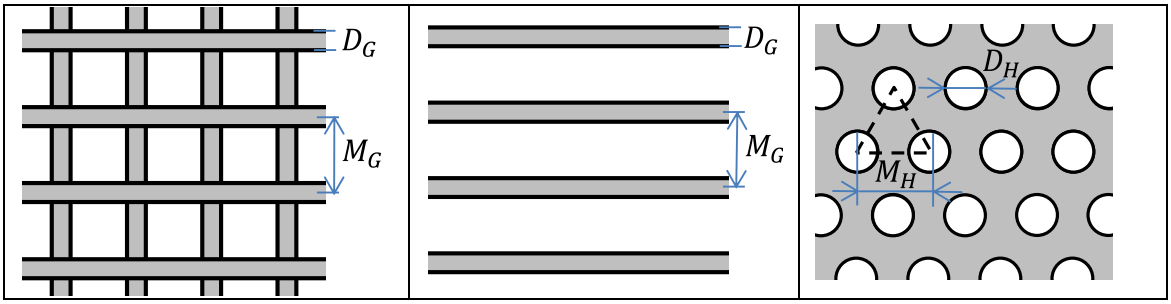

Figure 6.3 Sketch of turbulence generators that can be employed in grid turbulence flows. Left is a square mesh array of rods, middle is parallel array of rods and right is a perforated plate with the holes in hexagonal disposition.

From the geometric parameters depicted in Figure 6.3, the solidity of the turbulence generator is typically provided as it influences the turbulence produced. The solidity is the area ratio between the solid surface and the total surface. In the case of the perforated plate of Figure 6.3-right, which is the generator used on this measurement campaign, it can be calculated from:

$$\mathcal{S}_{PP} = 1 - \frac{\pi}{2\sqrt{3}} \frac{D_H^2}{M_H^2} \tag{6.1}$$

Perforated plates are easy to manufacture in a 3-D printer, so they are preferred in this study because they offer more flexibility when adjusting the required downstream turbulence parameters. Additionally, perforated plates are less likely to generate anisotropic turbulence than grids, especially when the turbulence intensity is high (Kondjoyan and Daudin, 1994).

Typically, grid turbulence is usually produced by placing the turbulence generator perpendicular to the stream inside a wind tunnel. However, in this PhD it is achieved by placing the perforated plate perpendicular to a round nozzle discharging into quiescent ambient air, as illustrated in the figure below, since an appropriate wind tunnel was not available. The main difference lies in that instead of having a boundary layer developing on the wall, a mixing layer develops between the jet and the quiescent air in the room. A sketch of the experimental setup is represented in the figure below.

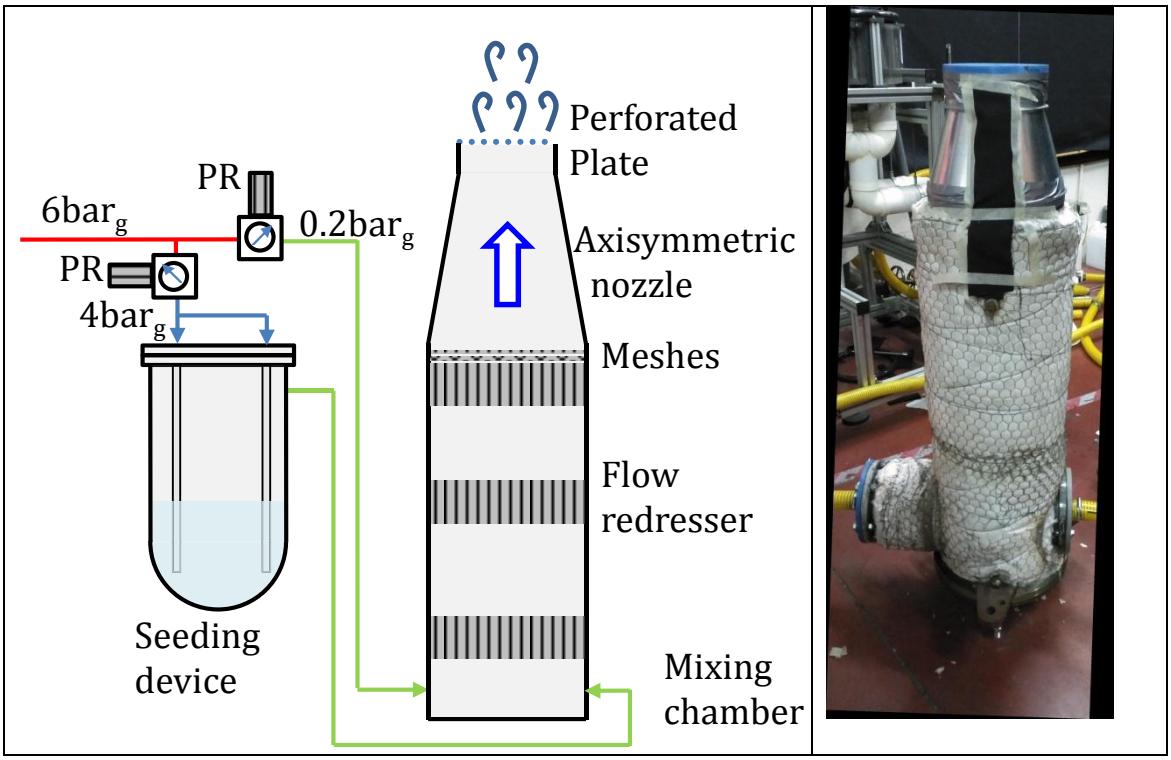

Figure 6.4 Left: Sketch of the experimental setup. Right: photo of the mixing chamber that produced the stream.

In order to produce the stream arriving at the perforated plate a mixing chamber was used; the air was fed from the compressed air system. Inside the mixing chamber a series of flow redressers and grid meshes of different sizes were placed, to make the flow uniform. Upstream of the perforated plate a contraction nozzle was placed, in order to reduce the turbulence and the boundary layer thickness that arrived to the perforated plate. The flow rate was adjusted by regulating the pressure upstream the mixing chamber. The particle tracers were obtained from the seeding device described in Legrand *et al.* (2017), which was supplied with air from the same compressed system port than the mixing chamber, as depicted in Figure 6.4. The flow with particles is then mixed with the main air stream at the bottom of the mixing chamber.

6.2.3 **Flow parameters characterization**

The parameters related with the flow which can be varied on the experimental installation are the following:

- Perforated plate: D_H and $\mathcal{S}_{PP}$ (or D_H and M_H). $\mathcal{S}_{PP}$ increases when M_H increases, for fixed D_H, as appreciated from expression (6.1).
- Flow facilities: Pressure at the inlet of the mixing chamber and diameter of the nozzle outlet (size of the perforated plate), D_{NOZZLE}.

The interaction of these parameters with the requirements of 6.1 is detailed next.

The first requirement associated with flow characteristics was related to the **turbulent large scales** ℓ_T. ℓ_T has to be larger than the smallest laser sheet thickness and larger than D_I, specifically: $\ell_T > 4D_I$ and $\ell_T > 4Th_{MIN}$ was imposed.

Large turbulent scales can be obtained by adjusting the geometric parameters of the perforated plate. Typically, in the literature, the large turbulent scales are characterized by the integral scale. As can be observed in the results of Liu *et al.* (2004) of Figure 6.5 the turbulent integral scale $\mathcal{L}$ is proportional to the holes diameter D_H, and it increases as well with the plate solidity (indicated by σ in Figure 6.5). Reynolds number is calculated on that work as UD_H/ν, where U is the mean velocity. The integral scale, also as observed on that work, increases with the dimensionless distance to the plate (see Figure 6.5). However, the increase of $\mathcal{L}$ with the distance should not be understood as the large turbulent scales increasing with the distance to the perforated plate. The increase of the integral scale is produced by the dissipation of the smallest scales as the turbulence advances with the stream, whereas the turbulent larger scales stay likely the same. This can be observed in Davidson (2004) or in Sagaut and Cambon (2008). For the turbulent large scales required on this work, the rule of thumb $\ell_T \sim D_H$ is taken. In addition, ℓ_T should also increase with the solidity of the perforated plate, as does the integral scale.

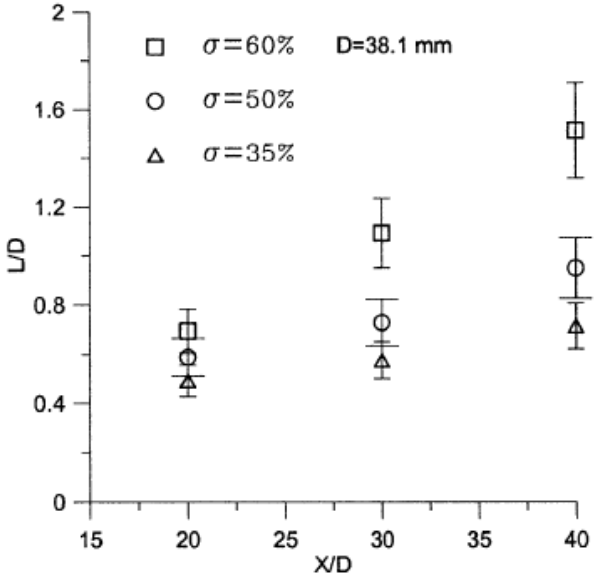

Figure 6.5 Variation of the integral scale $\mathcal{L}/D_H$ with x/D_H for D_H =38.1mm, Re=29,000. From Liu *et al.* (2004).

The **small length-scales** necessary (they need to be $<Th_{MAX}/30$) can be achieved by different means. To illustrate those means, the smaller length-scales are characterized below by Kolmogorov length-scale, defined as:

$$\eta = (\nu^3/\epsilon)^{1/4} \tag{6.2}$$

where ν is the kinematic viscosity and ϵ the mean dissipation rate. The kinematic viscosity is fixed by using air and by the temperature given by the compressed air facility. To decrease the smallest scales the dissipation must increase then. The dissipation can be estimated by:

$$\epsilon = A\, u'^3/\mathcal{L} \tag{6.3}$$

where A is a constant that depends on the turbulence type, u' is the rms turbulent fluctuation and $\mathcal{L}$ the integral scale. Constant A is usually ~1 for grid turbulence.

Combining both expressions gives:

$$\eta = \left(\frac{\nu^3 \mathcal{L}}{A u'^3}\right)^{1/4} \tag{6.4}$$

Reducing the small length-scales can be obtained then by increasing the velocity fluctuations u' or by reducing the integral scale.

u' is proportional to the stream velocity U, it can also be increased by increasing the perforated plate solidity (indicated by σ in Figure 6.6) or by measuring closer to the perforated plate, as is illustrated in Figure 6.6, from Liu *et al.* (2004).

The stream velocity U is limited by the flow rate that the facilities can provide and by the maximum flow rate that can be seeded properly. On the other hand, U could be increased by decreasing the exit area of the nozzle, for a fixed flow rate. The integral scale is varied as stated above.

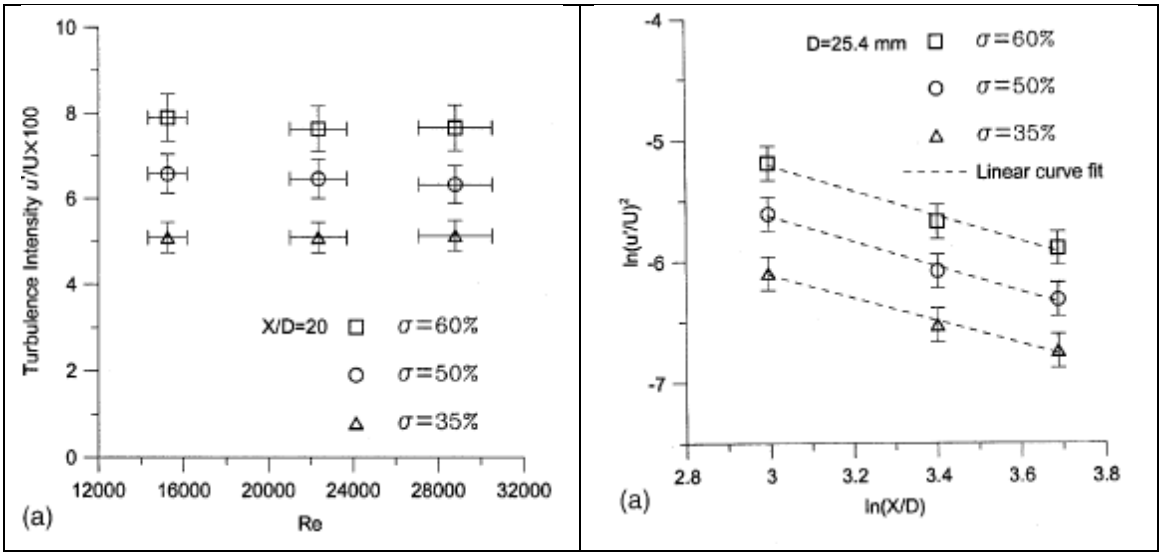

Figure 6.6 Left: Variation of u'/U with Re for D=38.1mm for x/D_H=20. Right: Variation of u'/U with x/D_H. From Liu *et al.* (2004).

The **velocity of Kolmogorov scales** also needs to be large enough for the small scales to have a sufficiently large displacement. The velocity is given by: $u_\eta=(\nu\epsilon)^{1/4}$. The dissipation can be varied as stated above. As can be appreciated, increasing ϵ results in larger u_η and in smaller η; both variations go in the direction of fulfilling the requirements.

The **displacement difference parameter a/D_P** estimated in Chapter 5 as: $a/D_P = \sqrt[3]{\epsilon \max(D_I, Th)}\,\Delta t M_0/D_P$ can be also varied through ϵ. In order to vary it, the same process than stated above for the variation of Kolmogorov scales should be followed. The rest of dependencies of this requirement are analyzed in 6.3.

To reduce the parameter related to **out-of-plane motion**, $u'\Delta t/Th$, u' can be varied as mentioned above. Variations of Δt and Th are part of the measurement campaign

requirements, but all cases studied should present values of $u'\Delta t/Th$<25%, which could be achieved by reducing u'.

The **field of view** has to be larger than the large turbulent scales $\mathcal{L}$ or ℓ_T. The field of view size is imposed by the PIV acquisition parameters; related to the flow, ℓ_T cannot be too large to fulfil this requirement. ℓ_T can be varied as mentioned above.

For turbulence to resemble as much as possible the theoretical **homogeneous** and **uniform turbulence**, the period of establishment of fully developed turbulence, as well as the jet mixing layer, should be avoided inside the FOV.

The period of establishment of fully developed turbulence varies through the literature, as mentioned above. Most works find it to be proportional to the turbulence generator geometric parameters, which on the case of the perforated plate are D_H and M_H. As to the extension of the period of establishment, the value of $\sim 10M_G$ of Lavoie *et al.* (2007) was taken as departing reference. As on that case the turbulence generator was a square array of round bars, the equivalent distance for the perforated plate was considered to be $\sim 10D_H$. In consequence, the measurement should be performed at a larger distance. The final measurement zone was determined by performing a preliminary measurement, so the flow features were the most suitable to the objectives. As is shown in section 6.5.5, neither uniformity nor homogeneity were reached in the measurement region. Other requirements were prioritized over these two, because recent studies, such as Liu *et al.* (2004) or Ertunc *et al.* (2010), show that perfect homogeneity may never be reached downstream the grid.

On the other hand, the jet potential core region (the region not affected by the mixing layer in average) length is $\sim 5D_{NOZZLE}$ (Hinze, 1975, where D_{NOZZLE} is the diameter at the nozzle exit where the perforated plate is placed, see Figure 6.4). The mixing layer does not stay at a fixed location and is unsteady, a smaller distance should have to be considered then, but this value was taken as initial reference. Additionally, in this case and given the turbulence produced by the perforated plate, it seems reasonable that this distance could be decreased even further (due to additional mixing). In consequence, the mixing layer influence could be reduced by reducing the turbulent fluctuations u' generated by the plate or by using a larger nozzle diameter D_{NOZZLE}. The maximum D_{NOZZLE} is also limited by the 3D printer available to manufacture the perforated plate, which can print objects up to approximately 20cm in size. As to u', it can be varied as stated above.

Statistically stationary condition

The statistically stationary condition is achieved by a steady feeding stream. As mentioned above, the feeding stream is produced by the compressed air facilities. The facilities are basically composed of three compressors and one deposit, where the air at high pressure is stored. As the compressed air deposit delivers air to the university facilities, the pressure in the experiment feeding line diminishes (red line in Figure 6.4). When the pressure reaches a certain threshold a compressor is switched on to fill up the deposit. This translates into pressure oscillations in the air feeding line of the installation.

The amplitude of the oscillations on the high pressure feed depends on the flow rate being used; typically, the higher the flow rate imposed the higher the pressure oscillations.

Amplitudes as high as 2 bar were observed in the feeding line; on cases with less demanding conditions the amplitude was still 0.5 bar. Those oscillations are reduced through the pressure regulation system; nevertheless, the oscillations remain and are propagated into the stream velocity. This can be observed in Figure 6.28, where the average streamwise velocity obtained with the final installation has been plotted.

Those variations in the stream velocity will have associated changes in the turbulent rms fluctuations, since both are proportional through the turbulent intensity (see Figure 6.6). Additionally, the temporal variations in the stream velocity could influence on some other way the turbulence being developed downstream of the perforated plate, due to some sort of history effect. Nonetheless, that is not expected to occur since the pressure fluctuations characteristic time is much larger than the turbulence characteristic times (the integral scale time is $T \sim \mathcal{L}/u' \approx 0.01$ seconds and the period of the pressure oscillations is ~ 5 minutes). Therefore, to the turbulence produced by the perforated plate the stream velocity should be locally stationary. Still, the variations of u' will induce variations on the errors produced for a same test case, which can difficult the analysis of the results.

Therefore, in order to reduce those oscillations, several possibilities were tested. The possible variations are on the pressure regulation system. The configurations tested included one pressure regulator, a pressure regulator with a needle valve, or two pressure regulators in series or in parallel. Additionally, the pressure regulator model was varied in those configurations. The oscillations were kept in all cases. The best results were obtained for a configuration with one pressure regulator designed for a low range of outlet pressures (from 0.1 to 3 bar gauge, bar_g), which had to be purchased for the experimental campaign. The other pressure regulators available had a larger working output pressure range, typically from around 0.5 to around 8 bar_g. As can be observed in Figure 6.4, where the final configuration is plotted, the pressure at the outlet of the regulator was of $0.2 bar_g$, which can explain the problems of the other pressure regulators tested. Nevertheless, those pressure regulators were also tested with additional pressure losses imposed by valves, so the pressure at the outlet of the regulator would be in the working range, and the oscillations were still important.

The problem of the statistically stationary condition could also be solved by using just the images which average velocity is contained within a certain range. However, that would result in having to acquire and analyze a very large number of images, to later use only those with the velocity within the defined range. That increases the overall required time to obtain the results and thus it was deemed necessary to optimize the installation so the effect of the oscillations would not influence on the results. The effect of the oscillations is studied in section 6.5.5.

6.3 PIV ACQUISITION PARAMETERS

The features related to the PIV technique that can be adjusted to fulfill the requirements are the following:

- Laser properties:
  - Laser sheet thickness.
  - Light wavelength, which in this case is fixed: λ=532nm.
- Seeding:
  - The size of the particles d_P.
  - The quantity of tracers.
- Camera lenses:
  - Magnification M_0.
  - f-number of the lenses $f^\#$. This parameter is also referred to as numerical aperture and is calculated as the ratio between the focal length to the aperture diameter: $f^\#=f/D$).
- The time delay between the laser pulses (Δt).
- The interrogation window size in pixels (IW_p) in the PIV algorithm.
- The acquisition camera (which in this case is fixed though):
  - Size of the sensor.
  - Size of a pixel d_r.

There are a couple parameters that require a more detailed characterization. Those are the laser sheet thickness and the seeding. The influence of the rest of the parameters in the requirements is in 6.3.3.

6.3.1 Laser sheet thickness characterization

The requirements that had to be fulfilled by the laser sheet are the following:

- SNR should be high enough, so outliers' occurrence and random errors do not interfere with the study.
- The largest thickness, Th_{MAX}, has to fulfill: $Th_{MAX}>4D_I$ (where D_I is the interrogation window in-plane dimension projected on the measurement region).
- All laser sheets employed should have an overlap above a 70%.

The laser sheet thickness can be varied by moving the laser focal point with respect to the region that is being photographed. This is possible to achieve thanks to the light sheet optics shown below. The light sheet optics is composed of two spherical lenses that change the focus length of the laser beam and one cylindrical lens that forms the light sheet (Lavision, 2007). As to the laser light power, it can be varied by changing the cylindrical lenses or also by changing the distance to the laser formation optics at which the measurement is performed. Indeed, when the light is spread over different surfaces the light intensity received by a particle changes.

Figure 6.7 Laser sheet formation optics. From LaVision (2007).

The laser profile analysis was carried out acquiring images with the PIV camera of the formed laser sheet. To obtain such images, a PVC (Polyvinyl chloride) sheet was placed at 45º respect to the laser propagation direction, and the PIV camera was placed perpendicular to the PVC sheet and looking towards it. The measurement setup is sketched in the left image of the figure below. To avoid any unnecessary uncertainty of the laser profile changing when the laser power changed, it was decided to characterize the laser profiles at full power, once the warm-up time had elapsed.

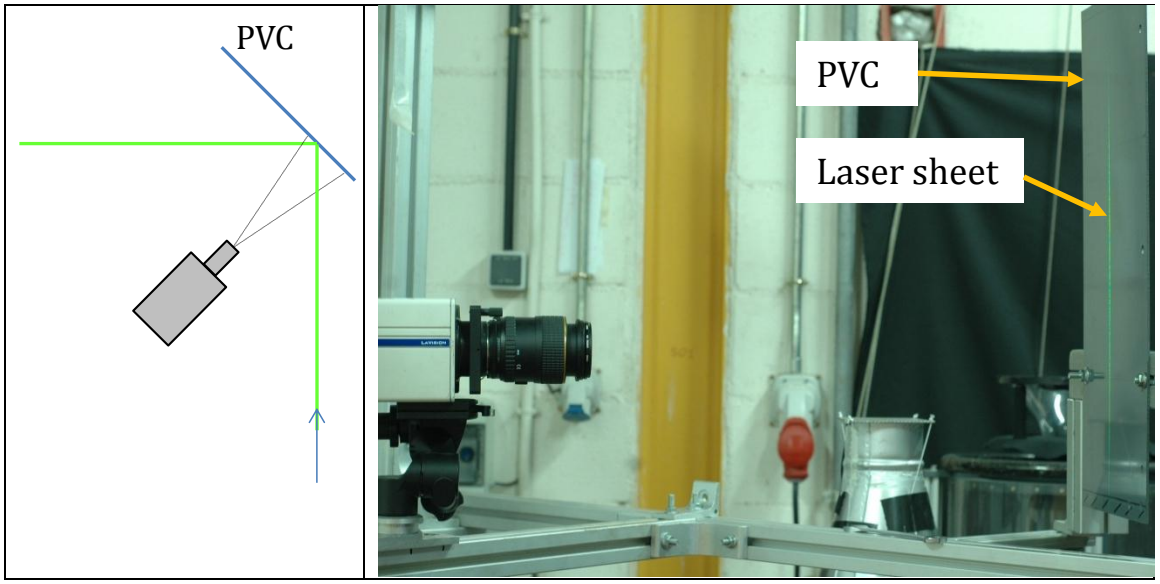

Figure 6.8 Left: sketch of the laser sheet characterization measurements (upper view). Right: photo of the setup: the PVC sheet and the laser sheet can be seen at the right of the image, and the camera taking the photo of the laser is on the left.

Taking photos of the laser sheet at full power required to reduce the light received by the camera, because the regions of the images illuminated by the laser could be saturated. In order to diminish the light received on the CCD sensors, the first option was to close the diaphragm of the lenses and to acquire the photos at minimum allowable aperture ($f^{\#}$=32). However, speckles appeared on the photo, as shown on the Figure 6.9 below, instead of the typical Gaussian-like profile:

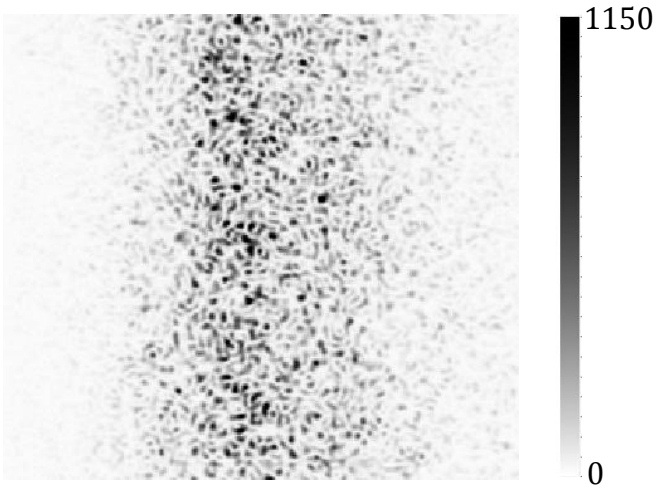

Figure 6.9 Speckles obtained when the laser sheet was photographed with $f^{\#}$=32. The colorbar indicates the light intensity, in arbitrary units.

The speckle patterns are produced by interference of the coherent laser light. They precluded from providing a proper laser profile characterization. An in-depth study of the speckle formation is out of the scope of the PhD but measurements of the laser profile without them were preferred. For that purpose, images were taken with the laser at 30% of the power and the diaphragm fully opened ($f^{\#}$=2.8) and no speckles were observed. However, with the laser shooting at full power and with $f^{\#}$=2.8 the laser profiles were saturated.

Therefore, in order to measure with the diaphragm fully opened and at full power, neutral-density (ND) filters were mounted on the camera lenses. One of the filters had a fixed darkening value of ND400 and the other one was an adjustable ND filter. The adjustable filter was regulated for each measured position of the formation optics so the maximum light value received by the camera was always close to the saturation value of the CCD. This was done to maximize the images dynamic range.

For each image, the laser was approximately vertical on it and it was sought for the laser to occupy just one quadrant of the camera, in order to avoid CCD read-out errors (Legrand *et al.*, 2014). The images were taken of the center of the laser beam, to avoid the peripheral beam regions. Magnification was 42pixels/mm to have at least ~20 pixels for the smallest laser sheet.

The data over which the estimations were calculated was obtained from the average of 10 images of each laser profile. Then, from the mean image the data of 100 horizontal lines was averaged, giving two lines of data $I_1(x)$ and $I_2(x)$ advancing in the horizontal direction for each laser pulse. Over $I_1(x)$ and $I_2(x)$ two estimations of the thickness are calculated (described below). For the final results plotted in Figure 6.11-right, the estimation values at two different positions within the image are averaged. The averaging process was done to reduce the oscillations that are given on the laser power and also to reduce the effect from the slight PVC imperfections. Background noise was removed by subtracting the mean image of a series of 10 images without the laser shooting. The laser profiles that can be obtained by the aforementioned averaging process are plotted in Figure 6.11-left.

Since the laser was not perfectly vertical inside the images, the angle of the laser profile to the vertical (see Figure 6.10) was taken into account in the calculations. As can be appreciated in Figure 6.10 the measured thickness Th_M will be larger than the real laser thickness over the photo (Th_C). This is because: (i) several horizontal lines of pixels are collapsed together on the average process and the laser is not at the exact same position over those lines and (ii) the calculation of the profiles thickness is performed over a horizontal line but the profile actually evolves in the perpendicular to the light sheet. Both effects are sketched on the image: where the red rectangle indicates the area used to calculate the average laser profile. It can be appreciated how the laser is placed at slightly different locations for each row of pixels. The calculated thickness Th_M and the real thickness over the sensor Th_C are approximately indicated in the image.

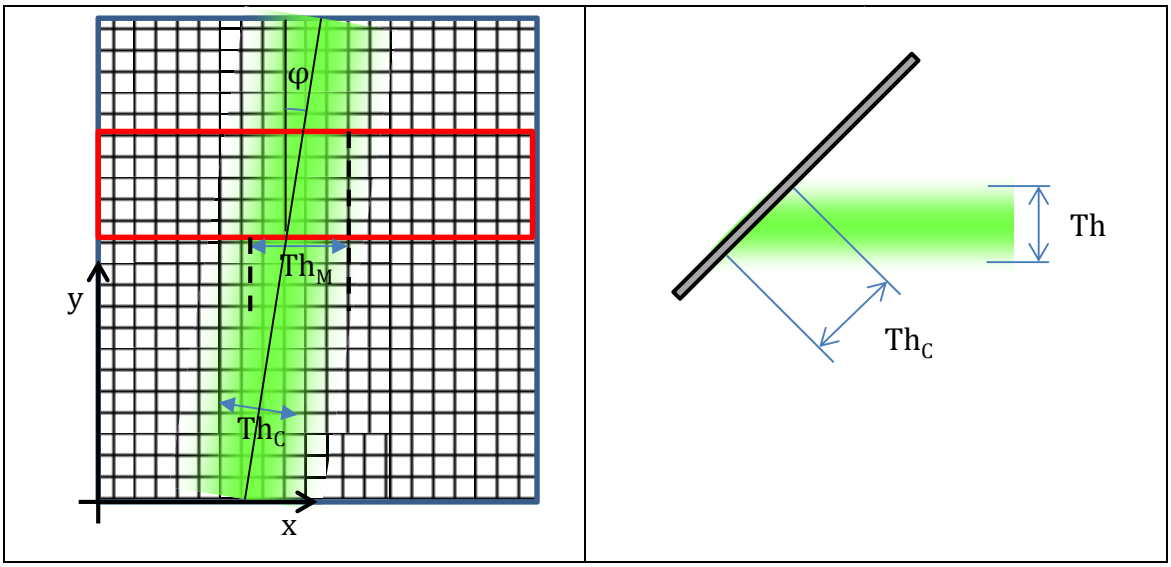

Figure 6.10 Left: Sketch of the projection of the laser sheet (green color) onto the CCD sensor. Right: laser sheet seen from the top and PVC sheet.

The following correction is used then, to account for the two effects mentioned above:

$$Th_C = (Th_M - \tan\varphi \, n_{lines}) \cos\varphi$$

Where Th_M is the value calculated with the estimations below over $I_1(x)$ and $I_2(x)$ and n_{lines} is the number of lines used in the averaging process, in this case 100.

A more correct methodology would have been interpolating the data over new points which followed the exact perpendicular direction to the laser sheet. However, as φ was small (exactly, φ=2.4º) the correction above was considered sufficient. Indeed, Th_M is increased by ~4 pixels with respect to Th_C due to the angle effect. This effect is only important on the thinnest laser sheets (of ~20pixels), which are not used in this work.

Finally, the laser thickness values given in Figure 6.11-right are obtained from the different Th_C indicated in Figure 6.10 multiplied by the sinus of 45º, to account for the angle between the PVC sheet and the laser direction, as illustrated in Figure 6.10-right.

$$Th = Th_C \sin 45$$

From $I_1(x)$ and $I_2(x)$, two different estimations were used to provide the laser sheet thickness:

1. The data points were fitted with a Gaussian Laser profile, and the value of the thickness was obtained from the adjusted parameter on the exponential. Both the data and the fitted exponential are plotted in Figure 6.11-right.

2. The thickness was obtained as the distance between the data points that had an e^{-2} intensity ratio with respect to the maximum intensity.

The results at a distance of 1.5m from the laser formation optics are plotted below; which was the distance where the measurements were performed. The two estimates mentioned above and the two laser profiles are plotted.

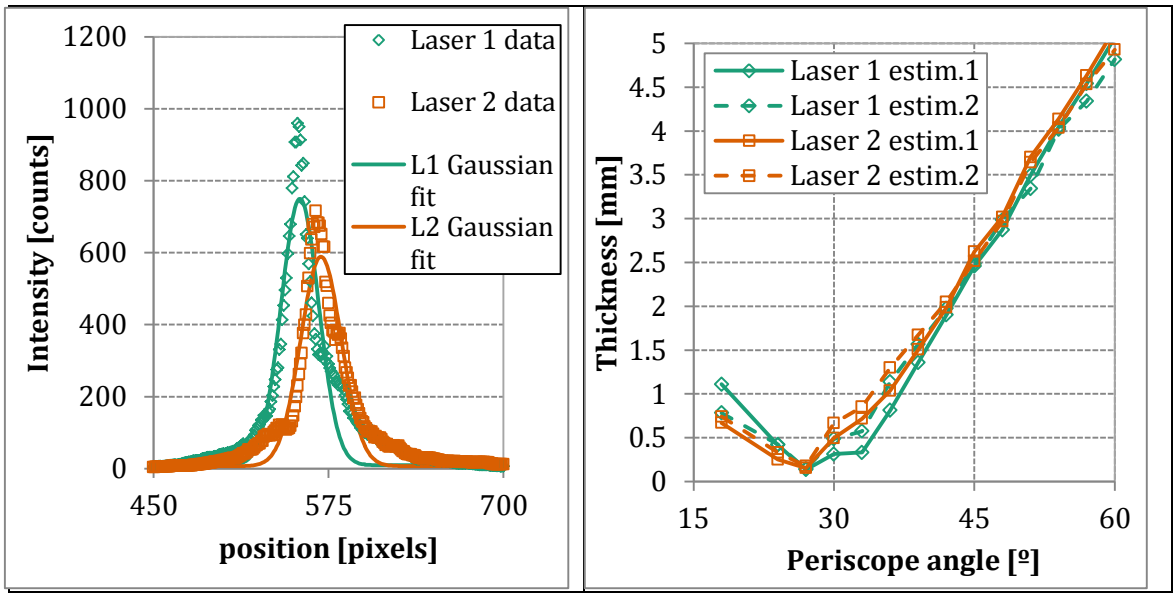

Figure 6.11 Left graphs: laser sheet profiles obtained by the averaging process described above, for one of the positions of the laser formation optics. Right: Laser sheet thickness profiles as a function of the angle turned on the laser sheet formation optics.

As can be appreciated in Figure 6.11-right, for the thinner laser sheets, there are larger differences between the two laser profiles and between the two thickness estimations. Hereinafter, the average value of the laser pulses and of the two estimations is provided.

It can be observed in Figure 6.11-left that the lasers had a misalignment offset. From the data measured the offset is of approximately 0.2mm, for the whole set of positions. The overlap is used to characterize the relative importance of this offset. It is obtained by integrating the laser intensity products normalized with each laser profile, as equation below shows:

$$Laser\ overlap = \frac{\int_{Q_S} I_1(x) I_2(x) \mathrm{d}x}{\sqrt{\int_{Q_S} I_1(x)^2 \mathrm{d}x \int_{Q_S} I_2(x)^2 \mathrm{d}x}} \tag{6.5}$$

In (6.5) the integration is performed along the CCD quadrant where the laser profile is (indicated by Q_S). This is not the same expression than Grayson *et al.* (2016) use. However, the one above is preferred due to the differences existing in intensity between the two laser profiles. The values provided in Grayson *et al.* (2016) on the influence of this

parameter are still used as guidance here, for lack of better ones. The value of the overlap is provided in Figure 6.12, calculated from $I_1(x)$ and $I_2(x)$ as defined above.

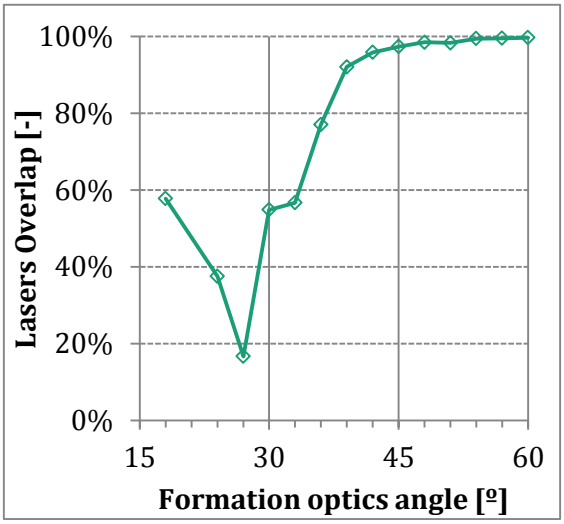

Figure 6.12 Overlap between the two laser profiles, as defined in (6.5)

As was mention on the requirements, the overlap should be above a 70%, for this parameter to not interfere with the characterization of spatial gradients errors. This is achieved first for an angle turned of 36º, which has an associated laser sheet thickness of 1.1mm. How the rest of requirements related to the laser sheet are fulfilled is detailed in section 6.4.

6.3.2 **Seeding device**

The following requirements are achieved on the seeding generator (cf. 6.1):

- The seeding droplets need to be small enough to follow the turbulence of the flow.
- The tracers need to scatter sufficient light, for which their size cannot be too small (the light scattered is proportional to their surface).
- The number of particles needs to be large enough for the PIV algorithm to find a displacement vector. Usually, an interrogation volume needs to contain around 10-20 particles to successfully provide a displacement.

The seeding device available was studied and characterized in Legrand *et al.* (2017). On that work, the droplet size and the volume fraction occupied by the particles are given as a function of the feeding pressure, the liquid employed (two were tested: pure Propylene-glycol -PG- or a solution of 60% in weight of PG and 40% in water) and the depth of the drilled holes into the liquid. For more details, the reader is referred to that paper. From the results of that study, it seemed that a priori the necessary requirements could be achieved by the seeder device.

However, for the seeding adjustment prior to the measurements, when the tracers were mixed with the main air flow (as depicted in Figure 6.4-left), barely any particles appeared on the images. In contrast, the particles, as going out of the seeder and without mixing them with the main air flow, were clearly visible and seemed to be enough for the flow rate required.

In order to diagnose and solve the problem many things were tested:

- The pressure losses of the air upstream the seeder were reduced.
- The pressure losses downstream of the seeder were varied with a butterfly valve. This was done to observe the capacity of the seeder of overcoming pressure.
- The seeded flow injection into the main flow was placed at different points within the experiment: (i) in the pipe upstream the mixing chamber with different types of junctions and (ii) each flow into a different inlet in the bottom of the mixing chamber. No benefits were observed.
- The possibility of turbulence and high velocities inside the tubes making the particles impact was researched as well, and did not seem to be the problem.

In parallel to the problem diagnosis, dedicated devices for seeding injection were developed, such as:

- Perforated plates which were hollow and allowed the circulation of seeded air through the inside were used. The perforated plate had additional holes to inject the seeding just upstream the measurement zone (see Figure 6.13). The aim of these devices was to reduce the droplets impact on the walls, when mixed with the high velocity main flow. Mixing the seeding with the main flow over a larger area and just before the measurement region should reduce this problem. Different models were 3D printed and tested without any improvement.
- A perforated tube (of 4 cm of diameter) going through the nozzle upstream the contraction and with drilled holes for expelling the seeded air. This device allowed choosing the angle of seeding injection with respect to the stream and had a good performance in terms of seeding. On the other hand, the modification of the main flow was high, which lead to the decision of developing a profiled tube; however, the cause for the seeding disappearing was found out before finishing the development so it was stopped.

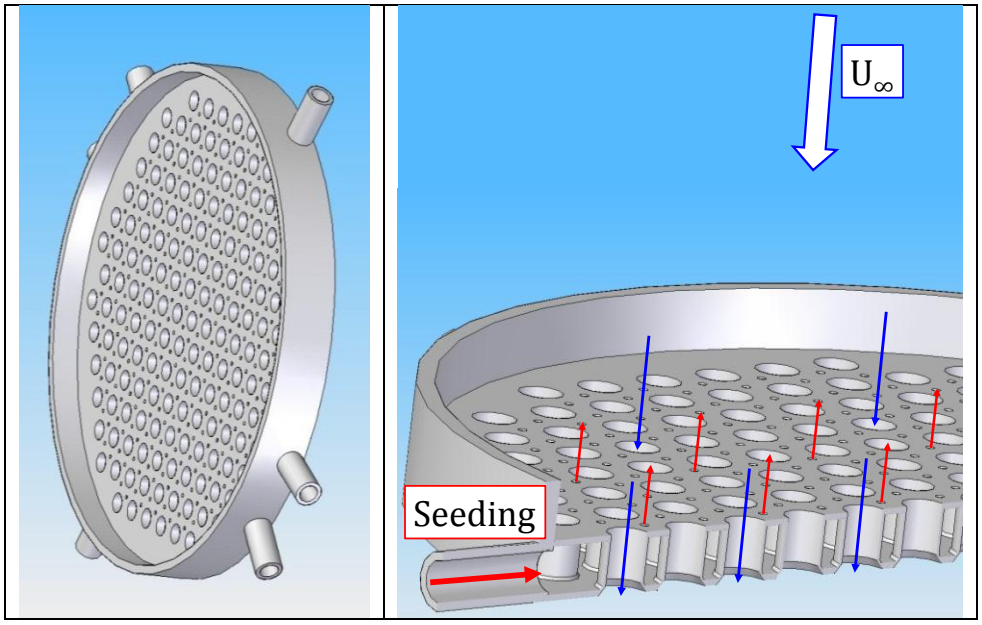

Figure 6.13 Left image: Perforated plate with additional holes for seeding injection. Right image: open section of the perforated plate of the left image. Red arrows illustrate where the seeded flow circulates and blue arrows where the main flow does.

The reason for the tracers disappearing was that the PG droplets were evaporating pretty quickly when they were mixed with the dry air from the compressed air facilities. Therefore, in order to solve the issue, another liquid was employed to generate the droplets (a solution based on food-grade glycols and demineralized water, Martin Harman™, 2015) instead of introducing the profiled pipe into the main flow to avoid perturbations to the stream. With the new liquid, the flow could be seeded at an acceptable level. The seeded flow was injected at the bottom of the mixing chamber, as indicated in Figure 6.4, and the perforated plate used was then a normal one.

The feeding pressure was set at 4 bar gauge, because a large flow rate of air needed to be seeded. Larger pressure values could be imposed at the inlet of the seeding device; however, this value was preferred to avoid the compressed air line pressure going below the imposed pressure on the seeder. That option could result in oscillations in the quantity of particles injected and was not considered.

The characterization on the particles size from Legrand *et al.* (2017) did not include this new fluid, so no measurements are available related to the particle size. However, on that work, a method is provided to estimate the particles size, and that is used here. Based on the 4 bar gauge pressure used to feed the seeder, on the ambient conditions (T=30ºC, p=0.9bar) and with the surface tension of the solution of 60% in weight of PG and 40% in water, the Sauter mean diameter obtained is D_{32}=1.66μm. Roughly, the particles diameter obtained should be then ~1.7μm.

To assess the capacity of the particles to follow the flow the Stokes number can be calculated. For such purpose, the Kolmogorov scale characteristic time is used (obtained from the turbulence imposed in 6.4), and the particles relaxation time (cf. 5.3.14). Kolmogorov scale characteristic time is estimated from $\tau_\eta \sim \eta/u_\eta$ which with η~0.1mm and u_η~0.15m/s (see section 6.4) gives τ_η~0.001 seconds. The Stokes number, defined as $St = 2\pi\tau_P/\tau_\eta$ is given in Table 6.1 below, together with the amplitude ratio and the phase calculated in 5.3.14:

Table 6.1 Relaxation time, Stokes number, amplitude ratio and phase expected for the tracer particles motion, related to Kolmogorov scales.

d_P [μm]	τ_P [μs]	St	Amplitude ratio	Phase
1.7	9.4	0.06	0.998	-3.6º

From the Stokes numbers calculated and per the results of Chapter 5, the particles size 1.7μm should fully recover the amplitude of the oscillations (it was recovered for Stokes up to 0.5). The phase, which is almost negligible, should not interfere with the characterization of the error of interest, as stated in 5.3.14.

As to the requirements of if the number of particles was sufficient and if the particles scattered sufficient light, this was verified to be this way on a preliminary test prior to the final measurements.

6.3.3 **Other PIV acquisition parameters**

The rest of requirements related to the PIV measurement technique, can be obtained as follows:

The **interrogation window size** (which needs to be smaller than smaller than $Th_{MAX}/4$) can be reduced by increasing the magnification of the setup or by using smaller interrogation windows in the PIV algorithm. Both are limited by the presence of a minimum number of particles per interrogation window, usually around 20 particles are considered sufficient (Keane and Adrian, 1990). The size of the interrogation window projected into the measurement region, D_I, is:

$$D_I = \frac{IW_p d_r}{M_0} \tag{6.6}$$

The smallest value of IW_p typically used is 16 pixels, and 32 pixels size normally provides good results, as in Chapter 4.

The **displacement difference parameter** $a/D_P = \sqrt[3]{\epsilon \max(D_I, Th)}\,\Delta t M_0/D_P$. As on this experimental campaign all laser sheet thicknesses are larger or of the same order than D_I, the parameter becomes $a = \sqrt[3]{\epsilon Th}\Delta t M_0$. It can be adjusted through ϵ as mentioned in 6.2.3. As to the PIV acquisition parameters, the variation of a through Δt is included on the measurement campaign objectives. If the values of a/D_P required result in imposing a Δt which would enhance much more other error different than that of spatial gradients (typically the out-of-plane motion errors), the rest of parameters should be tuned to avoid that. In that sense, the effect of the particle image size is clear. a can be further increased by enlarging the laser sheet effective thickness and the magnification M_0.

The **displacement** induced by **Kolmogorov scales** needs to be large enough for those scales to be properly characterized. The characteristic velocity is given by: $u_\eta=(\nu\epsilon)^{1/4}$ and the displacement by: $u_\eta \Delta t M_0/d_r$. Therefore, the magnification could be increased if for the lower Δt's envisaged in the experimental campaign the displacement was too small.

The **depth of field** (which needs to be as large as the largest laser sheet thickness: $\delta z \sim Th_{MAX}$) can be estimated by (Adrian and Westerweel, 2011):

$$\delta z \cong 4\left(1 + \frac{1}{M_0}\right)^2 f^{\#^2}\lambda \tag{6.7}$$

The depth of field can thus be increased by diminishing the magnification M_0 or by closing the aperture $f^\#$. The light wavelength, λ, is fixed.

In typical experimental arrangements, the **particles image diameter** is given by the diffraction limited diameter (Adrian and Westerweel, 2011). It is generally much larger than the geometric image diameter for magnification $M_0<1$ and common set of lenses $f^\#>1$:

$$d_s = 2.44(1 + M_0)f^\#\lambda \gg M_0 d_P \tag{6.8}$$

The particle image diameter should be between 2 and 3 pixels. Therefore, it can be varied through the magnification and the f-number of the camera lenses. Additionally, defocusing the particles is sometimes used to increase the size. However, that leads to a reduction in brightness (Olsen and Adrian, 2000), thereby decreasing the SNR. This latter option was not considered as possibility.

The **field of view** is adjusted by the magnification of the camera lenses. The FOV should be larger than the large turbulent scales, ℓ_T, but at the same time also should avoid the mixing layer and the period of establishment. The field of view is calculated from:

$$FOV = \frac{sensor\ size}{M_0} = \frac{15.2mm}{M_0} \tag{6.9}$$

The **out-of-plane motion** parameter $u'\Delta t/Th$ has to be kept below a 25%. This requirement can be achieved by choosing the combinations of Δt and laser sheet thickness accordingly. Additionally, u' can be varied as was mentioned in 6.2.3.

6.4 DEVELOPMENT OF THE FINAL SOLUTION

In this section, the design process is described. The measurement had to be adjusted after a preliminary test, but the idea was avoiding having to perform several tests until achieving the final design, for which this design process was followed.

In Table 6.2 the features related to the PIV technique that influence on several requirements at the same time are summarized. When a requirement is written under the "on one hand" column, it means that the parameter variation should help on fulfilling the requirement. It should be recalled that the objective of the measurement campaign is to characterize spatial gradients errors, and therefore other error sources should be kept at low values for the whole set of Δt's and laser sheet thicknesses employed in the measurement campaign.

Table 6.2 PIV measurement parameters that influence on several requirements of the dedicated experimental setup at the same time.

Parameter	Variation	On one hand	On the other
Magnification	Larger	Gives smaller interrogation windows and larger displacement differences *a.*	Reduces the depth of field. The particles inside an IW are reduced.
Magnification	Smaller	The depth of field increases. The particles inside an IW are increased.	The FOV increases[6].
$f^{\#}$	Larger	Produces larger depth of field.	Reduces particles light intensity. Increases particles image diameter[7].
Laser sheet thickness	Larger	Allows producing error due to laser sheet thickness and gradients interaction.	May produce error from particles low SNR.
Laser sheet thickness	Smaller	Allows reducing the error due to laser sheet thickness and gradients interaction.	May produce error from out-of-plane motion.
Δt	Smaller	Allows reducing the errors due to out-of-plane and spatial gradients.	The errors that scale with the pixel size could acquire too much importance.
Δt	Larger	Allows producing error due to laser sheet thickness and gradients interaction.	May produce error from out-of-plane motion instead of from spatial gradients.
Particles size	Larger	Gives brighter particle images.	Particles may not follow the smaller turbulent fluctuations.
IW size in pixels	Smaller	Gives smaller interrogation windows projected into the measurement.	Particles number inside the window is reduced.

Equally, the following features related to the turbulence of the flow are interconnected:

[6] That interferes with the requirement of the flow being homogeneous and uniform inside the FOV. On the other hand, the FOV should be larger than ℓ_T.

[7] Increasing the particles image diameter may not always be a bad thing; it can be good if the diameter is below 2 pixels.

Table 6.3 Perforated plate parameters that influence on several requirements of the dedicated experimental setup at the same time.

Flow feature	Variation	On one hand	On the other
Perforations size	Larger	Gives larger length-scales.	Increases period of establishment. Increases also the smaller length-scales.
PP solidity	Larger	Gives larger length-scales and velocity fluctuations.	Same than previous feature.
Feeding pressure	Larger	Gives larger velocity fluctuations.	Increases oscillations in the mean velocity value.
Nozzle exit area	Larger	Increases measurement region size.	Decreases turbulent fluctuations (due to the reduction in the free stream velocity).
Distance to PP	Larger	Allows avoiding the period of establishment of fully developed turbulence.	The mixing layer could interfere with the measurements. Kolmogorov scale increases, Kolmogorov velocity decreases and a/D_P decreases.

The final setup was obtained by taking into account these considerations. The process to choose a parameter is detailed below, with the objective values set initially. The final values with which the measurements were performed are given at the end of this section.

6.4.1 PIV acquisition parameters adjustment

As mentioned in section 6.3.1, the minimum laser sheet thickness that fulfilled the requirement of the overlap between both laser pulses was of 1.1mm. From this value, the maximum laser thickness was studied.

The maximum laser thickness Th_{MAX} needs to be fixed together with δz, as δz should be $\sim Th_{MAX}$. In addition, δz depends on the magnification M_0 which imposes as well the interrogation window size D_I (amongst other things, but this one was found to be the most restrictive). The interrogation window size has to be $D_I \leq 4Th_{MAX}$; for this reason it is fixed together with δz and Th_{MAX}. By dividing expressions (6.6) and (6.7) a relation between δz and D_I can be obtained:

$$\frac{\delta z}{D_I} = \frac{4\lambda}{d_r} M_0 \left(1 + \frac{1}{M_0}\right)^2 \frac{f^{\#2}}{IW_p}$$

This relation is plotted below in Figure 6.14, for varying M_0 and $f^{\#}$. By combining the requirements mentioned just above, it can be appreciated that $\delta z \geq 4D_I$. As can be seen below, this is accomplished for all magnification values plotted if $f^{\#} \geq 11$. The case $f^{\#}=8$ also attains values that serve for $M_0 \leq 0.2$. The IW size chosen is of 32 pixels, which is usually considered as the minimum limit to ensure valid measurements without large errors.

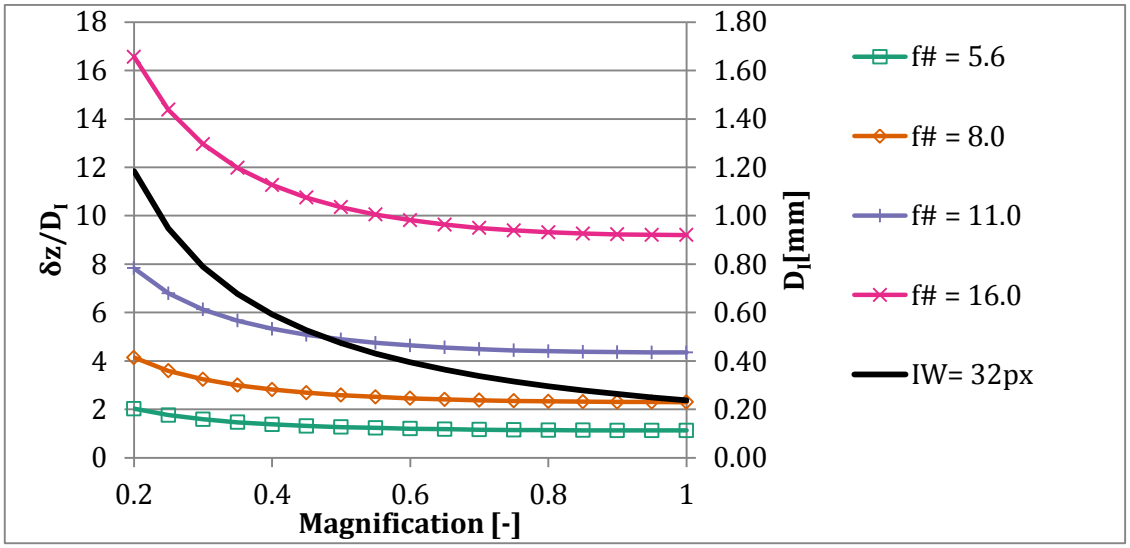

Figure 6.14 Variation of $\delta z/D_I$ and of D_I with M_0 and $f^{\#}$.

Additionally, by varying M_0 and $f^{\#}$ the particle image size is imposed as well (cf. 6.3.3). Consequently, Th_{MAX}, δz, D_I and D_P should be calculated together. The variation of δz and D_P with M_0 and $f^{\#}$ is plotted below in Figure 6.15. On both cases, the gray filled rectangles indicate values that should not be used. A minimum δz of 2mm has been plotted because the laser sheet thickness has to be increased, and Th_{MIN} is already of 1.1mm. In Figure 6.15-left, 4 times the size of a 32px interrogation window is also plotted, as that should be at least the value of Th_{MAX} and δz.

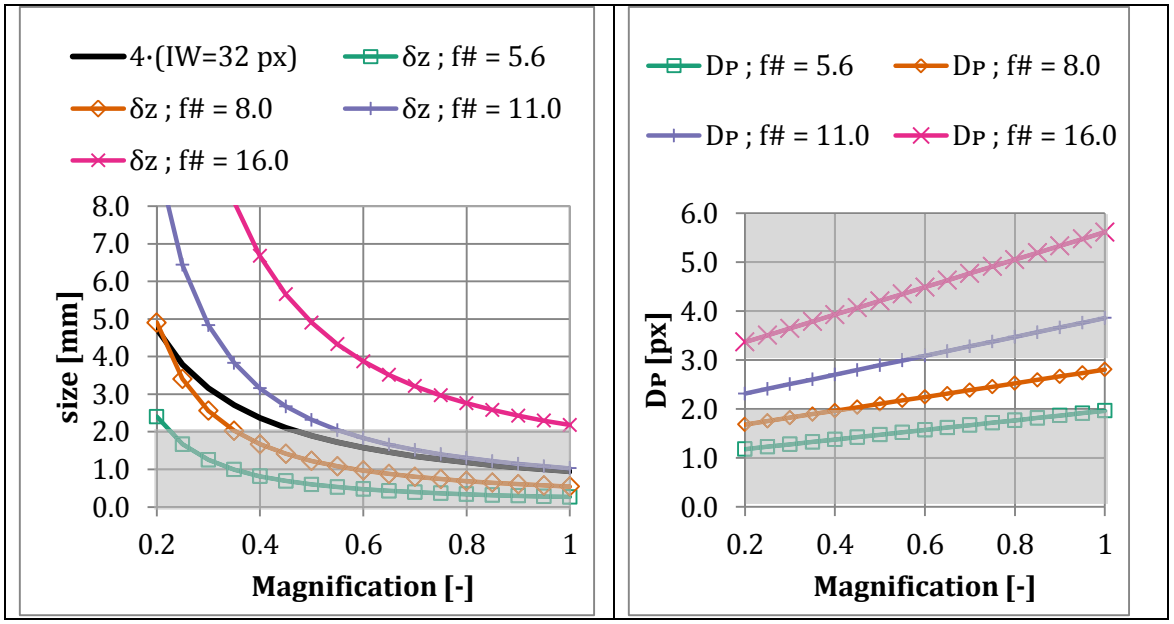

Figure 6.15 Left: variation of the depth of field (δz) and the interrogation window (IW) size with the magnification, for different f-numbers of the lenses. Right: Variation of the Airy disk size in pixels with the magnification, for different f-numbers of the lenses.

Much smaller magnification values than those plotted in the Figure 6.15 would probably not fulfill other requirements since the FOV gets too large. For example, for M_0=0.15 the FOV is of 10cm, which could present problems with the jet mixing layer having a too large presence inside the images. The maximum printable perforated plate is of 19cm in diameter and the measurements cannot be performed just after the plate, so the size of the

region available for measurements should be much smaller than that. In addition, for smaller magnification values than those plotted, Th_{MAX} would have to be increased considerably, which could result on very few light power received by particles. That could generate larger errors in determining the correlation peak location (cf. 5.3.10) and large outliers' occurrence, which could interfere with the characterization of spatial gradients errors.

As can be appreciated on the left graph of Figure 6.15 for $f^{\#}$=16 the depth of field surpasses the minimum stipulated largest laser sheet thickness value for all magnification values. However, for this $f^{\#}$ value the light received on the camera sensor could be greatly reduced. Additionally, the particle image size stays above 3 pixels for all M_0 values depicted, which is outside the advised range. Therefore, $f^{\#}$=11 was preferred. For this f-number, for M_0<0.55 δz surpasses already 2mm and D_P is below 3px. A value of M_0~0.4 was preferred, as that gives δz~3mm and that permits a larger effective increase of the laser sheet thickness, which should allow to better reveal the error variations. For M_0~0.4 the IW size is D_I~0.6mm and the Airy disk obtained from these choices is 2.7 pixels which falls within the acceptable range. The camera with these parameters is henceforth identified as camera 1.

Since a second camera was available, it was also set up in order to obtain images with different parameters without additional recording time. The parameters chosen were M_0~0.2 and $f^{\#}$=8. This camera (camera 2) should receive more light; however, the Airy disk is 1.7 pixels which could produce important peak-locking errors. For the second camera the aim was to process the images with 16pixels^2 windows to obtain the same IW size in mm than in the previous case. The camera for which the measurement campaign was designed is the camera 1, the purpose of this second camera was to record the images in case they could be useful.

Those magnification values give a field of view of ~4cm for camera 1 and of ~8cm for camera 2, which were taken into account for the target size of the jet potential core, fixed in the next subsection.

6.4.2 **Flow parameters adjustment**

With those parameters defined, the turbulent parameters can be calculated. Turbulent large scales objective was set to ℓ_{T}~$\mathcal{L}$~5mm, so there are scales much larger than D_I (0.6mm) and the thinnest laser sheet (1.1mm) in order to compare them with the ones with measurement errors. Larger values could be sought but that would result in (i) a larger Kolmogorov scale (see expression (6.4)) and (ii) on the period of establishment increasing in size, thus reducing the region where the measurement can be made. From the work of Liu *et al.* (2004) and for the large scale size chosen, the perforated plate diameter (D_H) was set to 10mm. As can be appreciated in Figure 6.5, $\mathcal{L}/D_H$≥0.4, and that should be also the case of ℓ_{T}. The large scales also fulfil ℓ_{T} <FOV, for both cameras.

The Kolmogorov scale size (η) imposed on the requirements as necessary to produce a significant error was ~1/30 of Th_{MAX}, as found on results from the PIV Simulator. With the thicker laser sheet of ~3mm that gives η~0.1mm. As per expression (6.4) the Kolmogorov scales can be expressed as: $\eta = \left(\nu^3 \mathcal{L}/(Au'^3)\right)^{1/4}$. For the value of constant A, 0.5 was taken. This value adjusted fairly well some preliminary tests with grid turbulence, the

turbulent flow used for the numerical tools described in 3.1 and also similar values are found in Yeung and Zhou (1997). With the integral scale value defined above, the target rms velocity fluctuation was set to ~0.5m/s, to achieve the required Kolmogorov scale. Kolmogorov scale velocity would be $u_\eta = \left(\nu A {u'}^3/\mathcal{L}\right)^{1/4}$ giving u_η ~0.15m/s (for that u' value).

In order to reach the required rms velocity fluctuation the stream velocity, the perforated plate solidity $\mathcal{S}_{PP}$ and the distance to the PP are the parameters available. The effect of those variables is summarized in Figure 6.6, from Liu *et al.* (2004). As appreciated from the figure the turbulent intensity u'/U is over 5% for all cases at x/D_H=20. As a result, the stream velocity objective was initially set to ~10m/s. For the perforated plate solidity, a value of 0.4 was chosen, which should still allow obtaining the required turbulent intensity without incurring into a too large period of establishment or large non-homogeneities or non-uniformities. Additionally, Liu and Ting (2007) show that a perforated plate with chamfered holes increases the turbulent fluctuations compared to straight holes. This result was used on the design on the perforated plate to enhance the turbulent fluctuations, placing the larger section downstream. Finally, the distance to the perforated plate for the initial test was set to be x/D_H~10 seeking to have the largest possible u', which would produce a smaller η and therefore the more observable spatial gradients errors, but should still avoid the period of establishment (that was the minimum distance mentioned above). Additionally, much larger distances may not be available due to the mixing layer developing inside the measurement region. After the initial test, the cameras were slightly moved away from the perforated plate, to $13D_H$, as sketched in Figure 6.16. At that distance, the required u' value was attained and the non-homogeneities and non-uniformities were reduced. The final stream velocity U was approximately 8.6m/s.

The exit diameter of the nozzle was chosen to be D_{NOZZLE} =17.5cm. That permitted to have some margin with regards to the mixing layer entering on the measurement zone. Also, with the stream velocity chosen previously, the compressed air facilities were able to feed the flow rate necessary of ~0.2m^3/s without large amplitude oscillations and the seeder was able to provide sufficient particles to perform PIV measurements (Legrand *et al.,* 2017). The maximum size was also limited by the 3D printer available to manufacture the perforated plate, which can print objects up to ~20cm in size. Once this parameter is set, the relation between the measurement regions and the mixing layer and period of establishment are illustrated in Figure 6.16 where the aspect ratios between parameters have been kept. As can be observed, the measurement plane contained the streamwise direction. The axes of both FOV were parallel to the stream and to the perforated plate, as illustrated on the sketch. The mixing layer plotted is the average one (i.e. the one that gives a jet potential core size of $5D_{NOZZLE}$). However, its position is not stationary and a larger area can be covered by it.

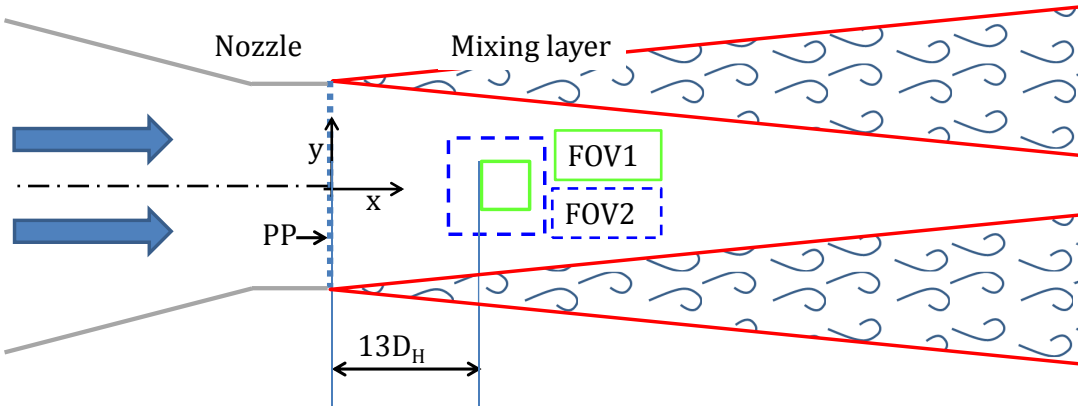

Figure 6.16 Sketch of the dedicated experimental setup. The nozzle is axisymmetric with respect to the dash-dotted black line.

Finally, the time delay between the laser pulses was calculated from the displacement discrepancy span desired. Results from both the PIV Simulator and synthetic images revealed that a range of a/D_P from ~0.2 to ~1 is in general sufficient for these errors to grow significantly to be distinguished. That allows calculating the time delays necessary, for which the estimation of a given on Chapter 5 is used: $a = \sqrt[3]{\epsilon Th}\Delta t M_0$. The time delays were calculated from the Th_{MIN}=1.1mm, to ensure all thicknesses attained the required a values. The time delay calculated this way, together with the out-of-plane parameter and the small scales displacement, are given in Table 6.4 for both cameras.

Table 6.4 Final parameters of the dedicated experimental setup for the thinnest laser sheet, for both cameras.

		Camera 1		Camera 2	
Δt [μs]	$u'\Delta t/Th$	a/D_P	$u_\eta \Delta t M_0/d_r$	a/D_P	$u_\eta \Delta t M_0/d_r$
20	1%	0.2	0.14	0.1	0.07
120	5%	0.9	0.85	0.7	0.42

In principle, after the preliminary error study of section 5.3, for those parameters the predominant error should be the ensemble of errors induced by spatial gradients. The measurement campaign then should allow characterizing the error value for different laser sheet thicknesses, as pursued. As for the smallest time delay the Kolmogorov scale displacement is of 0.15 pixels, it was decided to add a measurement at Δt=10μs to better assess the errors that scale with the pixel size (e.g. peak-locking). The calculation process of the parameters is detailed in section 6.5.3; the parameters values for the full set of test cases are provided in Table 7.3.

The final Kolmogorov scale size, as calculated in section 6.5.3, is η=0.12mm and u_η=0.14m/s. The final magnification value for camera 1 was M_0=0.37, which gives a δz=3.4mm and D_I=0.65mm. Camera 2 images have not been used at the end. The laser sheet thicknesses used were 1.1mm, 2mm and 3.5mm, with overlap values of 75%, 96% and 98%. 2 additional Δt's were added between those of Table 6.4, 50μs and 85μs, for all laser sheets. Additionally, for the widest laser sheet, two more Δt's were added to have a more smooth variation in a/D_P, 35μs and 67μs, plus the Δt of 10μs mentioned above.

As to the rest of requirements, focusing on the first camera only which was the only one used at the end, the large scales, ℓ_T, have been estimated in section 6.5.3.2 to be ~11mm. That gives $\ell_T/D_I \approx 17$, $\ell_T/Th_{MIN} \approx 10$ and FOV/$\ell_T \approx 4$. In consequence, all requirements

associated to the large scales are fulfilled and therefore the large-scales should be properly characterized.

6.5 FINAL ASPECTS OF RELEVANCE FOR THE RESULTS ANALYSIS

6.5.1 PIV Evaluation parameters and results calculation

The whole set of real PIV images was analyzed as follows. The images were not preprocessed, in order to not introduce additional factors into the analysis. Only the images of the first camera (the one with the smaller FOV) are used to calculate $S_{LL}(r)\{u\}$. The second camera results have not been considered necessary for the error characterization. The PIV evaluation and processing parameters were the following:

- Initial offset of the interrogation windows: 8.5m/s in the direction of the flow.
- Multi-grid approach, 2 steps per IW size, from 128 pixels to 32 pixels. The results from each intermediate step are smoothed in regions of 3x3 vectors. Overlap on the intermediate steps is of 50% and on the final one of 0%. The total number of vectors obtained is of 64x64.
- Symmetric image deformation with a bilinear grey level interpolation in all the steps except for the last one, where Whittaker interpolation was applied.
- 3 points in each direction Gaussian subpixel peak-fitting for determining the subpixel displacement.
- Round weighting on the last interrogation window size. The function is determined in section 3.3.4.1. The normalized response of PIV when this window is used is provided in 5.3.3 and is similar to the normalized response of a Gaussian function of D_I size at the e^{-2} waist points.

With respect to the validation of the vector fields, the same two post-processing methods than in synthetic images were used (cf. 3.3.4). The allowable vector range is the following in this case: the vectors had to be contained in the transversal direction in the range [-2,2]m/s and in the streamwise direction in the range [6.5,10.5]m/s. The vectors that pass the allowable vector range criterion are the ones used to calculate the $S_{LL}(r)\{u\}$ values that are shown in Chapter 7 section 7.3. The median filter validation is calculated with the same parameters than synthetic images (cf. 3.3.4), and it is only used to calculate the proportion of outliers used for the coherence of the theoretical estimations. The $S_{LL}(r)\{u\}$ values calculated from the vectors passing both validation criteria are shown in Annex III.

6.5.2 Calculation of $S_{LL}(r)\{u\}$

In chapter 7, for the calculation of $S_{LL}(r)\{u\}$ just the transversal velocity fluctuations (indicated by u_2 in Figure 6.17 below) are used. An average on the streamwise distances spanned by the measurement is used, removing the 5 top and bottom vector lines (about 3mm's in size), to calculate $S_{LL}(r)\{u\}$. The average on the streamwise distances allows improving the convergence of the measurements. However, the turbulence evolves as it advances with the flow (see section 6.2) and as a result, the dimensionless parameters identified to characterize the errors vary in the streamwise direction as well. Nevertheless, since the FOV is small the average for the streamwise positions should have little influence in the results, as is shown below. The value of $S_{LL}(r)\{u\}$ is given for each set of measurement parameters by:

$$S_{LL}(r)\{u\} = \frac{1}{N_x}\frac{1}{N_y}\frac{1}{N_t}\sum_x\sum_y\sum_t\langle[u_2(x,y+r;t)-u_2(x,y;t)]^2\rangle = \frac{1}{N_x}\sum_x S_{LL}(r;x)\{u\} \quad (6.10)$$

Where u_2 are the velocity fluctuations in transversal direction; x and y are the two in-plane directions, as indicated in Figure 6.17 below; t indicates the different time instances recorded; and $S_{LL}(r;x)\{u\}$ is the variation of $S_{LL}(r)\{u\}$ with streamwise distance x (obtained performing the average only in y and t), which is used for some considerations below.

For the calculation of $S_{LL}(r)\{u\}$ some vectors at the borders (5 and 7 mm for each side, 9 and 12 vector lines) were removed from the calculation on the transversal direction. The reasons to proceed in such a way are shown in 6.5.5. The image below illustrates the region used on the calculation (the region shaded in red is not used on the calculations):

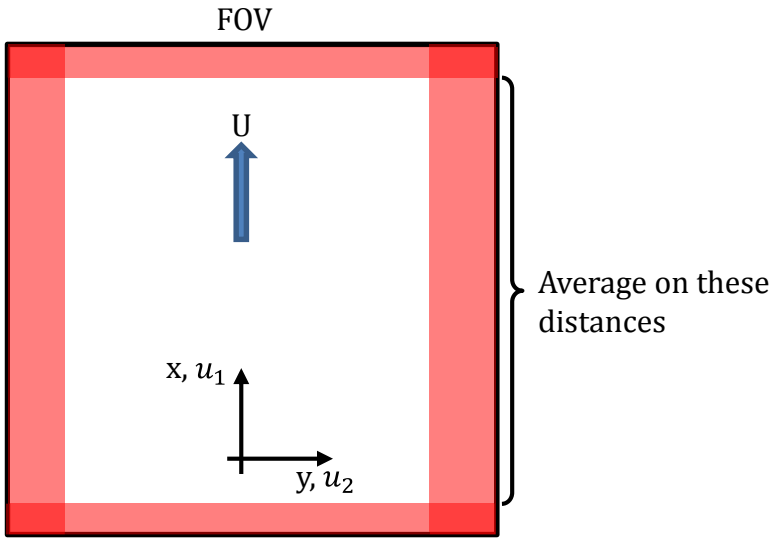

Figure 6.17 Region of an image used for the calculations of $S_{LL}(r)\{u\}$ for the dedicated experimental results.

The function $S_{LL}(r)\{u\}$ of the experimental flow and that of the flow used to generate the results of the numerical tools differ (obtained from a DNS, cf. 3.1). This difference is produced by the fact that the range of scales generated in the experimental setup is smaller than that of the DNS. Both are plotted in the graph below. The case used to obtain the experimental $S_{LL}(r)\{u\}$ is the one with Th=1.1mm and Δt=20μs, which should have the lowest errors.

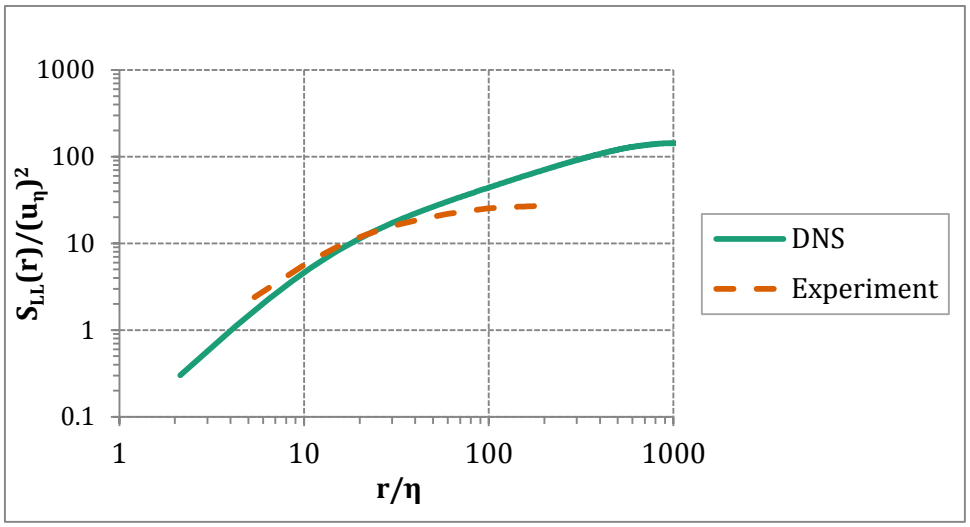

Figure 6.18 Comparison of the $S_{LL}(r)\{u\}$ of the experimental flow and that of the DNS used to generate the results of the numerical tools

6.5.3 Flow relevant parameters estimation

6.5.3.1 *Turbulent rms velocity fluctuations – u'*

This parameter, which influences also on the calculation of Kolmogorov scales, is defined as the standard deviation of the measurements. As was shown in section 6.2 its value changes with the streamwise position. The value of the turbulent rms fluctuations in the transversal direction (the second velocity component, which is the direction used to calculate $S_{LL}(r)\{u\}$) is given by:

$$u_2'(x) = \sqrt{\overline{u_2^2}} = \sqrt{\left(\frac{1}{N_f N_y}\right)\sum_y \sum_f \left(U_2(x,y;f) - \overline{U}_2(x,y)\right)^2}$$

Where $\overline{U}_2(x,y)$ is the time average vector field and $U_2(x,y;f)$ the instantaneous vector field at time instance *f*. As indicated by this expression, to obtain $u_2'(x)$ the average is performed over the different vector fields and over the transversal direction *y*. The value is plotted below.

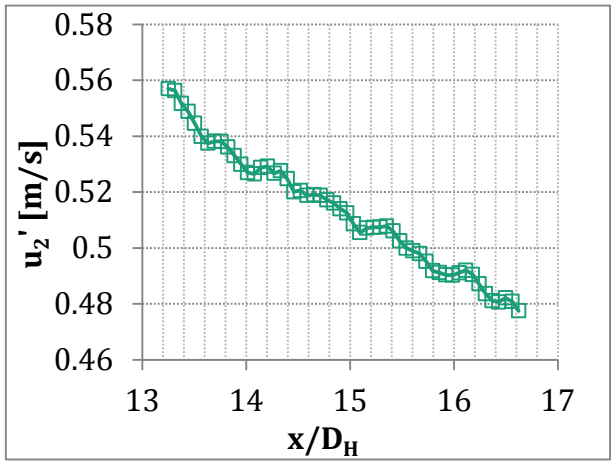

Figure 6.19 Variation of the transversal velocity fluctuations with the streamwise dimensionless distance to the perforated plate.

6.5.3.2 *Other flow parameters*

The mean dissipation rate allows calculating Kolmogorov scales, which, as seen in section 6.2.3, can be obtained from:

$$\eta = \left(\frac{\nu^3}{\epsilon}\right)^{1/4}$$

$$u_\eta = (\nu\epsilon)^{1/4}$$

Where ν is the kinematic viscosity of the working fluid (air) and ϵ is the mean dissipation rate of the turbulent flow. For the temperature of ~30°C on the days of the measurements, $\nu \cong 1.6 \cdot 10^{-5}[m^2/s]$.

Additionally, the displacement difference inside the interrogation volume is also estimated from the dissipation in this work:

$$a = \sqrt[3]{\epsilon\ell}\Delta t M_0$$

Where ℓ is the size of the largest eddy fitting in the volume, which on the cases of this measurement campaign it is the laser sheet thickness *Th*.

The mean dissipation rate has to be determined from the measurements. The advantage of Kolmogorov scale is that ϵ appears with a ¼ power; hence, the errors on the calculation of ϵ will have a reduced effect on the scales. In the case of a, the dissipation ϵ appears with a ⅓ power so again the errors on its calculation will be reduced.

For its calculation, De Jong *et al.* (2009) established that obtaining ϵ from $S_{LL}(r)\{u\}$ yields good results. Following De Jong *et al.* (2009), the method to estimate the dissipation rate relies on the value taken by $S_{LL}(r)$ on the inertial subrange, which is given by:

$$S_{LL}(r) = C_2(Re_\lambda)(\epsilon r)^{2/3} \tag{6.11}$$

$C_2(Re_\lambda)$ is a constant depending on the Taylor microscale Reynolds number; with Re_λ given by:

$$Re_\lambda = \frac{u'\lambda}{\nu} = \sqrt{\frac{15}{\nu\epsilon}}u'^2 \tag{6.12}$$

From (6.11) it is possible to obtain ϵ when the distance r lies in the inertial subrange:

$$\epsilon = \left(\frac{S_{LL}(r)}{C_2(Re_\lambda)}\right)^{3/2}\left(\frac{1}{r}\right) \tag{6.13}$$

As ϵ depends on Re_λ (through C_2) and viceversa, ϵ is obtained iteratively, starting from $C_2(\infty)$=2.12. The values of C_2 for finite Re_λ are obtained from the results of Yeung and Zhou (1997). On that work, DNS simulations are carried out for different Reynolds numbers, and that allows retrieving the following data:

Table 6.5 Variation of C_2 with the Taylor Reynolds number. Obtained from Yeung and Zhou (1997).

Re_λ	C_2
38	1.53
90	1.88
140	1.99
180	2.15
240	2.15

The data was fitted with the polynomial below, which is used on the iterative process:

$$C_2(\mathrm{Re}_\lambda) = -2 \cdot 10^{-5}\mathrm{Re}_\lambda^2 + 0.0082\mathrm{Re}_\lambda + 1.2517$$

The values obtained from Yeung and Zhou (1997) and the polynomial fit are plotted below:

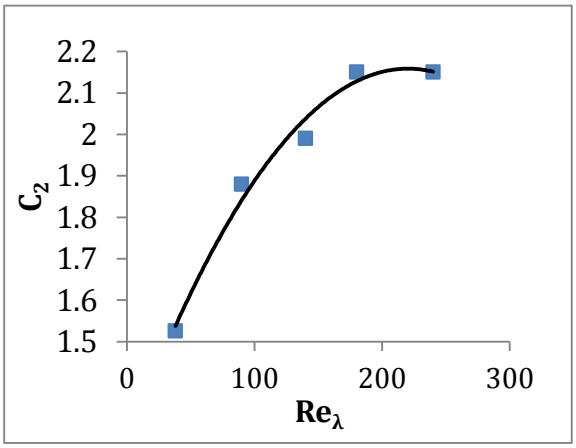

Figure 6.20 Variation of C_2 with the Taylor Reynolds number. Square symbols, data retrieved from Yeung and Zhou (1997); line, polynomial fit used.

The value of $S_{LL}(r)$ in the inertial subrange for the calculation of ϵ is obtained from the case with the lowest thickness and the smallest time delay measured (i.e. Th=1.1mm and Δt=20μs). This case should be amongst the ones with less error. In order to identify the value of $S_{LL}(r)$ in the inertial subrange, $S_{LL}(r)/r^{2/3}$ is a more convenient representation, which is plotted below for three streamwise distances x:

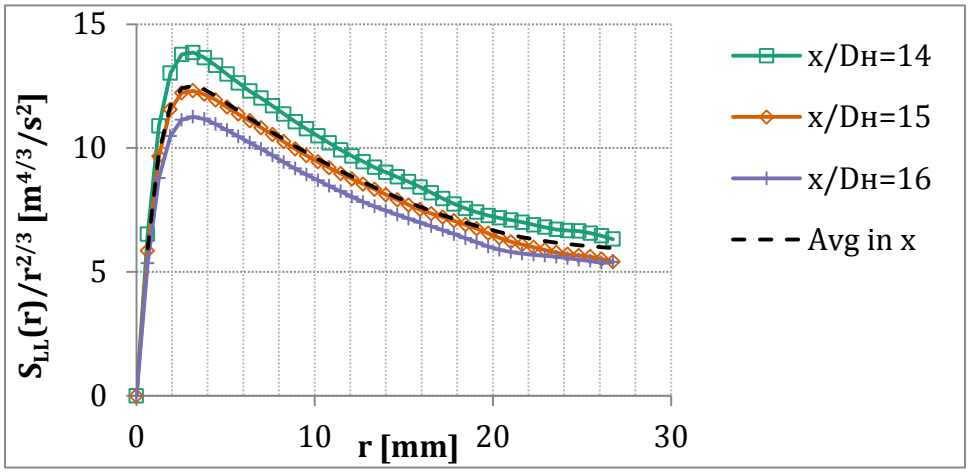

Figure 6.21 Variation of $S_{LL}(r)/r^{2/3}$ with distance r for three different streamwise distances and for the average of all streamwise distances.

In the figure above, the average of $S_{LL}(r;x)$ in all streamwise positions is also plotted by a black dashed line.

With the maximum values of $S_{LL}(r;x)/r^{2/3}$ (which correspond to the inertial range), $\epsilon(x)$ is calculated, which allows to determine $\eta(x)$ and $u_\eta(x)$. Both are plotted below as a function of the streamwise distance to the perforated plate. $\epsilon(x)^{1/3}$ is plotted as well, as it gives a:

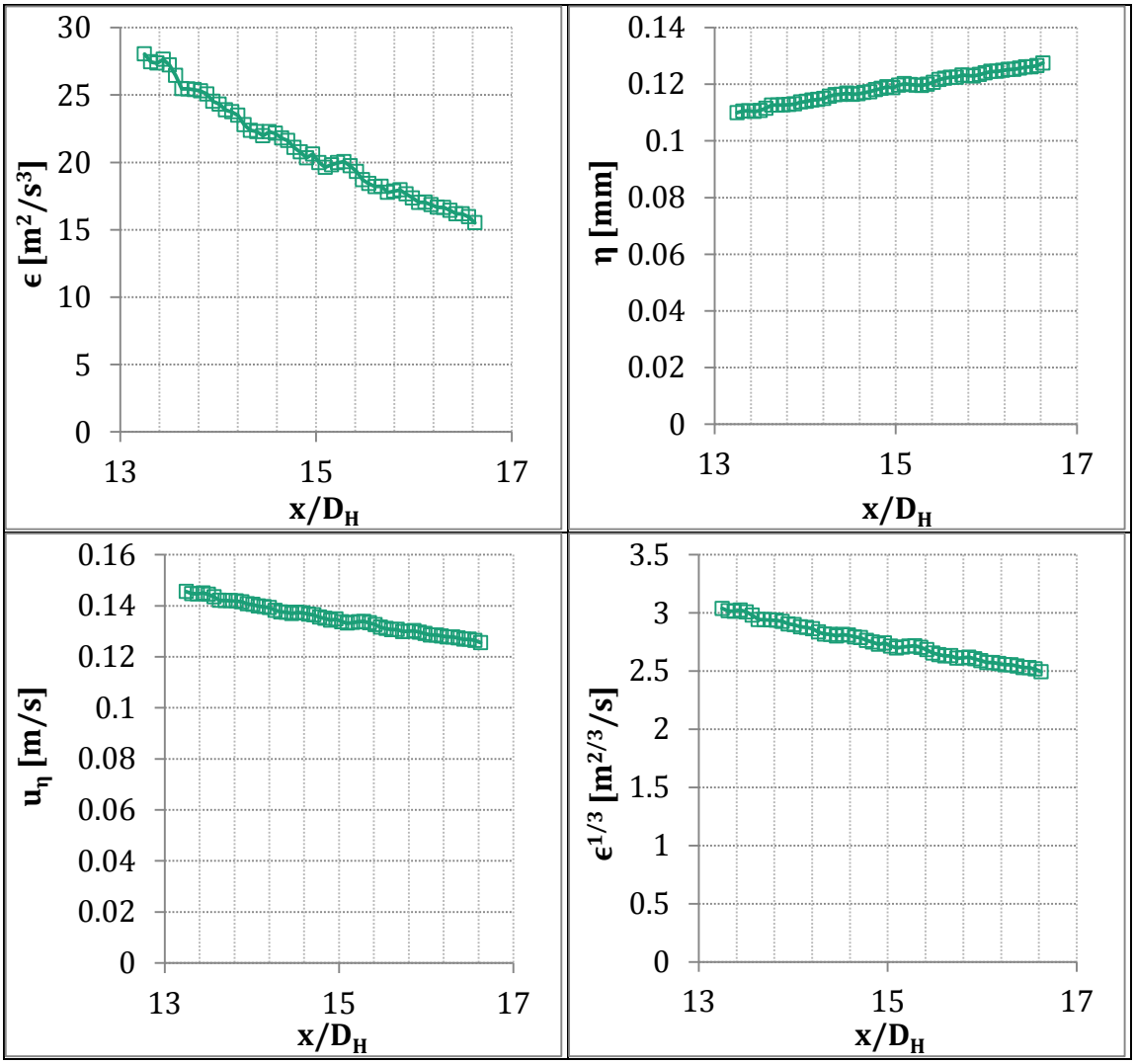

Figure 6.22 Variation of the mean dissipation rate, Kolmogorov length-scale and characteristic velocity and the mean dissipation rate at a 1/3 power with the streamwise dimensionless distance to the perforated plate.

As can be observed in the graphs above, all variables vary with the streamwise distance; then, the errors associated with those parameters would do the same. As mentioned above (see 6.5.2), $S_{LL}(r)\{u\}$ is calculated from the average of $S_{LL}(r;x)\{u\}$ at the available x distances. In consequence, $S_{LL}(r)\{u\}$ incorporates different error values into its calculation. However, in the transversal direction similar variations are given, as is shown in subsection 6.5.5.2. Those variations cannot be avoided and thus it has been preferred to calculate $S_{LL}(r)\{u\}$ from the average of $S_{LL}(r;x)\{u\}$ to improve the convergence of the results.

The values of ϵ, η and u_η used to construct the dimensionless parameters associated with the experimental results are calculated then the average of $S_{LL}(r;x)\{u\}$ given in expression

(6.10). u_2' is calculated as the rms of the values provided in the graph of Figure 6.19. That yields the following values:

Table 6.6 Experimental flow parameters

u_2' [m/s]	ϵ [m²/s³]	Re_λ	η [mm]	u_η [m/s]
0.51	21	55	0.118	0.135

It is possible to determine other flow parameters from the ones determined above. Taylor micro-scale can be obtained from expression (6.12):

$$\lambda = \frac{\mathrm{Re}_\lambda \nu}{u_2'} = 1.7 \text{ mm}$$

The large length-scales, ℓ_T, can be linked with Taylor micro-scale and Kolmogorov scales, with the expression below (from Pope, 2000):

$$\ell_T = \left(\frac{\lambda}{\sqrt{10}\eta^{2/3}}\right)^3 = 11.7 \text{ mm}$$

6.5.3.3 *Particles image diameter*

This parameter has been obtained from the auto-correlation of an image with itself, as is typically done. The result is a particle image diameter $D_P \cong 2.1$px, as defined by the distance between the e^{-2} waist points. This definition is the same than the one used in Chapter 3 for the numerical tools. In Chapter 6 The Airy disk size d_S was used, which is defined as the distance between the $e^{(-3.67)}$ waist points (Olsen and Adrian, 2000). The equivalence between both diameters is $D_P = \sqrt{2/3.67}d_s$. Therefore, for this D_P value, d_S=2.8px, coherent with the estimation provided above in section 6.3.3.

6.5.4 Characterization of errors that do not influence on the results

Some errors given for real images that do not appear for the numerical tools are assessed below. These errors should not interfere with the study of the errors of interest of Chapter 7 and for this reason are explained here. Also, as was commented in 6.3.2, the particles slip error should not interfere with the study.

6.5.4.1 *CCD read-out errors*

The effect of this error source can be seen on Figure 6.23, obtained from the average velocity field of the measurement case with the smallest time delay (Δt =10μs, for which $u_2' \cong 0.26$px). The read-oud error induces a positive displacement over the left half of the image and negative displacement over the right half. As a result, a discontinuity appears in the middle of the velocity map.

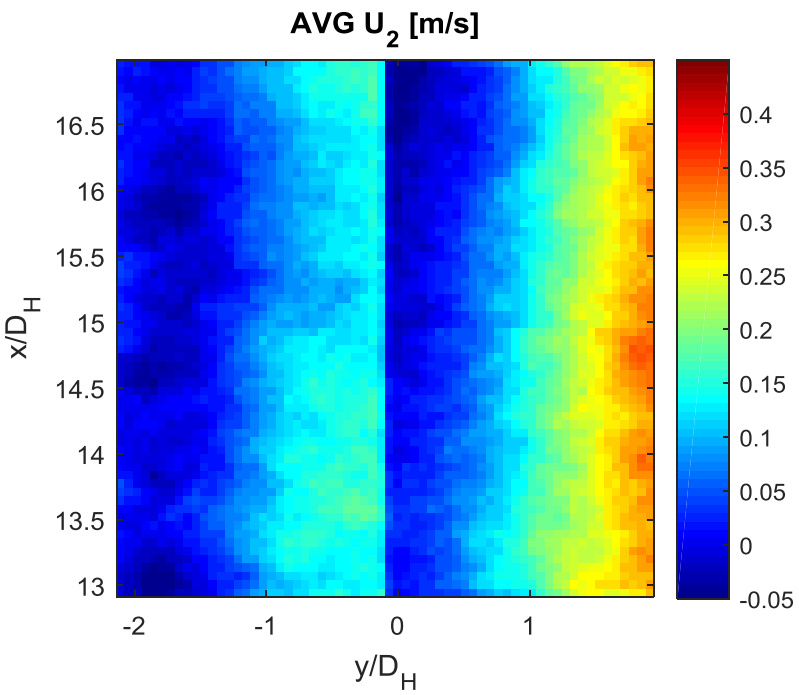

Figure 6.23 Average velocity field for the test case with Δt=10μs. The CCD read-out errors induce a discontinuity at the middle of the field

The CCD read-out error induces a jump in velocity of ~0.12m/s, which for the case plotted is ≅0.06pixels. The displacement induced on each half of the camera should be approximately constant for a whole test case, since seeding was homogeneous and the error depends mostly on the light intensity change between the two exposures. Therefore, this effect should be removed when $S_{LL}(r)\{u\}$ is calculated from the velocity fluctuations, as is the case.

6.5.4.2 *Projection errors*

In Chapter 5, the following estimation was provided for these errors (for the pixels close to the sensor border, which are the ones with more error from this source):

$$\frac{\varepsilon_{proj}}{u'} = 1 + \frac{1000 d_r}{z_0}$$

Where z_0 is the distance between the sensor and the lenses and d_r is the pixel size. For the camera and the lenses used: d_r=7.4μm and z_0~140mm. That yields ε_{proj}/u'~5% and $\varepsilon_{proj}/u_\eta$~20%. As can be observed on the results of chapter 7, the errors of interest reach much larger values than this one. Therefore, it is not expected that this source should cause an appreciable effect in $S_{LL}(r)\{u\}$.

6.5.5 **Deviations from ideal homogeneous isotropic turbulence conditions**

On this subsection, some differences to the homogeneous turbulence case (the one theoretically obtained downstream the grid) are addressed and their possible influence on the results is commented.

6.5.5.1 *Uniformity*

A flow is uniform when the velocity average is independent of position. In the case of grid turbulence, different reasons could be behind the flow not being uniform (high grid

solidity, manufacturing imperfections, non-uniform stream arriving to the grid,…). For these particular measurements, the flow was not uniform where the measurements were obtained, as can be observed from the image below. In the image, the average velocity in time divided by u_2' is plotted, considering a u_2'~0.5m/s constant for all the field of view.

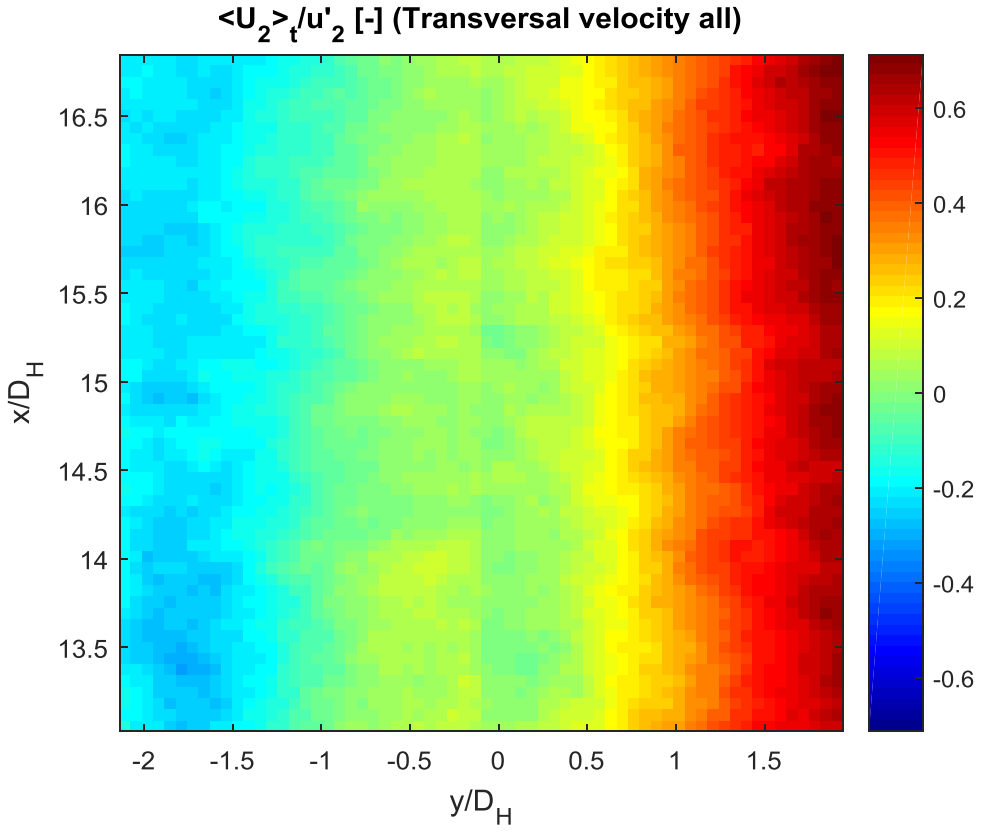

Figure 6.24 Time average of velocity U_2(x,y;t) for the case Th=1.1mm, Δt=85μs divided by 0.5m/s (which is approximately u_2').

It can be observed that the average velocity field in the FOV can contain variations as high as the rms velocity fluctuation. In order to reduce, at least partially, the possible effect of those non-uniformities and of the non-homogeneities shown in the next point, the vectors used in the transversal direction were reduced. A portion of $0.5D_H$ was removed on the left part and $0.7D_H$ on the right part for the calculations of $S_{LL}(r)\{u\}$ (5 and 7 mm respectively).

In order to assess the effect of the non-uniformities remaining, $S_{LL}(r)\{u\}$ is calculated from the instantaneous velocity $\boldsymbol{U(x;t)}$, from the instantaneous fluctuation velocity $\boldsymbol{u(x;t)}$ and for the temporal average of the different realizations $\langle \boldsymbol{U(x;t)} \rangle_t$. The comparison is plotted below in terms of $S_{LL}(r)\{u\}/(r\epsilon)^{2/3}$, for the case with the lowest Th and lowest Δt:

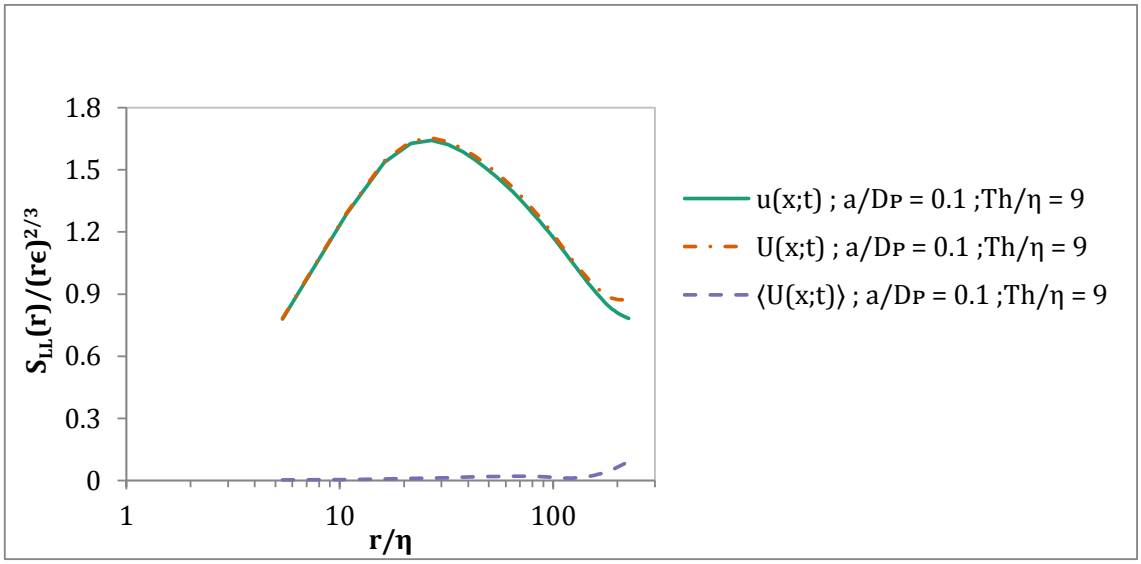

Figure 6.25 Difference on $S_{LL}(r)/(r\epsilon)^{2/3}$ when the function is calculated by either the instantaneous velocity field U(x;t), from the fluctuations velocity field u(x;t) or the average velocity field ⟨U(x;t)⟩, for the lowest Δt and the smallest laser sheet.

In the graph above there is barely any difference appreciated between $S_{LL}(r)\{u\}$ and $S_{LL}(r)\{U\}$, except for the large scales. It is interesting that the difference between $S_{LL}(r)\{u\}$ and $S_{LL}(r)\{U\}$ seems to be $\sim S_{LL}(r)\{\langle U\rangle_t\}$,which has overall a negligible value (again, except for the large scales). To show that it is not a matter of the representation, the differences in $S_{LL}(r)$ for the lowest thickness are shown also. $\Delta S_{LL}(r)\{u\}$ is calculated for the different Δt cases with respect to the $S_{LL}(r)\{u\}$ of the lowest time delay for that thickness, as described in more detail in section 7.3. The differences are calculated from the instantaneous velocity $\boldsymbol{U(x;t)}$ and from the instantaneous fluctuation velocity $\boldsymbol{u(x;t)}$ and are plotted in Figure 6.26. It can be verified over the value of the differences in $\Delta S_{LL}(r)\{u\}$ that the results are almost equal except for the large scales (r/η>80).

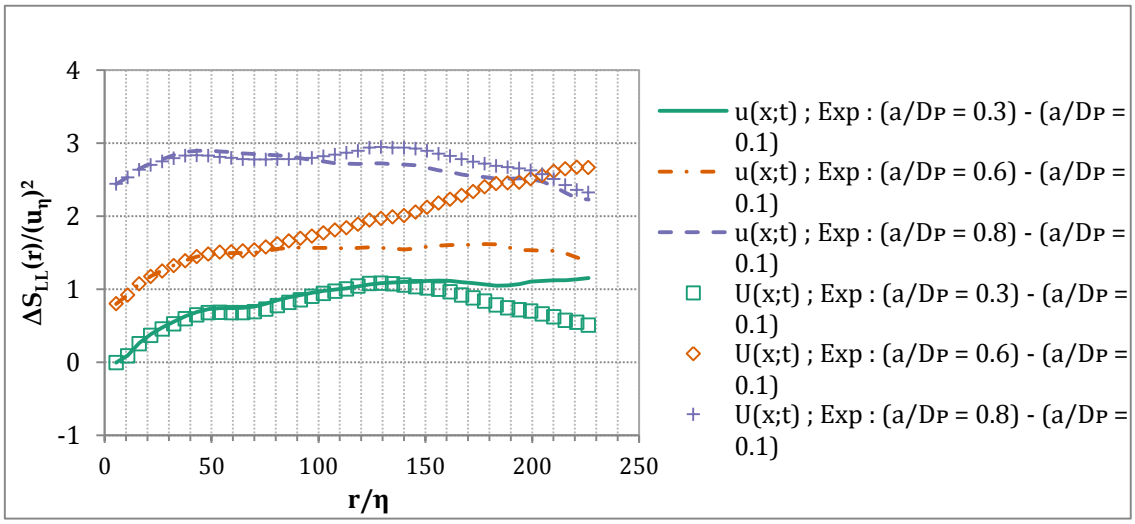

Figure 6.26 Effect on $\Delta S_{LL}(r)$ when the function is calculated by either the instantaneous velocity field U(x;t) (symbols) or from the fluctuations velocity field u(x;t) (lines), for the thinnest laser sheet (Th/η~9).

As previous research shows (for example Ertunc *et al.* (2010), among others), the flow should transition to a more uniform condition as the distance from the perforated plate increases. However, *u'* will reduce, and given the restriction on *u'* for obtaining a small

enough Kolmogorov scale η, measuring much further to the perforated plate was not possible. In any case, the effect from the non-uniform average flow seems to be negligible on $S_{LL}(r)\{u\}$ except scales larger than $r/\eta \sim 100$.

6.5.5.2 *Homogeneity*

Previous research (Liu *et al.* (2004) or Ertunc *et al.* (2010)) shows that turbulence produced by a grid may never reach complete **homogeneity** on the perpendicular direction to the stream (as is conventionally assumed). That makes the flow differ from the one employed by the computer tools described in 3.1. In order to quantify the importance of those variations, the inhomogeneity factor defined by Ertunc *et al.* (2010) is calculated, for the velocity on the transversal direction y:

$$I_{u_2'}(x,y) = \frac{\left(u_2'(x,y) - \langle u_2'(x,y)\rangle_y\right)}{\langle u_2'(x,y)\rangle_y}$$

On the expression above, the average $\langle u_2'(x,y)\rangle_y$ is calculated only over the region where the coefficient is plotted. Below the two images show the value of the coefficient for the full vector field and for the region that is used at the end for the calculation of $S_{LL}(r)\{u\}$:

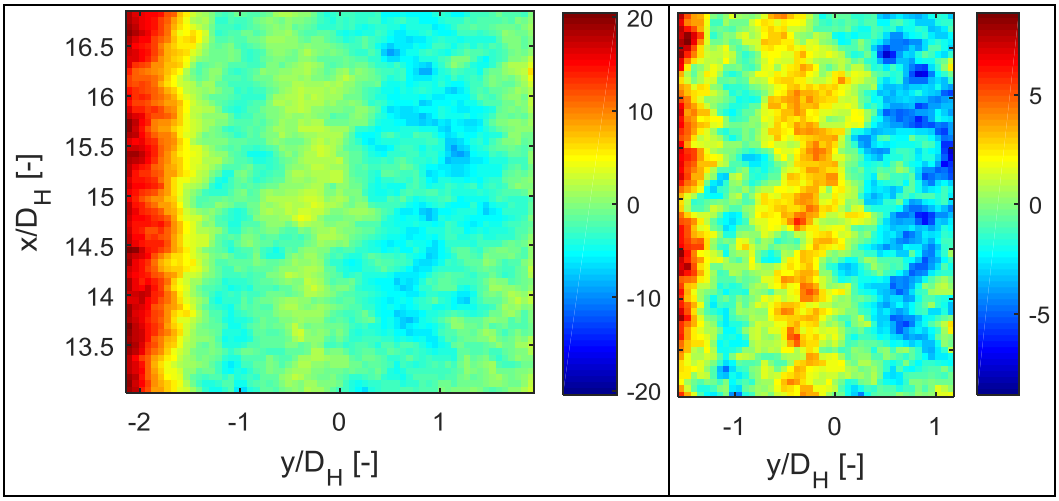

Figure 6.27 Inhomogeneity factor (percentage) of the transversal *rms* velocity fluctuations. Left: full measurement region, right: region used for the calculation of $S_{LL}(r)\{u\}$.

As can be observed, the coefficient reaches a value of 20% when calculated over the whole FOV. When only the region for the calculation of $S_{LL}(r)\{u\}$ is plotted (removing $0.5D_H$ on the left side and $0.7D_H$ on the right side), $I_{u_2'}$ gets reduced ~2 times, as can be observed on Figure 6.27-right. Nevertheless, $I_{u_2'}$ still reaches ±10% within the region selected for the calculation.

Those non-homogeneities appeared on Figure 6.27 will be inevitably integrated into the calculation of $S_{LL}(r)\{u\}$. Indeed, on the case of just making an average on the different time instances (i.e. no average for the different positions), the distance r would still advance through the non-homogeneities. The effect of non-homogeneities would be similar than that of the variations of turbulence in the streamwise direction described in 6.5.3. In consequence, since the non-homogeneities will influence anyhow, the option chosen was to calculate the average in time, and for the available streamwise and transversal

positions, as has been described in 6.5.2. That should allow increasing the convergence of the results.

6.5.5.3 *Statistically stationary*

As mentioned in section 6.2.3, the stream arriving to the perforated plate had oscillations in velocity. The oscillations in velocity produced for the final setup can be observed in Figure 6.28 below, where the average streamwise velocity in the FOV is plotted for each time instance recorded (for the test case with Δt=20μs and *Th*=1.1mm).

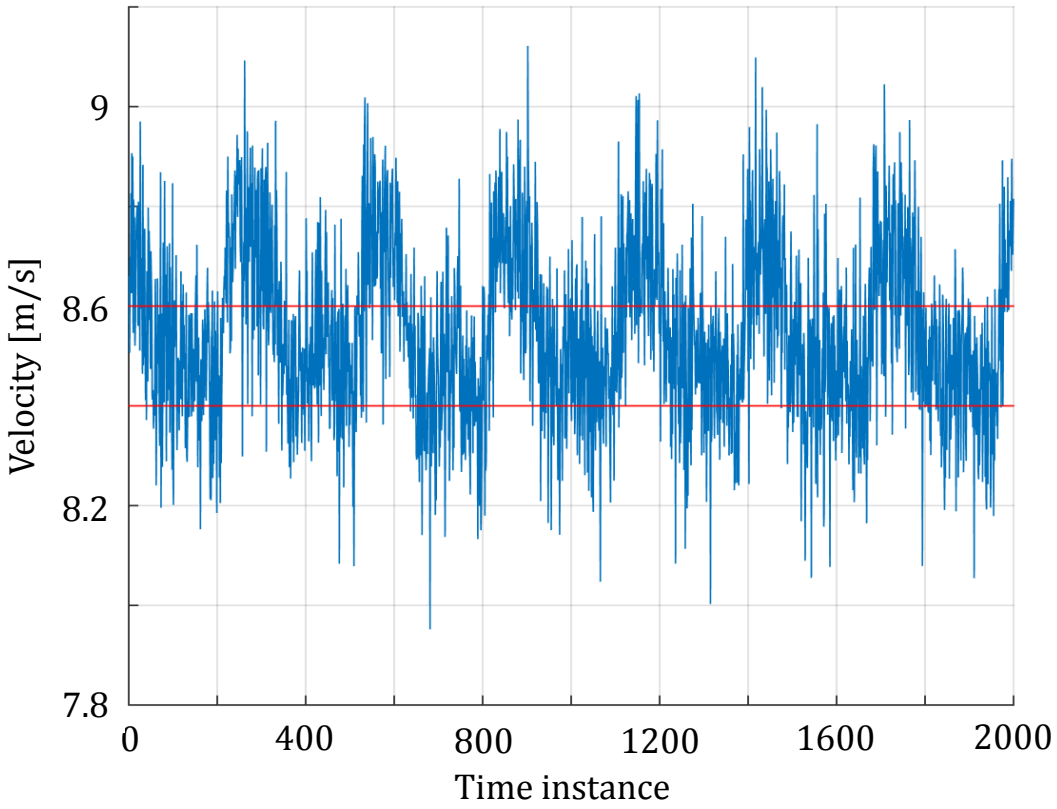

Figure 6.28 Average stream-wise velocity in the FOV as a function of the image count of a test case. Acquisition rate ~1Hz. The high frequency oscillations are produced by the turbulence of the flow, whereas the low-frequency oscillations by the feeding pressure variations.

Those oscillations of the stream velocity translate into oscillations of the turbulent fluctuations downstream of the perforated plate, which could modify the error values. In order to assess the effect of the variations, $S_{LL}(r)\{u\}$ calculated from the whole set of time instances and $S_{LL}(r)\{u\}$ calculated from the time instances which average stream-wise velocity falls within a certain range (the velocities comprised between the red lines of Figure 6.28), are compared. Additionally, the velocity fluctuations on the second case are obtained from the instantaneous velocity minus the average velocity obtained with only the time instances which fall within the velocity range. The comparison is plotted in Figure 6.29 below in terms of differences of the $S_{LL}(r)\{u\}$ of each Δt minus the $S_{LL}(r)\{u\}$ of the smallest Δt, for the thinnest laser sheet. Further details into this calculation can be found in 7.3.

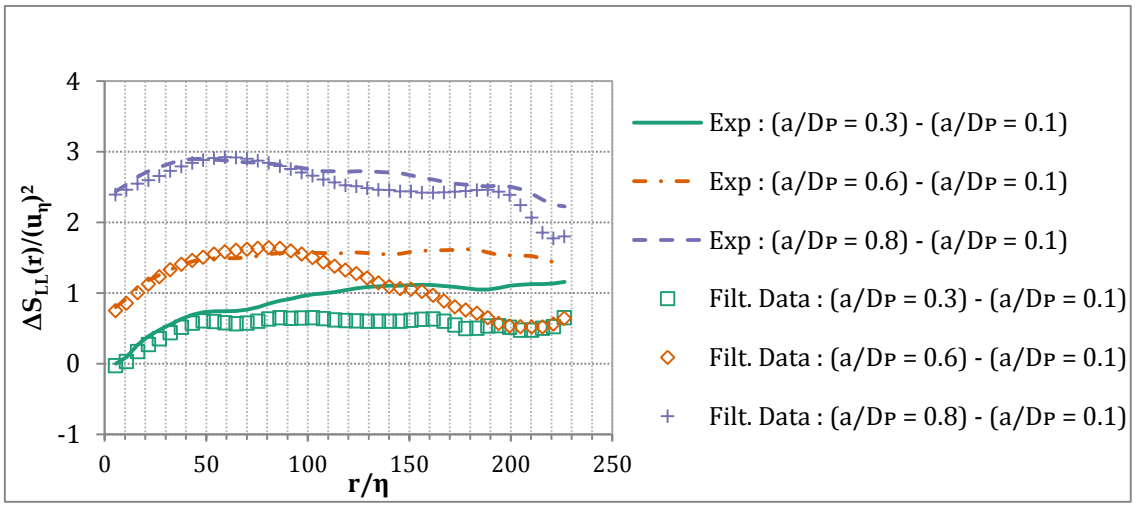

Figure 6.29 Effect on $\Delta S_{LL}(r)$ when the function is calculated by the whole set of fluctuations velocity fields u(x;t) available for a test case (lines), or from just those which average velocity falls within a certain range (symbols), for the thinnest laser sheet (Th/η~9).

As can be appreciated, some differences are induced from this fact on $\Delta S_{LL}(r)\{u\}$ at the larger scales (for r/η>60). Nonetheless, the small scales should be useful for the comparisons to the numerical tools. Moreover, up to r/η>100 the $\Delta S_{LL}(r)\{u\}$ induced by the variation of Δt is more important than the variation in $S_{LL}(r)\{u\}$ due to the non-stationarity of the flow. Therefore, the error characterization presented in section 7.3 should be valid up to those values of r/η. For r/η>100 both the non-stationarity and the uniformity could blur the errors influence on $S_{LL}(r)\{u\}$.

6.5.5.4 *Stream misalignment with the images*

The mean flow was not perfectly aligned with the images vertical direction. In order to assess the possible misalignment, the transversal and streamwise average velocity components (average in time and in the FOV) are compared: $\langle U_2 \rangle$ is below a 1% percent of $\langle U_1 \rangle$. Therefore, there is not expected influence from this fact.

Chapter 7 **Results and discussion**

This chapter presents the error characterization obtained by the different tools devised in the methodology. Measurements are done over three different sources: experimental images, synthetic images, and PIV Simulator cases. In contrast to the case of experimental images, both for synthetic images and for the PIV Simulator, the real velocity value is known. This allows determining the real error value. Experimental images are required to check the coherence of the results obtained with the simplified former tools, although their real velocity field details are unknown.

The aim is to study the error distribution along the length-scales of the flow. As commented in chapter 5, for such purpose the second order structure function, $S_{LL}(r)$, was identified as the most suitable tool. Besides applying it to the measured velocity field to obtain $S_{LL}(r)\{u_M\}$, when the real velocity is known, both $S_{LL}(r)\{u_R\}$ *and* $S_{LL}(r)\{\varepsilon\}$ provide insight into the error characteristics ($\varepsilon = u_R - u_M$ indicates the error field).

In addition, the total average error is also studied. An estimation of the total error was proposed in Chapter 5 section 5.3.5, to assess the error induced by turbulent spatial gradients. The coherence of this estimation with the value provided by the numerical tools allows validating the error structure proposal and the importance of the spatial gradients errors detailed in this work in respect to other errors.

Despite other characterizations, in line with the objectives of this PhD, the focal purpose of the results in this chapter is to quantify the PIV measurement envelope in terms of the coupled bounds between the laser sheet thickness Th and Δt.

In respect to the good practice procedures for PIV measurements, this chapter offers a comparison of the importance between the error from other error sources and the one coming from the commented coupling between laser sheet thickness and time between laser pulses. The final section of this chapter assesses the relevance of this error in regard to industrial facilities error handling practices.

7.1 RESULTS BASED ON THE PIV SIMULATOR MEASUREMENTS

Section 5.3 presents a preliminary analysis identifying several coupled error sources that could influence on the result of a PIV measurement, when dealing with turbulent flows. The PIV Simulator (cf. 3.2) has been developed in this PhD, to uncouple some of them. This tool simplifies the processing in a way that only the following sources of error are present:

- Low-pass effect: A correlation within the control volume is still being performed to obtain the displacement. This means that a kind of averaging is present, generating a low-pass to some degree. Nevertheless, the correlation procedure is non-linear so other effects have to be taken into account as commented below.
- Peak-split effect: When the difference of particle displacements within the interrogation volume is larger than the particle diameter, several correlation peaks arise in the correlation map. This may:
    - Reduce measurement errors, due to the reduction of the effective low-pass volume, as commented in 5.3.5.1.
    - Increase measurement errors: if the strongest correlation peak does not correspond to the particles located near the center of the interrogation window, a peak-split error arises. This may introduce spurious small spatial scales content, acting in the opposite sense than the low-pass error (cf. section 5.3). Two sources can generate these errors:
        - Particles misplacement errors: The random location of tracers in the control volume, generates random deviations from the velocity that corresponds to the center of such volume ($\xi_{\Delta u}$, cf. 5.3.5.1 and 5.3.4).
        - Group-locking: the most frequent displacement tends to generate the strongest correlation peak, independently of the location of the particles in the control volume (cf. 5.3.6). This error implies a systematic deviation correlated with the velocity, instead of random, that adds to the previous one.

    The couple of values Th and Δt that provide the optimum peak-split effect is commented along this chapter.

As only these errors are present, the PIV Simulator tests allow for their study, isolating them from influence coming from other error sources. The vector fields generated to study PIV error with the PIV Simulator share the following common characteristics:

- Interrogation window size D_I=6.4η, with no window weighting.
- The particle image size is D_P/D_I =0.065, i.e. D_I=15.4D_P. Compared to η, D_P=0.416η.
- Vector fields' spacing is D_I = 6.4η. There is no overlap between the interrogation windows.
- Gaussian laser profile. Where the thickness Th corresponds to the zone where the intensity is larger than e^{-2} the central value.
- Each interrogation volume contains N=90 particles.

Generalization of this study to other values of these parameters is based on theoretical reasoning. The error study is based on variations of Th and Δt. The values are chosen in a

way that the results can be checked in the dedicated experimental setup commented in section 7.3. Th and Δt are normalized as follows:

- The time between laser pulses made dimensionless with Kolmogorov time scale $\Delta t/\tau_\eta$.
- The laser sheet thickness made dimensionless with Kolmogorov length-scale Th/η.
- The dimensionless characteristic displacement difference in the interrogation volume a/D_P is a relevant parameter that can be obtained as a function of the previous two. As in this study the interrogation window D_I is always smaller than the laser sheet thickness Th, the displacement difference can be estimated as:

$$a/\eta = \sqrt[3]{\epsilon Th}\Delta t/\eta = (Th/\eta)^{1/3}\,\Delta t/\tau_\eta \Rightarrow a/D_P = 2.40(Th/\eta)^{1/3}\,\Delta t/\tau_\eta \qquad (7.1)$$

  This dimensionless characteristic displacement corresponds to the expected turbulent fluctuation velocity for eddies of the size of the laser sheet thickness, multiplied by the time between laser pulses. It shall be noted that although the value provided by expression above is the one used to identify the results in this chapter, the errors are calculated from the value of a calculated by replacing $\sqrt[3]{\epsilon Th}$ by $S_{LL}(r=Th)\{u_R\}$. $S_{LL}(r=Th)\{u_R\}$ should give a better characterization of the velocity differences at distance Th.

The range of variation of these parameters for this study is given in the table below:

Table 7.1 Measurement parameters of the results analyzed on this section.

Th/η	$\Delta t/\tau_\eta$	a/D_P characteristic	a/D_P from $S_{LL}(r=Th)\{u_R\}$
8.6	-	0.00	0.00
8.6	0.027	0.13	0.12
8.6	0.070	0.34	0.32
8.6	0.119	0.58	0.54
8.6	0.166	0.81	0.76
17.1	-	0.00	0.00
17.1	0.027	0.17	0.20
17.1	0.070	0.43	0.51
17.1	0.119	0.73	0.88
17.1	0.166	1.02	1.22
29.9	-	0.00	0.00
29.9	0.027	0.20	0.27
29.9	0.070	0.52	0.69
29.9	0.119	0.88	1.18
29.9	0.166	1.23	1.64

In the table three test cases have been added with a/D_P=0. These test cases have been obtained from the average of the velocities of the particles seeded inside the corresponding measurement volume. This corresponds to the theoretical value of the correlation for $D_P \rightarrow \infty$, as commented in section 3.2.2.

7.1.1 Total average error value

The total error is defined as: $\varepsilon_T = (1/2(\varepsilon_{1,T}^2 + \varepsilon_{2,T}^2))^{1/2}$ where $\varepsilon_{i,T} = (\langle(u_i^M - u_i)^2\rangle_{x,t})^{1/2}$. This information is equivalent to the one provided by $S_{LL}(r)\{\varepsilon\}$ for $r \to \infty$. Further details can be found in 5.2.2.

In the figure below the value of the error ε_T compared to u_η and to u' is plotted as a function of a/D_P for the three laser sheet thicknesses generated with the PIV Simulator. The estimated value of ε_T, obtained from section 5.3.5 and recalled below, is plotted for comparison:

$$\varepsilon_T^2 \sim \overbrace{0.35^2 S_{LL}\left(r = 0.25 r_A \sqrt{D_I^2 + Th^2}\right)\{u_R\}}^{\varepsilon_{LPF}^2} + \overbrace{\frac{S_{LL}(r = Th)\{u_R\}}{r_A N}}^{\xi_{\Delta u}^2} \qquad (7.2)$$

In the expression above, the first term corresponds to low-pass errors and the second term to peak-splitting errors. In both terms a ratio r_A<1 appears. This ratio accounts for the reduction induced by peak-splitting in the effective measurement volume size that contributes to the correlation. Further details can be found in 5.3.5. The low-pass error is calculated based on the distance: $r_A d_{eq,1D} = r_A\sqrt{D_I^2 + Th^2}$ which is referred to through this chapter as the effective equivalent 1D size. It shall be noted that, following section 5.3.5, for the calculation of this distance, the value of D_I used should be D_I=8.6η=6.4·(4/3)η, i.e. the original D_I size multiplied by 4/3, to compensate for the fact that the laser sheet thickness is Gaussian and the interrogation window has no weighting. N is the number of particles, which equals 90.

In the graph below, both errors are represented for the test cases generated with the PIV Simulator:

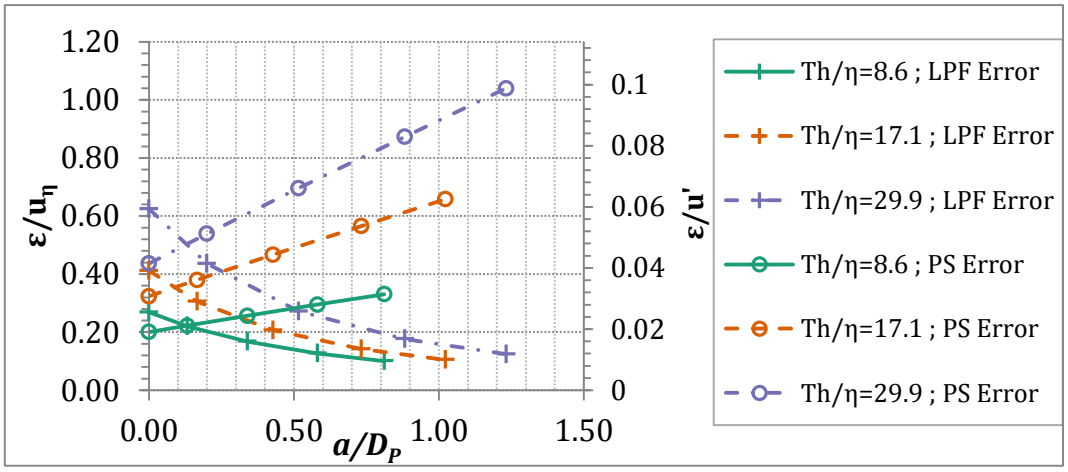

Figure 7.1 Break-down of the theoretical error estimation into: low-pass filtering errors (plus symbols) and peak-splitting errors (circles), for the cases studied with the PIV Simulator.

The following can be observed from the figure:

- For $a/D_P \to 0$, both errors are of the same order of magnitude. As the laser sheet thickness increases the low-pass errors grow faster than peak-splitting errors.
- For increasing a/D_P values, peak-splitting errors quickly surpass the contribution of low-pass errors to the total error.

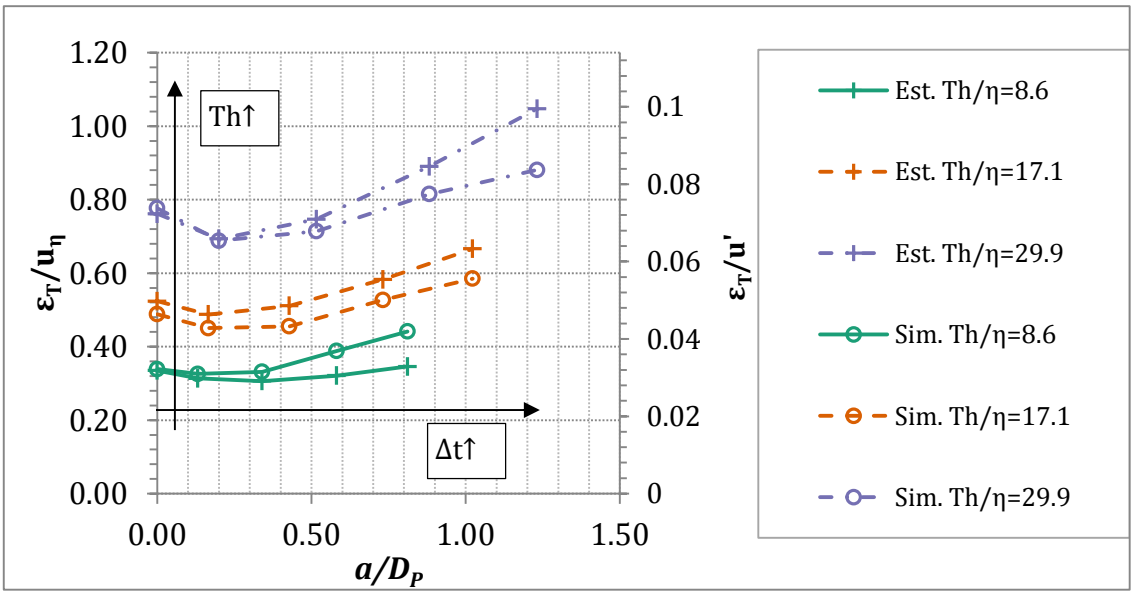

Figure 7.2 Total error average value. Comparison between the PIV Simulator results (circles) and the theoretical estimation (plus symbols).

The following can be observed from the figure:

- There is a minimum value of ε_T as a function of a/D_P, for each laser sheet thickness; roughly, $a/D_P \sim 0.2$ seems the optimum value. There is an initial decrease in ε_T, produced by the reduction of the low-pass filter effective size. This can be appreciated in Figure 7.1, where the error break-down is plotted. After that, the error increases with a/D_P due to a larger increase of peak-splitting errors than the decrease of low-pass errors.
- It can be seen also that the error increases as well with the laser sheet thickness for both the estimate and the PIV Simulator results, due to increase of both low-pass and peak-splitting errors.
- The estimation provides values within a 25% of the values provided by the PIV Simulator, which is acceptable given the simplicity of the estimation. The estimate construction, based on a low-pass effective size reduction and peak-splitting errors increase is coherent with the results observed. This indicates that the dominant error sources have been incorporated correctly into the estimate.

7.1.2 Error distribution along the length-scales of the flow

As commented above, $S_{LL}(r)$ has been chosen as the key tool for length scale analysis. Chapter 5 shows that $S_{LL}(r)\{signal\}$ provides the signal content for distances r, considering that this content includes the contribution from smaller scales. The implications for the analysis of this chapter are that: (i) a zone where $S_{LL}(r)\{signal\}$ does not increase is a zone where the signal has no additional contribution from those scales and the content comes from smaller scales, (ii) a zone with increasing $S_{LL}(r)\{signal\}$ is a zone with scales that contribute actively to the content of this function besides the content coming from smaller scales. Further details on these matters can be found in chapter 5 sections 5.1 and 5.2.

The particular dimensionless forms of $S_{LL}(r)$ chosen for length-scales representations, as detailed in section 5.2, are:

- Error field: $S_{LL}(r)\{\varepsilon\}/u_\eta^2$, which allows to assess how the errors cumulate along the different scales, r.
- Velocity field:
  - $S_{LL}(r)\{u\}/(r\epsilon)^{2/3}$ provides a general view on the errors relative to the magnitude of the turbulent signal in the inertial range.
  - $\Delta S_{LL}(r)\{u\}/u_\eta^2 = (S_{LL}(r)\{u_R\} - S_{LL}(r)\{u_M\})/u_\eta^2$, the dimensionless difference between the real and the measured value of the function. It is used for comparisons between cases and with the theoretical estimations. Additionally, for large r distances it provides the error in the measured TKE or similar quadratic velocities as $S_{LL}(r)\{u\} = 2\cdot rms(u)^2$ for large r.
- Correlation coefficient between u and ε, $C_{u\varepsilon}(r)$. It indicates systematic coupling between velocity and error, adverse for derived magnitude calculations like TKE.

7.1.2.1 *Error field*

The length-scale analysis of the error field further unveils its structure. The variation of $S_{LL}(r)\{\varepsilon\}$ with the laser sheet thickness is represented below for the lowest Δt analyzed. Figure 7.3-left plots $S_{LL}(r)\{\varepsilon\}/(u_\eta)^2$. Figure 7.3-right corresponds to $S_{LL}(r)\{\varepsilon\}$ divided by the maximum value of $S_{LL}(r)\{\varepsilon\}$ reached for that set of measurement parameters.

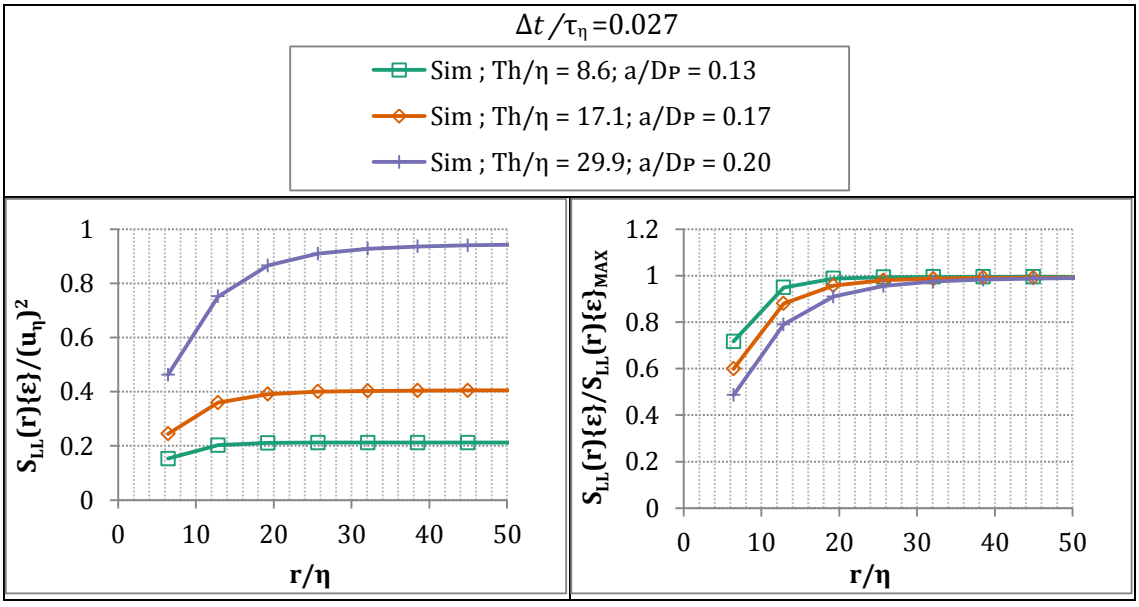

Figure 7.3 Variation of $S_{LL}(r)\{\varepsilon\}$ with *Th* for fixed Δt. Left: $S_{LL}(r)\{\varepsilon\}/(u_\eta)^2$, right: $S_{LL}(r)\{\varepsilon\}/S_{LL}(r)\{\varepsilon\}_{MAX}$.

The following aspects related to the error topology can be observed in the figure:

- Increasing the laser sheet thickness results in a larger distance for $S_{LL}(r)\{\varepsilon\}$ to approach a constant value. This distance is proportional to the effective equivalent 1D size: $r_A d_{eq,1D} = r_A\sqrt{(Th^2+D_I^2)}$. It is roughly 2.75 times $r_A d_{eq,1D}$ (oscillates between 2.4 and 2.9 times $r_A d_{eq,1D}$ for the thickest and the thinnest laser sheet respectively). Therefore, the range of scales on which error is introduced grows with the laser sheet thickness. Also, since $S_{LL}(r)\{\varepsilon\} = 2(\varepsilon_T^2 - R_{LL}(r)\{\varepsilon\})$ (cf. 5.2.1.2) the fact that

$S_{LL}(r)\{\varepsilon\}$ increases indicates $R_{LL}(r)\{\varepsilon\}$ is non-zero and varies with r, i.e. there are spatial scales where the errors have a certain spatial coherence (correlation).

As can be observed, $S_{LL}(r)\{\varepsilon\}$ presents very little variation for $r>Th$. For this reason, the error estimate proposed in this work provides only the value of ε_T and not how the error cumulates with r/η in $S_{LL}(r)\{\varepsilon\}$. The region $r<Th$ contains inevitably too large relative errors and is not of interest to this PhD.

Below, $S_{LL}(r)\{\varepsilon\}/(u_\eta)^2$ is plotted for the three laser sheet thicknesses varying the Δt.

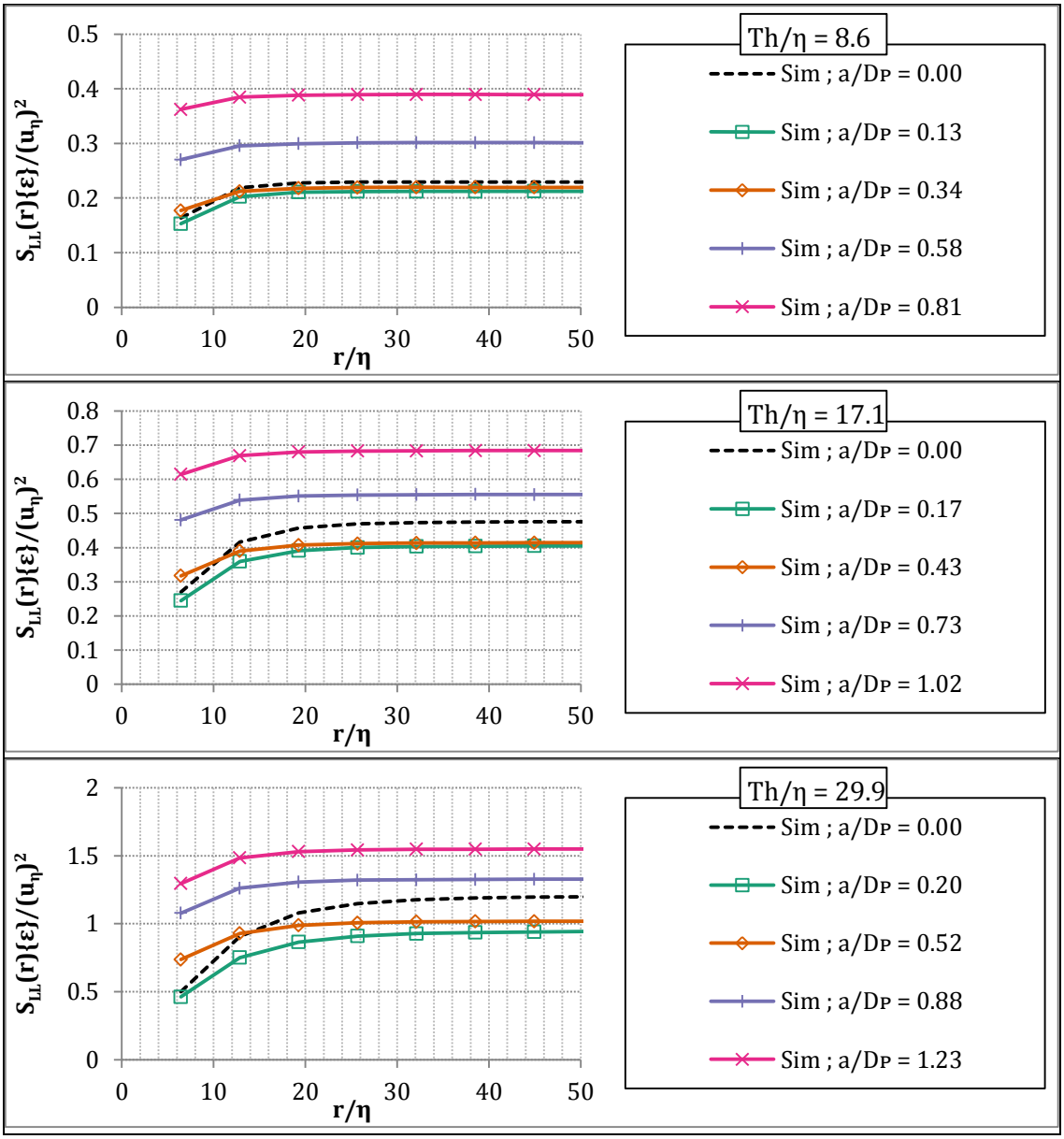

Figure 7.4 Variation of $S_{LL}(r)\{\varepsilon\}/(u_\eta)^2$ with Δt for the three laser sheet thicknesses simulated.

As in Figure 7.2, the case of a/D_P=0 represents the low-pass filtering case employed also on the velocity field study. Also, for large r, the minimum value of ε is around a/D_P = 0.2. Additionally, the following characteristic can be observed on the graphs:

- For each laser sheet thickness, the scale value, r required for $S_{LL}(r)\{\varepsilon\}$ to achieve 99% of the asymptote is the largest for the lowest a value. This change in the trend

of $S_{LL}(r)\{\varepsilon\}$ is attributed to the increase of peak splitting phenomenon reducing the effective low-pass effect volume, as mentioned above.

7.1.2.2 *Velocity field*

The results from varying the time delay are plotted below, for the thinnest and the widest simulated laser sheet thickness. The error-free value of $S_{LL}(r)\{u\}$, calculated from the DNS vector fields is identified as "DNS".

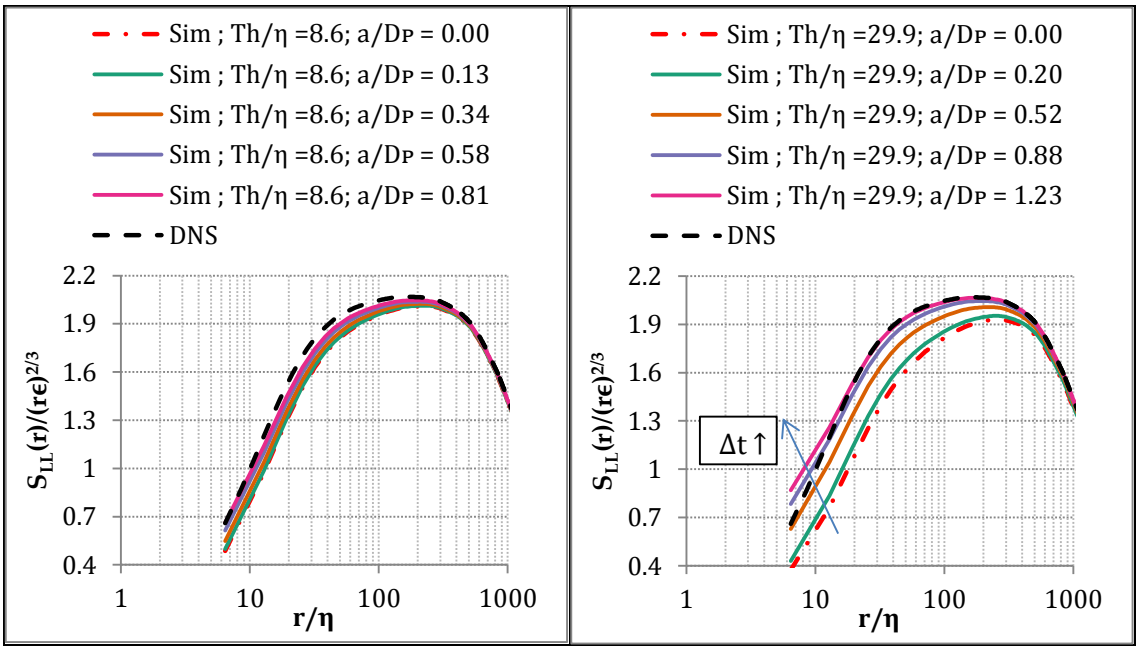

Figure 7.5 Variation of $S_{LL}(r)\{u\}/(r\epsilon)^{2/3}$ with Δt for Th/η=8.6 (left) and Th/η=29.9 (right). The $\Delta t/\tau_\eta$ values that correspond to each line can be checked at Table 7.1.

This figure exposes the following characteristics of the combination of low-pass and peak-splitting errors:

- Relative errors are larger for smaller scales.
- An increase in a/D_P produces $S_{LL}(r)\{u\}$ to achieve larger values. This is a result of the peak splitting induced on the correlation map, which reduces the effective low-pass size and increases peak-splitting errors. Both effects make $S_{LL}(r)\{u\}$ to increase.
- The variation induced by the same Δt increment is larger for larger Th.

In order to better evaluate the errors, the figures below plot the differences between the real value of $S_{LL}(r)\{u\}$ (that of the DNS) and the value of $S_{LL}(r)\{u_M\}$ for the different measurement parameters. First, the $\Delta S_{LL}(r)\{u\}$ for varying Th are plotted below for the smallest Δt (where low-pass errors dominate and the peak-split effect is minimum). In the figure, the estimation proposed in this work of $\Delta S_{LL}(r)\{u\}$ (cf. 5.3.5.2) has also been plotted. The estimation is recalled here:

$$\Delta S_{LL}(r)_{PS} = p\left(\frac{r}{r_A d_{eq,1D}}\right)\left[f\left(d_{eq,1D}, a/D_P\right)\varepsilon_{LPF} - 2\varepsilon_{LPF}^2\right] - 2\xi_{\Delta u}^2 \qquad (7.3)$$

Where: $f\left(d_{eq,1D}, a/D_P\right) = 2\sqrt{2}\left(C_5\left(S_{LL}\left(r = 2d_{eq,1D}\right)\{u_R\}\right)^{1/2} + \sqrt{2}u_\eta\, a/D_P\right)$

And $p\left(\frac{r}{r_A d_{eq,1D}}\right) = 2\left(\frac{r}{2r_A d_{eq,1D}}\right) - \left(\frac{r}{2r_A d_{eq,1D}}\right)^2$ for $r < 2d_{eq,1D}$, while $p = 1$ for $r \geq 2d_{eq,1D}$. p is a parabola used to account for low-pass errors growth. The rest of terms were recalled in in expression (5.23) above. For large r, $\Delta S_{LL}(r)_{PS}$ is proportional to the difference between the real TKE and the measured TKE (see 5.2.1.1).

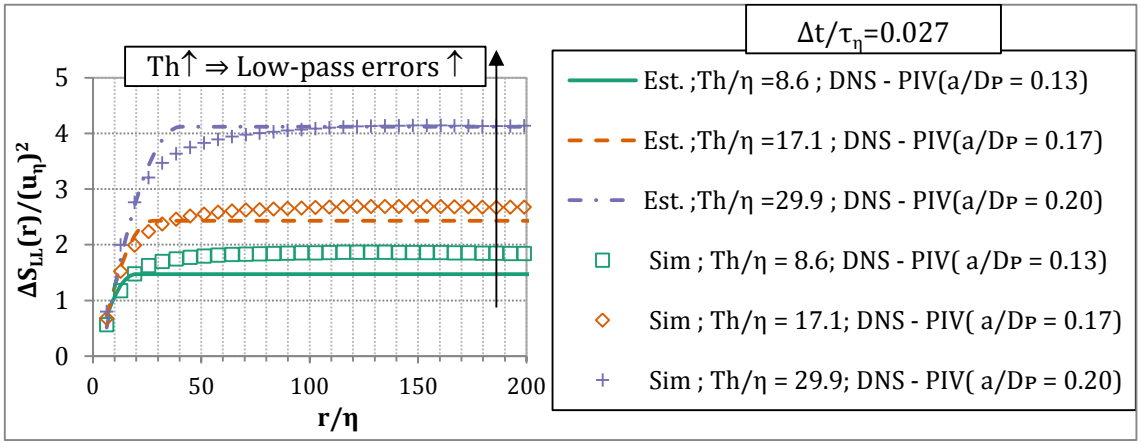

Figure 7.6 Variation of $\Delta S_{LL}(r)\{u\}/(u_\eta)^2$ with *Th*. Comparison of the estimation proposed in this work with the PIV Simulator results.

The following error characteristics can be extracted from this figure:

- An increase of *Th* translates into larger low-pass errors which induce a decrease in $S_{LL}(r)\{u\}$ (i.e. larger $\Delta S_{LL}(r)\{u\}$).
- The difference $\Delta S_{LL}(r)\{u\}$ reaches almost a constant value for large *r*. The 99% of the value for large *r* is achieved at a distance $r=r_1$ (which changes with *Th*) indicating that for scales of size $\ell \geq r_1$ $S_{LL}(r)\{u_M\}$ varies the same than $S_{LL}(r)\{u_R\}$. As commented in subsection 5.3.3 this implies that the influence of low-pass errors for those scales is negligible. The ratio r_1/Th is 3.7 for the thickest plane and increases to 7.6 for the thinnest one. With respect to the effective equivalent 1D size, $r_A d_{eq,1D}$, the ratio $r_1/r_A d_{eq,1D}$ oscillates between 5.5 for the thickest plane and 7.5 for the thinnest one. The difference in the ratios given here and those given for $S_{LL}(r)\{\varepsilon\}$ is commented in subsection 7.1.2.3.
- The estimate captures closely the value of $\Delta S_{LL}(r)\{u\}$ for large r/η. The largest difference to the PIV Simulator is of a 25% (for the thinnest laser sheet) which is considered acceptable given the simplicity of the estimate.
- For values of r < r_1, the estimate departs further from the $\Delta S_{LL}(r)\{u\}$ value. This indicates that the growth of low-pass errors is more complex than predicted by a polynomial. Obtaining a more complex estimate is left for future work.
- Considering that, for large *r*, $TKE = (3/4)S_{LL}(r)\{u\}$; the fact that $\Delta S_{LL}(r)\{u\}$ is positive indicates that the measured TKE is generally underestimated. The underestimation is more apparent, the larger *Th* is. A relevant issue that is further commented later in this chapter is the fact that the TKE is significantly larger than ε_T^2 for all these cases (small a/D_P).

Figure 7.7 shows the plots of $\Delta S_{LL}(r)\{u\}$ corresponding to the comparison of the estimator proposed and the PIV Simulator results, for varying Δt. The three laser sheet thicknesses

generated with the PIV Simulator are plotted. The 5 cases plotted for each thickness have the same Δt values, but the a/D_P value changes following expression (7.1).

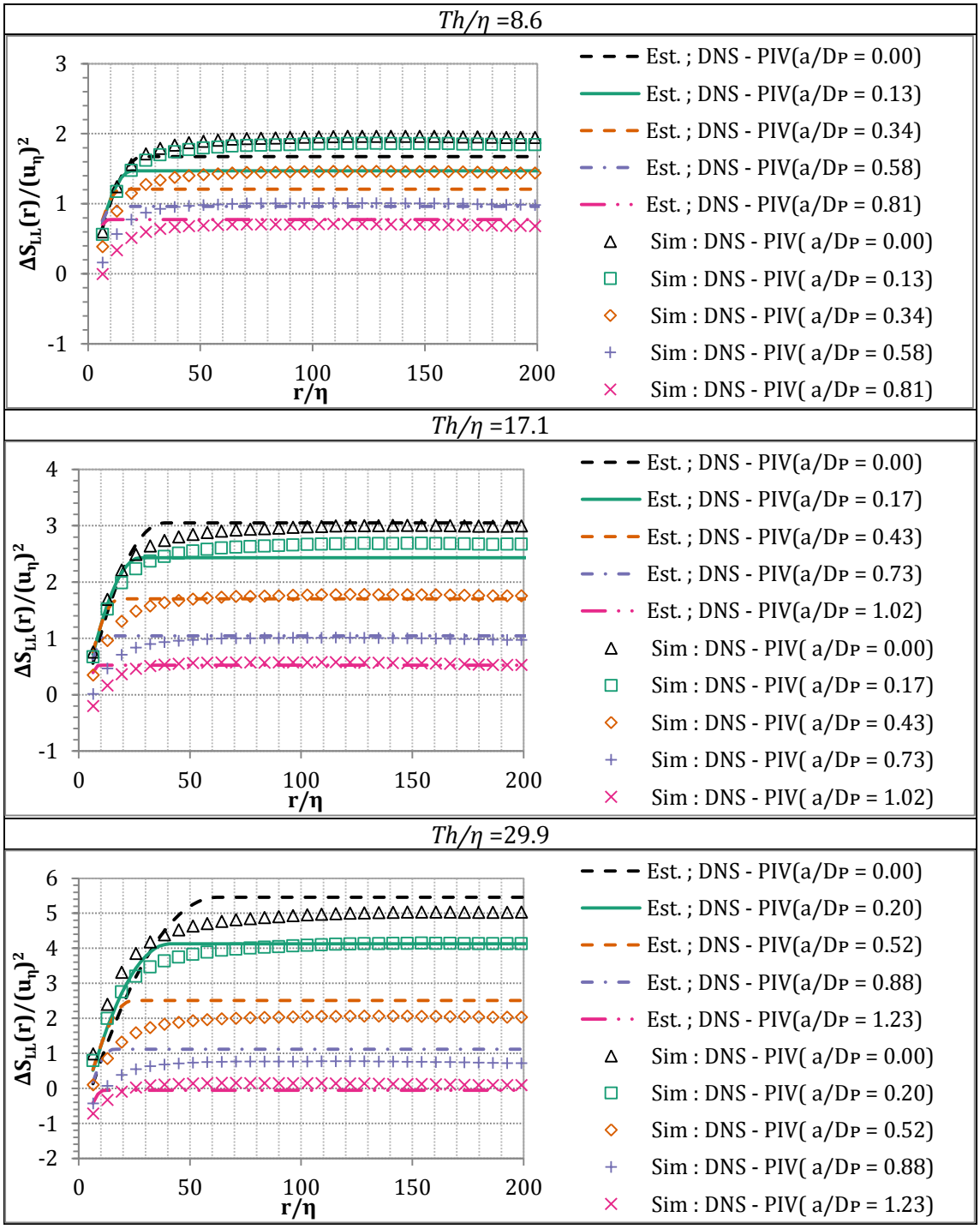

Figure 7.7 Variation of $\Delta S_{LL}(r)\{u\}/(u_\eta)^2$ with Δt. Upper graph, Th/η=8.6, middle graph, Th/η=17.1, bottom graph Th/η=29.9.

Additional characteristics of the combination of low-pass and peak-splitting errors can be extracted from this figure:

- Although relative errors were larger for smaller scales, here it can be observed that the absolute error content increases for increasing scales (r/η), up to a zone where no additional error content is added.

- This last zone with constant ΔS_{LL}(r) indicates that for large scales neither the low-pass nor the peak-splitting seem to produce additional errors.
- For large Δt, large Th and small r/η, $\Delta S_{LL}(r)\{u\}$ becomes negative (i.e. the measured $S_{LL}(r)\{u\}$ has larger signal content than the real $S_{LL}(r)\{u\}$). This is coherent with the prediction in 5.3.5, indicating that the peak-splitting error amplifies small scales by mixing information from different depths in the laser sheet plane.
- As can be observed, the estimate predicts values that are quite close to the results of the PIV Simulator. The largest differences (in relative terms) are given for the smallest laser thickness, where the estimate tends to under predict the variations with a/D_P given by the PIV Simulator for the lowest laser sheet. The differences are small and thus are considered acceptable.
- It can be observed that increasing Δt results in larger measured TKE, for the cases plotted. It reaches the real TKE for the largest Th and largest Δt. But care should be taken as this result is not relaying on a better measurement but in the competition between errors that generate a systematic increase of measured TKE and errors that generate a systematic decrease in TKE. The optimal setting would depend on the measurement conditions through expression (7.3). This optimal setting would be different to the optimal setting for minimizing ε_T^2.

Some of the details exposed by Figure 7.5 are here also evident: (i) $S_{LL}(r)\{u\}$ is larger for larger Δt (i.e. the $\Delta S_{LL}(r)\{u\}$ decreases and eventually becomes negative) and (ii) for larger Th, a certain increase in Δt produce larger error differences.

7.1.2.3 *Correlation between the error and the velocity fields*

In the previous analysis it is evident that $\Delta S_{LL}(r)\{u\}$ presents generally much larger variations than $S_{LL}(r)\{\varepsilon\}$. This draws the attention to the comparison between both. Both can be compared by means of the correlation coefficient, defined in section 5.2.1.3. The correlation coefficient can be obtained from the sum of both functions, as follows (cf. 5.2.1.3):

$$C_{u\varepsilon} = \frac{1}{2}\frac{\Delta S_{LL}(r)\{u\} + S_{LL}(r)\{\varepsilon\}}{\sqrt{S_{LL}(r)\{u^R\}S_{LL}(r)\{\varepsilon\}}} = \frac{\left\langle \left(\delta u^R(x,r)\delta\varepsilon(x,r)\right)\right\rangle_x}{\sqrt{\left\langle \left(\delta u^R(x,r)\right)^2\right\rangle\left\langle \left(\delta\varepsilon(x,r)\right)^2\right\rangle}}$$

Figure 7.6 plots these correlation coefficients for the different cases:

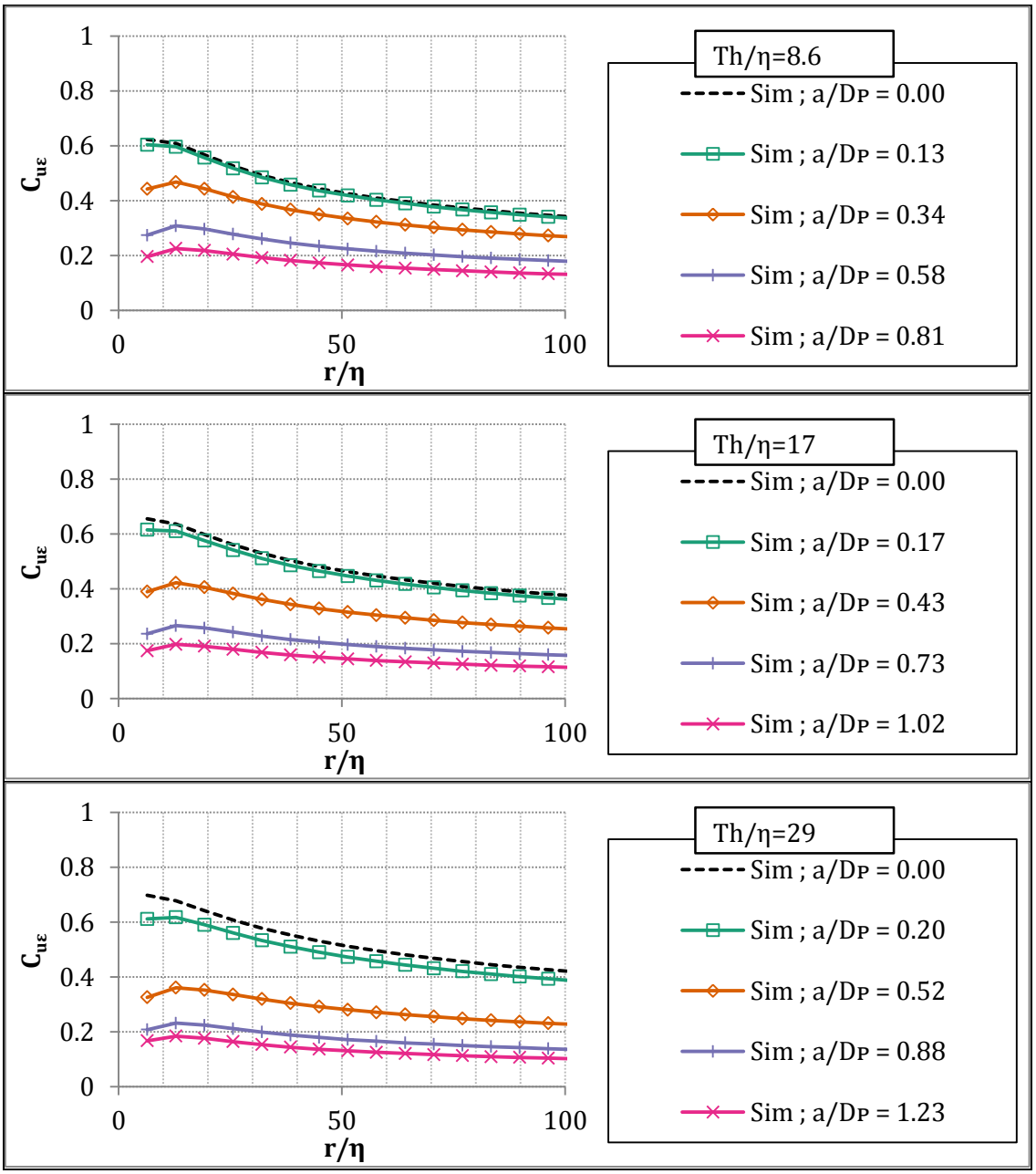

Figure 7.8 Variation of the $C_{u\varepsilon}$ with Δt, for the three laser sheet thicknesses simulated.

The following aspects can be observed on the graphs of Figure 7.8:

- The cases with a/D_P=0 (where low-pass errors are largest) show the largest positive correlation between velocity and error.
- As a/D_P increases the correlation coefficient goes towards 0, indicating larger presence of random errors (produced by peak-splitting) and smaller importance of coherent errors (low-pass errors). Thus, group-locking errors, that are described to produce a negative correlation (see Chapter 5 section 5.3.6), are less important than peak-splitting random errors.

This correlation between error and velocity explains the following issues:

- For the cases plotted in Figure 7.3, the distance required for $S_{LL}(r)\{\varepsilon\}$ to stop increasing is related mainly to low-pass errors, as it happens for $\Delta S_{LL}(r)\{u\}$ at

Figure 7.6. However, it can be observed that the distances at which $\Delta S_{LL}(r)\{u\}$ and $S_{LL}(r)\{\varepsilon\}$ reach a constant value differ: for $\Delta S_{LL}(r)\{u\}$, r is $>5d_{eq,1D}$, but for $S_{LL}(r)\{\varepsilon\}$ r is $\sim 3d_{eq,1D}$. This is easily explain by the fact that:

- The contribution of $\delta\varepsilon(r)^2$ becomes small for $r>r_A d_{eq,1D}$ in both $S_{LL}(r)\{\varepsilon\}$ and $\Delta S_{LL}(r)\{u\}$, in respect to the value accumulated up to that scale. This explains the distance $r\sim 3r_A d_{eq,1D}$ for $S_{LL}(r)\{\varepsilon\}$.
- For larger scales, the behavior of $\Delta S_{LL}(r)\{u\}$ is explained by the expression commented in chapter 5 (cf. 5.2.1.3):

$$\Delta S_{LL}(r)\{u\} = 2C_{u\varepsilon}(r)\sqrt{S_{LL}(r)\{u_R\}S_{LL}(r)\{\varepsilon\}} - S_{LL}(r)\{\varepsilon\}$$

  It can be noted that even when $S_{LL}(r)\{\varepsilon\}$ has reached an almost constant value, if $C_{u\varepsilon}(r)\sqrt{S_{LL}(r)\{u_R\}}$ varies, so does $\Delta S_{LL}(r)\{u\}$. This is so because $\langle\delta\varepsilon(r)\delta u(r)\rangle$ (which is the same than the first term in expression just above) keeps increasing because of the increase of $\delta u(r)$ with increasing scales, despite the much slower increase of $\delta\varepsilon(r)$. This happens up to r in the order of several times $d_{eq,1D}$, where $\delta\varepsilon(r)$ does not increase anymore with r.

- Given that, for large r, the error on TKE can be related to $\Delta S_{LL}(r)\{u\}$. It can be observed that the existence of correlation may affect dramatically this measure. Small $\langle\varepsilon^2\rangle$ with large $\langle\varepsilon u\rangle$ may generate more error than larger $\langle\varepsilon^2\rangle$, provided that $\langle\varepsilon u\rangle$ is zero (non-correlated). Thus, the optimum measurement parameters would differ depending on if the objective is to measure the velocity or to measure derivative quantities like the TKE.

7.1.3 **PIV Simulator analysis summary**

In summary, the results observed up to this point can be described by:

- When Δt increases:
  - The effective size of the low pass-filter associated to the nonlinear behavior of the correlation diminishes: less particles contribute to the correlation peak due to the appearance of peak-splitting phenomenon. This reduces low-pass errors.
  - There is an increase of peak-splitting errors (also produced because less particles contribute to the correlation peak due to the increase of the displacements in respect to the particle size).
- When *Th* increases:
  - The effective size of the low pass-filter increases. This increases low-pass errors.
  - Peak-splitting errors increase as well, due to the presence of larger velocity differences inside the measurement volume.

The results are summarized in the figure below, obtained from the theoretical estimations, for the parameters of the PIV Simulator. The colorbar represents the total error divided by the turbulent *rms* velocity fluctuations *u'*, and contours are also indicated by the red continuous lines. The green broken lines indicate the value of a/D_P from expression (7.1).

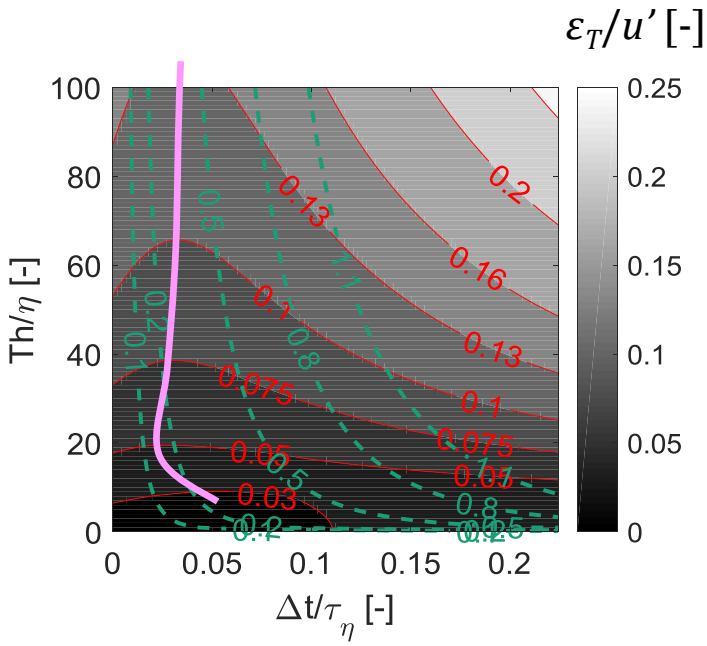

Figure 7.9 Estimated total error as a function of Δt and *Th* for the parameters used in the PIV Simulator results.

In absence of other error sources, the order of magnitude for the best measurement of the velocity is Δt such that a/D_P is ~0.3 and Th as low as possible. The particular value of $\Delta t/\tau_\eta$ is plotted with a magenta line for the values of the cases presented in this chapter. For other values of D_I, D_P or N, the corresponding plot has to be done based on the theoretical estimations given.

For measurements of squared velocities (e.g. TKE) the recommendation is to use an a/D_P value that minimizes $\Delta S_{LL}(r)\{u\}$ by compensating the error components with opposite sign in expression (7.3): $f\left(d_{eq,1D}, a/D_P\right)\varepsilon_{LPF}$ and $(\varepsilon_{LPF}^2 + \xi_{\Delta u}^2)$. This is given in the image below, obtained from the estimation of $\Delta S_{LL}(r)$ of large r values. In this case, the a/D_P values are plotted by the blue broken line. Again a magenta line defines the optimal values for the cases presented in this section. As for the previous image, for other values of D_I, D_P or N, the corresponding plot has to be done based on the theoretical estimations given.

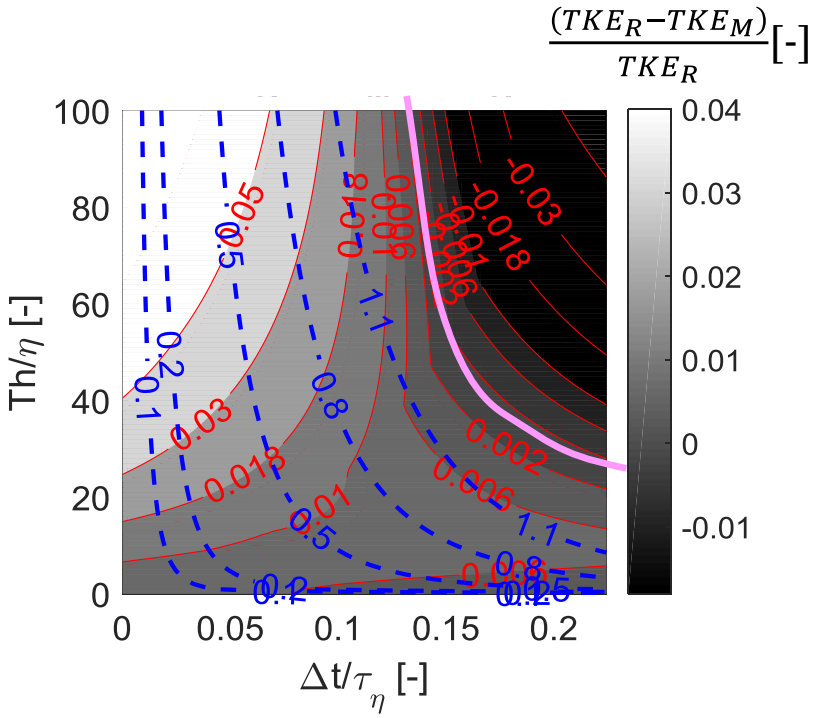

Figure 7.10 Estimated error in the turbulent kinetic energy, as a function of Δt and *Th*, for the parameters used in the PIV Simulator results.

7.2 SYNTHETIC IMAGES

Using synthetic images instead of the PIV Simulator, implies including more error sources in the results. In fact, almost all relevant PIV errors identified in 5.3.1 come into play, except for CCD read-out errors, projection errors and particles' slip. The generation of Synthetic images without background noise and with fill factor unity may also reduce the magnitude of some errors in respect to the case of real images, where all error sources are present. Specifically, the values of the random errors in determining the correlation peak location, peak-locking errors and the outliers' occurrence could be influenced from those facts. The results from synthetic images serve as a validation of the PIV Simulator results and to assess the importance of the errors studied in the previous point in respect to other sources. On synthetic images the error sources that are included (and that are a priori not negligible, see section 5.3 and subsection 5.3.17) are the following:

- Low-pass effect (already present in the PIV simulator analysis and detailed in 5.3.3).
- Peak-splitting errors (already present in the PIV simulator analysis):
  - Random errors due to particles misplacement, $\xi_{\Delta u}$, (studied in 5.3.5.1).
  - Systematic errors in determining the correlation peak location, (i.e. group locking) (studied in 5.3.6).
- Peak-locking systematic errors (detailed in 5.3.7).
- Random errors in determining the correlation peak location due to spatial discretization, $\xi_{\Delta x}$, (studied in 5.3.10).
- Outliers occurrence (studied in 5.3.12).

The common characteristics to all vector fields are the following: the interrogation window size D_I and the vector fields' resolution is the same, 6.4η (32 pixels final interrogation window size). The processing includes an iterative multigrid processing of 8 steps from windows of 256 pixels down to 32. Only a Gaussian laser profile is used on the study, which thickness is defined at the e^{-2} waist points. The particles per pixel (ppp) are 0.09 which gives approximately 90 particles per interrogation volume. The particles image size was of 2.2 pixels at the e^{-2} waist points. Magnification is such that η is 5px. The processing parameters and validation details are further detailed in chapter 3, section 3.3.4. The interrogation windows are weighted before calculating the correlation, with a weighting function studied in 3.3.4.

It should be noted that, with the processing parameters employed, low-pass and peak-splitting errors should be reduced with respect to the PIV Simulator. Indeed, the fact that for the analysis of synthetic images a multi-grid scheme with image deformation is used and that the interrogation window is weighted can reduce the mentioned errors (see Chapter 5 sections 5.3.3 and 5.3.5). Those factors have been integrated in the estimate as those sections describe.

For synthetic images, the characteristic displacement difference inside the interrogation volume a/D_P is defined by: $(a/D_P)_C=\sqrt[3]{(\epsilon Th)}\Delta tM_0/D_P$. In addition, the actual value used to calculate the errors ($(a/D_P)_S$), is also provided in the table. $(a/D_P)_S$ is obtained replacing $\sqrt[3]{(\epsilon Th)}$ by $S_{LL}(r=Th)\{u_R\}$, and incorporating the reductions of the displacement difference

due to image deformation and image discretization described in 5.3.5.3. Those factors can reduce a/D_P a maximum of a 30%.

The vectors used for the whole analysis in this section were validated by a post-processing of an allowable vector range, as described in 3.3.4.

The cases that will be analyzed on this subsection are the following ones.

Table 7.2 Measurement and error parameters of the results analyzed on this section (where d_r is the camera pixel size and M_0 the magnification factor).

Th/η	$\Delta t/\tau_\eta$	$(a/D_P)_C$	$(a/D_P)_S$	$u'\Delta t M_0/d_r$	$u_\eta \Delta t M_0/d_r$	$u'\Delta t/Th$
4.4	0.027	0.11	0.07	1.42	0.13	6.5%
4.4	0.070	0.29	0.18	3.67	0.35	16.7%*
4.4	0.119	0.50	0.30	6.27	0.59	28.5%*
4.4	0.166	0.70	0.42	8.75	0.83	39.8%*
8.6	0.027	0.13	0.10	1.42	0.13	3.3%
8.6	0.070	0.32	0.25	3.67	0.35	8.5%
8.6	0.119	0.55	0.43	6.27	0.59	14.6%*
8.6	0.166	0.77	0.60	8.75	0.83	20.4%*
17.2	0.027	0.16	0.14	1.42	0.13	1.7%
17.2	0.070	0.41	0.35	3.67	0.35	4.3%
17.2	0.119	0.70	0.61	6.27	0.59	7.3%
17.2	0.166	0.97	0.85	8.75	0.83	10.2%
29.5	0.027	0.19	0.18	1.42	0.13	1.0%
29.5	0.070	0.49	0.47	3.67	0.35	2.5%
29.5	0.119	0.83	0.80	6.27	0.59	4.3%
29.5	0.166	1.16	1.11	8.75	0.83	6.0%

* These cases have been generated with and without out-of-plane motion (u_3=0 at the whole flowfield), to compare errors when removing this error source.

In relation to the sets of parameters used for the PIV Simulator, the additional laser sheet thickness set (for Th/η=4.4) has been generated to study the effect of turbulent out-of-plane motion. This case is only analyzed in 7.2.1. Also, there are slight differences (below a 2%) on the laser sheet thickness size relative to Kolmogorov scales, as compared to the PIV Simulator. This is induced by the fact that the algorithms have slightly different constraints in the interrogation volume sizes that can be imposed.

7.2.1 **Total average error value**

In Figure 7.11 the value of the total average error ε_T compared to u_η and to u' is plotted as a function of a/D_P for the three laser sheet thicknesses used for the analysis of the spatial gradients effect (Th/η ≅8.6, Th/η ≅17.2 and Th/η ≅29.5). On the figure, the images generated without out-of-plane motion are used for the two larger Δt's of the Th/η≅8.6 (see Table 7.2). The left graph compares the results of the PIV Simulator with the synthetic images (only for reference to the analysis in the previous section, because as mentioned, the expected value of errors should differ) and the right graph compares the estimated ε_T with the synthetic images.

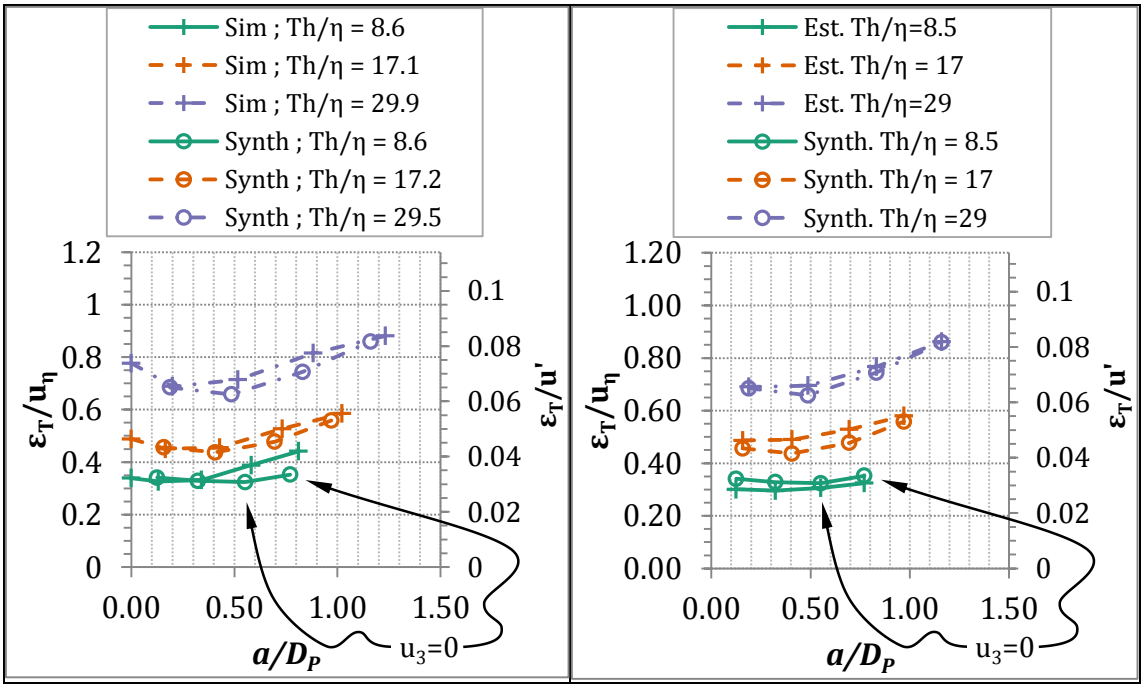

Figure 7.11 Variation of the total error ε_T with a/D_P for the three laser sheet thicknesses in common for both numerical tools. Left: comparison of PIV Simulator (plus signs) and synthetic results (*circle* signs), right: comparison of PIV Simulator (plus signs) and synthetic results (*circle* signs),

The following can be observed from the figure:

- For the lowest laser sheet and lowest a/D_P value, it can be appreciated that the synthetic images have a slightly larger error than both the PIV Simulator and the estimation. This should be associated to the fact that for synthetic images there are additional sources of error which can get important for low Δt: the random errors in determining the correlation peak location, $\xi_{\Delta x}$, and peak-locking systematic errors.
- As Δt increases, synthetic images stay at lower error values than the PIV Simulator. This is especially remarkable for the lowest thickness. This should be related to the factors mentioned in section 5.3.5 that can reduce peak-splitting influence: image discretization and image deformation. In the estimate, where those factors are integrated, more similar variations to synthetic images are observed.
- The estimate gives very close values to the results of synthetic images. On the PIV Simulator larger differences were observed. Any smaller difference than those obtained for the Simulator should be attributed to the variability of the estimate. They do not mean a better estimate as no change has been done on it.
- There is a minimum value of ε_T with a/D_P for each laser sheet thickness, which for synthetic images falls at $a/D_P \approx 0.5$. In addition to the error decrease given for the PIV Simulator, for synthetic images the random errors in determining the correlation peak location and peak-locking errors decrease with Δt. When the decrease is compensated by peak-splitting errors, ε_T increases.
- There are no substantial differences between the error values of synthetic images and of the PIV Simulator. It could be concluded then that roughly, the errors that were given for the PIV Simulator should be the most relevant as well for synthetic images in the explored conditions.

Effect of out-of-plane motion

It is possible also to study the value of the out-of-plane motion parameter for which the total error starts to significantly increase. In section 5.3.9 the parameter $u'\Delta t/Th$ was suggested as a mean of providing an overall characterization. The results of the global error as a function of $u'\Delta t/Th$ are below, only for synthetic images. On the graph, the images for the laser sheet thickness of Th/η=8.6 were generated with out-of-plane motion (contrarily to the results in Figure 7.11). The additional laser sheet thickness generated with synthetic images is also plotted; this case is plotted with and without out-of-plane motion (continuous pink line with x sign and broken pink line with triangles respectively).

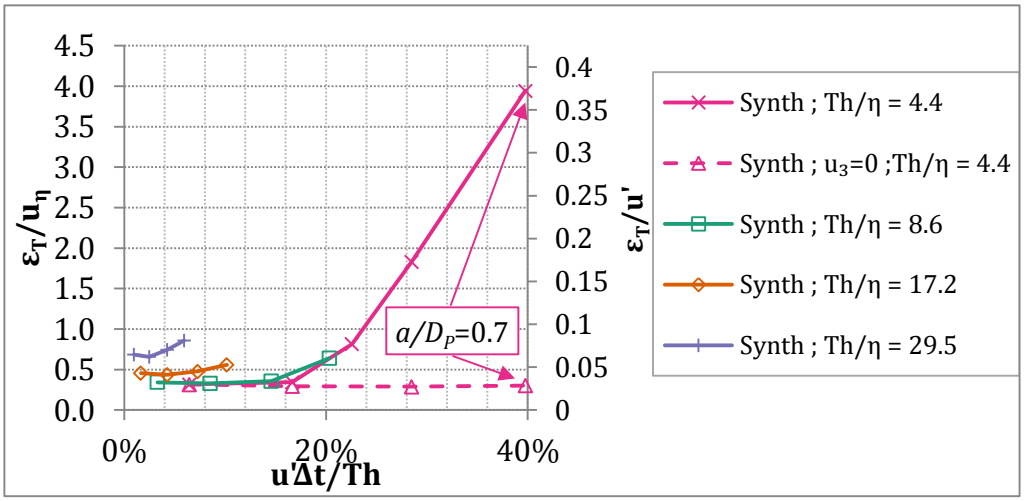

Figure 7.12 Variation of the total error ε_T with $u'\Delta t/Th$.

For the two largest thicknesses, the error increase is mostly produced by peak-splitting errors and therefore those thicknesses are not used for out-of-plane characterization. For both smaller laser sheet thicknesses, it can be observed that:

- For $u'\Delta t/Th$ up to 17% the values taken by ε_T can be explained by spatial gradients, random errors in determining the correlation peak location and low pass effect error sources.
- At around $u'\Delta t/Th$=20% the total error starts to increase quickly. For the Th/η=8.6, for $u'\Delta t/Th$=20.4%, the error increases around $0.2u_\eta$ with respect to the previous case with smaller $u'\Delta t/Th$. This increase should be induced mostly by out-of-plane motion outliers, since as the results of Figure 7.11 show, without out-of-plane motion, the error increase is of only $0.03u_\eta$ (case of a/D_P=0.77). The thinnest laser sheet also has an important error increase, starting at a similar value of $u'\Delta t/Th$. As can be observed from the graph, when the out-of-plane is set to zero the error increase is not produced, indicating that indeed the out-of-plane should be responsible for the error production and not the spatial gradients.

7.2.2 Error distribution with the length-scales of the flow

$S_{LL}(r)\{\varepsilon\}$ shows for synthetic images a close behavior to that of the PIV Simulator (cf. 7.1.2.1). Only the small variations for global error shown in Figure 7.11 arise. Thus, the whole set of graphs of subsection 7.1.2.1 have not been plot to avoid being repetitive. Only

the comparison between the PIV Simulator and synthetic images for the largest laser sheet is shown below, as example.

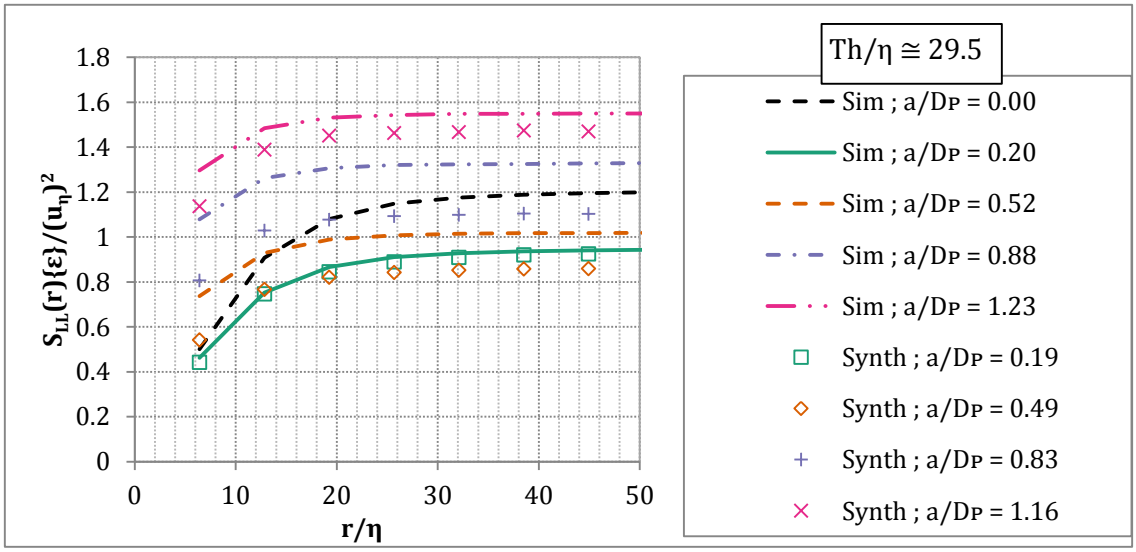

Figure 7.13 Variation of $S_{LL}(r)\{\varepsilon\}/(u_\eta)^2$ with Δt for the three common laser sheet thicknesses. Comparison of the results of the PIV Simulator (lines) with synthetic images (symbols).

As can be observed in the graph, for synthetic images the distance at which $S_{LL}(r)\{\varepsilon\}$ reaches a constant value also diminishes with Δ*t,* as for the PIV Simulator. The closeness of these plots indicates LPF errors and peak-splitting errors are included among the dominant errors in these cases (i.e. the inclusion of the other errors does not change $S_{LL}(r)\{\varepsilon\}$ significantly). This verifies the existence of cases where LPF and PS errors are significant and thus relevance of their modeling.

Below, $\Delta S_{LL}(r)\{u\}$ and the correlation coefficient $C_{u\varepsilon}(r)$ are analyzed and commented.

7.2.2.1 *Velocity field*

This section uses $\Delta S_{LL}(r)\{u\}$ to further evaluate the effect of the additional errors in respect to the estimation of LPF and Peak-splitting errors. First, the differences between the real value of $S_{LL}(r)\{u\}$ and the measured value are plotted below as a function of *Th*, for the smallest Δt. Only the comparison to the estimation is shown in this plot because the estimation incorporates the different factors that take into account the multigrid processing, differently to the PIV Simulator results.

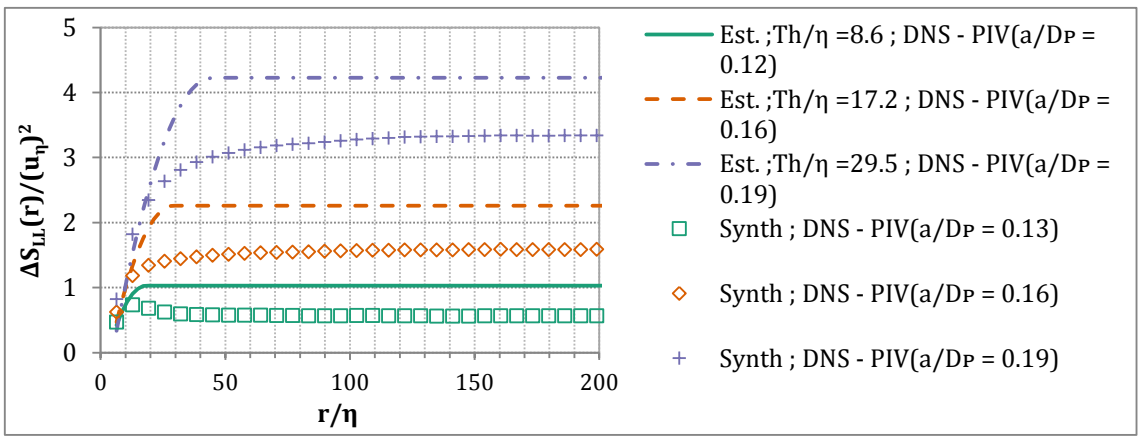

Figure 7.14 Variation of $\Delta S_{LL}(r)\{u\}/(u_\eta)^2$ with *Th*. Comparison of the results of the PIV Simulator (lines) with those of synthetic images (symbols). $\Delta t/\tau_\eta$ =0.027 in all cases.

Comparing the $\Delta S_{LL}(r)\{u\}$ of synthetic images to that provided by the estimation, it can be observed that:

- There is a difference in $\Delta S_{LL}(r)\{u\}$ for all three laser sheet thicknesses. Recalling from expression (7.3) that for large r:

  $$\Delta S_{LL}(r)_{LPFPS} = \sqrt{8}\left(C_5\sqrt{S_{LL}(r = 2d_{eq,1D})\{u_R\}} + \sqrt{2}u_\eta\, a/D_P\right)\varepsilon_{LPF} - 2(\varepsilon_{LPF}^2 + \xi_{\Delta u}^2)$$

  And given that Figure 7.11 indicates that the estimation of $(\varepsilon_{LPF}^2 + \xi_{\Delta u}^2)$ closely reproduces in these cases the behavior of $\varepsilon_T^2 \sim (\varepsilon_{LPF}^2 + \xi_{\Delta u}^2 + \varepsilon_{additional}^2)$ given by synthetic images, the results indicate a systematic overestimation of the LPF error or a small error that is negatively correlated to the velocity field.

Below, the $\Delta S_{LL}(r)\{u\}$ for varying Δt with fixed Th are plotted. The left column shows the difference between the synthetic images results and the estimate that only considers LPF and PS errors, and the right column the comparison between synthetic images and the PIV Simulator.

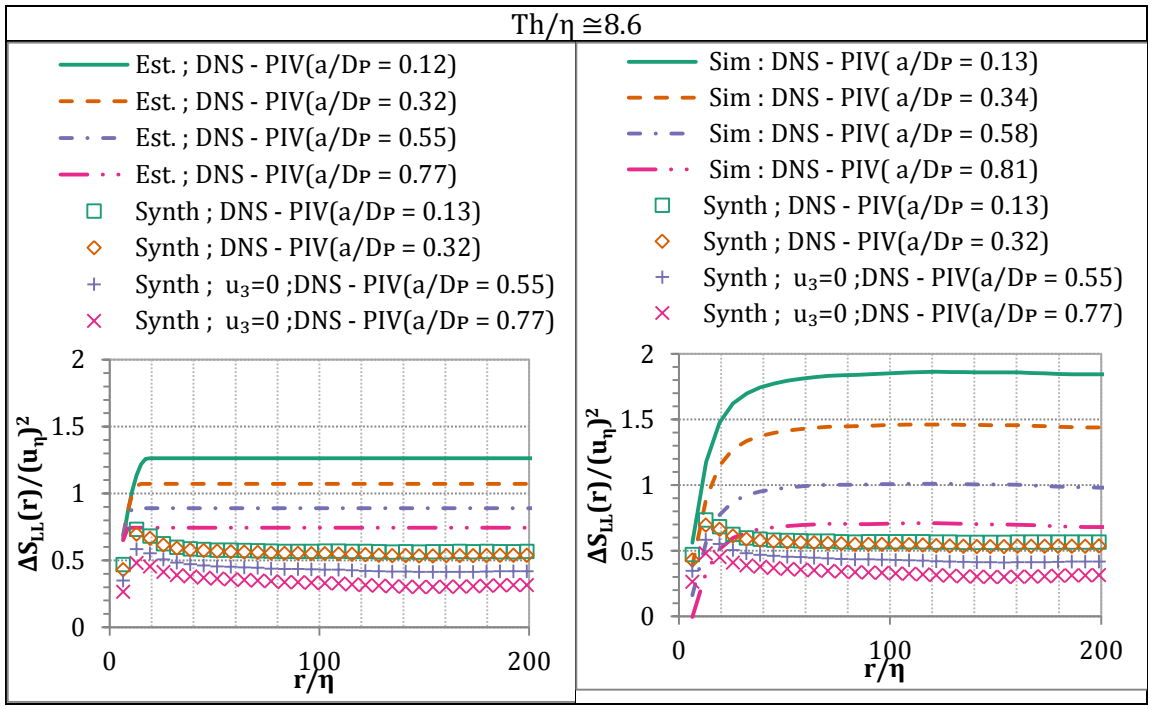

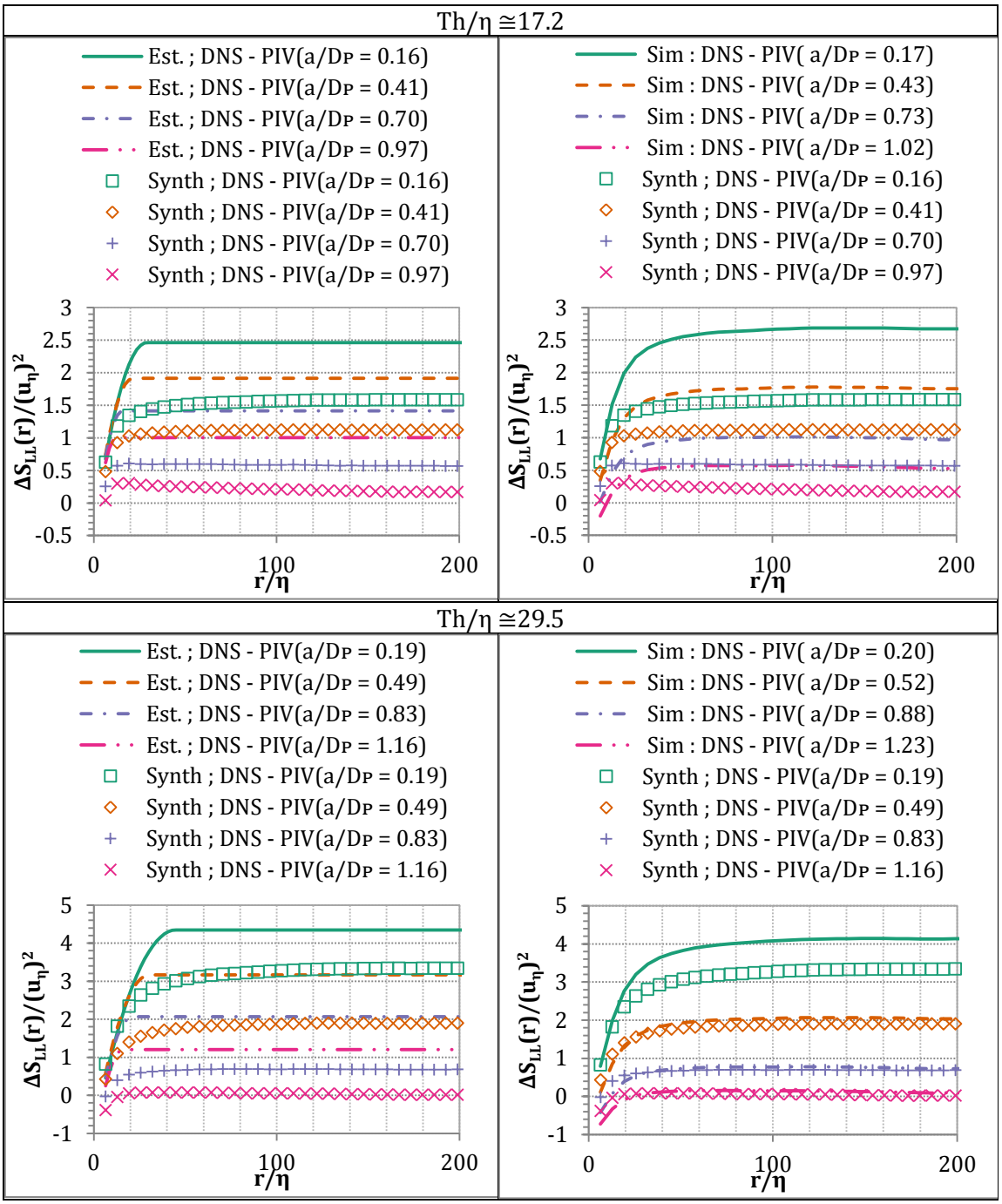

Figure 7.15 Variation of $\Delta S_{LL}(r)\{u\}/(u_\eta)^2$ with Δt. Upper graph, Th/η=8.6, middle graph, Th/η=17.1, bottom graph Th/η=29.9. Left: comparison of the estimation (lines) with synthetic images (symbols), for equivalent measurement parameters. Right column: comparison of PIV Simulator results (lines) with synthetic images (symbols), for equivalent measurement parameters.

The following differences are highlighted in this figure:

- Synthetic images present in general $\Delta S_{LL}(r)$ values closer to 0, compared to the PIV Simulator. As is shown below, this is induced by the smaller correlation value. For the largest Th/η the results of synthetic images match perfectly those of the PIV Simulator, except for the smallest Δt.
- For all cases the $\Delta S_{LL}(r)$ based on the estimation from LPF and PS errors is always significantly larger than the one corresponding to Synthetic images where some additional errors are included. Additionally, Figure 7.11 indicates that differences

in ε_T are small for all cases. The analysis of these differences in section 7.2.2.3 indicates that this difference is produced by errors correlated with the velocity (peak-locking errors) and also by a possible overestimation of low-pass errors or an underestimation of peak-splitting errors.

To further insight into the error, next subsection evaluates the correlation factor between error and velocity for the different cases.

7.2.2.2 *Correlation between the error and the velocity fields*

The difference between the correlation coefficient $C_{u\varepsilon}$ in the simulator cases (from section 7.1.2.3) and the one for synthetic images is plotted in figure below. Plots are organized for variations of Δt at each *Th* case.

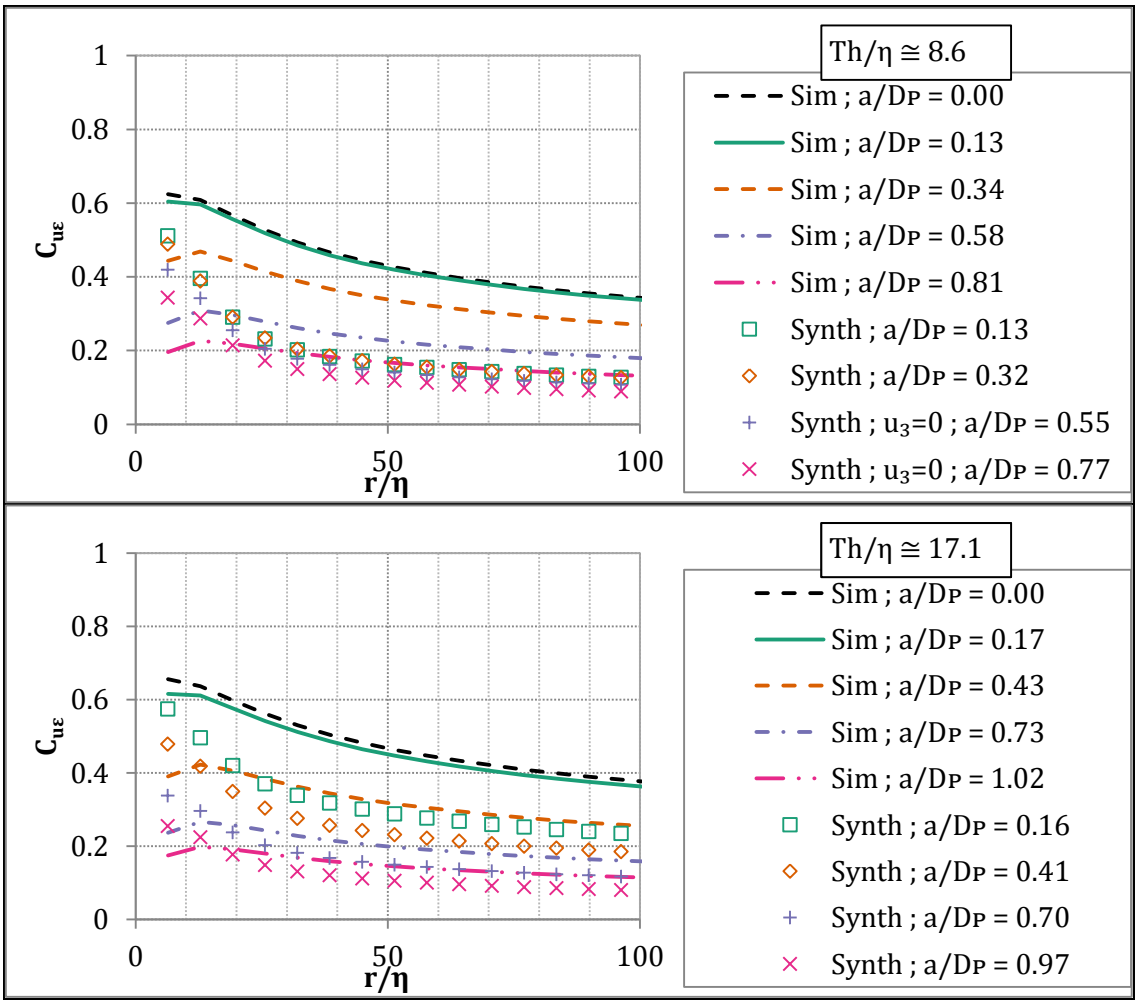

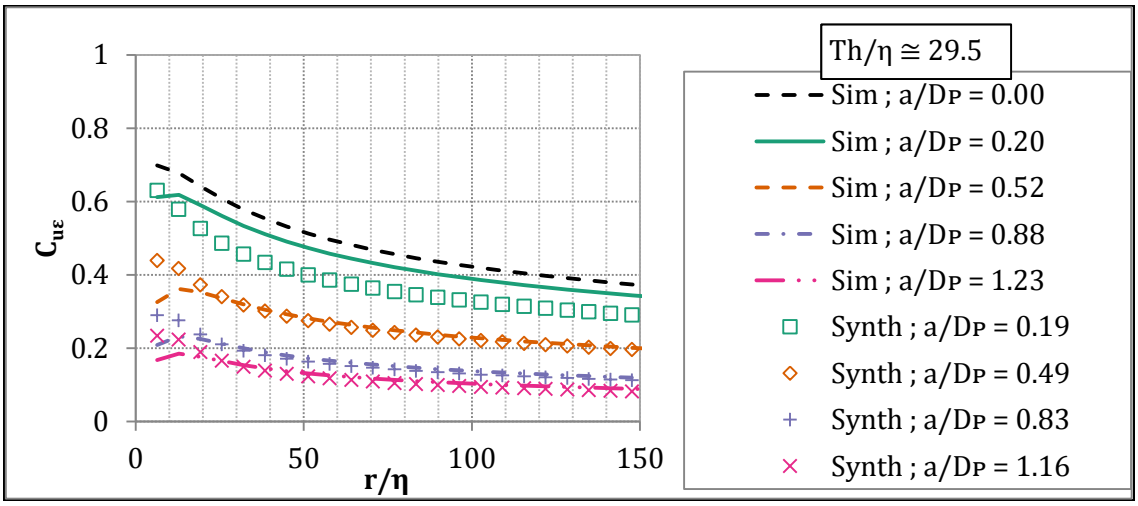

Figure 7.16 Variation of the $C_{u\varepsilon}$ with Δt, for the three laser sheet thicknesses simulated.

The comparison between both tools indicates the following differences:

- In general, synthetic images present smaller values of the correlation coefficient. This should be related to larger presence of other errors for synthetic images at low a/D_P values, errors that are not correlated with the velocity and thus diminish the correlation. Those errors should the random errors in determining the correlation peak location, $\xi_{\Delta x}$, (described in 5.3.10) or peak-locking errors (5.3.7).

7.2.2.3 *Assessment of the differences between the estimation and synthetic images*

This subsection explains the differences in $\Delta S_{LL}(r)\{u\}$ between synthetic images and the estimation. The difference between the $\Delta S_{LL}(r)$ estimated and that obtained from synthetic images is plotted below, for the 12 test cases related with spatial gradients error (those plotted in Figure 7.15). In the graph, only the $\Delta S_{LL}(r)$ values for large r/η are plotted, where $\Delta S_{LL}(r)$ becomes constant.

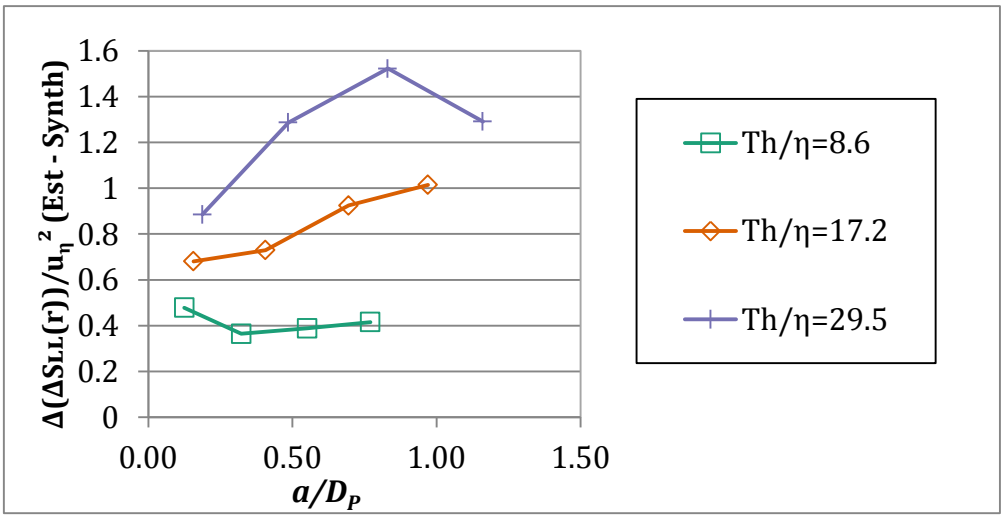

Figure 7.17 Comparison of the $\Delta S_{LL}(r)$ value estimated and that provided by synthetic images.

The following sources of error are included in synthetic images and not in the estimation (below only those not discarded in the preliminary error analysis of section 5.3 are quoted):

- Subpixel interpolator errors, which as per the analysis below can explain the difference between the estimate and synthetic images for the lowest a/D_P value.
- Outliers' occurrence, which in principle could explain the difference between the estimate and synthetic images for the larger a/D_P values. However, the fact that the error of synthetic images is so close with the estimation is not coherent with the occurrence of outliers, as they increase the error greatly (see Figure 7.12, for Th/η~4.4).

Since the additional errors given for synthetic images cannot explain the differences plotted in Figure 7.17 for large a/D_P values, some additional factors related with the accuracy of the estimate that can explain this difference have been compiled below, after the analysis of the subpixel interpolator errors.

Subpixel interpolator errors

Two error sources are associated with the image subpixel interpolator:

- Peak-locking systematic errors (cf. 5.3.7.2).
- Random errors random errors in determining the correlation peak location ($\xi_{\Delta x}$) (cf. 5.3.10).

Peak-locking systematic errors were estimated to produce a reduction in the correlation coefficient between the velocity and the error field (cf. 5.3.7.2). As a consequence, it was estimated that $\Delta S_{LL}(r)$ should vary by (with respect to the peak-splitting estimation): $-\sqrt{8}\left(C_6\left[S_{LL}\left(r=2d_{eq,1D}\right)\{u_R\}\right]^{1/2}+\sqrt{2}u_\eta\, a/D_P\right)\varepsilon_{PL}$. The values are plotted in the graph below, considering an ε_{PL}=0.02 pixels and C_6=0.5·C_5=0.34:

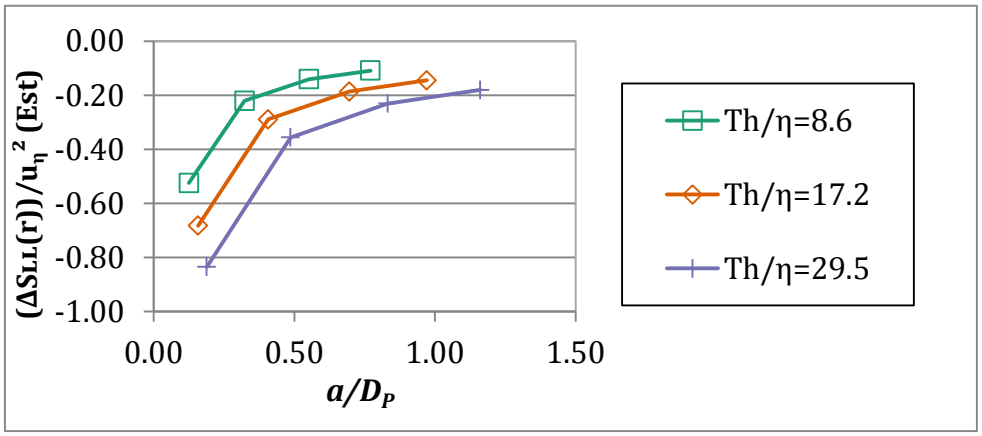

Figure 7.18 Estimation of the modification of $\Delta S_{LL}(r)$ from peak-locking errors.

- As can be observed, the estimation predicts that with peak-locking errors, the value of $\Delta S_{LL}(r)$ should diminish. This effect is especially important for the lower Δt values.

The estimation of order of magnitude of the effect from $\xi_{\Delta x}$ for all test cases in $\Delta S_{LL}(r)\{u\}$ is not provided. For a $\xi_{\Delta x}$ of 0.05 pixels the $\Delta S_{LL}(r)\{u\}$ of synthetic images would diminish by ~$0.3(u_\eta)^2$ with respect to the estimation of LPF+PS for the lowest Δt. However, this value of $\xi_{\Delta x}$ represents an error of ~$0.37u_\eta$ and such a large error increase would have been observed in the total average error analysis of Figure 7.11.

In consequence, peak-locking errors could generate the offset given between the estimation and synthetic images for the lowest Δt, but its effect reduces for large Δt's and thus these errors cannot explain the whole difference given for the larger Δt's. The effect of peak-locking error can be observed clearly when the vectors are validated in the post-processing with an additional step to that used in the graphs of Figure 7.15 (the median filter described in 3.3.4). In that case $\Delta S_{LL}(r)\{u\}$ increases with Δt for Th/η=8.6 (see Annex II where those results are plotted). This tendency should be produced by the reduction of the effect of peak-locking error and peak-splitting errors being removed by the validation. More precisely, $\Delta S_{LL}(r)\{u\}$ increases for this Th by $0.6(u_\eta)^2$, which is roughly the difference observed between the estimation and synthetic images for the lowest Δt.

Factors related with the estimate accuracy

The offset given between the estimate and synthetic images at large a/D_P values, should be explained by a combination of the following factors:

- The low-pass error has been overestimated. Two factors can be associated to this fact: (i) the improvement produced by the multigrid approach in the normalized response (cf. 5.3.3.1) has been neglected in the estimate of low-pass errors, and (ii) the reduction of low-pass errors that window weighting achieves has been underestimated. The multigrid approach improves the normalized response for wavelengths ℓ where it has already a very large value (NR≈0.95, see Figure 5.7). As it turns out, a very small improvement of NR for those wavelengths (for example from 0.95 to 0.97) can produce a large low-pass error decrease (in that example, of a 50%), as the error produced at wavelength ℓ is $\varepsilon_\ell \sim(1\text{-}NR(\ell))\cdot u_\ell$. If the main contribution to low-pass errors is produced in these wavelengths, this factor alone could explain the offset between the estimation and synthetic images.
- The reduction of a/D_P assumed to occur in synthetic images has been overestimated. In section 5.3.5.3 an estimation was provided for reducing a/D_P due to image discretization and image deformation (which is reduced between a 10 and a 30%). If this reduction has been overestimated, peak-splitting errors would be larger and low-pass errors would be smaller for synthetic images than for the estimation. As a consequence, the $\Delta S_{LL}(r)$ of synthetic images goes towards a lower value, thus inducing this difference. It is possible that peak-splitting hinders the capacity of image deformation to reduce displacement differences, thus leading to this fact. This is also coherent with the fact that for $Th/\eta\sim29$ (which is where LPF and PS errors are the most important) the $\Delta S_{LL}(r)$ of synthetic images and of the PIV Simulator are almost the same.
- Out-of-plane loss of pairs: this additional loss of pairs can generate a further reduction of low-pass errors and a further increase of peak-splitting errors, as commented in 5.3.5.1. As a result of both, $\Delta S_{LL}(r)$ should go towards lower values for synthetic images, whereas it does not so for the estimate as this effect was not included.

Researching these factors is left for future work. As has been observed in Figure 7.15 and Figure 7.14 $\Delta S_{LL}(r)$ presents variations with the measurement parameters similar to those given by the estimation. This indicates that the errors of interest of this work are also of importance for synthetic images.

7.2.3 **Synthetic images analysis summary**

As a result of the study on synthetic images, it could be concluded that peak-splitting and low-pass errors are relevant in PIV measurements, validating the conclusions extracted with the PIV Simulator. Additionally, for some of the cases presented here, the following errors that can have an effect in $\Delta S_{LL}(r)$ have been identified:

- The peak-locking errors, which can make $\Delta S_{LL}(r)$ to diminish. Those errors should have an effect of $\sim(u_\eta)^2$ for the lowest Δt case presented in this section; however, when Δt increases the effect of those errors diminishes.

In addition, synthetic images results incorporate as well a laser sheet thickness for which a large out-of-plane motion was sought. It was observed that when $u'\Delta t/Th$>20% the outliers produced by the out-of-plane motion produce an important error increase, of the order of that produced by peak-splitting errors given in this work. That value is considered then as advised limit.

7.3 DEDICATED EXPERIMENTAL SETUP

On the results of this part, real images from the dedicated experimental setup described in Chapter 6 are employed. Aside from some additional errors which have been estimated to produce a negligible effect in $S_{LL}(r)\{u\}$ (cf. Chapter 6 section 6.3.2 and section 6.5.4) the following differences to synthetic images are encountered:

- Cameras fill factor is ~60%. It could influence the peak-locking errors and random errors in determining the correlation peak location (Westerweel, 1998).
- The real images have background noise. Random errors in determining the correlation peak location could be influenced from this fact, and also outliers' occurrence.
- Particle images may not be perfectly Gaussian in shape, whereas on synthetic images this was imposed to be this way. Again random errors in determining the correlation peak location and peak-locking systematic errors could be influenced.
- Lasers are not perfectly Gaussian in shape and they present a misalignment offset of 0.2mm (see Chapter 6 section 6.3.1). This should induce correlation degradation and outliers' occurrence (Grayson *et al.*, 2016).

PIV processing parameters are detailed in 6.5.1. The vectors used to calculate the $S_{LL}(r)\{u\}$ values shown in this section are those that pass an allowable vector range criterion, specified in 6.5.1. In the Annex III, the values of $S_{LL}(r)\{u\}$ obtained with an additional validation step (a median filter validation) are plotted as well.

Just the first camera results are used in this section (cf. Chapter 6). For that camera, magnification is 50pix/mm (M_0=0.37) so η is 6px. The number of images recorder of each test case is indicated in Table 7.3[8]. For all cases the interrogation in-plane dimension was 32px, i.e. $D_I/\eta \cong 5.4$. The particles per pixel were estimated to be around 80-90 on a case with the laser sheet thickness 1.1mm. The seeding was not adjusted when the measurement parameters varied, so on the larger laser sheet thicknesses more particles should be present for each interrogation window. On the other hand, this effect should be attenuated by out-of-focus effects. The depth of field was of 3.4mm and so the particles should lose in importance the further they are from the focused plane.

The test matrix, together with the error parameters is shown in Table 7.3 below. Two values of a/D_P are provided, the characteristic displacement difference, defined by: $(a/D_P)_C=\sqrt[3]{(\epsilon Th)}\Delta t M_0/D_P$, and the actual value used to calculate the errors ($(a/D_P)_S$), obtained replacing $\sqrt[3]{(\epsilon Th)}$ by $S_{LL}(r=Th)\{u_M\}$, and incorporating the reductions of the displacement difference due to image deformation and image discretization described in 5.3.5.3. The value of $S_{LL}(r=Th)\{u_M\}$ used for this calculation is that given by the test case marked in green in the table below (which should be the case with smaller error).

The PIV Simulator vector fields and synthetic images were generated seeking the same values of the dimensionless parameters associated to the error from spatial gradients: D_I/η, Th/η and a/D_P (D_I and Th are slightly different due to the numerical codes restrictions). However, the turbulence created on the experimental setup and for the

[8] The number of images is not the same because the laser heads had a problem with a thermal sensor during the experimental campaign, which made that laser to stop shooting suddenly

numerical tools was of different characteristics (Re_λ is 430 for the numerical tools and 55 on the experiment). In consequence, the error parameters associated with the large scales, $u'\Delta tM_0/d_r$ and $u'\Delta t/Th$, do not match.

Table 7.3 Measurement and error parameters of the dedicated experimental setup test cases.

Th [mm]	Δt [μs]	N_{imags}	Th/η	$\Delta t/\tau_\eta$	$(a/D_P)_C$	$(a/D_P)_S$	$u'\Delta tM_0/d_r$	$u_\eta \Delta tM_0/d_r$	$u'\Delta t/Th$
1.1	**20**	**2000**	**9.3**	**0.023**	**0.14**	**0.12**	**0.51**	**0.14**	**0.9%**
1.1	50	2000	9.3	0.057	0.34	0.31	1.29	0.34	2.3%
1.1	85	2000	9.3	0.098	0.58	0.52	2.18	0.58	3.9%
1.1	120	2000	9.3	0.138	0.82	0.73	3.08	0.82	5.6%
2	**20**	**2000**	**16.9**	**0.023**	**0.17**	**0.15**	**0.51**	**0.14**	**0.5%**
2	50	2000	16.9	0.057	0.42	0.38	1.29	0.34	1.3%
2	85	2000	16.9	0.098	0.71	0.65	2.18	0.58	2.2%
2	120	1276	16.9	0.138	1.00	0.92	3.08	0.82	3.1%
3.4*	10	1200	28.8	0.011	0.10	0.10	0.26	0.07	0.2%
3.4*	**20**	**2000**	**28.8**	**0.023**	**0.20**	**0.19**	**0.51**	**0.14**	**0.3%**
3.4*	35	1500	28.8	0.040	0.35	0.33	0.90	0.24	0.5%
3.4*	50	1877	28.8	0.057	0.50	0.48	1.29	0.34	0.8%
3.4*	67	2000	28.8	0.077	0.67	0.64	1.72	0.46	1.0%
3.4*	85	2000	28.8	0.098	0.85	0.81	2.18	0.58	1.3%
3.4*	120	2000	28.8	0.138	1.20	1.15	3.08	0.82	1.8%

* on these cases the limiting depth is given by the depth of field. Nevertheless, for these cases $Th \cong 3.5$mm.

In this section, the errors can only be assessed with $\Delta S_{LL}(r)\{u\}$ as the real velocity field is not available. In the numerical tools analysis, $S_{LL}(r)\{u\}$ of the DNS was used as reference to calculate the differences. For this section, the values measured for a set of measurement parameters have to be used as reference. For the laser sheet thickness variation analysis, the case of Δt=20μs and Th=1.1mm is taken as reference (row marked in light green in Table 7.3 above). For the Δt variations, for each laser sheet thickness measured the case which has Δt=20μs is used (rows that use bold letters). The equivalent differences are calculated with the estimation and with the synthetic images results. In this case the $\Delta S_{LL}(r)\{u\}$ plotted changes of sign with respect to the one plotted on the previous two sections. In the graphs below, an increase in $\Delta S_{LL}(r)\{u\}$ is associated with an increase in $S_{LL}(r)\{u\}$.

7.3.1 Error distribution with the length-scales of the flow

In Chapter 6 section 6.5.5, some deviations of the experimental measurements to the ideal homogeneous turbulence case are described. As it turns out, the flow obtained in the measurement region was neither uniform, nor homogeneous nor statistically steady. As a result, it was preferred to not use the whole measurement region for the calculations, as indicated in chapter 6 section 6.5.5, to reduce the effect of those deviations. In addition, due to these deviations the whole range of r/η cannot be used for the comparisons to the

numerical tools. As indicated in section 6.5.5 the deviations should not interfere with the parametrical variations for r/η<100, and that is the range analyzed in this section.

7.3.1.1 *Velocity field*

Below, the Δt influence on $S_{LL}(r)\{u\}/(r\epsilon)^{2/3}$ can be observed, for the smallest and the largest laser sheet thickness. On the larger laser sheet thickness, Th/η~29, three additional time delays to those employed so far on this chapter were measured.

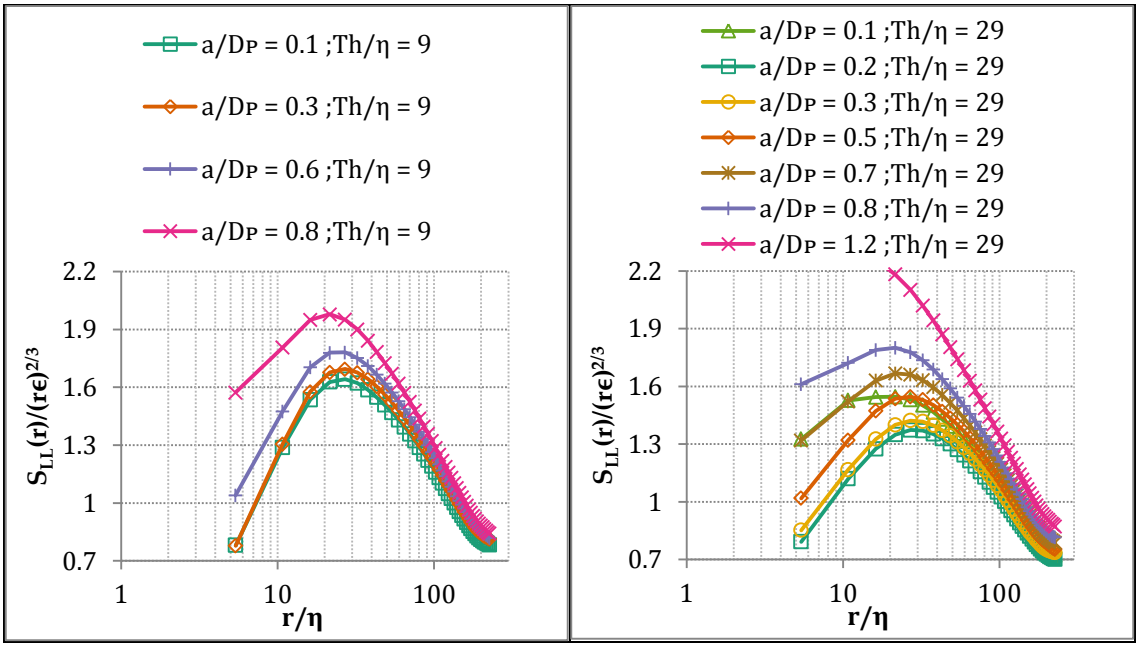

Figure 7.19 Variation of $S_{LL}(r)\{u\}/(r\epsilon)^{2/3}$ with Δt, for fixed laser sheet thickness, for the real images results. Left is the smallest thickness, right is the largest.

The following characteristics are observed in the figure:

- $S_{LL}(r)\{u\}$ divided by $(r\epsilon)^{2/3}$ has a different shape than for the numerical tools: the maximum is reached at a much shorter distance and the inertial range extends for a much shorter length. That is induced by the fact that the turbulence of the flow is different (for the numerical tools Re_λ≈433 and for the real images Re_λ≈55).
- The tendencies observed are the same than for the numerical tools. Only the case with Th/η~29 and a/D_P = 0.1 shows a different tendency that is analyzed below.
- The relative differences experienced by the results from real images seem larger.

In order to compare the results to those of the numerical tools, the differences in $S_{LL}(r)\{u\}$ are plotted below in Figure 7.20, for the cases with the smallest Δt (20μs) and varying Th: $\Delta S_{LL}(r)\{u\}$= $S_{LL}(r)\{u\}$ (Δt=20μs, Th=##)- $S_{LL}(r)\{u\}$(Δt=20μs, Th=9η). Left is the comparison to the estimation and right to synthetic images. The estimation is obtained from the measured $S_{LL}(r)\{u\}$ of the case with Δt=20μs and Th=9η, which is the case used for the calculation of all the error parameters.

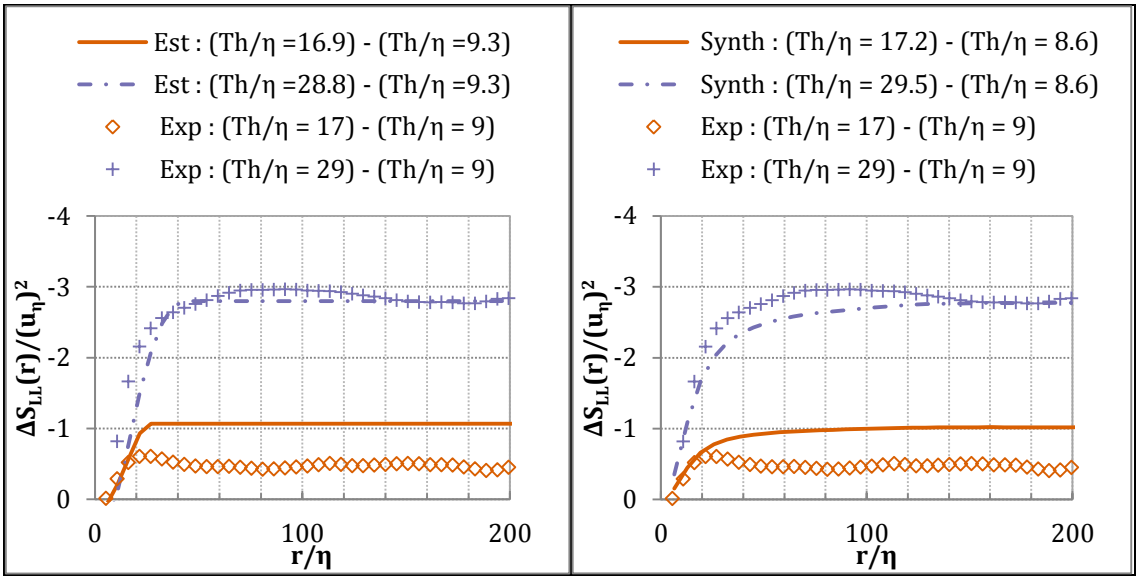

Figure 7.20 Variation of $\Delta S_{LL}(r)\{u\}/(u_\eta)^2$ with *Th*. Comparison of the results of real images (symbols) with the PIV Simulator (lines) on the left and with synthetic images (lines) on the right.

The following characteristics can be appreciated from the graph:

- The real images provide quite similar values to synthetic images and to the estimator. More detailed analyses on the effects that produce such variation of $\Delta S_{LL}(r)\{u\}$ are in 7.2 and 7.1.

Below, the differences in $S_{LL}(r)\{u\}$ for each laser sheet thickness are plotted. As was mentioned above, the case to which the differences are calculated is the one with Δt=20μs, for all three thicknesses. The differences are compared to the estimation on the left column and to synthetic images on the right column. The largest laser sheet thickness cases are represented into two graphs, the first one contains the same time delays than the other two thicknesses. On the thinnest laser sheet, the synthetic images results used are those without out-of-plane motion, when available (see Table 7.2).

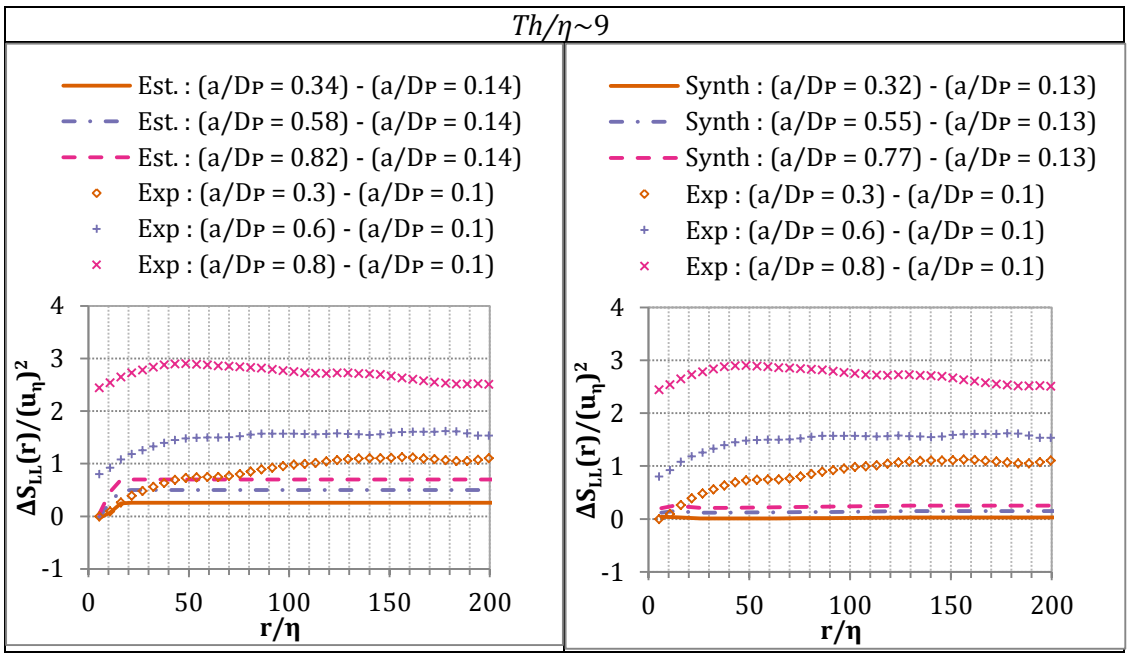

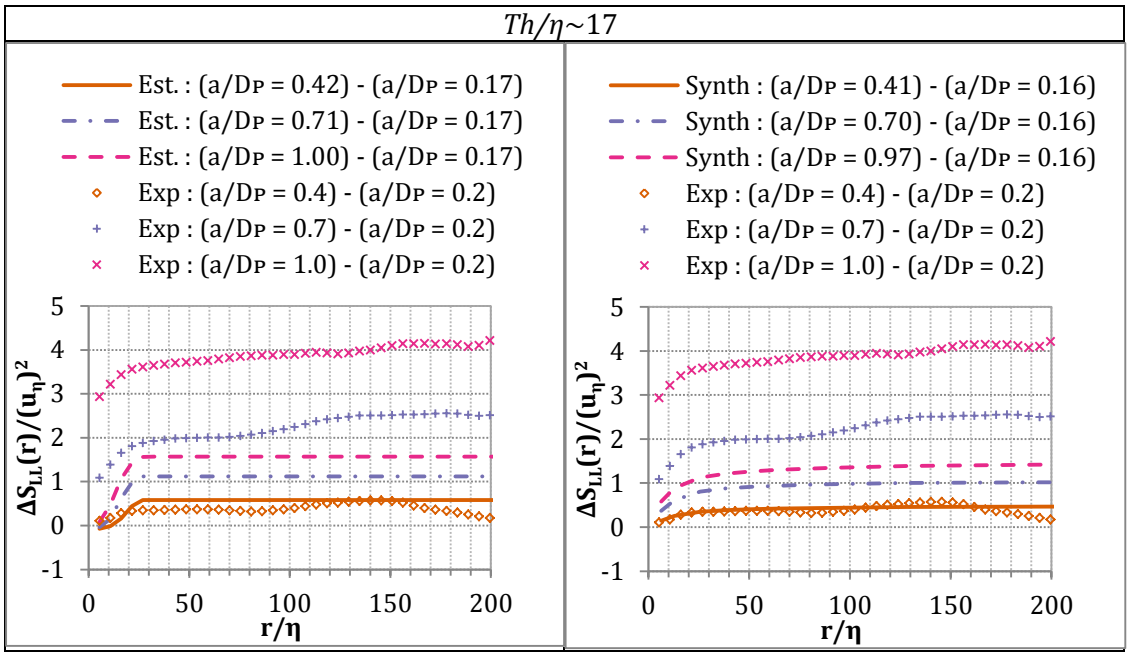

Figure 7.21 Variation of $\Delta S_{LL}(r)\{u\}/(u_\eta)^2$ with Δt. Comparison of the results of real images (symbols) with the estimation (lines) on the left and with synthetic images (lines) on the right.

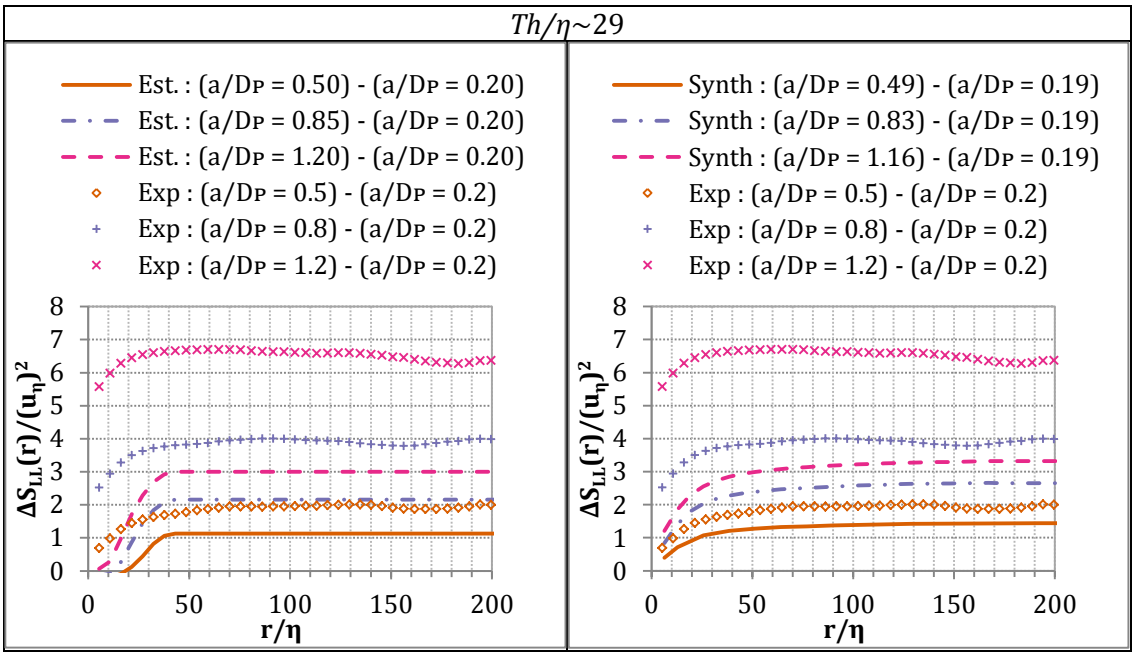

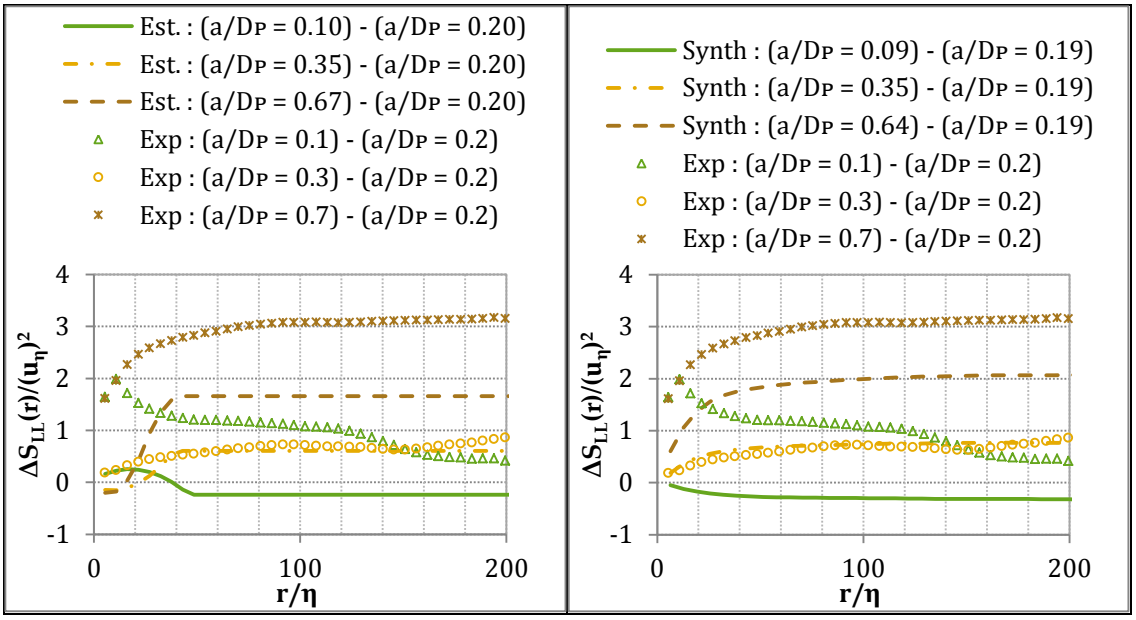

Figure 7.22 Variation of $\Delta S_{LL}(r)\{u\}/(u_\eta)^2$ with Δt. Comparison of the results of real images (symbols) with the estimation (lines) on the left and with synthetic images (lines) on the right. Th/η~29 for both graphs.

The following differences between real images results and numerical tools results can be observed in the figures:

- Most of the dedicated experiment $\Delta S_{LL}(r)\{u\}$ values are larger than the values provided by synthetic images and the estimations. The differences are largest in relative terms for the thinnest laser sheet. For the other two laser sheets there are test cases which $\Delta S_{LL}(r)\{u\}$ matches the corresponding case of the estimation or of synthetic images, typically those with smaller a/D_P. As the analysis in 7.3.1.2 indicates, the overall larger $\Delta S_{LL}(r)\{u\}$ seem produced by outliers' occurrence.
- The $\Delta S_{LL}(r)\{u\}$ of case of a/D_P=0.1 ($Th/\eta\approx29$) shows a clear discrepancy to both synthetic images and the estimator. Both the sign and the shape of $\Delta S_{LL}(r)\{u\}$ (with the maximum difference for the lower distances r/η) differ. The observed change in the tendency should be produced by the random errors in determining the correlation peak location and/or by peak-locking systematic errors. These errors are estimated and commented in 7.3.1.2.

All in all, when low-pass and peak-splitting errors should dominate (for the largest thickness) the values of $\Delta S_{LL}(r)\{u\}$ show the best resemblance. The tendencies and in some cases even the values show coherence to those of synthetic images and the estimation, except for the smallest Th. The sources of difference are analyzed in the next subsection.

7.3.1.2 *Assessment of differences to synthetic images*

In the comparison of results above, some differences have been encountered. Related to peak-splitting errors effect, the following factors have been identified:

- An underestimated u_η for the experimental results should produce larger $\Delta S_{LL}(r)\{u\}$. However, it does not justify why the discrepancies in $\Delta S_{LL}(r)\{u\}$ are larger at the smallest Th than at the largest.

- Lower particles' brightness and higher background noise level of experimental images may result in larger outliers' occurrence as Δt increases, for all thicknesses. Again, it does not justify why the discrepancies in $\Delta S_{LL}(r)\{u\}$ are larger at the smallest *Th*.
- Larger random errors from the light intensity change of overlapping particles (cf. section 5.3.9) due to the lasers misalignment. However, in that section the effect was assessed to be negligible.
- Outliers' occurrence is important already at the smallest *Th* for the experimental results, but it is not so for synthetic images. The theoretical estimations below point in this direction.

On the other hand, the case with a/D_P=0.1 and $Th/\eta\approx$29 has also a different tendency than synthetic images and the estimation. That could be produced because of peak-locking systematic error and the random errors in determining the correlation peak location and are also assessed below.

Outliers occurrence estimation

The methodology of section 5.3.12 for outliers effect assessment, requires an estimation the proportion of outliers remaining in the vector fields (henceforth, p_{out}). The estimate of p_{out} used here is simply the same proportion of vectors detected as outliers by the post-processing validation criterion (the allowable vector range, as described in 6.5.1), i.e. p_{out}=1-$p_{valid,1}$, where $p_{valid,1}$ is the proportion of valid vectors detected by this criterion. As to the velocity of outliers required for the estimation, u_{out}, it is taken as half of the maximum velocity imposed on the allowable vector range, i.e. u_{out}=1m/s.

In the same section 5.3.12, it was estimated that for low *r* values, the main $\Delta S_{LL}(r)\{u\}$ contribution from outlier vectors should be $2p_{out}(u_{out})^2$, with respect to the measured $S_{LL}(r)\{u\}$ with no outlier vectors. The values obtained from this estimate and the differences observed between synthetic and real images in Figure 7.21 and Figure 7.22 are plotted in the figure below (only the 4 Δt's available for all three thicknesses are plotted):

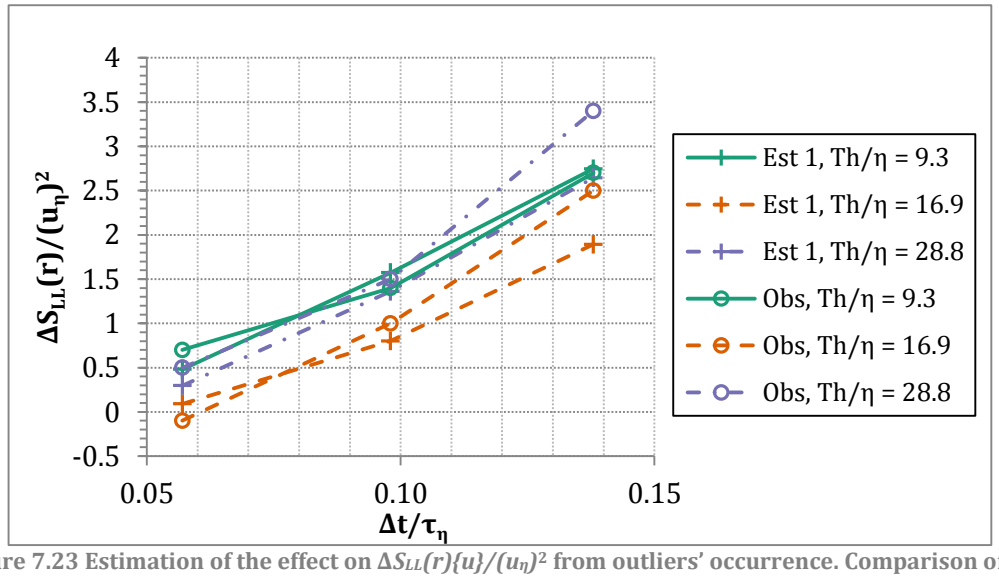

Figure 7.23 Estimation of the effect on $\Delta S_{LL}(r)\{u\}/(u_\eta)^2$ from outliers' occurrence. Comparison of the estimation (lines with + symbol) against the difference observed between synthetic and real images (lines with circle symbol).

Comparing the results in the graph above, the following can be mentioned:

- The estimation provides values very close to the values observed; it is almost even the difference between synthetic images and real images, for some cases. Plus, it predicts a larger outliers' occurrence for $Th/\eta\sim9$ than for $Th/\eta\sim17$. This was mentioned as an explanation of why for that thickness the discrepancies are the largest between the experiment and the numerical tools results.

The following factors could explain the fact that more outliers are produced for $Th/\eta\sim9$ than for $Th/\eta\sim17$:

- For $Th/\eta\sim9$, the overlap between the two lasers pulses calculated in Chapter 6 was of 75% but for $Th/\eta\sim17$ if a 96%.
- For the experimental images, the number of particles per interrogation volume is the smallest of all the three thicknesses, because the seeding was not adjusted. Nevertheless, the number of particles was estimated to be ~90 for this laser sheet thickness, which was the number of particles in synthetic images and no issues were observed. Additionally, the larger the thickness the more the light power spreads, which should reduce the benefit of having more particles.

In consequence, it seems more plausible that the outliers are produced due to the misalignment offset between the laser sheets, which makes the $Th/\eta\sim9$ to show the largest $\Delta S_{LL}(r)\{u\}$ differences to synthetic images. The estimate also indicates larger proportion of outliers for the experimental results than on the synthetic images results, which explains the larger $\Delta S_{LL}(r)\{u\}$ values overall.

Subpixel interpolator errors

The additional case of the $Th/\eta\approx29$ with Δt=10μs (a/D_P=0.1 in Figure 7.22) exhibits larger $S_{LL}(r)\{u\}$ than the case with the $Th/\eta\approx29$ with Δt=20μs for real images, but it does not so for synthetic images or for the estimation. This difference is likely due to random errors in determining the correlation peak location, $\xi_{\Delta x}$ (cf. 5.3.10), and peak-locking errors (cf. 5.3.7.2). The effect of those errors in $\Delta S_{LL}(r)\{u\}$ is estimated below.

The estimation of $\xi_{\Delta x}$ indicates that considering this error alone both for synthetic images and real images an increase in $\Delta S_{LL}(r)\{u\}$ should be produced. For a $\xi_{\Delta x}$ of 0.05 pixels, $\Delta S_{LL}(r)\{u\}$ would increase $0.4(u_\eta)^2$ when going from Δt=20μs to Δt=10μs; the same increase is predicted for synthetic and real images. In consequence, it would be required for $\xi_{\Delta x}$ to be larger for real images than for the synthetic images to explain the different values observed, which is possible. If for real images $\xi_{\Delta x}$ reaches 0.1 pixels whereas for synthetic images it has a lower value, this difference would be explained.

Peak-locking systematic errors could also be responsible of this difference. This is so because for the dedicated experimental setup $u'\cong0.26$px and for synthetic images $u'\cong0.7$px. Therefore, as commented in 5.3.7, for real images peak-locking errors should always have the same sense. For synthetic images, although $u'<1$px, there are still displacements above 1px, inducing errors in both senses and thereby with less effect in $\Delta S_{LL}(r)\{u\}$. The estimation of peak-locking systematic errors for real images is then the one identified as case (ii) in section 5.3.7, whereas for synthetic images is the one identified as

case (i). Both are provided in the table below. The value provided in the table is the variation in the $\Delta S_{LL}(r)\{u\}$ given by peak-splitting (ε_{PL}=0.02pixels is considered and the error is assumed to be of anti-peak-locking type, as was obtained in section 5.3.7.1):

Table 7.4 Estimation of the effect in $\Delta S_{LL}(r)$ of peak-locking systematic errors

Parameters		$(\Delta S_{LL}(r))/(u_\eta)^2$	$(\Delta S_{LL}(r))/(u_\eta)^2$
Δt [μs]	$\Delta t/\tau_\eta$	Real images	Synthetic images
10	0.011	2.17	1.6
20	0.023	1.20	0.8

As can be observed, the predicted effect is larger for real images than for the synthetic images. A combination of the two sources studied in this subsection can produce the difference observed between synthetic images and real images for this particular Δt.

7.3.2 **Experimental validation conclusions**

The following aspects have been observed on this section, related to the errors of interest:

- The low-pass effect induced by the laser sheet thickness is given as well on the experimental results. On the largest laser thickness the $\Delta S_{LL}(r)\{u\}$ goes to $\sim 3u_\eta^2$, with respect to the lower thickness. Additionally, the lower thickness case is also filtered and the $\Delta S_{LL}(r)\{u\}$ obtained compared to the DNS was of $\sim 2u_\eta^2$ on the PIV Simulator and $\sim u_\eta^2$ on synthetic images (the actual difference of synthetic images was of $\sim 0.5u_\eta^2$ but that includes a $\Delta S_{LL}(r)\{u\}$ of $\sim 0.5u_\eta^2$ due to subpixel interpolator errors). Therefore, the total error on $S_{LL}(r)\{u\}$ from this source on the experimental setup is expected to be $\sim 4u_\eta^2$.
- Related to the time variations, it has been observed that the same tendency is given on the experimental setup results than for the numerical tools. The values do not match, but the theoretical estimations indicate that this seems produced by the influence of outliers' occurrence. For the largest laser thickness, the maximum $\Delta S_{LL}(r)\{u\}$ observed is of $\sim 6u_\eta^2$ for the experimental setup, of $3u_\eta^2$ for synthetic images and of $4u_\eta^2$ for the PIV Simulator results.

In conclusion, the errors characterized in the PIV Simulator appear as well, validating the conclusions of section 7.1.3. In the case of real images, outliers' occurrence can enhance the effect of peak-splitting errors.

7.4 MEASUREMENT ENVELOPE QUANTIFICATION

With $S_{LL}(r)\{\varepsilon\}$ it is possible to provide empirical values to the hypotheses of Nogueira *et al.* (2012) that motivated this PhD, as detailed in chapters 1 and 2. In that work, different requirements were formulated to obtain optimized PIV turbulence measurements. The requirements linked turbulent flow features with PIV acquisition parameters. Specifically, those studied in this PhD involve the coupling of Δt and the laser sheet thickness: (i) related with the spatial gradients induced by the turbulence and (ii) related with the out-of-plane motion induced by turbulence.

The requirement related to the spatial gradients effect is $Th \leq f_3 \ell_L$ (see 1.2.2). Basically, the requirement states that the laser sheet thickness cannot surpass f_3 times the lowest length-scale to be characterized (ℓ_L) without the error on that scale being larger than a certain percentage. This requirement has been the main focus of this PhD, and with the results of this chapter it is possible to provide a value of f_3. In order to obtain the value of f_3, $(S_{LL}(r)\{\varepsilon\}/S_{LL}(r)\{u\})^{1/2}$ is used, as it roughly should provide the relative error of a scale, as mentioned in Chapter 5 section 5.2.1.2. This data is only available for the PIV Simulator and synthetic images results and gives the following plots:

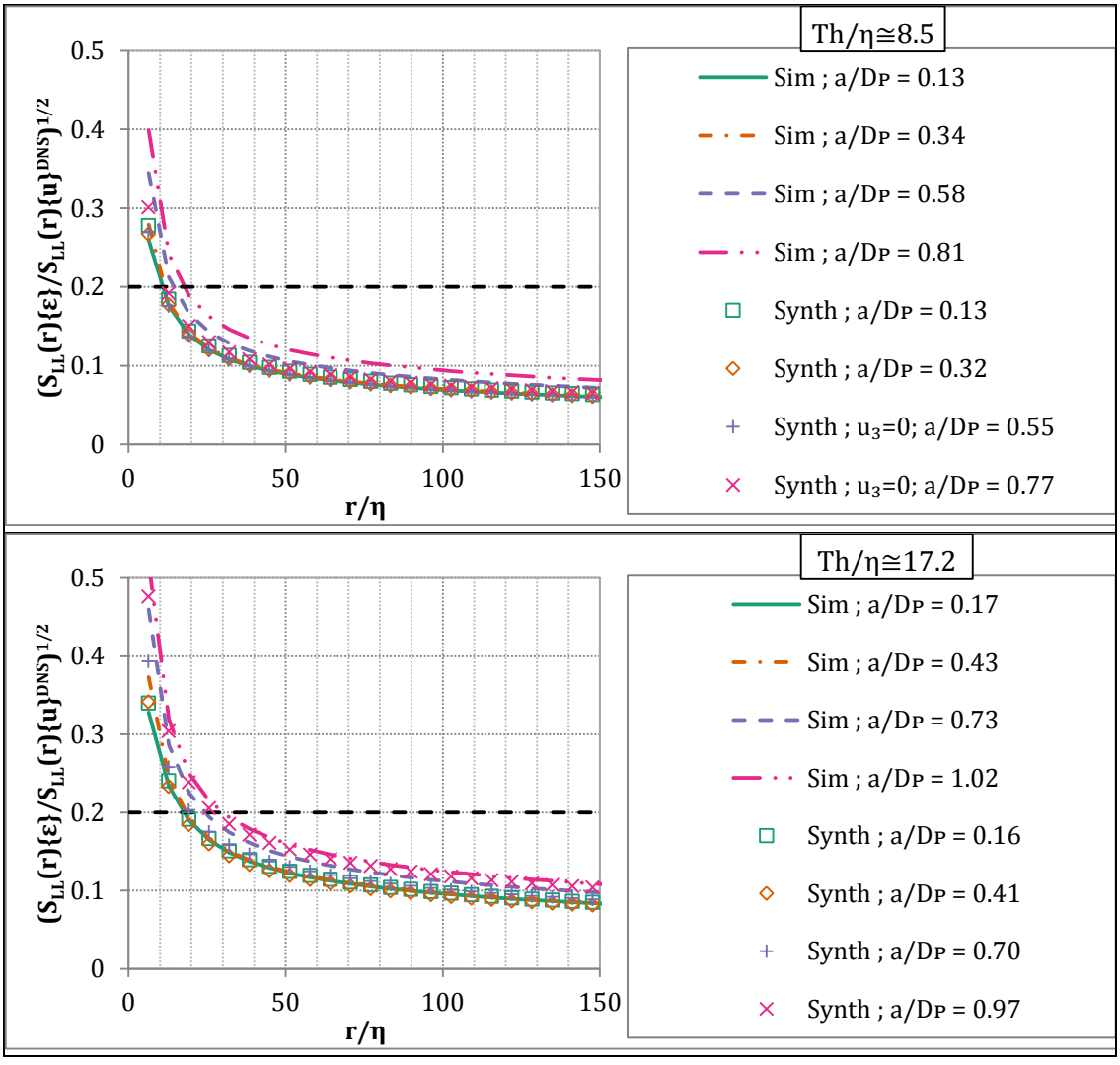

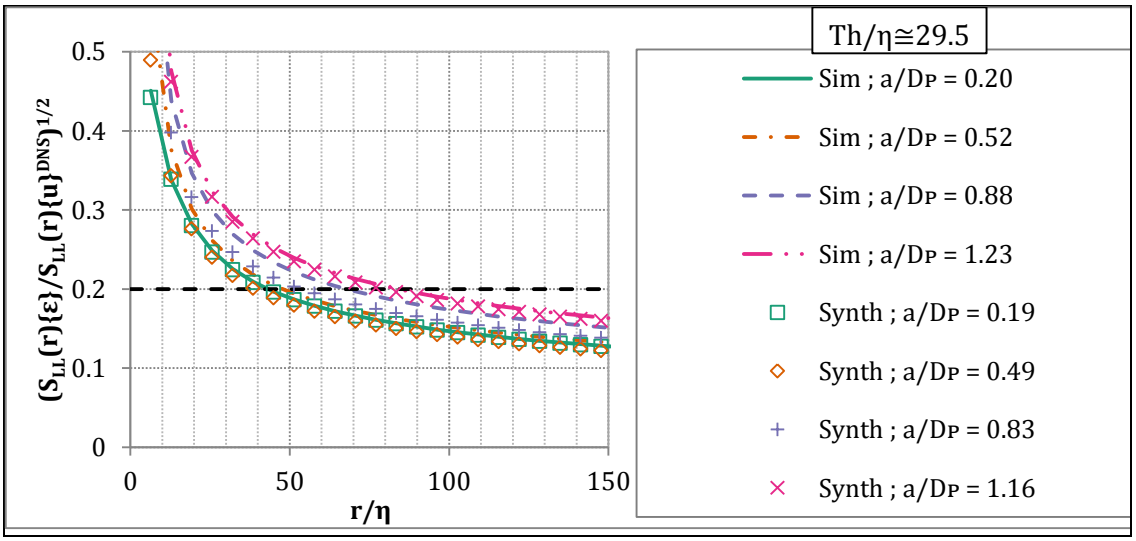

Figure 7.24 Variation of the error fraction of a scale with Δt, for the three laser sheet thicknesses available in both numerical tools. PIV Simulator results are represented by lines and synthetic images results are represented by symbols.

For the lowest time delay, the requirement $Th \leq f_3 \ell_L$ translates into (considering that the lowest scale ℓ_L is the one with a 20% of error on $(S_{LL}(r)\{\varepsilon\}/S_{LL}(r)\{u\})^{1/2}$):

Th/η	ℓ_L/η (Sim)	ℓ_L/η (Synth)	f_3 (PIV Simulator)	f_3 (Synthetic images)
8.5	11	13	0.78	0.66
17.2	19	19	0.9	0.91
29.5	45	45	0.66	0.66

However, as has been observed, Δt also influences on the error induced by the laser sheet thickness. For the highest measured time delay:

Th/η	ℓ_L/η (Sim)	ℓ_L/η (Synth)	f_3 (PIV Simulator)	f_3 (Synthetic images)
8.5	19	13	0.45	0.66
17.2	32	30	0.53	0.57
29.5	83	83	0.36	0.35

To avoid the influence of the interrogation window on the coefficient value, the case of $Th/\eta \sim 30$ is the one employed. If the errors related to the subpixel interpolator (systematic peak-locking and the random errors in determining the correlation peak location) allow measuring at low a/D_P values, then f_3=0.66. If that is not the case and Δt has to be increased to reduce the importance of those errors then the value for the coefficient at large a/D_P values is f_3=0.35. In conclusion:

$$Th \leq \begin{cases} 0.66\ell_L; \text{ for } a/D_P \sim 0.2 \\ 0.35\ell_L; \text{ for } a/D_P \sim 1.0 \end{cases}$$

In any case, it should be possible to obtain the limiting value for other set of measurement parameters from the proposed estimation of ε_T and a measurement of $S_{LL}(r)\{u\}$ of the corresponding flow. For the value of $S_{LL}(r)\{\varepsilon\}$, the following can be used: $S_{LL}(r)\{\varepsilon\} \sim 2(\varepsilon_T)^2$, which has been shown to work for $r > Th$, the region of interest to this work.

The validity of these values on real PIV images was checked through $\Delta S_{LL}(r)\{u\}$. It has been observed that low-pass filtering errors on real images produce similar values than for the numerical tools, thereby validating f_3 for low a/D_P values. On the other hand, peak-splitting errors induce larger $\Delta S_{LL}(r)\{u\}$ for real images than for the numerical tools; however, it has been shown that the larger values are very likely due to occurrence of outliers (cf. 7.3.1.2). Outliers' occurrence depends on many other factors than peak-splitting errors and thus their influence has not been integrated into the f_3 value. For large a/D_P values, the value that can be obtained from the estimates of this work can be used as starting value of the coefficient f_3. This value would have to be reduced to account for outliers' occurrence.

As to the second requirement, related to the out-of-plane motion, on the work of Nogueira *et al.* (2012) it was formulated as:

$$u_T \Delta t \leq 0.2 Th$$

Where u_T is the characteristic velocity of the largest turbulent scales. On this work, the parameter $u'\Delta t/Th$ has been used, since u' can be more easily estimated than u_T. In any case, both should be of the same order. It was found on the results of synthetic images (cf. 7.2.1) that a reasonable limit seems to be $u'\Delta t/Th$=20%. This limit could not be validated on the dedicated experimental setup because either peak-splitting errors or the laser profiles misalignment interfered.

7.5 MAGNITUDE OF THE ERRORS OBJECTIVE IN RESPECT TO OTHER ONES. RELEVANCE IN REFERENCE TO INDUSTRIAL FACILITIES ERROR HANDLING PRACTICE

To conclude this chapter, the different errors that have been observed are compiled below, together with the parameters that produce them. This allows revealing the importance of the errors objective of this PhD as compared to others already characterized by the research community. The following errors have been observed to appear in real images, as the analysis in $\Delta S_{LL}(r)\{u\}$ revealed (see Figure 7.20, Figure 7.21 and Figure 7.22):

- The low-pass effect errors are estimated to increase from $0.22u_\eta$ (for $Th{\sim}9\eta$) to $0.54u_\eta$ (for $Th{\sim}29\eta$). Related to the rms turbulent velocity fluctuations, u', this supposes $0.09u'$.
- Peak-splitting errors, induced by spatial gradients in the out-of-plane direction, are estimated to reach a maximum value of $0.81u_\eta$, for $Th{\sim}29\eta$ and a/D_P=1.2. Related to u', this supposes $\sim 0.22u'$. For $Th{\sim}9\eta$ and a/D_P=0.14 the value of these errors is of $0.27u_\eta$ or $0.07u'$.
- Peak-locking systematic errors and random errors in determining the correlation peak location are typically assumed to be between 0.01 and 0.1 pixels (cf. 5.3.7 and 5.3.10). In the case of the lowest Δt measured (Δt=10μs, for which $u'\Delta tM_0$ =0.26 pixels) an error of 0.1 pixels supposes $0.38u'$. Compared to the largest Δt measured (Δt=120μs) 0.1 pixels suppose only $0.03u'$.

It was also studied, for synthetic images, the effect of a turbulent out-of-plane loss of pairs. This error source becomes the dominant one for $u'\Delta t/Th$ above ~25%; however, when $u'\Delta t/Th$ is below ~20% it is negligible.

Additionally, for the errors below their effect was removed or not appreciated in $S_{LL}(r)\{u\}$ (see Chapter 6 section 6.5.4 and 7.3.1.2):

- CCD read-out errors, estimated to be ~0.06pixels, produce a $0.23u'$ velocity gap between quadrants for the lowest Δt measured, (Δt=10μs). However, for the largest Δt the gap only supposes $0.02u'$.
- Light intensity change errors due to the lasers profiles offset: ~0.04pixels due to the laser profiles offset: $\sim 0.08u'$ in the lowest Δt measured for that laser sheet thickness and $0.013u'$ for the largest Δt measured for that laser sheet thickness.
- Perspective projection errors can produce $\sim 0.05u'$ of maximum error, independent of the measurement parameters. The error depends on the camera sensor and on the lenses employed for the measurement, which did not change in these measurements.

As shown in the previous compilation the errors objective of this work could be non-negligible if the measurement parameters are non-properly selected. As shown in 7.1.3, the total error increases with the laser sheet thickness, and it presents an optimum value with a/D_P. Considering only the error induced by spatial gradients, large measurement sizes with respect to Kolmogorov scales should be avoided, and also displacement discrepancies a/D_P>0.5. For a/D_P above this value peak-splitting errors increase, and in addition, for PIV images the appearance of peak-splitting favors outliers' occurrence.

Finally, thanks to the measurement campaigns completed with other PIV centers, the possible relevance of the errors objective of this PhD in wind tunnel measurements can be inferred. In those measurement campaigns it was observed that, in general, the objective was both to maximize the data yield and at the same time obtain large enough displacements.

Since the magnification of the setups is mostly imposed by the size of the measurement region, the displacements were adjusted by setting the Δt. Displacements in the order of 10 pixels or larger were sought in these campaigns for the mean flow. The idea of this error handling practice is maximizing the dynamic velocity range (DVR) by reducing the importance of the subpixel interpolator errors. However, increasing the Δt too far could lead to production of peak splitting phenomenon and the errors associated, as has been seen through this chapter. As a result, the DVR could be reduced and not increased.

The laser sheet thickness was set from previous measurement experience and taking into account out-of-plane motion and other possible constraints (such as not burning the model, see chapter 4 for further details). If the laser sheet is enlarged too far to avoid out-of-plane motion errors, that could lead to important low-pass and peak-splitting errors (depending on Δt). In consequence, increasing the laser sheet thickness could be counter-productive in terms of error reduction.

As a consequence of the importance of both parameters, it is advised to calculate, from the preliminary measurements used to adjust the acquisition parameters, the error parameters compiled in section 5.3.16. This set of parameters helps to assess which errors will be produced, and if so, with what importance. The estimate of $\epsilon \sim A{u'}^3/\mathcal{L}$ can be used for calculating a/D_P, η and u_η which, together with a measurement of $S_{LL}(r)\{u\}$ allow estimating the total error. In order to calculate ϵ, the integral length-scale $\mathcal{L}$ can be assumed to be of the order of the size of the larger vortices observed in the preliminary measurements; A can be considered to be ~0.5; and u' can be calculated from the statistics of the preliminary measurement. In addition, the laser sheet profiles would have to be characterized. For such purpose, the device used by the DLR and described in Chapter 4 section 4.1.1.1, something similar to the tool used in Chapter 6, or the device employed by Grayson *et al.* (2016) could serve this purpose.

Chapter 8 **Conclusions**

The research of this PhD has been undertaken to assess the capacity of PIV for measuring turbulent flows, and its possibilities for discriminating length-scales information. The scope is focused on the interaction between the laser sheet thickness and the time between pulses with turbulent spatial gradients. The objectives of the PhD have been reached achieving the following conclusions:

8.1. Conclusions regarding error assessment methodology

For error assessment, a successful methodology has been found by performing 4 steps: (i) Theoretical rationale, (ii) PIV Simulator, (iii) Synthetic images and (iv) Dedicated experimental setup. Interaction and iteration between the different steps, rather than a successive lineal progression has been necessary to achieve the results.

Within this frame, two aspects are particular to this PhD:

1) The development of the "PIV Simulator" tool has allowed for effectively uncoupling part of the errors under study. This way, the capability of PIV to manage gradients within the interrogation volume has been studied as a function of Δt and the laser sheet thickness, without coupling with other errors like outliers' occurrence and image discretization errors. On this work, for the test cases analyzed the results indicate that these errors alone can reach around an 8% of the turbulent *rms* velocity fluctuations *u'*.
2) Another relevant particularity of this PhD regarding the methodology is the suitability of the use of the second order longitudinal velocity structure function ($S_{LL}(r)\{u\}$), commonly used in turbulent studies, as a tool for studying length-scales error distributions. The main advantages of the function are (i) its straightforward calculation and (ii) its accumulation of error from smaller scales into the evaluated scale. In this work, the function has been used in the following forms:
    - $\Delta S_{LL}(r)\{u\}$ which provides the error for the velocity differences at a distance r. Due to the characteristics of $S_{LL}(r)\{u\}$, it directly provides the error in the turbulent kinetic energy (at large r values), without any need for error integration.
    - $S_{LL}(r)\{\varepsilon\}$, the second-order longitudinal structure function applied to the error field, which provides the magnitude of the velocity errors for a turbulent scale r.

    The difference between both of them has been observed to depend on the correlation between the velocity and the error field, $C_{u\varepsilon}$. This correlation coefficient is of importance for the error in derived magnitudes (e.g. the *TKE*).

8.2 Conclusions regarding errors sources and magnitude assessment

The following error sources have been analyzed in this PhD, and their variation with Δt and Th assessed (valid for $Th>D_I$):

- Low-pass errors: these errors grow in importance with Th/η. Δt also influences on the final low-pass error value, through the gradients parameter a/D_P, due to the reduction of the effective measurement volume induced by peak-splitting phenomenon. Specifically, the following estimate has been found to provide acceptable values of the error observed:

$$\varepsilon_{LPF} \approx 0.34\sqrt{S_{LL}(r = 0.25 r_A d_{eq,1D})\{u\}}$$

  Where $d_{eq,1D}$ is a characteristic distance that encompasses for the measurement volume filtering, given by: $d_{eq,1D}=\sqrt{(D_I^2+Th^2)}$ and r_A is a coefficient that accounts for the reduction of the number of particles that actually contribute to the displacement obtained, given by:

$$r_A = \frac{\pi/2}{\left(\frac{a}{D_P}\right)^2 + 2\sqrt{2}\left(\frac{a}{D_P}\right) + \frac{\pi}{2}}$$

$$\frac{a}{D_P} = \frac{\sqrt{S_{LL}(r = Th)\{u\}}\Delta t M_0}{D_P}$$

  In this work, a/D_P has been calculated from $S_{LL}(r)\{u\}$. However, when the function is not available, an estimate of the parameter can be obtained from $\sqrt[3]{(\epsilon Th)}\Delta t M_0/D_P$.

- Peak-splitting errors. Two sources have been identified as enhanced by peak-splitting phenomenon: particles misplacements errors (random) and group-locking errors (systematic). These errors increase with Δt and Th, following expression below:

$$\xi_{\Delta u} \approx \sqrt{\frac{S_{LL}(r = Th)\{u\}}{r_A N}}$$

  Where N is the number of particles inside the interrogation volume.

- The total error induced by these two sources (average error of the instantaneous velocity measurement) is given by:

$$\varepsilon_T^2 \approx \varepsilon_{LPF}^2 + \xi_{\Delta u}^2$$

  Considering only these two error sources, there is an optimum a/D_P value that gives the minimum total error for a given measurement volume, that can be obtained in each case by recurring to the expressions above.

- As a result of the combination of both sources, the smallest length-scale that can be characterized with less than a threshold error is imposed by the laser sheet

thickness. In this work, the scales that keep the error under a 20% are those with size $\ell \geq 1.5Th$. Other thresholds can be imposed and the associated ratio to Th obtained by recurring to the error estimates provided here and a measurement of the $S_{LL}(r)\{u\}$ of the flow.

- Whereas the optimum measurement for the instantaneous velocity is governed by the total error given above, that may not be the case for derived magnitudes. In those cases, the correlation between the velocity and the error field may play a key role. In this work, the error in quadratic velocity quantities (such as the turbulent kinetic energy or the *rms* velocity fluctuations u') has been assessed as well, as it is provided by $\Delta S_{LL}(r)\{u\}$ at large r values. The following estimate has been obtained:

$$TKE_R - TKE_M \approx \frac{3}{4}\left[2\sqrt{2}\left(0.67\left(S_{LL}\left(r = 2d_{eq,1D}\right)\{u_R\}\right)^{1/2} + \sqrt{2}u_\eta\, a/D_P\right)\varepsilon_{LPF} - 2\varepsilon_{LPF}^2 - 2\xi_{\Delta u}^2\right]$$

Where r_A, ε_{LPF} and $\xi_{\Delta u}$ are those provided above. The measurement of such magnitudes can be favored by allowing peak-splitting to be important, because it reduces the first term and increases the second. However, that can result in larger velocity errors, as indicated by the image below.

The different test cases analyzed in this work include other errors. Those that have been found relevant are plotted together with the errors on which this PhD focused in the Δt – Th map below. Th is divided by Kolmogorov scale η and Δt is used to obtain the displacement in pixels of u':

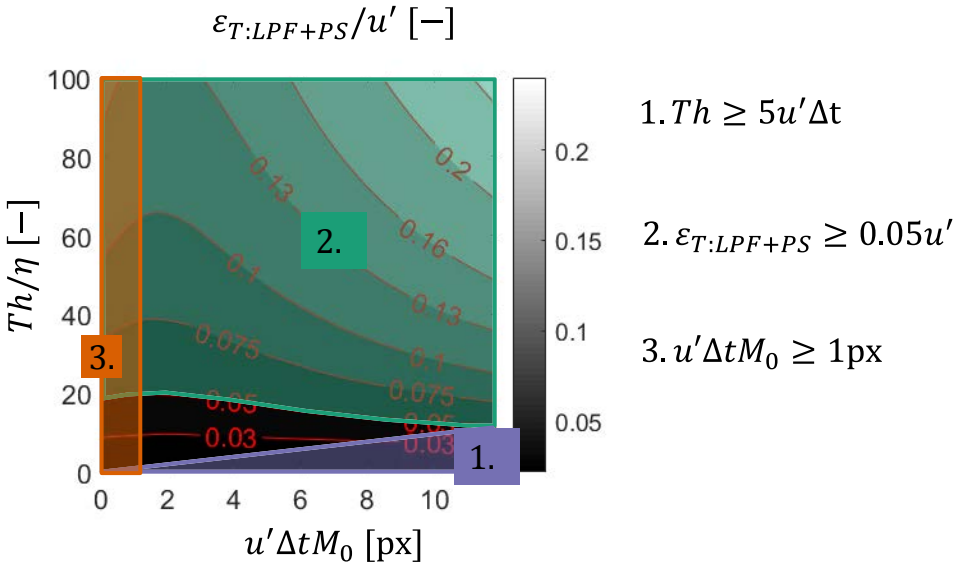

The following limitations are plotted, based on the parameters of the synthetic images employed in this work:

1. Limitation imposed by out-of-plane motion: it has been observed that for $Th \geq 5u'\Delta t$ outliers' occurrence gets too important. Then, it dominates the total error value, thereby the limitation plotted. The total error measured on synthetic images surpasses 5%% of the turbulent *rms* fluctuations u' above this limit.

2. The moment at which the total error (only from peak-splitting and low-pass errors) surpasses a 5% of the turbulent *rms* fluctuations *u'*.
3. Limitation on the minimum displacement. This limitation has not been explored in this work, but for any PIV measurement the total error induced by the subpixel resolution of the algorithm would surpass the 5% of *u'* at some point when the displacements get too low.

References

Adrian, R. J. (1991). Particle-imaging techniques for experimental fluid mechanics. *Annual Reviews in Fluid Mechanics, 23*(1)*,* 261-304.

Adrian, R. J. (1997). Dynamic ranges of velocity and spatial resolution of particle image velocimetry. *Measurement Science and Technology*, *8*(12), 1393.

Adrian, R. J. (2005). Twenty years of particle image velocimetry. *Experiments in Fluids*, *39*(2), 159–169.

Adrian, R. J., & Westerweel, J. (2011). *Particle Image Velocimetry.* Cambridge University Press. ISBN: 978-0-521-44008-0.

Arroyo, M. P., & Greated, C. A. (1991). Stereoscopic particle image velocimetry. *Measurement Science and Technology*, *2*(12), 1181.

Astarita, T. (2008). Analysis of velocity interpolation schemes for image deformation methods in PIV. *Experiments in Fluids*, *45*(2), 257–266.

Astarita, T., & Cardone, G. (2005). Analysis of interpolation schemes for image deformation methods in PIV. *Experiments in Fluids*, *38*(2), 233–243.

Atkinson, C., Buchmann, N. A., Amili, O., & Soria, J. (2013). On the appropriate filtering of PIV measurements of turbulent shear flows. *Experiments in Fluids*, *55*(1), 1654.

Atkinson C., Oberleithner, K. & Soria, J. (2014). PIV Illumination Intensity: An Unexpected Source of Error in Particle Displacement and Calibration. *17th International Symposium on Applications of Laser Techniques to Fluid Mechanics*, Lisbon, Portugal, 07-10 July.

Batchelor, G. K., & Townsend, A. A. (1948). Decay of isotropic turbulence in the initial period. *Proceedings of the Royal Society of London, 193,* 539-558.

Bendat, J., Piersol, A. (2010) Random Data. Analysis and Measurement Procedures. John Wiley & Sons, Hoboken, New Jersey. ISBN: 978-0470248775

Benedict, L. H., & Gould, R. D. (1996). Towards better uncertainty estimates for turbulence statistics. *Experiments in Fluids*, *22*, 129–136.

Burden, R. L., & Faires, J. D. (2002). *Análisis numérico, 7a. edición.* International Thomson Editores, S.A. ISBN 978-9706861343.

Buschmann, M. H., & Gad-El-Hak, M. (2003). Debate Concerning the Mean-Velocity Profile of a Turbulent Boundary Layer. *AIAA Journal*, *41*(4), 565–572.

Charonko, J. J., & Vlachos, P. P. (2013). Estimation of uncertainty bounds for individual particle image velocimetry measurements from cross-correlation peak ratio. *Measurement Science and Technology*, *24*(6), 65301.

Clark, T. T., & Zemach, C. (1998). Symmetries and the approach to statistical equilibrium in isotropic turbulence. *Physics of Fluids*, *10*(11), 2846–2858.

Davidson, P. A. (2004). *Turbulence.* Oxford University Press. ISBN: 978-0198529491.

De Gregorio, F. (2014). Helicopter Fuselage Drag Reduction Investigation. *Proceedings of the 17th International Symposium on Applications of Laser Techniques to Fluid Mechanics*. Lisbon, Portugal, 7-10 July.

De Jong, J., Cao, L., Woodward, S. H., Salazar, J. P. L. C., Collins, L. R., & Meng, H. (2009). Dissipation rate estimation from PIV in zero-mean isotropic turbulence. *Experiments in Fluids*, *46*(3), 499–515.

Elsinga, G. E., Scarano, F., Wieneke, B., & van Oudheusden, B. W. (2006). Tomographic particle image velocimetry. *Experiments in Fluids*, *41*(6), 933–947.

Ertunç, Ö., Özyilmaz, N., Lienhart, H., Durst, F., & Beronov, K. (2010). Homogeneity of turbulence generated by static-grid structures. *Journal of Fluid Mechanics*, *654*, 473–500.

Foucaut, J. M., Carlier, J., & Stanislas, M. (2004). PIV optimization for the study of turbulent flow using spectral analysis. *Measurement Science and Technology*, *15*(6), 1046–1058.

George, W. K., Wang, H., Wollblad, C., & Johansson, T. G. (2001). Homogeneous turbulence and its relation to realizable flows. *14th Australasian Fluid Mechanics Conference*, Adelaide, Australia, 10-14 December, 41–48.

Grant, I. (1997). Particle image velocimetry: A review. *Proceedings of the Institution of Mechanical Engineers, Part C: Journal of Mechanical Engineering Science*, *211*(1), 55–76.

Grayson, K., de Silva, C. M., Hutchins, N., & Marusic, I. (2016). Laser light sheet profile and alignment effects on PIV performance. *18th International Symposium on Applications of Laser and Imaging Techniques to Fluid Mechanics*. Lisbon, Portugal, 4-7 July.

Hart, D. P. (2000). Super-resolution PIV by recursive local-correlation. *Journal of Visualization*, *3*(2), 187–194.

Hinsch, K. D. (1995). Three-dimensional particle velocimetry. *Measurement Science and Technology*, *6*(6), 742.

Hinsch, K. D. (2002). Holographic particle image velocimetry. *Measurement Science and Technology*, *13*(7), R61.

Hinze, J. O. (1975). *Turbulence*. Second Edition. McGraw-Hill Book Company, Inc. ISBN: 0-07-029037-7.

Hjelmfelt, A. T., & Mockros, L. F. (1966). Motion of discrete particles in a turbulent fluid. *Applied Scientific Research*, *16*(1), 149–161.

Huang, H. T., Fiedler, H. E., & Wang, J. J. (1993). Limitation and improvement of PIV. *Experiments in Fluids*, *15*(3), 168–174.

Jiménez, R., Nogueira, J., & Legrand, M. (2016a). Simple tools to unveil characteristics of PIV Coupled errors. *Proceedings of the 18th International Symposium on Applications of Laser and Imaging Techniques to Fluid Mechanics.* Lisbon, Portugal, 4-7 July.

Jiménez, R., De Gregorio, F., Legrand, M., & Nogueira, J. (2016b). Characterization of the Flow around a Helicopter Fuselage Equipped with Vortex Generators for Drag Reduction. *Proceedings of the 18th International Symposium on Applications of Laser and Imaging Techniques to Fluid Mechanics.* Lisbon, Portugal, 4-7 July.

Kähler, C. J., Scharnowski, S., & Cierpka, C. (2012). On the uncertainty of digital PIV and PTV near walls. *Experiments in Fluids*, *52*(6), 1641–1656.

Kähler, C. J., Sammler, B., & Kompenhans, J. (2002). Generation and control of tracer particles for optical flow investigations in air. *Experiments in Fluids*, *33*(6), 736–742.

Keane, R. D., & Adrian, R. J. (1990). Optimization of particle image velocimeters. Part I : Double pulsed systems. *Measurement Science and Technology*, *1*, 1202–1215.

Keane, R. D., & Adrian, R. J. (1992). Theory of cross-correlation analysis of PIV images. *Applied Scientific Research*, *49*(3), 191–215.

Keane, R. D., & Adrian, R. J. (1992). Theory of cross-correlation analysis of PIV images. *Applied Scientific Research*, *49*(3), 191–215.

Knopp, T., Buchmann, N. A., Schanz, D., Eisfeld, B., Cierpka, C., Hain, R., … Kähler, C. J. (2015). Investigation of scaling laws in a turbulent boundary layer flow with adverse pressure gradient using PIV. *Journal of Turbulence*, *16*(3), 250–272.

Kolmogorov, A. N. (1941). The local structure of turbulence in incompressible viscous fluid for very large Reynolds numbers. *Doklady Akademii Nauk Sssr*, *30*(4), 301–305. Reprinted in 1991, *Proceedings of the Royal Society A. Mathematical, Physical and Engineering Sciences, 434* (1890), 9-13.

Kompenhans, J., Reichmuth, J. (1986). Particle imaging velocimetry in a low turbulent wind tunnel and other flow facilities. *Proceedings of the IEEE Montech'86 conference*, Montreal, Canada, October. AGARD conference proceedings no. 399, paper 35.

Kondjoyan, A., & Daudin, J. D. (1995). Effects of free stream turbulence intensity on heat and mass transfers at the surface of a circular cylinder and an elliptical cylinder, axis ratio 4. *International Journal of Heat and Mass Transfer*, *38*(10), 1735–1749.

LaVision (2007). FlowMaster. *Product Manual for DaVis 7.2*.

LaVision (2007). Sheet optics: Divergent. *Product Manual.*

Lavoie, P., Avallone, G., De Gregorio, F., Romano, G. P., & Antonia, R. a. (2007). Spatial resolution of PIV for the measurement of turbulence. *Experiments in Fluids*, *43*(1), 39–51.

Legrand, M. (2008). *Estudio y Caracterización de un Quemador Estabilizado por Giro.* PhD Thesis, Carlos III University of Madrid, Spain.

Legrand, M., Nogueira, J., Rodriguez, P. A., Lecuona, A., & Jimenez, R. (2017). Generation and droplet size distribution of tracer particles for PIV measurements in air , using propylene glycol / water solution. *Experimental Thermal and Fluid Science*, *81*, 1–8.

Legrand, M., Nogueira, J., Vargas, A. A., Ventas, R., & Rodríguez-Hidalgo, M. C. (2014). CCD image sensor induced error in PIV applications. *Measurement Science and Technology*, *25*(6).

Legrand, M., Nogueira, J., Ventas, R., & Lecuona, A. (2012). Simultaneous assessment of peak-locking and CCD readout errors through a multiple Δt strategy. *Experiments in Fluids*, *53*(1), 121–135.

Li, Y., Perlman, E., Wan, M., Yang, Y., Meneveau, C., Burns, R., … Eyink, G. (2008). A public turbulence database cluster and applications to study Lagrangian evolution of velocity increments in turbulence. *Journal of Turbulence*, *9*(31), 1–30.

Liu, R., & Ting, D. S. K. (2007). Turbulent Flow Downstream of a Perforated Plate: Sharp-Edged Orifice Versus Finite-Thickness Holes. *Journal of Fluids Engineering*, *129*(9), 1164–1171.

Liu, R., Ting, D. S. K., & Rankin, G. W. (2004). On the generation of turbulence with a perforated plate. *Experimental Thermal and Fluid Science*, *28*(4), 307–316.

Lourenco, L. M., Gogineni, S. P., & LaSalle, R. T. (1994). On-line particle-image velocimeter: an integrated approach. *Applied Optics, 33*(13), 2465–2470.

Maciel, Y., Rossignol, K.-S., & Lemay, J. (2006). A study of a turbulent boundary layer in stalled-airfoil-type flow conditions. *Experiments in Fluids*, *41*(4), 573–590.

Martin Harman (2016), *Security Data Sheet Martin Smoke and Haze Fluids*. Retrieved from http://www.martin.com/en-us/support/product-details/pro-smoke-high-density

Masullo, A., & Theunissen, R. (2016). "Improvement of PIV dynamic range in the presence of velocity gradients using multiple correlation peak analysis and self-adaptive windows". *Proceedings of the 18th International Symposium on Applications of Laser and Imaging Techniques to Fluid Mechanics.* Lisbon, Portugal, 4-7 July.

Mathieu, J., & Scott, J. (2000). *An Introduction to Turbulent Flow.* Cambridge University Press. ISBN: 978-0521775388.

Mathworks. (2015). *Random Number Generation: User's Guide* (r2015a). Retrieved February 16, 2016 from http://es.mathworks.com/help/matlab/random-number-generation.html

McCleney, A. B., Clement, S.A, & Bardet, P.M. (2016). Multi-scale, long recording, time-resolved PIV for turbulence statistics and uncertainty reduction in a turbulent jet. *Proceedings of the 18th International Symposium on Applications of Laser and Imaging Techniques to Fluid Mechanics.* Lisbon, Portugal, 4-7 July.

Meynart, R. (1980). Equal velocity fringes in a Rayleigh-Benard flow by a speckle method. *Applied Optics*, *19*(9), 1385–1386.

Meynart, R. (1982). Convective flow field measurement by speckle velocimetry. *Revue de Physique Appliquée (Paris) 17*(5), 301-305.

Nobach, H., & Bodenschatz, E. (2009). Limitations of accuracy in PIV due to individual variations of particle image intensities. *Experiments in Fluids*, *47*(1), 27–38.

Nogueira, J., Jiménez, R., Legrand, M. & Lecuona, A. (2014). PIV error sensitivity analysis for free turbulent flow characterization. *17th International Symposium on Applications of Laser Techniques to Fluid Mechanics*, Lisbon, Portugal, 07-10 July.

Nogueira, J., Lecuona, A., Legrand, M., Rodriguez, P. A., Ventas, R., & Rodríguez-Hidalgo M. C. (2012). Setup optimization for PIV measurements in presence of turbulence. *16th International Symposium on Applications of Laser Techniques to Fluid Mechanics*. Lisbon, Portugal, 09-12 July, 2012.

Nogueira, J., Lecuona, A., Nauri, S., Legrand, M., & Rodríguez, P. A. (2009). Multiple Δt strategy for particle image velocimetry (PIV) error correction, applied to a hot propulsive jet. *Measurement Science and Technology*, *20*(7), 74001.

Nogueira, J., Lecuona, A., Nauri, S., Legrand, M., & Rodríguez, P. A. (2011). Quantitative evaluation of PIV peak locking through a multiple Δt strategy: relevance of the rms component. *Experiments in Fluids*, *51*(3), 785–793.

Nogueira, J., Lecuona, A., & Rodríguez, P.A. (1997). Data validation, false vectors correction and derived magnitudes calculation on PIV data. *Measurement Science and Technology*, *8*(12), 1493–1501.

Nogueira, J., Lecuona, A., & Rodríguez, P. A. (1999). Local field correction PIV: on the increase of accuracy of digital PIV systems. *Experiments in Fluids*, *27*(2), 107–116.

Nogueira, J., Lecuona, A., & Rodríguez, P. A. (2001). Identification of a new source of peak locking, analysis and its removal in conventional and super-resolution PIV techniques. *Experiments in Fluids*, *30*(3), 309–316.

Novara, M., Schanz, D., Reuther, N., Kähler, C. J., & Schröder, A. (2016). Lagrangian 3D particle tracking in high-speed flows: Shake-The-Box for multi-pulse systems. *Experiments in Fluids*, *57*(8), 128.

Olsen, M. G., & Adrian, R. J. (2000). Out-of-focus effects on particle image visibility and correlation in microscopic particle image velocimetry. *Experiments in Fluids*, *29*(SUPPL. 1), S166–S174.

PIVTec GmbH (2010). *PIVview software manual, version 3.0.9*. Retrieved September 15, 2014 from http://www.pivtec.com/

Poelma, C., Westerweel, J., & Ooms, G. (2006). Turbulence statistics from optical whole-field measurements in particle-laden turbulence. *Experiments in Fluids*, *40*(3), 347–363.

Pope, S. B. (2000). *Turbulent flows*. Cambridge University press. ISBN: 978-0521598866.

Prasad, A. K., & Adrian, R. J. (1993). Stereoscopic particle image velocimetry applied to liquid flows. *Experiments in Fluids*, *15*(1), 49–60.

Prasad, A. K., Adrian, R. J., Landreth, C. C., & Offutt, P. W. (1992). Effect of resolution on the speed and accuracy of particle image velocimetry interrogation. *Experiments in Fluids*, *13*(2), 105–116.

Raffel, M.; Willert, C.; Wereley, S.; Kompenhans, J. (2007). *Particle Image Velocimetry: A Practical Guide*. Springer-Verlag Berlin Heidelberg. ISBN 3-540-72307-2.

Reuther, N., Schanz, D., Scharnowski, S., Hain, R., Schröder, A., & Kähler, C. J. (2015). Experimental investigation of adverse pressure gradient turbulent boundary layers by means of large-scale PIV*. 11th International Symposium on Particle Image Velocimetry,* 14-16 September, Santa Barbara, CA (United States of America).

Richardson, L. F. (1922). *Weather Prediction by Numerical Process.* Cambridge University Press.

Roach, P. E. (1987). The generation of nearly isotropic turbulence by means of grids. *International Journal of Heat and Fluid Flow*, *8*(2), 82–92.

Saarenrinne, P., & Piirto, M. (2000). Turbulent kinetic energy dissipation rate estimation from PIV velocity vector fields. *Experiments in Fluids*, *29*(1), S300--S307.

Saarenrinne, P., & Piirto, M. (2000). Turbulent kinetic energy dissipation rate estimation from PIV velocity vector fields. *Experiments in Fluids*, *29*(1), S300–S307.

Sagaut, P., Cambon, C. (2008). *Homogeneous Turbulence Dynamics.* Cambridge University Press. ISBN: 978-0521855488

Scarano, F. (2002). Iterative image deformation methods in PIV. *Measurement Science and Technology*, *13*(1), R1.

Scarano, F. (2013). Tomographic PIV: principles and practice. *Measurement Science and Technology*, *24*(1), 12001.

Scarano, F., & Riethmuller, M. L. (1999). Iterative multigrid approach in PIV image processing with discrete window offset. *Experiments in Fluids*, *26*(6), 513–523.

Scarano, F., & Riethmuller, M. L. (2000). Advances in iterative multigrid PIV image processing. *Experiments in Fluids*, *29*(7), S051–S060.

Sciacchitano, A., Neal, D. R., Smith, B. L., Warner, S. O., Vlachos, P. P., Wieneke, B., & Scarano, F. (2015). Collaborative framework for PIV uncertainty quantification: comparative assessment of methods. *Measurement Science and Technology*, *26*(7), 74004.

Sciacchitano, A., Wieneke, B., & Scarano, F. (2013). PIV uncertainty quantification by image matching. *Measurement Science and Technology*, *24*(4), 45302.

Stein, J. (2000). *Digital Signal Processing: a Computer Science perspective.* John Wiley and Sons, Inc. ISBN: 978-0471295469.

Tanaka, T., & Eaton, J. K. (2007). A correction method for measuring turbulence kinetic energy dissipation rate by PIV. *Experiments in Fluids*, *42*(6), 893–902.

Timmins, B. H., Wilson, B. W., Smith, B. L., & Vlachos, P. P. (2012). A method for automatic estimation of instantaneous local uncertainty in particle image velocimetry measurements. *Experiments in Fluids*, *53*(4), 1133–1147.

Townsend, A. A. (1976). *The Structure of Turbulent Shear Flow*. Cambridge University Press. ISBN: 978-0521298193.

Wereley, S. T., & Meinhart, C. D. (2001). Second-order accurate particle image velocimetry. *Experiments in Fluids*, *31*(3), 258–268.

Wernet, M. P. (2005). Symmetric phase only filtering: a new paradigm for DPIV data processing. *Measurement Science and Technology*, *16*(3), 601–618.

Westerweel, J. (1993) *Digital Particle Image Velocimetry — Theory and Application.* PhD Thesis. Delft University of Technology, the Netherlands.

Westerweel, J. (1994). Efficient detection of spurious vectors in particle image velocimetry data sets. *Experiments in Fluids*, *16*(3), 236–247.

Westerweel, J. (1997). Fundamentals of digital particle image velocimetry. *Measurement Science and Technology*, *8*(12), 1379–1392.

Westerweel, J. (1998). Effect of sensor geometry on the performance of PIV. *9th International Symposium on Applications of Laser Techniques to Fluid Mechanics*. 13-16th July, Lisbon (Portugal).

Westerweel, J. (2000). Theoretical analysis of the measurement precision in particle image velocimetry. *Experiments in Fluids*, *29*(Suppl. 1), S3–S12.

Westerweel, J. (2008). On velocity gradients in PIV interrogation. *Experiments in Fluids*, *44*(5), 831–842.

Westerweel, J., Dabiri, D., & Gharib, M. (1997). The effect of a discrete window offset on the accuracy of cross-correlation analysis of digital PIV recordings. *Experiments in Fluids*, *23*(1), 20–28.

Westerweel, J., Elsinga, G. E., & Adrian, R. J. (2013). Particle Image Velocimetry for Complex and Turbulent Flows. *Annual Review of Fluid Mechanics*, *45*(1), 409–436.

Wieneke, B. (2005). Stereo-PIV using self-calibration on particle images. *Experiments in Fluids*, *39*(2), 267–280.

Wieneke, B. (2015). PIV uncertainty quantification from correlation statistics. *Measurement Science and Technology*, *26*(7), 74002.

Willert, C. (1997). Stereoscopic digital particle image velocimetry for application in wind tunnel flows. *Measurement Science and Technology*, *8*(12), 1465.

Willert, C. E., & Gharib, M. (1991). Digital particle image velocimetry. *Experiments in Fluids*, *10*, 181–193.

Yeung, P. K., & Zhou, Y. (1997). Universality of the Kolmogorov constant in numerical simulations of turbulence. *Physical Review E*, *56*(2), 1746–1752.

ANNEXES

Annex I: Calculation of *E(κ)* from 2D-2C data

All the possibilities below only work for homogeneous turbulence. The data available are the in-plane velocities u_1 and u_2, defined in a 2D plane. The following have been identified:

1. From the measured velocity fields u_1 and u_2, both the longitudinal, $E_{11}(\kappa_1)$, and transversal, $E_{22}(\kappa_1)$, one-dimensional spectra are calculated, by recurring to expression (5.13). *E(κ)* is obtained from the following expression (Pope, 2000):

$$E(\kappa) = -\kappa\left(\frac{d}{d\kappa}\left(\frac{1}{2}E_{11}(\kappa_1) + E_{22}(\kappa_1)\right)\right)$$

2. Departing from the 1D auto-correlation (longitudinal and transverse) functions $f(r)$ and $g(r)$ the velocity correlation tensor is obtained, in all 3D spatial directions. From that, $\Phi_{ij}(\boldsymbol{\kappa})$ is obtained, from expression (5.8) and then $E(\kappa)$ from expression (5.9) and (5.10).

   $f(r)$ and $g(r)$, that can be obtained from the measurements, and are defined as:

$$f(r) = \langle u_1(\boldsymbol{x} + \boldsymbol{e_1 r})u_1(\boldsymbol{x})\rangle / \langle u_1^2\rangle$$

$$g(r) = \langle u_2(\boldsymbol{x} + \boldsymbol{e_1 r})u_2(\boldsymbol{x})\rangle / \langle u_2^2\rangle$$

   $R_{ij}(\boldsymbol{r})$ can be expressed in terms of $f(r)$ and $g(r)$ as (Pope, 2000):

$$R_{ij}(\boldsymbol{r}) = u'^2\left(g(r)\delta_{ij} + [f(r) - g(r)]\frac{r_i r_j}{r^2}\right)$$

   So, summing up:

$$u_1, u_2 \Rightarrow f(r), g(r) \Rightarrow R_{ij}(\boldsymbol{r}) \Rightarrow \Phi_{ij}(\boldsymbol{\kappa}) = \mathcal{F}_{[x,y,z]}\{R_{ij}(\boldsymbol{r})\} \Rightarrow E(\kappa) = \oint \Phi_{ii}(\boldsymbol{\kappa})$$

3. Again, departing from the 1D auto-correlation (longitudinal and transverse) functions $f(r)$ and $g(r)$, the sum of the diagonal components of the two point velocity correlation tensor is calculated ($\sum_i R_{ii}(\boldsymbol{r})$). The sum can be expressed as (Davidson, 2004):

$$\sum_i R_{ii}(\boldsymbol{r}) = u'^2\big(f(r) + 2g(r)\big)$$

   The function depends only on $r=|\boldsymbol{r}|$, i.e. it has spherical symmetry. Then, a Fourier transform in spherical coordinates can be employed, giving (Davidson, 2004):

$$E(\kappa) = \frac{2}{\pi}\int_0^{+\infty} R(r)\kappa r \sin(\kappa r)\, dr$$

   In the transform, $R(r)$ has been used: $R(r) = 1/2\sum_i R_{ii}(\boldsymbol{r})$.

4. The two-point correlation function R_{ij} is calculated in the 2D measurement planes (for i,j=1,2) in the 2D measurement planes. That information is used to obtain

$R_{ij}(\boldsymbol{r})$ (for *i,j*=1,2,3) in the 3D space, by interpolation. Then, the Fourier transform in *x,y,z* is used to obtain $\Phi_{ij}(\boldsymbol{\kappa})$ and then *E(κ)* is obtained as in case 2.

$$R_{ij}(x,y,0) \Rightarrow R_{ij}(\boldsymbol{r}) \Rightarrow \Phi_{ij}(\boldsymbol{\kappa}) = \mathcal{F}_{[x,y,z]}\{R_{ij}(\boldsymbol{r})\} \Rightarrow E(\kappa) = \oint \Phi_{ii}(\boldsymbol{\kappa})$$

Annex II: Effect of the validation criteria in the results of synthetic images

In the graphs below the comparison between the PIV Simulator and synthetic images results, in terms of $\Delta S_{LL}(r)$, is shown, for the three laser sheet thickness that are used in Chapter 7 to analyze spatial gradients effects. The synthetic images results are obtained from the vectors that pass two validation criteria, an allowable vector range and a median filter, as detailed in section 3.3.4:

Th/η ~9

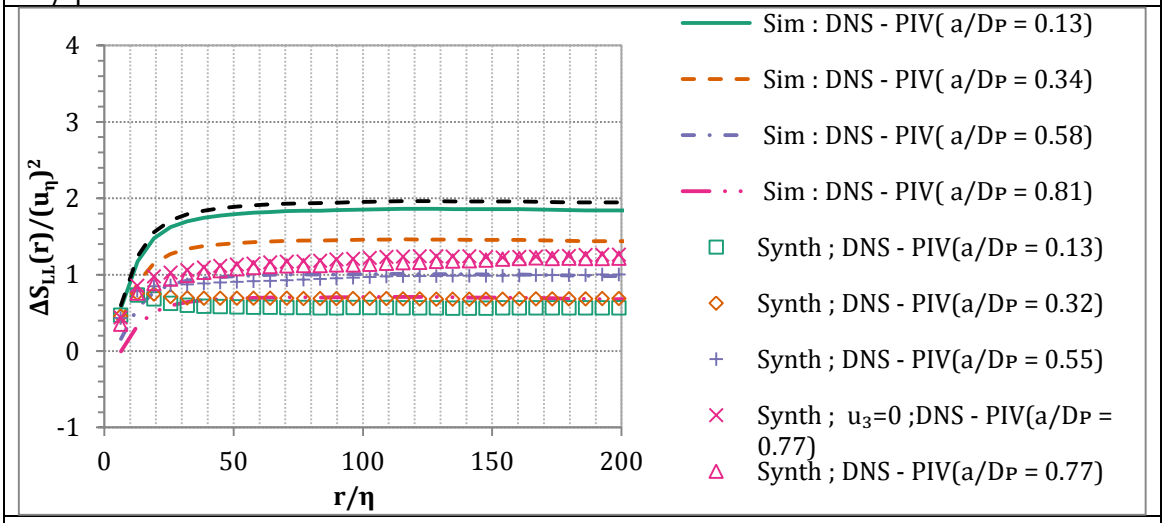

Th/η ~17

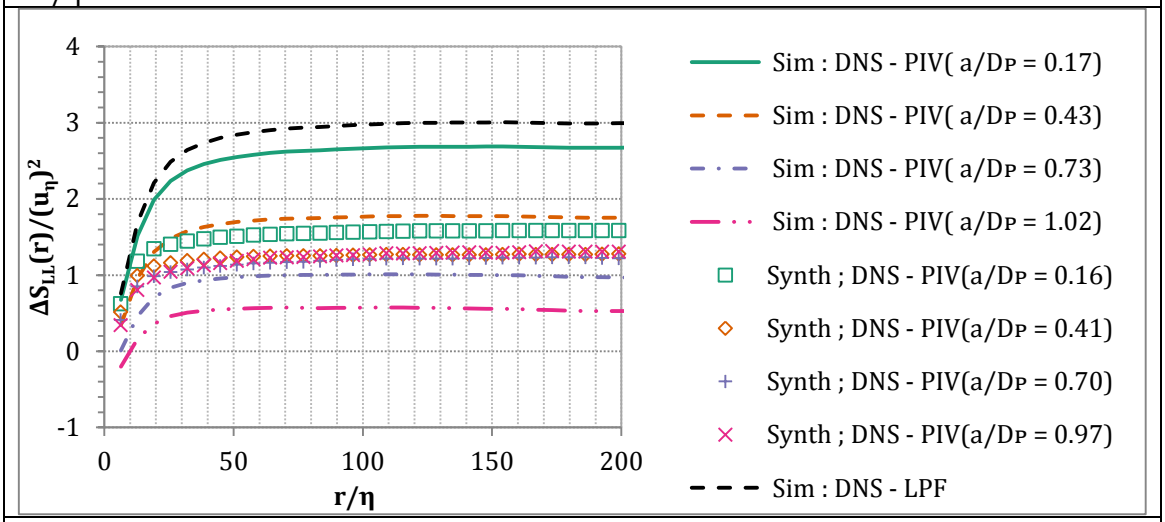

Th/η ~29

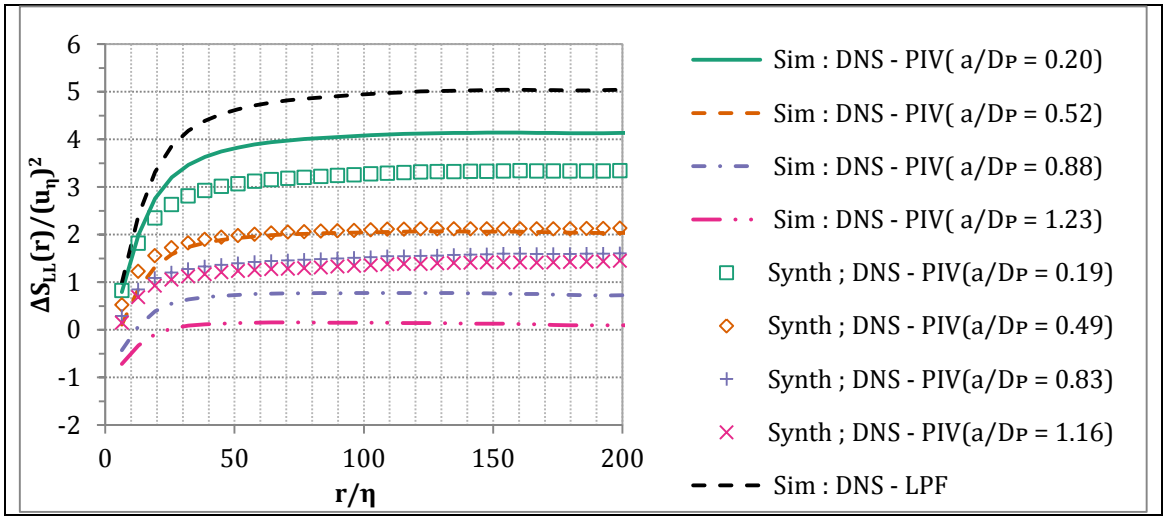

From the graphs, it can be observed that:

- For the Th/η=8.6 it can be observed that $\Delta S_{LL}(r)\{u\}$ increases with Δt (i.e. $S_{LL}(r)\{u\}$ decreases). This should be produced by the random errors in determining the correlation peak location, $\xi_{\Delta x}$, and peak-locking errors, decreasing and the peak-splitting influencing very little (or nothing at all).
- For the Th/η=17.2 and 29.5 the value of $\Delta S_{LL}(r)\{u\}$ decreases with Δt. The decrease is smaller than when using only the first validation step. This fact could be explained because the possible outliers are removed or because the vectors with larger peak-splitting errors are removed.
- The results with both validation steps show barely any effect on the smallest Δt cases and therefore no effect on the low-pass effect observed on the laser sheet thickness variation.

Annex III: Effect of the validation criteria in the results of real images

In the graphs below the comparison between the PIV Simulator and synthetic images to the experimental images results, in terms of $\Delta S_{LL}(r)$, is shown, for the three laser sheet thickness that are used in Chapter 7 to analyze spatial gradients effects. Both the synthetic images results and real images results are obtained from the vectors that pass two validation criteria, an allowable vector range and a median filter, as detailed in sections 3.3.4 and 6.5.1:

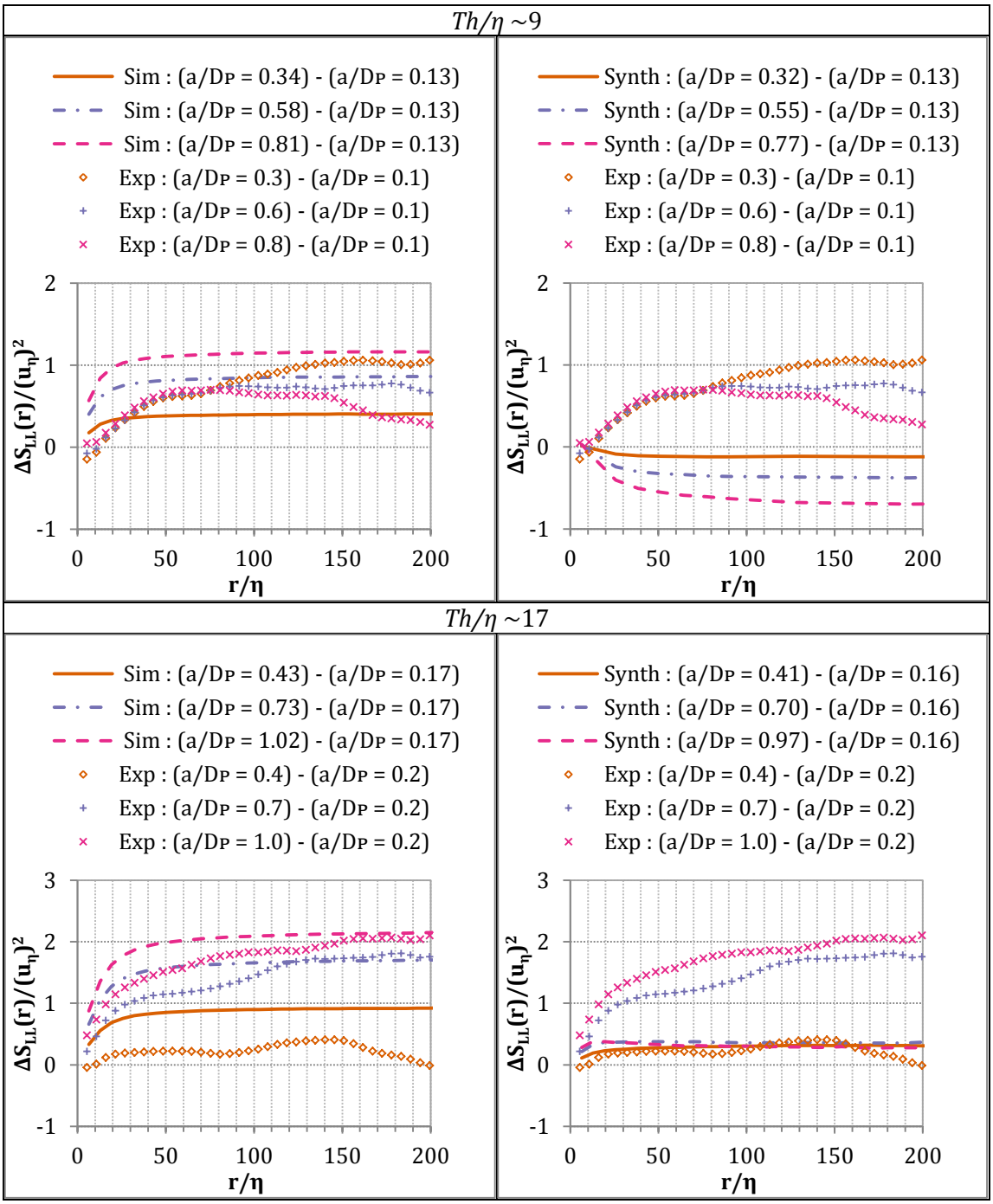

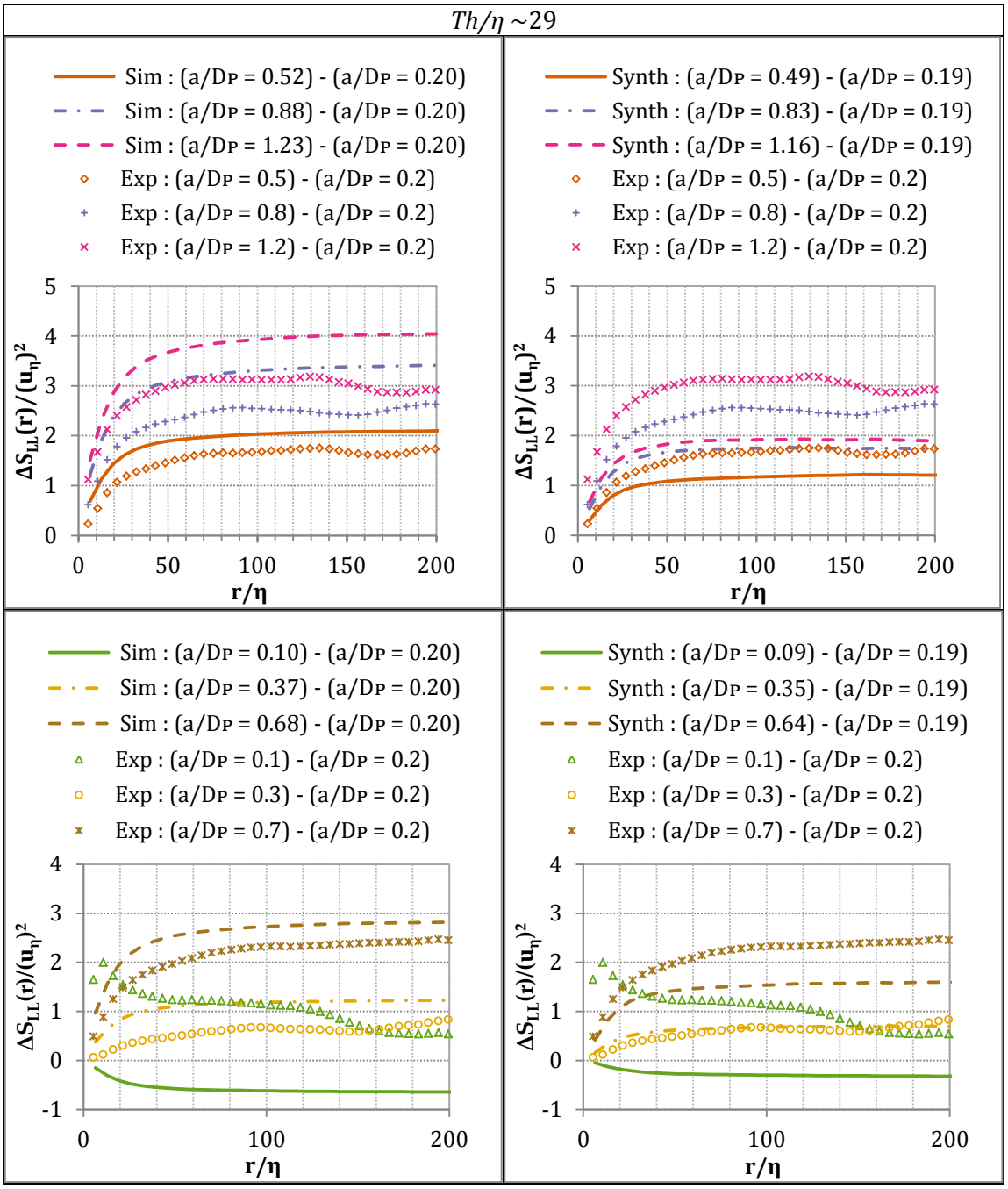

The following observations can be made from these results:

- For the smallest *Th*, the same increase is given for all Δt's, with only slight variations in the small scales (aside from the variations in the large scales induced by the problems described in section 6.5.5). The experimental results do not follow the same tendency than synthetic images either, for which $\Delta S_{LL}(r)\{u\}$ gets more negative as Δt increases (which is analyzed in the previous annex). As to the experimental results tendency, the fact that there is a negative $\Delta S_{LL}(r)\{u\}$ at the small scales could be explained by the reference case having peak-locking errors, as was mentioned already. As to the positive $\Delta S_{LL}(r)\{u\}$ on larger scales, it is very likely produced by either undetected outliers and/or peak-splitting phenomenon.

- For the medium and larger laser sheet thickness, peak-splitting and or outliers increase progressively the $\Delta S_{LL}(r)\{u\}$ values observed. The experimental results are above the values predicted by synthetic images and below the values predicted by the PIV Simulator.